University of Bath

UNIVERSITY OF BATH

University of Bath

PHD

Simulation of pulsatile flow in baffled permeable channel for membrane filtration system

Wang, Yuyan

Award date:
1993

Awarding institution:
University of Bath

Link to publication

SIMULATION OF PULSATILE FLOW IN

BAFFLED PERMEABLE CHANNEL FOR

MEMBRANE FILTRATION SYSTEM

submitted by

Yuyan Wang

for the degree of PhD

of the University of Bath

1993

UMI Number: U552458

UMI

Dissertation Publishing

UMI U552458

ProQuest

DEDICATION

"Truth does not depart from human nature"

Confucius

TO MY PARENTS

ACKNOWLEDGEMENTS

CONTENTS

INDEX OF FIGURES

INDEX OF TABLES

ABSTRACT

Concentration polarization and fouling are the major bottlenecks limiting more extensive large scale industrial implementation of membrane technology. One of the common approaches taken to combat concentration polarization and fouling is to improve the hydrodynamic conditions at the membrane surface thereby reducing the concentration build-up at the wall. This is achieved most simply by operating with turbulent cross-flow or by modification of the channel geometry. The performance can, for ultrafiltration (Finnigan et al. 1989) and microfiltration (Howell et al. 1992b), also be improved by using pulsatile flow in baffled systems.

In this project an approach is developed using Computational Fluid Dynamics(CFD) for the calculation of flow pattern, shear rate, vortex strength, pressure drop and phase shift, power consumption, particles advection and diffusion and boundary concentration and flux in a permeable channel by using baffles alone and in the combination of pulsatile flow with a group of numerical simulation programs.

Experimental flow visualisation and simulated flow patterns are compared with a reasonable consistency. The comparisons between the analytically calculated and numerically simulated shear rate, pressure drop and power density in the conventional tube with steady flow suggest that the models are not only qualitatively correct but also provide quantitative accuracy.

Flow patterns in a central baffle situation are somewhat different from those with wall baffles. In the former case the vortex formed behind the baffle

intensifies with increasing Reynolds Number but does not fill the entire space between the obstructions, whilst, in the latter case the recirculating region grows to fill the entire baffle space. For central baffles, there is an additional vortex formed near the tube wall when the Reynolds Number reaches about 200. The wall suction at levels realistic for membrane permeation does not distort the macroscopic flow field. No distortion was observed with 1% of the flow going through the wall in a length of the tube diameters. Flow patterns are identified on a Re_o/St diagram for Re_o in the range [5 , 1000] and St in the range [0.1 , 4].

The wall shear rate in central baffles is much higher that with either wall baffles or without baffle. In steady flow with central baffles, the dimensionless wall shear rate linearly increases as Reynolds number increases whereas with wall baffles and without baffles it stays constant. For unsteady state, the dimensionless wall shear rate in all three cases is a monotonically increasing function of Reynolds number. In a rectangular module the Re_o/St diagram in term of average wall shear rate has shown when $Re_o > 150$ it may have a maximum in the middle of the Strouhal number range at about $St = 0.5$.

The vortex strength at the instant of zero flow is larger for wall baffles than with central baffles at $St = 1$, and greater with central baffles than with wall ones at small St and vice versa at intermediate St. The maximum with respect to Strouhal number exists at about $St = 0.5$ for both tubular and rectangular modules.

There is a phase shift between the pressure and velocity fluctuation which can lead to a significant power consumption reduction for the system. For the case of creeping flow the pressure is in phase with the velocity. As Re_o or St increases there is a progressive increase in the phase shift for both tubular and

rectangular module.

The comparison of power consumption among baffles alone and in the combination of pulsatile flow shows that central baffles uses more energy than wall baffles and illustrates that pulsatile flow uses less energy than steady flow in the central baffles and no baffles case. With wall baffles the curves for steady and oscillatory flow are similar, with the latter being lower, for the greater part of the Re range when $St = 1$. With central baffles an optimum $St = 0.1$ exists for the minimum power density. For the dependency on baffle flow area ratio with central baffles PD increases sharply when baffle area increases while with wall baffles it appears more constant.

By solving the coupled mass balance and osmotic model the local flux and wall concentration are obtained. The illustrative results of flux enhancement up to 66% and less energy consumption ascertain the earlier experimental discovery that ultrafiltration and microfiltration performance can be improved by using pulsatile flow in a baffled membrane system. Central baffles are superior to wall baffles in tubular module and baffles are superior to no baffle in rectangular module at large Re. The addition of pulsations significantly enhanced the fluxes and reduced the wall concentrations for Re greater than 100. When expressed on a power consumption basis, using the same energy a pulsatile process achieves higher membrane flux. At low flowrate pulsatile flow without any baffle provides a better performance because baffled systems were shown to dissipate energy more effectively and at higher flowrate the combination of central baffles with pulsatile flow is the best.

CHAPTER 1

INTRODUCTION

1.1 Motivation for the Study

The advent of sophisticated electronic computers has made it possible to predict flow behaviour and the kinds related to flow based upon suitable mathematical description and numerical implementation. Such study of numerical investigation of fluid mechanics in known as Computational Fluid Dynamics (CFD). Currently, CFD is being applied to a wide area of engineering fields, as tabulated in Table I.

Table I Engineering fields and application of CFD

Engineering fields	Applications
Aeronautics	Space shuttle, Hypersonic plane, STOL design
Biomechanics	Artificial heart, Blood vein prostheses
Biotechnology	Beer production, Bioreactor design
Civil engng.	Tsunami wave, Skyscraper, Harbour designs
Electronics	Semiconductor production, IC cooling
Mechanics	Turbojet design, Car engine design
Meteorology	Weather prediction, Typhoon course prediction
Nuclear engng.	Thermal hydraulics, MHD analyses

CFD has attracted attention in the process industries where it has not only been developed technically--in improved numerical methods, modelling of various phenomena and validation of applications--but also in its ease of use for the engineer.

During the modern development of membrane separation processes, early workers recognized the intimate relationship between mass transfer and convective fluid flow. With the appearance of a comprehensive treatise dealing with momentum, energy, and mass transport, models of varying complexity were developed linking convective fluid flow and mass transport for pressure-driven membrane processes. Although membranes have been packaged in pressure modules of various designs, in the majority the feed solution moves across the membrane in tangential flow (also called cross-flow), allowing fluid to be removed laterally by suction through the duct or channel walls. It has been known for some time that the performance of a pressure-driven membrane process is related to the tangential fluid mechanics across the membrane surface and that the build-up of dissolved solutes can be predicted and controlled at the membrane-solution interface through an understanding of the fluid mechanics and mass transfer. A detailed understanding of the fluid mechanics is a prerequisite to study mass transport problems such as concentration polarisation and fouling.

Concentration polarization and fouling is the major bottleneck limiting the rate of large scale industrial implementation of membrane technology. One of the common approaches taken to combat concentration polarization and fouling is to improve the hydrodynamic conditions at the membrane surface. This is achieved

most simply by operating with turbulent cross-flow or by modification of the channel geometry. Finnigan et al. (1989) and Howell et al. (1992b) established that ultrafiltration and microfiltration performance can be improved by using pulsatile flow in a baffled channel membrane system, and a central baffle system is considered to give a best all-round performance of the baffled systems investigated on a flux and power consumption basis. Baffles were shown to be dissipating energy more effectively than a conventional system. Fluxes of similar magnitude could be obtained in a conventional system but only at a much greater power consumption. The important and critical factors in the pulsatile flow technique appear to be the vortex mixing mechanism, that is reversing flow forming eddies and convecting the eddy from the wall to the main body of the fluid, and a steady streaming mechanism. The fluid in the left of each cell moves anticlockwise from cycle to cycle while the fluid in the right of each cell moves clockwise from cycle to cycle. These phenomena produces a complex time dependent eddy pattern which increases fluid mixing and raises the wall shear rate and ultimately the flux enhancement is achieved. This thesis is a simulation study of the flow patterns, particle motion, boundary concentration and flux which occur during unsteady flow in a baffled permeable channel. Such kind of simulation can facilitate a greater understanding of the filtration by supplying both a qualitative flow image which is difficult to be experimentally visualized in a membrane system when the effect of the permeation flux through the membrane on the flow pattern is accounted for and a quantitative assessment of several important variables so that it is possible for one to optimise the ideal hydrodynamic conditions. The important criteria include

a) generate high shear rate/scouring at the membrane surface;

b) produce good radial mixing avoiding stagnant regions;

c) produce minimal axial dispersion which is especially important for thickening operation where plug flow is desirable;

d) generate higher fluxes for the same energy consumption as a conventional system.

It is also valuable to achieve best performance in term of, such as maximum vortex strength, maximum wall shear rate, maximum average distance of particle migration and lower boundary concentration etc..

1.2 Literature Review

Before describing the scope of this work, numerical simulation of incompressible Newtonian fluid flow and cross-flow filtration in constricted tubular and rectangular channels are reviewed.

As is well-known, the computational methods for fluid flow are roughly categorized into two typical numerical schemes: the Finite Difference Method (FDM) and the Finite Element Method (FEM). The essential difference of both is the way of spatial discretisation. In FDM, the differential equation (PDE's) are directly replaced by the finite-differencing, and the solution is obtained at each grid. The scheme for incompressible fluid flow is described well in the book written by Roache (Roache 1976). On the other hand, in FEM, the weak forms of PDE's are discretized in an indirect manner that is using a basis function for

solution expansion. Consequently, one can seek the FEM solution in larger solution spaces where weaker differentiability than that of the original PDE is required, and the FEM solution can be found over the whole computational domain. FDM takes much less computational effort and FEM is better for complicated geometry and boundary conditions.

Hung and Macagno (1966) studied flow downstream of a two dimensional expansion, and observed that the length of the recirculating region varied linearly with Reynolds number. They solved the problem using a vorticity/stream function formulation, and found that it was computationally faster and more accurate to increase gradually flow in the channel, solving the unsteady flow equations rather than immediately try to solve the steady flow equations.

Mills (1968) and Greenspan (1973) have studied numerically flow through an orifice. When the Reynolds number is zero Mills showed that equal sized recirculating regions exist upstream and downstream of the orifice. The symmetry is necessary due to the direction independence of creeping flows.

A numerical solution for steady flow and heat transfer in a tube containing spaced baffles has been calculated by Rowley and Patankar (1984). As the Reynolds number increase, recirculating regions grow until they fill the entire inter-baffle space. Rowley and Patankar found that the presence of baffles in steady laminar flow can cause a decrease in the heat transfer from the tube wall.

Solution of flow equations through periodically smoothly varying tubes have been used largely to model the flow through packed beds and porous media in order to calculate pressure drop, mass transfer and flow dispersion. Chow and Soda (1972) found an analytic solution for steady flow in a wavy walled tube of long wavelength, and predicted both separation and reattachment would occur on the divergent parts of the tube.

Cheng et al (1972,1973) investigated oscillating flow in a two dimensional channel containing a square symmetrical obstruction on each of the channel walls. As the flow accelerates eddies form both downstream and upstream of the obstructions with the downstream eddy larger.

Bellhouse et al. (1973) developed a high-efficiency membrane oxygenator which combined large laminar oscillations with a much smaller mean flow through a wavy-walled channel to achieve high mass transfer rates. To explain the mechanism of this enhancement Sobey (1980, 1983, 1985a) considered flow ranges close to the operating conditions of a membrane oxygenator and numerically analyzed unsteady flows in a sinusoidal wavy-walled channel for laminar flow. Oscillatory flow was found to induce a vortex formation/ejection cycle believed to be responsible for enhanced mass transfer in the membrane oxygenator.

Ralph (1986,1987, 1988) extended the Re_0 and St range investigated by Sobey(1980) for the wavy-walled tube geometry of the membrane oxygenator device and identified eight different flow structures and Re_0/St diagram Figure 1

in term of vortex strength. He also reported that the pressure drop may vary non-sinusoidally, even though the imposed variation in flow rate is sinusoidal because energy may be stored in strong vortices formed during the acceleration phase of the flow cycle, and partially returned to the main flow later.
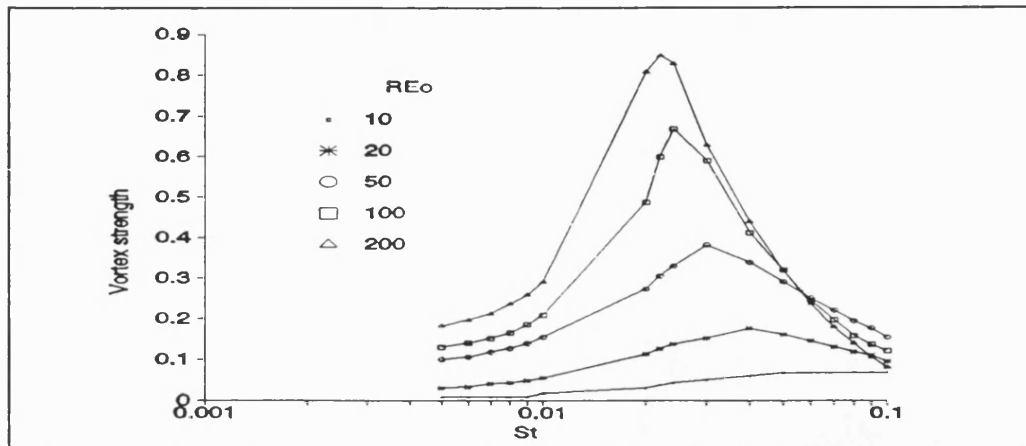
Figure 1 Ralph's Re_0/St diagram in term of vortex strength.

Howes (1988) studied the flow patterns and particle motion in wall baffles tubular channel using numerical simulation and flow visualisation which supports the earlier assertion that pulsatile, reversing flow in this kind of channel provides a mechanism for forming eddies and convecting the eddy from the wall to the main body of the fluid and identified seven different flow regimes.

Nishimura et al. (1989) numerically and experimentally studied the effect of the Strouhal number ($d/4\pi x_0$) on several flow characteristics in a wavy-walled channel. They found that although oscillatory flow is characterised by a vortex formation/ejection cycle for any Strouhal number, the peak of vortex strength appears at an intermediate Strouhal number for both instantaneous flow and

steady streaming and the time required for erosion of the ejected vortex at the centerline of the tube is closely related to the vortex strength at the instant of zero flow rate.

Howes et al. (1991) reported numerically generated flow visualisation simulations for a 2D rectangular channel which can contain periodic wall baffles. For unsteady flows in this geometry a regime of chaotic advection is observed when baffles are present. They found that the unsteadiness takes one of two forms: a "natural" unsteadiness caused by a symmetry breaking instability of the flow, or a "forced" unsteadiness generated by applying an oscillatory component to the flow.

Johnson et al. (1992) reported simulation of blood flow in a straight, deformable vessel assuming a functional form of the solution in order to simplify the required computations. The resulting equations are cast in finite-difference form and solved explicitly. The model illustrates the dependence of flow rate and shear rate on the amplitude of the vessel wall motion and the phase difference between the applied pressure difference and the oscillations of the vessel radius.

Granger et al. (1989) presented an analytical solution for the axial and transverse steady flow fields in laminar flow in porous channels for both a rectangular channel with one porous wall and a porous tubular channel and concluded that long channels with high permeability membranes can have significant departures from the constant permeation rate.

Schmitz et al. (1990) developed a trajectory steady state model of buoyant spherical particles moving near the microfiltration membrane using hydrodynamic field.

Pangrle et al. (1991) used FEM to study steady, incompressible, laminar flow in porous tube systems. The Navier-Stokes equations were used to describe the phenomena in the tube and shell space while the continuum theory of Brinkman was used to describe flow in the porous tube wall. The solution method provided velocities and pressure for a wide range of Reynolds numbers and operational modes. The model was then used to investigate the effect of shell diameter and tube length on the flow field for closed shell, closed end, and cross flow operation. Their results showed that decreasing shell diameter can decrease shell side flow in closed shell operation, cause the ejection velocity to be a nonlinear function of axial position in closed end operation and decrease permeate rate in cross flow operation.

Bashir et al. (1992) presented a theoretical development which describes the time- and space-dependent flux during cross-flow filtration of a microbial suspension under laminar flow conditions. The treatment is based on the numerical solution of the set of non-stationary momentum and material balance equations. A time moving boundary condition at the porous wall describes the dynamics of cake build-up and flux decline.

Table II Summary of previous numerical simulation work on pulsatile flow in the constricted channel

Authors	Geometry	Parameter-range	Method of Solution
Sobey(1980)	Wavy-walled channel	$Re_o = 3.75 - 150$ $St = 0.005 - 0.02$	Finite difference Dufort-Frankel for Vorticity, over-relaxation for Stream
Ralph(1986)	Wavy-walled tube	$Re_o = 10 - 300$ $St = 0.0001 - 1$	similar to the above
Howes(1988)	Wall baffled tube	$Re_o = 5 - 640$ $St = 0.25 - 4$	similar to Sobey's with multigrid convergence acceleration
Nishmura et al(1989)	same as Sobey's	$Re_o = 36.6$ $St = 0.01 - 0.173$	Galerkin finite element
Howes et al (1991)	Wall baffled channel	$Re_o = 100 - 300$ $St = 1$	similar to Howes' (1988)
Mackay et al(1991)	Wall and central baffled tube	$Re_o = 40 - 200$ $St = 1$	similar to Howes' (1988)

1.3 Scope of this Thesis

Flow patterns for pulsatile flow through a central baffled tube and one-side wall baffled rectangular channel appear not to have been previously studied. Several programmes using finite differences has been developed from the existing code to solve the Navier-Stokes and continuity equations for laminar axisymmetric and asymmetric incompressible Newtonian flow in such tubular and rectangular channels. Flow regimes for pulsatile flow have been identified and compared with the available experimental flow visualisation.

The effect of the oscillatory Reynolds number and the Strouhal number on the wall shear rate and vortex strength are evaluated.

A method for modelling cross-flow filtration has been developed which generates the flow field by solving the time-dependent Navier-Stokes equations and then the local flux, pressure and the wall concentration along the membrane are calculated by mass balances and an osmotic pressure model with the pre-generated flow field. The comparison between different geometry and hydrodynamic conditions is drawn on a flux and power consumption basis.

The power consumption of the conventional and baffled systems under steady and pulsed flow conditions is compared to determine whether the filtration performance of the baffled systems is superior to that of a conventional system at the same power input.

1.4 Contents of this Thesis

This thesis contains seven chapters. The mathematical procedure for simulation is developed in the second chapter. The third chapter details the results for flow patterns and the comparisons with experimental visualisation. Chapter four contains the quantitative analysis of wall shear rate and vortex strength. Chapter five contains the pressure drop results and the comparison on power consumption between conventional and baffled pulsatile system. Chapter six develops an approach for modelling cross-flow filtration. The final chapter contains discussion and conclusions of the work carried out in the thesis.

CHAPTER 2

GOVERNING EQUATION AND ITS SOLUTION

The theoretical description presented here is restricted to material relevant to this investigation. Section 2.1 describes the hydrodynamic, geometric parameters and various models used to characterise the baffled tubular/rectangular membrane system under steady and pulsed flow conditions. Section 2.2 details numerical algorithm for solving these mathematical models.

2.1 Mathematical model and its parameters

2.1.1 General modelling approach

The main objectives of process simulation are to have a cost-efficient tool for experimental guidance. Three basic modelling methodologies can be distinguished: Empirical, stochastic, and deterministic. The deterministic approach is exclusively employed in modelling membrane transport and is used in this thesis. A system conceptualisation and mathematical modelling framework which is employed in this work is given in Figure 2. The simulation used for this work is in three parts:

a *fluid mechanics model*

which generates the velocity field;

a *particle motion procedure*

   which calculates the locations of marker particles as they are advected

   and/or diffused by the velocity field;

an *osmotic pressure model associated with convection-diffusion of species*

   for evaluating concentration near the membrane surface and permeate

   flux.

   The numerical simulation are incorprated with the graphic visulization to

show itself which consists of Stream fuction contour, velocity vector fields and

particle trajectories.

INPUT DATA

(1) System Parameters
(a) Channel geometry
(b) Fluid properties
(c) Membrane characteristics

(2) Operational Conditions
(a) Maximum flow rate
(b) Applied pressure
(c) Solute concentration

(3) Boundary Conditions
(a) Initial wall flux

SUBMODELS

| Flow Model (a) N.S. (b) Particle Transportation | Mass-Transfer Model Convection-diffusion of species | Auxiliary Model Membrane osmotic pressure |

SOLUTION TECHNIQUES

Finite difference schemes

RESULTS and APPLICATION

(1) Comprehensive Computer
      Simulation Model
(a) Flow pattern
(b) Particle trajectory

(2) Investigation and Prediction of:
(a) Enhancement of flux
(b) Optimal design

Figure 2 Conceptualisation and mathematical modelling framework

2.1.2 Hydrodynamics and Geometry

For a conventional tubular/rectangular membrane system the Reynolds number, Re, which represents the ratio of inertial to viscous forces, is sufficient to fully describe the flow conditions existing within the membrane channel. However this is no longer true when baffles and superimposing pulsatile flow are involved. Consequently several additional parameters have been defined to fully describe the hydrodynamic and geometric conditions. Here d is the membrane internal diameter; U_m is the mean velocity based on the volumetric flow area divided by the channel cross-sectional area; x_0 is the amplitude; f is the frequency of oscillation; L is the centre to centre distance between adjacent baffles; A_f and A_{et} are the free area of contraction and the empty channel respectively; v_p is the maximum pulsed velocity defined as $v_p = 2\pi f x_0$.

The *net Reynolds number*, **Re**, is defined as:

$$Re = \frac{\rho U_m d}{\mu} \tag{1}$$

The *oscillatory Reynolds number*, **Re$_o$**, is defined as:

$$Re_o = \frac{\rho v_p d}{\mu} \tag{2}$$

The *Strouhal number*, **St**, is defined as:

$$St = \frac{d}{4\pi x_0} \tag{3}$$

The *net to peak flow ratio*, **NFR**, is defined as:

$$NFR = \frac{v}{v+v_p} = \frac{Re}{Re+Re_o}$$ (4)

The baffle geometry is specified in terms of the shape and the three parameter:

a) the *interbaffle spacing ratio:*

$$\lambda = \frac{L}{d} \qquad \textit{for tubular}$$

(5)

$$\lambda = \frac{L}{H} \qquad \textit{for rectangular}$$

b) the *amplitude ratio:*

$$\frac{x_0}{L}$$ (6)

c) the *baffle flow area ratio:*

$$\beta = \frac{A_f}{A_{et}}$$ (7)

The geometric configurations considered in this work are tubular channel with central baffles, tubular channel with wall baffles and rectangular channel with wall baffles which are schematically illustrated in Figure 4 for the diagram of the baffles configuration and Figure 3 for the geometric configuration for numerical simulation.

TUBULAR CHANNEL WITH WALL BAFFLES

$$2R$$

$$\longleftarrow \quad L \quad \longrightarrow$$
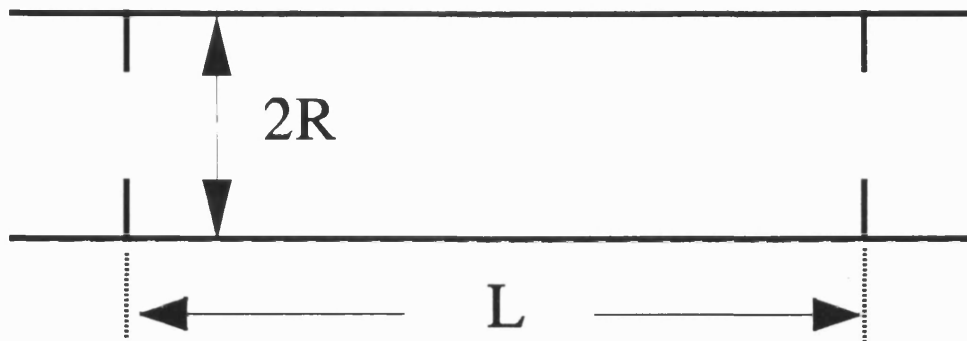
TUBULAR CHANNEL WITH CENTRAL BAFFLES

RECTANGULAR CHANNEL WITH WALL BAFFLES

$$H$$
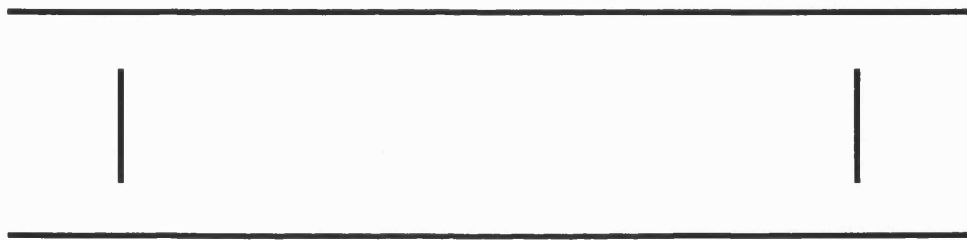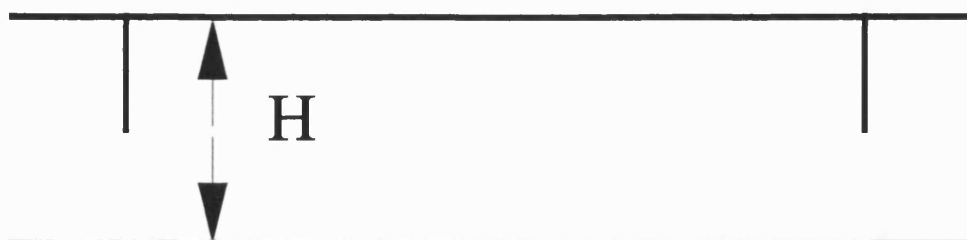
Figure 3 Baffles configuration considered in this thesis
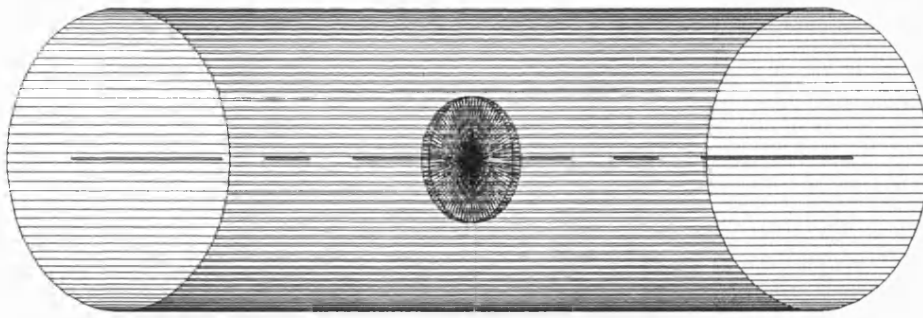
Wall baffle
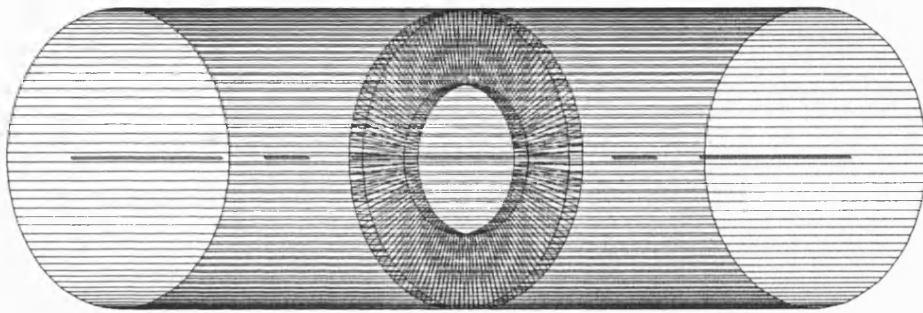
Rectangular channel
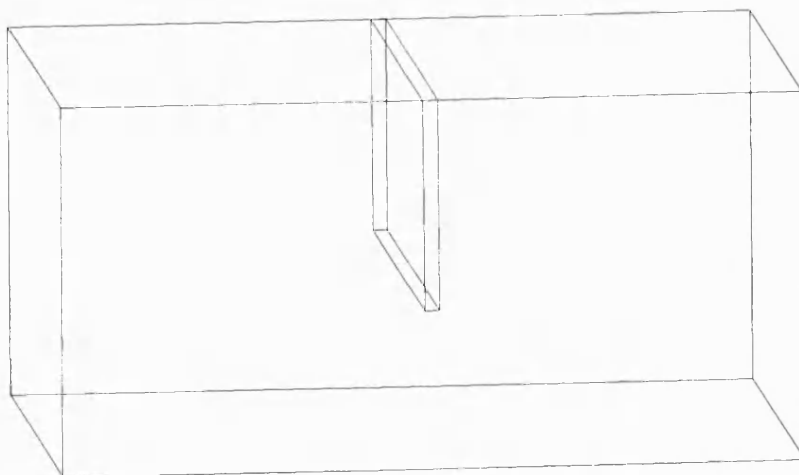
Figure 4 Geometric configuration for numerical simulation

2.1.3 Flow model

The complete set of equations for the motion of a fluid is the Navier-Stokes equations. These equations describe all the details of the flow. They form a closed set of equations and numerical methods are available to solve them. The solution requires a spatial grid which is resolved on a scale that is smaller than the smallest length scales present in the flow.

For laminar flow in a porous tubular or rectangular channels the general Navier-Stokes equations are valid. The following assumptions are applied.

Flow model assumptions:

Tubular channel	Rectangular channel
Newtonian fluid,	Newtonian fluid,
incompressible fluid,	incompressible fluid,
symmetry around the tube axis,	forces of gravity are very small.
forces of gravity are very small.	

The two dimension primitive-variable formation of Navier-Stokes equations are written

Tubular channel

$$\rho\left[\frac{\partial\bar{u}}{\partial\bar{t}}+\bar{u}\frac{\partial\bar{u}}{\partial\bar{x}}+\bar{v}\frac{\partial\bar{u}}{\partial\bar{r}}\right]=\frac{\partial\bar{p}}{\partial\bar{x}}+\mu\left[\frac{\partial^2\bar{u}}{\partial\bar{x}^2}+\frac{1}{\bar{r}}\frac{\partial\bar{u}}{\partial\bar{r}}+\frac{\partial^2\bar{u}}{\partial\bar{r}^2}\right]$$

$$\rho\left[\frac{\partial\bar{v}}{\partial\bar{t}}+\bar{u}\frac{\partial\bar{v}}{\partial\bar{x}}+\bar{v}\frac{\partial\bar{v}}{\partial\bar{r}}\right]=\frac{\partial\bar{p}}{\partial\bar{r}}+\mu\left[\frac{\partial^2\bar{v}}{\partial\bar{x}^2}+\frac{1}{\bar{r}}\frac{\partial\bar{v}}{\partial\bar{r}}+\frac{\partial^2\bar{v}}{\partial\bar{r}^2}-\frac{\bar{v}}{\bar{r}^2}\right] \qquad (8)$$

$$\frac{\partial\bar{u}}{\partial\bar{x}}+\frac{\bar{v}}{\bar{r}}+\frac{\partial\bar{v}}{\partial\bar{r}}=0$$

Rectangular channel

$$\rho\left[\frac{\partial\bar{u}}{\partial\bar{t}}+\bar{u}\frac{\partial\bar{u}}{\partial\bar{x}}+\bar{v}\frac{\partial\bar{u}}{\partial\bar{y}}\right]=\frac{\partial\bar{p}}{\partial\bar{x}}+\mu\left[\frac{\partial^2\bar{u}}{\partial\bar{x}^2}+\frac{\partial^2\bar{u}}{\partial\bar{y}^2}\right]$$

$$\rho\left[\frac{\partial\bar{v}}{\partial\bar{t}}+\bar{u}\frac{\partial\bar{v}}{\partial\bar{x}}+\bar{v}\frac{\partial\bar{v}}{\partial\bar{y}}\right]=\frac{\partial\bar{p}}{\partial\bar{y}}+\mu\left[\frac{\partial^2\bar{v}}{\partial\bar{x}^2}+\frac{\partial^2\bar{v}}{\partial\bar{y}^2}\right] \qquad (9)$$

$$\frac{\partial\bar{u}}{\partial\bar{x}}+\frac{\partial\bar{v}}{\partial\bar{y}}=0$$

The above equations can be presented in dimensionless form below, with velocities scaled with peak oscillatory velocity ($2\pi f x_0$), dimensions scaled with the tube radius (R) in tubular channel case or channel width (H) in rectangular channel case, and time with the frequency of oscillation(f). For flows with no oscillatory component the scaling is slightly different: velocities are scaled with the mean velocity(U), and time with a combination of the mean velocity and the tube radius (U/R) or the channel width (U/H).

Tubular channel

$$\frac{\partial u}{\partial t} + \frac{1}{St}\left[u\frac{\partial u}{\partial x} + v\frac{\partial u}{\partial r}\right] = -\frac{1}{St}\frac{\partial p}{\partial x} + \frac{2}{ReSt}\left[\frac{\partial^2 u}{\partial x^2} + \frac{1}{r}\frac{\partial u}{\partial r} + \frac{\partial^2 u}{\partial r^2}\right]$$

$$\frac{\partial v}{\partial t} + \frac{1}{St}\left[u\frac{\partial v}{\partial x} + v\frac{\partial v}{\partial r}\right] = -\frac{1}{St}\frac{\partial p}{\partial r} + \frac{2}{ReSt}\left[\frac{\partial^2 v}{\partial x^2} + \frac{1}{r}\frac{\partial v}{\partial r} + \frac{\partial^2 v}{\partial r^2} - \frac{v}{r^2}\right] \qquad (10)$$

$$\frac{\partial u}{\partial x} + \frac{v}{r} + \frac{\partial v}{\partial r} = 0$$

Rectangular channel

$$\frac{\partial u}{\partial t} + \frac{1}{St}\left[u\frac{\partial u}{\partial x} + v\frac{\partial u}{\partial y}\right] = -\frac{1}{St}\frac{\partial p}{\partial x} + \frac{2}{ReSt}\left[\frac{\partial^2 u}{\partial x^2} + \frac{\partial^2 u}{\partial y^2}\right]$$

$$\frac{\partial v}{\partial t} + \frac{1}{St}\left[u\frac{\partial v}{\partial x} + v\frac{\partial v}{\partial y}\right] = -\frac{1}{St}\frac{\partial p}{\partial y} + \frac{2}{ReSt}\left[\frac{\partial^2 v}{\partial x^2} + \frac{\partial^2 v}{\partial y^2}\right] \qquad (11)$$

$$\frac{\partial u}{\partial x} + \frac{\partial v}{\partial y} = 0$$

In this work the stream-function vorticity formulation is employed because the pressure is no longer explicit in the equations. The stream-function vorticity equations makes use of the vorticity (ω) and stream-function (Ψ)

Tubular channel

$$\omega = \frac{\partial v}{\partial x} - \frac{\partial u}{\partial r}$$

$$u = \frac{1}{r}\frac{\partial \psi}{\partial r} \qquad (12)$$

$$v = -\frac{1}{r}\frac{\partial \psi}{\partial x}$$

Rectangular channel

$$\omega = \frac{\partial v}{\partial x} - \frac{\partial u}{\partial y}$$

$$u = \frac{\partial \psi}{\partial y} \tag{13}$$

$$v = -\frac{\partial \psi}{\partial x}$$

The equations for ω and Ψ are obtained by applying the curl operator to Equation (10) or (11) so that pressure term disappears and to (12) or (13). The results are

Tubular channel

$$\frac{\partial \omega}{\partial t} = -\frac{1}{St}\left(u\frac{\partial \omega}{\partial x} + v\frac{\partial \omega}{\partial r} - \frac{v\omega}{r} \right) + \frac{2}{ReSt}\left(\frac{\partial^2 \omega}{\partial x^2} + \frac{1}{r}\frac{\partial \omega}{\partial r} + \frac{\partial^2 \omega}{\partial r^2} - \frac{\omega}{r^2} \right) \tag{14}$$

$$\frac{\partial^2 \psi}{\partial^2 x} + \frac{\partial^2 \psi}{\partial^2 r} - \frac{1}{r}\frac{\partial \psi}{\partial r} = -r\omega \tag{15}$$

Rectangular channel

$$\frac{\partial \omega}{\partial t} = -\frac{1}{St}\left(u\frac{\partial \omega}{\partial x} + v\frac{\partial \omega}{\partial y} \right) + \frac{1}{ReSt}\left(\frac{\partial^2 \omega}{\partial x^2} + \frac{\partial^2 \omega}{\partial y^2} \right) \tag{16}$$

$$\frac{\partial^2 \psi}{\partial^2 x} + \frac{\partial^2 \psi}{\partial^2 y} = -\omega \tag{17}$$

The movement of a particle located at (x,y) at time t is defined by the following equation

$$\bar{u} = \frac{d\bar{x}}{dt}, \quad \bar{v} = \frac{d\bar{y}}{dt} \tag{18}$$

The dimensionless form of the above equation is

$$\frac{dx}{dt} = \frac{1}{St} u(x,y)$$

$$\frac{dy}{dt} = \frac{1}{St} v(x,y) \tag{19}$$

2.1.4 Filtration model

Permeate flux across a membrane depends on a transmembrane pressure gradient as the driving force. Different models are found in the literature to modify the pressure gradient in order to predict permeate flux under various consideration. A number of authors have presented impressive evident in favour of a more or less wholly osmotic limitation of flux (Trettin et al 1981, Wales 1981 and Vilker et al 1981). In this work, we have chosen to concentrate on the osmotic aspect of polarisation. The osmotic theory depends on the kind of molecules retained by the membrane, which describes the general shape of the curve.

Filtration model assumptions:

the solute is a macromolecule,

A completely osmotic limitation to flux,

The solute is completely retained by the membrane.

Under these assumptions the following mass balance and a form of Darcy's Law can be written (Clifton 1984).
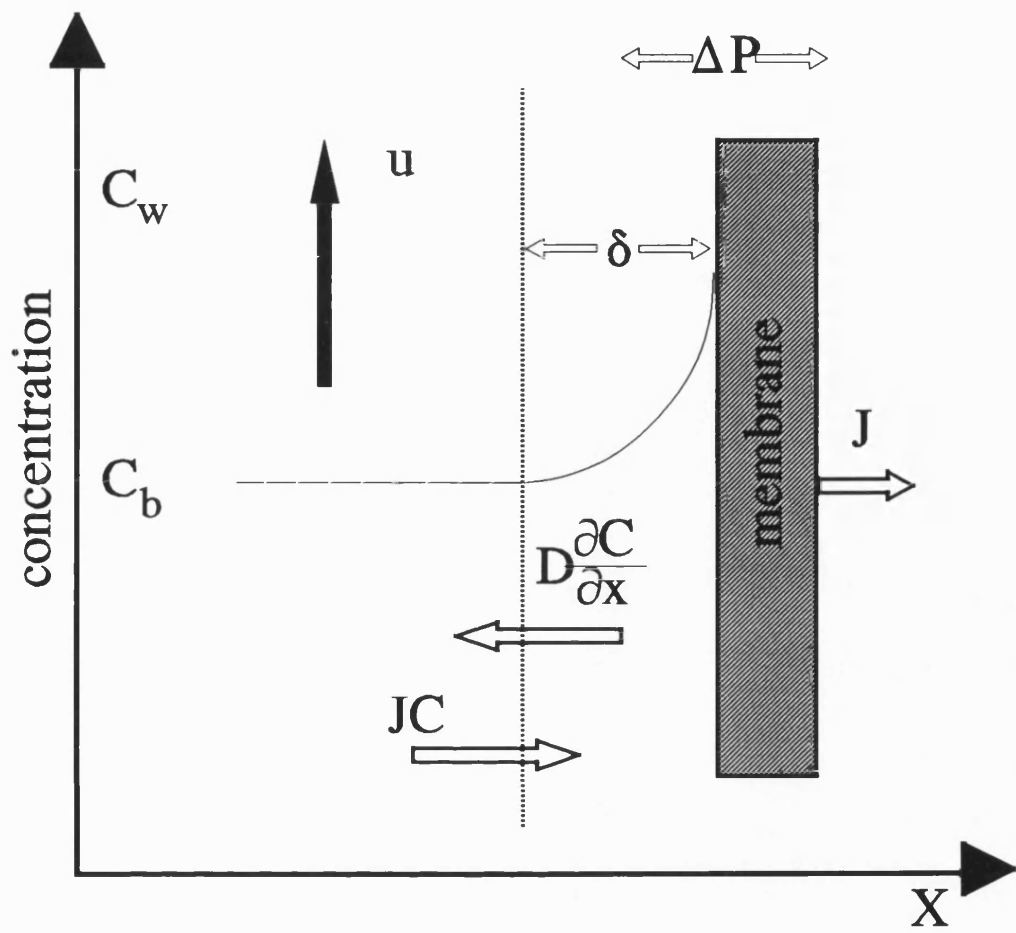
Figure 5 The mass balance of membrane-retained species

At steady state:

Diffusion = Convection

$$JC = D\frac{\partial C}{\partial x} \tag{20}$$

Integration across δ:

$$J = k\ln\left(\frac{C_w}{C_b}\right) \tag{21}$$

$$J = \frac{\Delta P_{TM} - \Pi}{\mu(R_m + R_f)} \qquad (22)$$

where C_w is the wall surface concentration

C_b is the bulk solute concentration

k is the local mass transfer coefficient

J is the local membrane flux

μ is the solvent viscosity

R_m is the membrane resistance

R_f the resistance of any fouling layer (assumed zero here)

ΔP_{TM} the local transmembrane pressure

The variation of osmotic pressure (Π) with concentration is usually expressed by the virial expansion:

$$\Pi(C_w) = a_1 C_w + a_2 C_w^2 + a_3 C_w^3 \qquad (23)$$

where a_1, a_2 and a_3 are the osmotic virial coefficients, the first of them corresponds to the van't Hoff law.

2.2 Computer model

In this section, numerical algorithms for solving the above mathematical models are detailed.

2.2.1 Navier-Stokes solver

The computer model for Navier-Stokes equations (14) - (19) is a finite difference solver with multigrid convergence acceleration. The scheme used is based on work of Sobey (1980) for furrowed channels, and Howes (1988) for wall baffled tubes. The flow chart of the numerical algorithm is given in Figure 6 below:
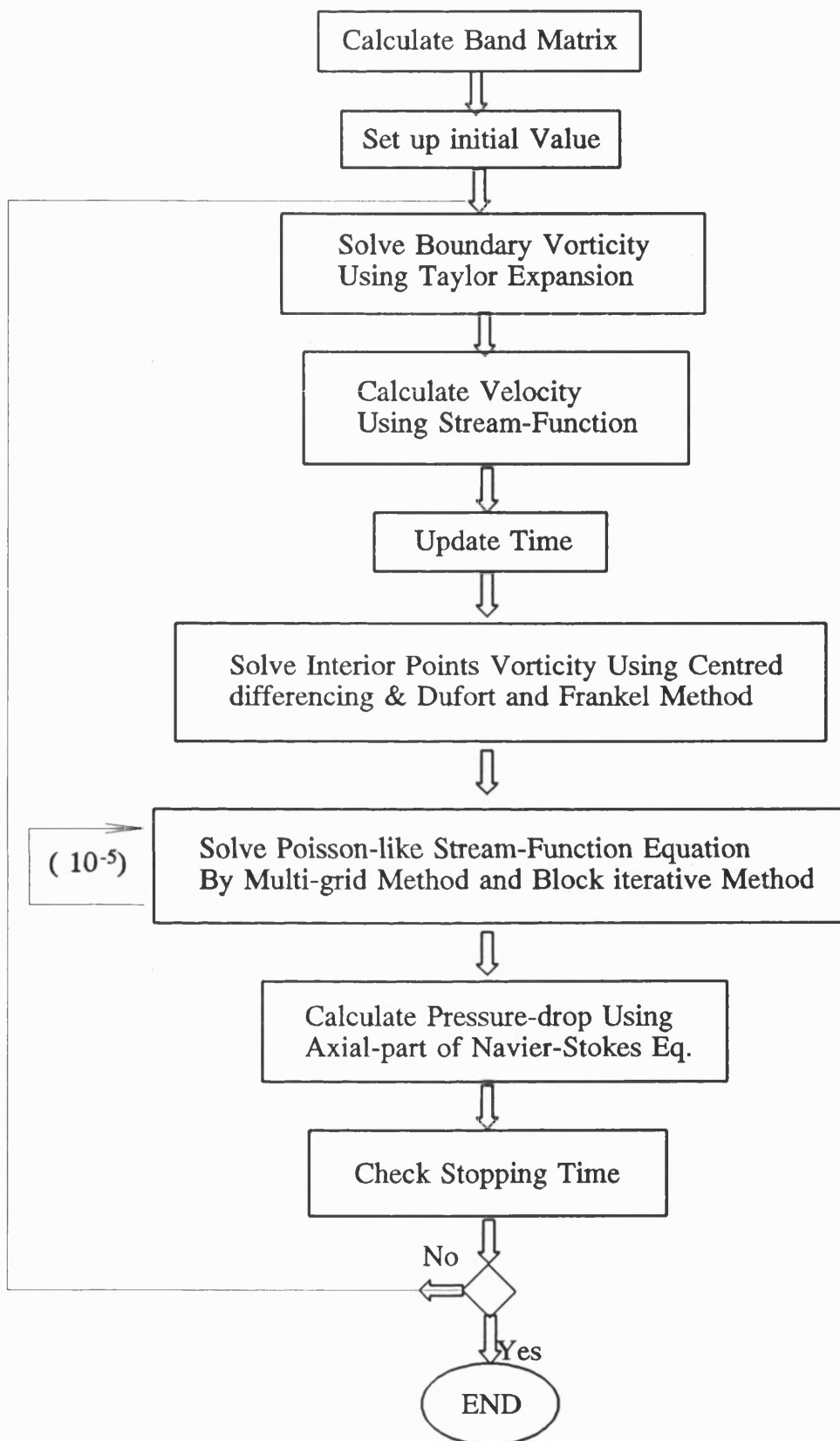
Figure 6 Flow chart for numerical algorithm for flow field and pressure drop

In order to solve equations (14) - (19), boundary and initial conditions must be set. Initially the fluid is considered to be at rest. In the tubular channel case, at the centreline, r=0 the stream-function is set:

$$\psi \mid_{r=0} = 0 \qquad\qquad (24)$$

At the centreline, by symmetry:

$$\omega \mid_{r=0} = 0 \qquad\qquad (25)$$

$$v \mid_{r=0} = 0 \qquad\qquad (26)$$

$$\frac{\partial u}{\partial r} \mid_{r=0} = 0 \qquad\qquad (27)$$

Integrating equation (12) for tubular channel and (13) for rectangular channel:

$$\psi \mid_{r=1} = \frac{\overline{U}_i}{2U_R} \qquad \text{\textit{for tubular channel}}$$

$$\hspace{6cm} (28)$$

$$\psi \mid_{y=1} - \psi \mid_{y=0} = \frac{\overline{U}_i}{U_R} \qquad \text{\textit{for rectangular channel}}$$

where $\bar{U}_i$ is the instantaneous velocity through the channel, U_R is the reference velocity:

$$U_R = \begin{cases} 2\pi f x_0, & \textit{for unsteady} \\ \textit{mean velocity}, & \textit{for steady} \end{cases} \tag{29}$$

Since the baffles are impermeable,

$$\psi\big|_{baffle} = \psi\big|_{wall}, \quad \textit{for wall baffle}$$
$$\psi\big|_{baffle} = 0, \quad \textit{for central baffle} \tag{30}$$

The wall vorticity is determined by combination equation (15) or (17) with the no-slip condition at the wall or the given wall flux v_w for the wall suction case. The inflow/outflow boundary conditions are assigned by the periodic nature of the walls.

The concentration boundary layer for liquid permeation lies very close to the membrane surface as the Schmidt number is large ($\sim 10^5$). To improve resolution near the wall the transformation $s = r^2$ is made.

Initially the fluid is at rest, so vorticity and stream-function are zero throughout the channel. At the first time step, a potential flow solution is found for the stream-function. For subsequent time steps, the vorticity transport equation (14) or (16) was used to step forward in time. The Poisson-like equation (15) or (17) was then solved for the stream function using a block iterative

method with multigrid convergence acceleration and velocities obtained from the definition of the stream function. Central differencing is used for accuracy and the explicit leapfrog method of Dufort and Frankel (Roache 1976) used for the time stepping of vorticity transport equation. Appendix 2 contains the finite difference equations used at each of the steps for the rectangular channel. The results obtained here were mostly carried out using a mesh with both 40 axial and radial increments(42 × 41 nodes) in the tubular channel and 66 x 41 nodes in the rectangular channel. The size of the time step was determined by stability considerations, and values used were in the range 1×10^{-4} - 5×10^{-3}. The dimensionless time used for the establishment of complete development of the flow was 6 - 10. Fluid oscillations were generated by oscillating the instantaneous velocity through the channel, such that $\bar{U}_i$ = $U_R \cdot FNT$ where FNT is the oscillatory source function. In most cases, sinusoidal source function were employed:

$$FNT = \begin{cases} 1 & \textit{steady} \\ NFR + \sin(2\pi t) & \textit{oscillatory} \end{cases} \tag{31}$$

where t is the dimensionless time $t = \omega \bar{t}/2\pi$ for an oscillation of angular frequency ω. t = 0 was taken at the point when oscillatory velocity was zero. Other oscillatory source function square-wave and break-sin wave are also tried. Boundary conditions, oscillatory source functions and initial stream-function distribution are now summarised below.
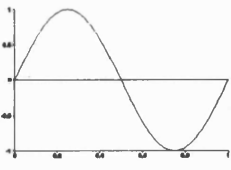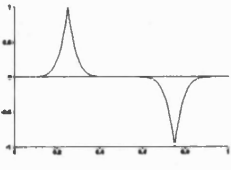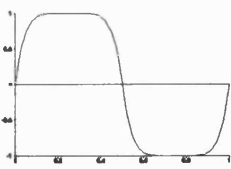
Table III Boundary conditions for tubular channel

$\Psi|_{r=0}=0$, $\Psi|_{r=1}=\bar{U}_i/2U_R$	wall baffle $\Psi|_{baffle}=\Psi|_{r=1}$	central baffle $\Psi|_{baffle}=0$
$\omega|_{r=0}=0$, $\omega|_{baffle}=-1/r\partial^2\Psi/\partial x^2$	no wall suction $\omega=-\partial^2\Psi/\partial r^2|_{r=1}$	wall suction $\omega=-\partial^2\Psi/\partial r^2-\partial^2\Psi/\partial x^2|_{r=1}$
$v|_{r=0}=0$	$v|_{r=1}=0$	$v|_{r=1}=V_w$
$\partial u/\partial r|_{r=0}=0$, $u|_{r=1}=0$	periodic conditions $\Psi|_{x=0}=\Psi|_{x=L}$, $\omega|_{x=0}=\omega|_{x=L}$	

Table IV Boundary conditions for rectangular channel

$\Psi|_{y=0}=-\bar{U}_i/2U_R$, $\Psi|_{y=1}=\bar{U}_i/2U_R$, $\Psi|_{baffle}=\Psi|_{y=1}$		
$\omega|_{baffle}=-\partial^2\Psi/\partial x^2$	no wall suction $\omega=-\partial^2\Psi/\partial y^2|_{y=0,1}$	wall suction $\omega=-\partial^2\Psi/\partial x^2-\partial^2\Psi/\partial y^2|_{y=0,1}$
$v|_{y=1}=0$	$v|_{y=0}=0$	$v|_{y=0}=V_w$
$u|_{y=0,1}=0$	periodic conditions $\Psi|_{x=0}=\Psi|_{x=L}$, $\omega|_{x=0}=\omega|_{x=L}$	

Oscillatory source functions

Name	Form	Plot
Sin	Equation (31)	
Break -sin	$\sin(2\pi t)$ in Equ (31) is replaced by: $(4\text{mod}(t))^6\sin(2\pi\text{mod}(t))$, $0 \le \text{mod}(t) \le .25$ $(1-4\text{mod}(t))^6\sin(2\pi(.5-\text{mod}(t)))$, $.25 \le \text{mod}(t) \le .5$ $(4\text{mod}(t)-1)^6\sin(2\pi(\text{mod}(t)-.5))$, $.5 \le \text{mod}(t) \le .75$ $(4-4\text{mod}(t))^6\sin(2\pi(1-\text{mod}(t)))$, $.75 \le \text{mod}(t) \le 1$	
Square -wave	$\sin(2\pi t)$ in Equ (31) is replaced by: $1-(4\text{mod}(t)-1)^6$, $0 \le t \le .5$ $-1+(4\text{mod}(t)-3)^6$, $.5 \le t \le 1$ here $\text{mod}(t) = t-[t]$	

$$Q+\Delta SF/2-V_w(X-X_L)$$

$$Q+\Delta SF/2$$

$$Q$$

$$Q-\Delta SF/2$$

$$0$$

$$X_L \qquad X_R$$

tubular channel

Here $\Delta SF=V_w*\Delta X*Win\_length$

$$Q$$

$$QY-(Q+\Delta SF/2)(1-Y) \qquad QY-(Q-\Delta SF/2)(1-Y)$$

$$-Q$$

$$-Q+\Delta SF/2$$

$$-Q-\Delta SF/2$$

$$-Q-\Delta SF/2+V_w(X-X_L)$$

$$QY-(Q+\Delta SF/2-V_w(X-X_L))(1-Y)$$
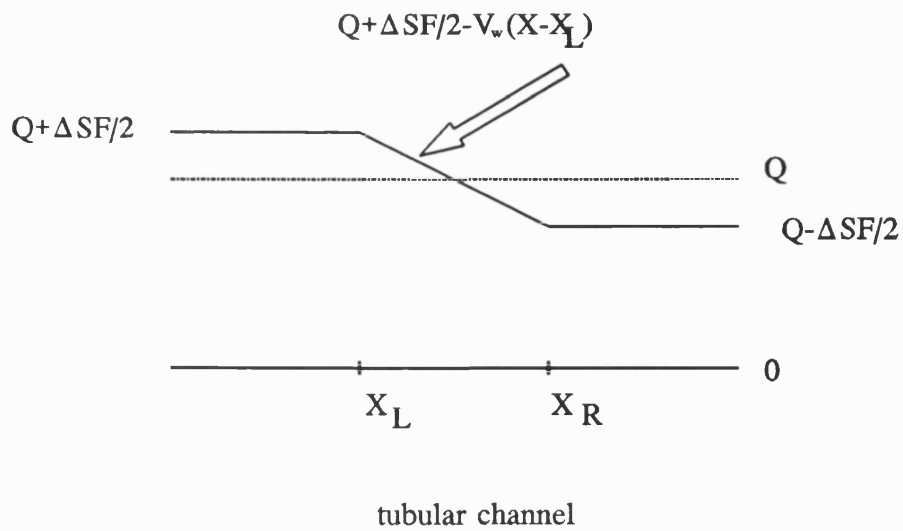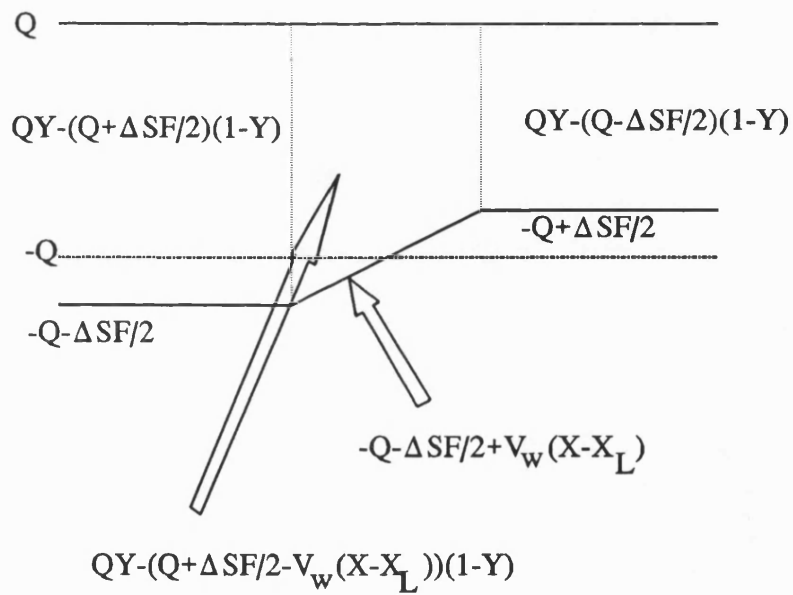
rectangular channel

Figure 7 The initial stream-function distribution (see A2.5.2)

2.2.2 Particle trajectory solver

At the beginning of a cycle a single region from x=0 to x=L is filled with marked fluid particles. Numerically this involved distributing approximately 4000 marked particles throughout the region. Variation in the channel geometry would then produce a change in the exact number of particles used in each geometry. The fluid velocities had been calculated in advance and stored at each time step throughout the cycle. The particles paths were then determined by interpolation within the grid of known velocities to obtain the velocity at the particles' current position. Then a finite difference scheme analoguous to equation (19) was used to calculate the particle position after a short time using the known velocity. Once all the particles had been moved the process could be repeated at the new time and in this way the motion of the fluid particles from within the original section of the channel could be followed. The diffusion of particles was simulated by adding a random motion to the advection at each time step. The diffusion of a cloud with molecular diffusivity D over a time interval Δt may be simulated by describing the cloud as a large number of particles and giving each of these particles as independent random velocity:

$$\bar{v} = \sqrt{\frac{2D}{\Delta t}} \; \chi_{random}(0,1) \hspace{2cm} (32)$$

$\chi_{random}(0,1)$ is the Gassian distribution of mean 0 and variance 1.

It should be noticed that particles have no substance other than as markers of

points within the fluid.

2.2.3 Power consumption solver

The pressure profile which we presented here was obtained using the following numerical procedure. The axial component of the Navier Stokes equations is given by

Tubular channel

$$\frac{\partial u}{\partial t} + \frac{1}{St}\left(u\frac{\partial u}{\partial x} + v\frac{\partial u}{\partial r}\right) = -\frac{1}{St}\frac{\partial P}{\partial x} + \frac{2}{ReSt}\left(\frac{\partial^2 u}{\partial x^2} + \frac{1}{r}\frac{\partial u}{\partial r} + \frac{\partial^2 u}{\partial r^2}\right) \qquad (33)$$

Rectangular channel

$$\frac{\partial u}{\partial t} + \frac{1}{St}\left(u\frac{\partial u}{\partial x} + v\frac{\partial u}{\partial y}\right) = -\frac{1}{St}\frac{\partial P}{\partial x} + \frac{2}{ReSt}\left(\frac{\partial^2 u}{\partial x^2} + \frac{\partial^2 u}{\partial y^2}\right) \qquad (34)$$

Integration across one cell at any fixed radial position gives,

Tubular channel

$$\frac{1}{St}\int_0^L \frac{\partial P}{\partial x}dx = -\int_0^L \frac{\partial u}{\partial t}dx - \frac{1}{St}\int_0^L u\frac{\partial u}{\partial x}dx - \frac{1}{St}\int_0^L v\sqrt{2s}\frac{\partial u}{\partial s}dx$$
$$+ \frac{2}{ReSt}\int_0^L \left(\frac{\partial^2 u}{\partial x^2} + 4\left(\frac{\partial u}{\partial s} + s\frac{\partial^2 u}{\partial s^2}\right)\right)dx \qquad (35)$$

Rectangular channel

$$\frac{1}{St}\int_0^L \frac{\partial P}{\partial x}dx = -\int_0^L \frac{\partial u}{\partial t}dx - \frac{1}{St}\int_0^L\left(u\frac{\partial u}{\partial x}+v\frac{\partial u}{\partial y}\right)dx + \frac{2}{ReSt}\int_0^L\left(\frac{\partial^2 u}{\partial x^2}+\frac{\partial^2 u}{\partial y^2}\right)dx \qquad (36)$$

After some manipulation we arrive at the differential pressure drop ΔP,

Tubular channel

$$\Delta P(t,s) = -St\int_0^L \frac{\partial u}{\partial t}dx + \int_0^L v\omega\,dx - \frac{2}{Re}\int_0^L\left(\frac{\omega}{\sqrt{s}}+2\sqrt{s}\frac{\partial \omega}{\partial s}\right)dx \qquad (37)$$

Rectangular channel

$$\Delta P(t,y) = -St\int_0^L \frac{\partial u}{\partial t}dx + \int_0^L v\omega\,dx - \frac{2}{Re}\int_0^L \frac{\partial \omega}{\partial y}dx \qquad (38)$$

If the fluid velocities are known at any instant, the pressure drop across each baffled section can be determined from equation (35), (37) or (38) by numerically integrating the right hand side of the equation. We chose to use Simpsons rule for the integration. The associated power densities (PD) for the system were

obtained by integration over one complete cycle of equation (36), (39):

$$PD = \frac{1}{TV} \int_0^T \Delta P(t) \, Q(t) \, dt \qquad (39)$$

where T is the period of oscillation, V the volume of the cell and Q the instantaneous volumetric flow.

2.2.4 The filtration model solver

We (Howell et al. 1992a) have shown that the wall suction at levels realistic for membrane permeation does not distort the macroscopic flow field. No distortion was observed with 1% of the flow going through the wall in a length of the tube diameters. Membrane flux is typically 15% in > 250 tube diameters (i.e. < 0.1% for a length of one tube diameter).

The above observation allow us to store the results of the flow field calculation and then solve the membrane permeation problem locally. Having associated equations (21) and (22) together, we are able to predict membrane flux J and boundary concentration C_w at any point along the membrane surface provided transmembrane pressure ΔP_{TM} and mass transfer coefficient k are given by solving the nonlinear equation which we have solved using Newton-Raphson algorithm,

$$R_m k \ln(C_w) + a_1 C_w + a_2 C_w^2 + a_3 C_w^3 - \Delta P_{TM} - R_m k \ln(C_b) = 0 \qquad (40)$$

ΔP_{TM} can be obtained through the equation (35), (37) or (38)

$$\Delta P_{TM} = P_{inlet} + \Delta P/2$$

The local mass transfer coefficient is assumed to be given by a combination of local fluid dynamic and physical properties. Traditional correlations give the Sherwood Number as a function of the Reynolds Number but this has little meaning in a local sense where flow is changing rapidly in space and time. The tubular Lèvêque equation was converted to a form where the velocity was expressed by the wall shear rate. This is then used to give the value of k using the previously computed flow field to supply wall shear rates:

$$\dot{\gamma} = \frac{\partial \overline{u}}{\partial \overline{r}}\Big|_{\overline{r}=1} = \frac{U_R}{R}\frac{\partial u}{\partial r}\Big|_{r=1} = \frac{U_R}{R}\dot{\gamma} \qquad \textit{for tubular channel}$$

$$\dot{\gamma} = \frac{\partial \overline{u}}{\partial \overline{y}}\Big|_{\overline{y}=0} = \frac{U_R}{H}\frac{\partial u}{\partial y}\Big|_{y=0} = \frac{U_R}{H}\dot{\gamma} \qquad \textit{for rectangular channel} \qquad (41)$$

For pipe flow with closed walls this leads to (Porter 1972)

$$k' = 0.816\left(\frac{\dot{\gamma}D^2}{L}\right)^{0.33} \qquad (42)$$

Finally the flow chart of the numerical algorithm for the filtration model is summarised in Figure 8 below:

```
┌─────────────────────────────────┐
│ Read input pressure drop and    │
│ wall shear rate from CFD results│
└─────────────────────────────────┘
                 ⇓
┌─────────────────────────────────┐
│ Calculate mass transfer coefficient locally │
│ using Leveque empirical correlation         │
└─────────────────────────────────┘
                 ⇓
┌─────────────────────────────────┐
│ Solve osmotic pressure model with the │
│ association of mass balance model using│
│ Newton-Raphson root-finding method    │
└─────────────────────────────────┘
                 ⇓
┌─────────────────────────────────┐
│ Output $C_W$ and $J(x)$         │
└─────────────────────────────────┘
```
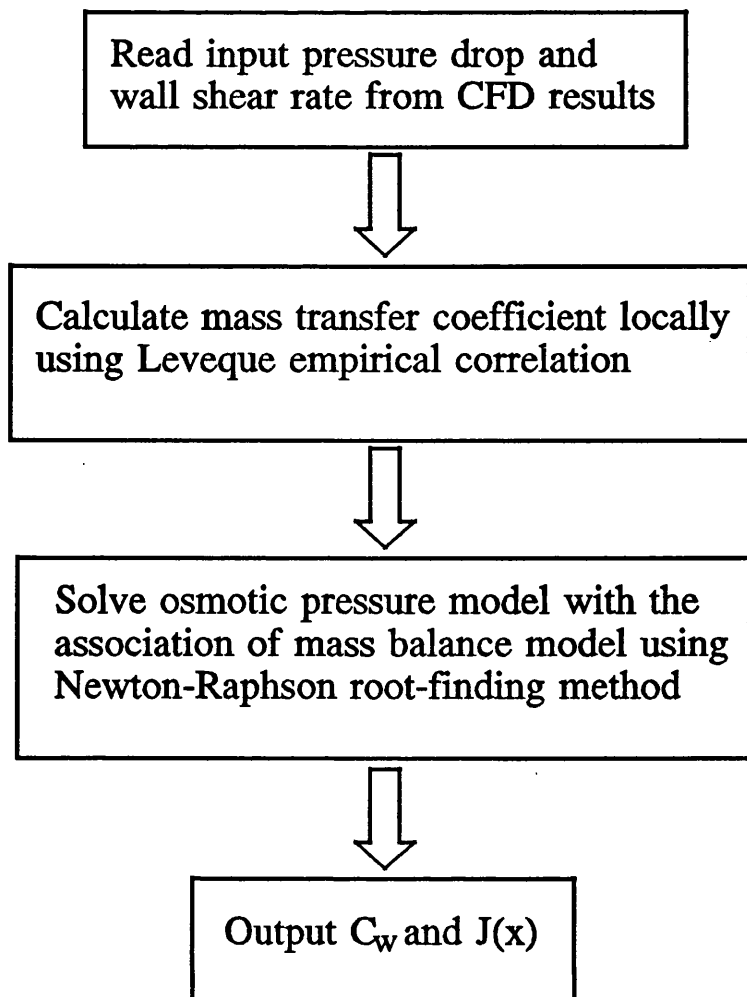
Figure 8 Flow chart of numerical algorithm for the filtration model

2.2.5 Graphic plot

NAG graphics library was used in the streamline, velocity vector field and particle motion plot programs. The brief description of these programs is included in Appendix 1.

CHAPTER 3

FLOW PATTERN RESULTS

This chapter contains flow pattern results for steady flow and oscillatory flow in baffled tubular and rectangular channels with or without wall suction. The comparison between numerically simulated flow patterns and the available experimental visualisation is given. Flow pattern calculation have been carried out using a mesh with both 40 axial and transverse increments(42 x 41 nodes) for Re = 1-600, St = .0326-2, β = 0.4 and λ = 1.5. The reason why β = 0.4 and λ = 1.5 is chosen is that from experimental flow pattern studies (Brunold et al. 1989) an optimum geometry for mixing was established with a baffle area constriction of the order 50% and a baffle spacing of the order of 1.5 tube diameters, although they used a rectangular channel case with a geometry is slightly different from ours. In order to improve the visual presentation, the stream function contours are chosen such that there are 10 contour lines in the unseparated region and 10 contours in the recirculating region. Flow is from left to right in each of the steady flow diagrams and in t = 0$^+$ of the oscillatory flow diagrams. The flow direction is indicated by arrow symbols in the diagrams.

The terminology used in this chapter is as follows; Each interbaffle spacing is called a cell. It is said to occupy x proportion when vortex downstream of each baffle occupies a certain proportion(x) of the distance between adjacent baffles.

The mainstream flow is referred to as the <u>bulk</u> flow. Flow is said to be <u>chaotic</u> when the flow does not appear to repeat with any frequency. When the streamline detach or attach to the channel wall or baffle this is referred to as <u>separation</u>, more rigorously, when at any point the wall or baffle vorticity has opposite sign to the flux through the channel then the flow has separated. The flow is said to be <u>laminar</u> when the bulk flow retains its streamline nature. With pulsed flow, laminar flow refers to <u>unsteady laminar</u> flow where the flow maintains its laminar character over the acceleration and deceleration phases of the cycle.

3.1 Steady flow patterns

3.1.1 Steady flow pattern without wall suction

Figure 9 shows the numerically predicted steady flow patterns for both wall and central baffles with $\beta = .4$, $\lambda = 1.5$ and $Re_n = 1$, 100 and 200 respectively in tubular module. In the case of the wall baffle, as the net flow Reynolds number Re_n increases a downstream vortex develops behind the baffle. At $Re_n = 200$ the vortex completely occupies the wall space between the baffles. The central baffle case is partially different where the vortex formed behind the baffle intensifies with increasing Reynolds Number but does not fill the entire space between the obstructions.

For central baffles two flow regimes are observed as shown in Figure 10 with the comparison between the simulated and experimental visualisation which

has been obtained by Finnigan (Finnigan 1990). The first flow regime is at low Reynolds number where the flow is almost entirely laminar with only one vortex forming immediately downstream of the baffle. Separation of the streamlines from the tube wall occurs but most of the streamlines remain relatively parallel to the central line. Finnigan pointed out that the flow is relatively slow moving in the wall region as particles gradually accumulate at the top of the tube and form a "semi-stagnant" region where material moves slowly from one cell to the next (Finnigan 1990). The second is characterised by another vortex formation near the tube wall when the Reynolds Number reaches about 200. The bulk flow moves or snakes between these two vortices in a fashion which is referred as the snake effect (Finnigan 1990). This snake effect is the dominant feature of this type of flow regime. As Re_n increases the streamlines become turbulent in nature and the general flow pattern becomes asymmetric and more chaotic. Because of symmetry assumption in flow model used for tubular module it seems impossible to further predict flow patterns when Re_n is above 300 and flow goes considerably asymmetric in this case.
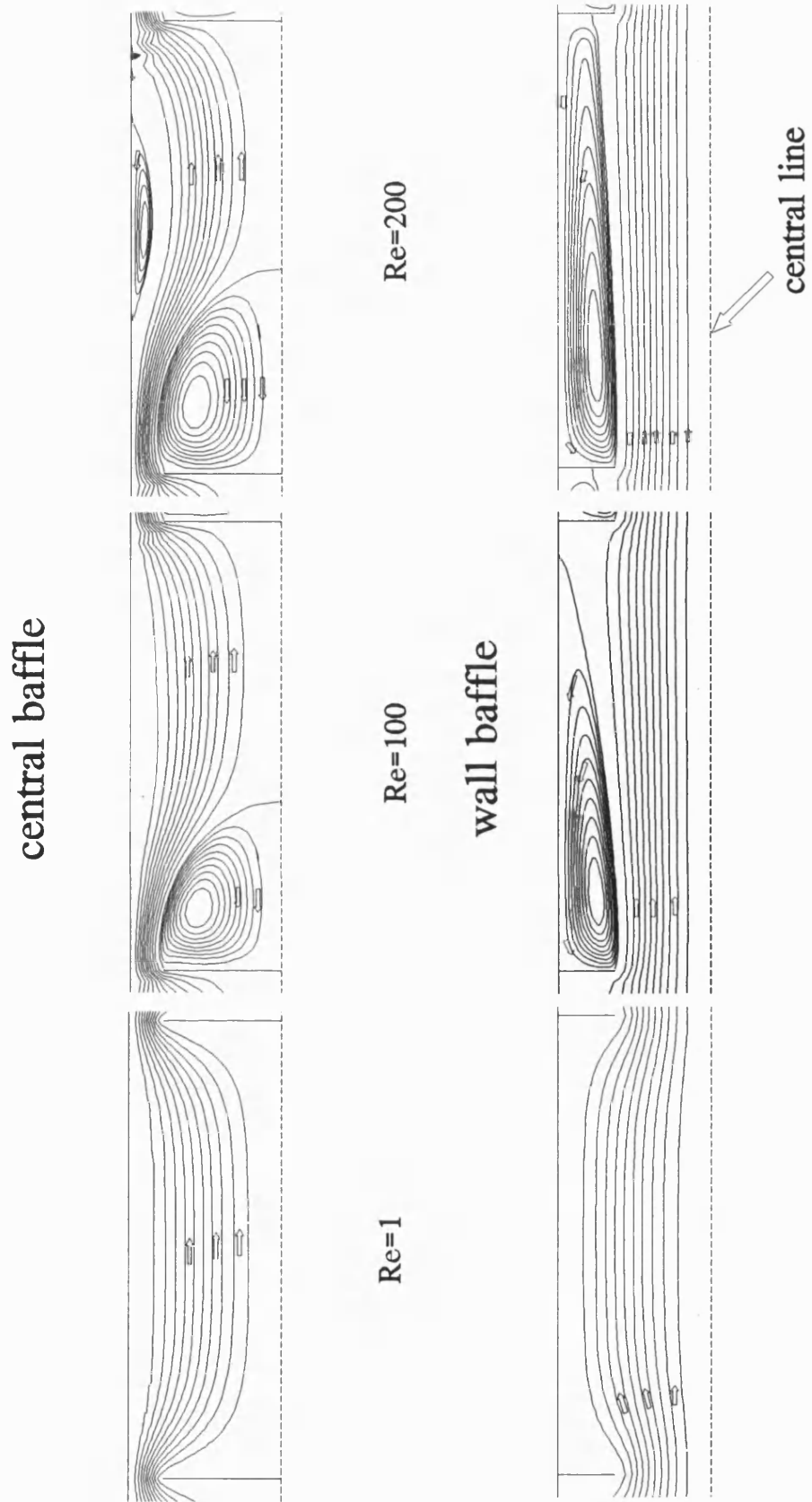
Figure 9 Simulation of steady flow within wall and central baffled tube
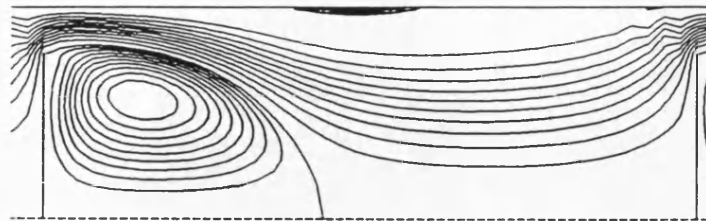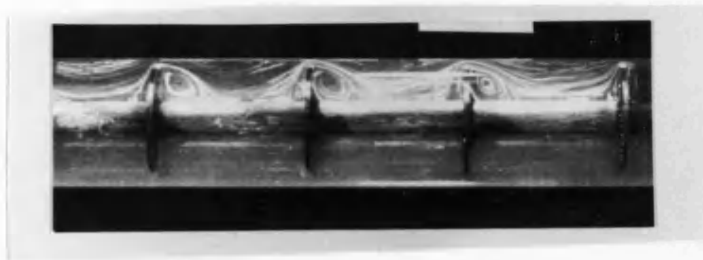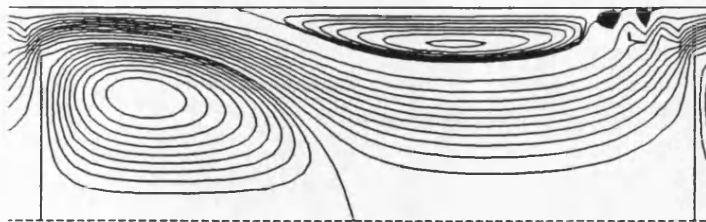
Figure 10 Comparison between numerical and experimental flow patterns of steady flow within central baffled tube.

Figure 12 shows steady flow patterns in rectangular channel for $Re_n = 1$, 100 and 200 respectively with $\beta = 0.4$, $\lambda = 1.5$. Our simulations show that the introduction of periodic baffles produces a periodic eddy shedding when Reynolds number Re_n is above 70. Diagrams in Figure 12 for $Re_n = 100$ and $Re_n = 200$ are plotted at dimensionless time $t = 10$. This phenomenon that steady flow produces unsteadiness in baffled channel was reported by Howes et al (1991) in the following geometry shown in Figure 11.

L/H = 1.5
B/H = 0.25
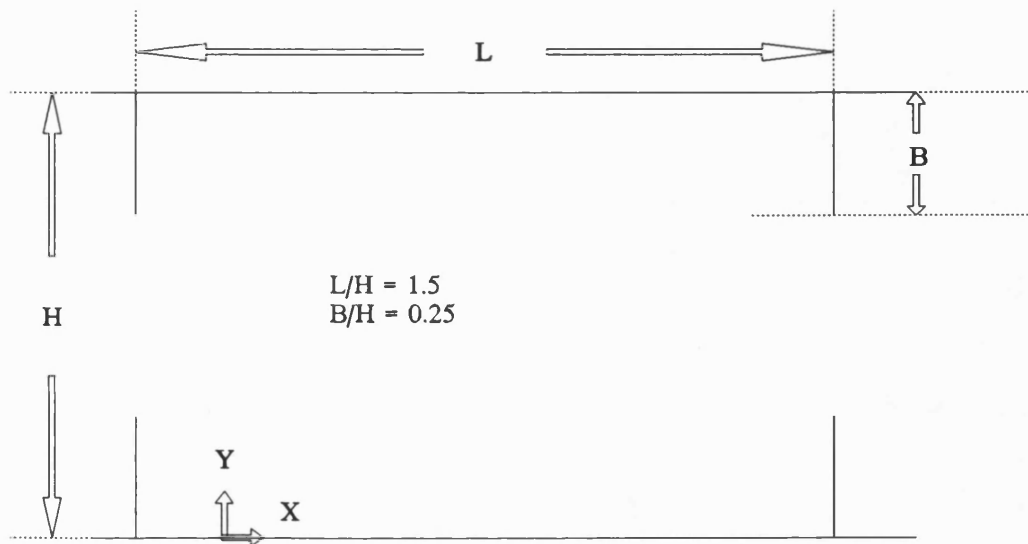
Figure 11 rectangular channel geometry used by Howes et al

Figure 13 shows the time evolution at $t = 0.25$, 0.5, 0.75 and 1.0 for steady flow patterns $Re_n = 70$, $\beta = 0$, $\lambda = 1.5$. It seems that there is no difference at all these time point, which suggests that the unsteadiness is merely produced by the introduction of periodic baffles. This unsteadiness is likely to result in a small increase in the pressure drop. The enhancement in mixing and transfer rates, however, would undoubtedly improve the transfer efficiency compared with an unbaffled device.

Re = 1
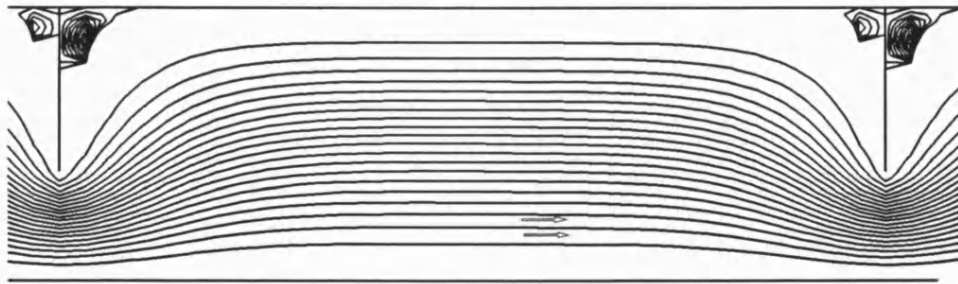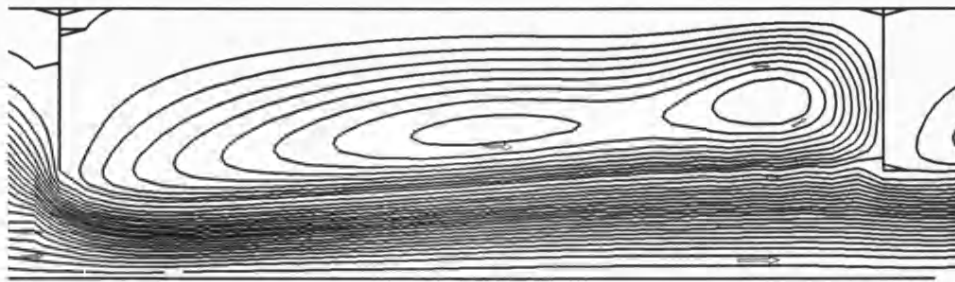
Re = 100
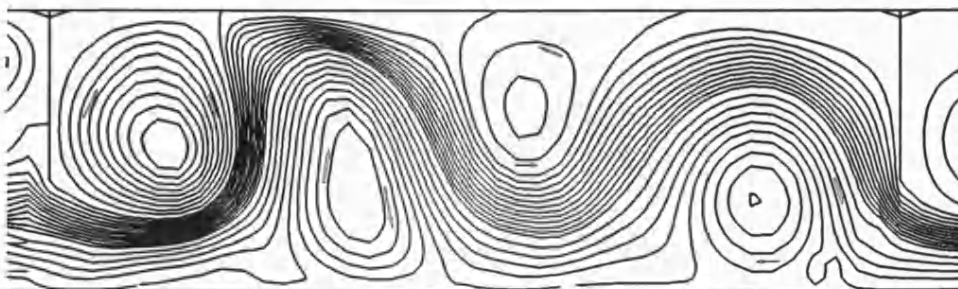
Re = 200

Figure 12 Simulation of Steady flow in rectangular channel
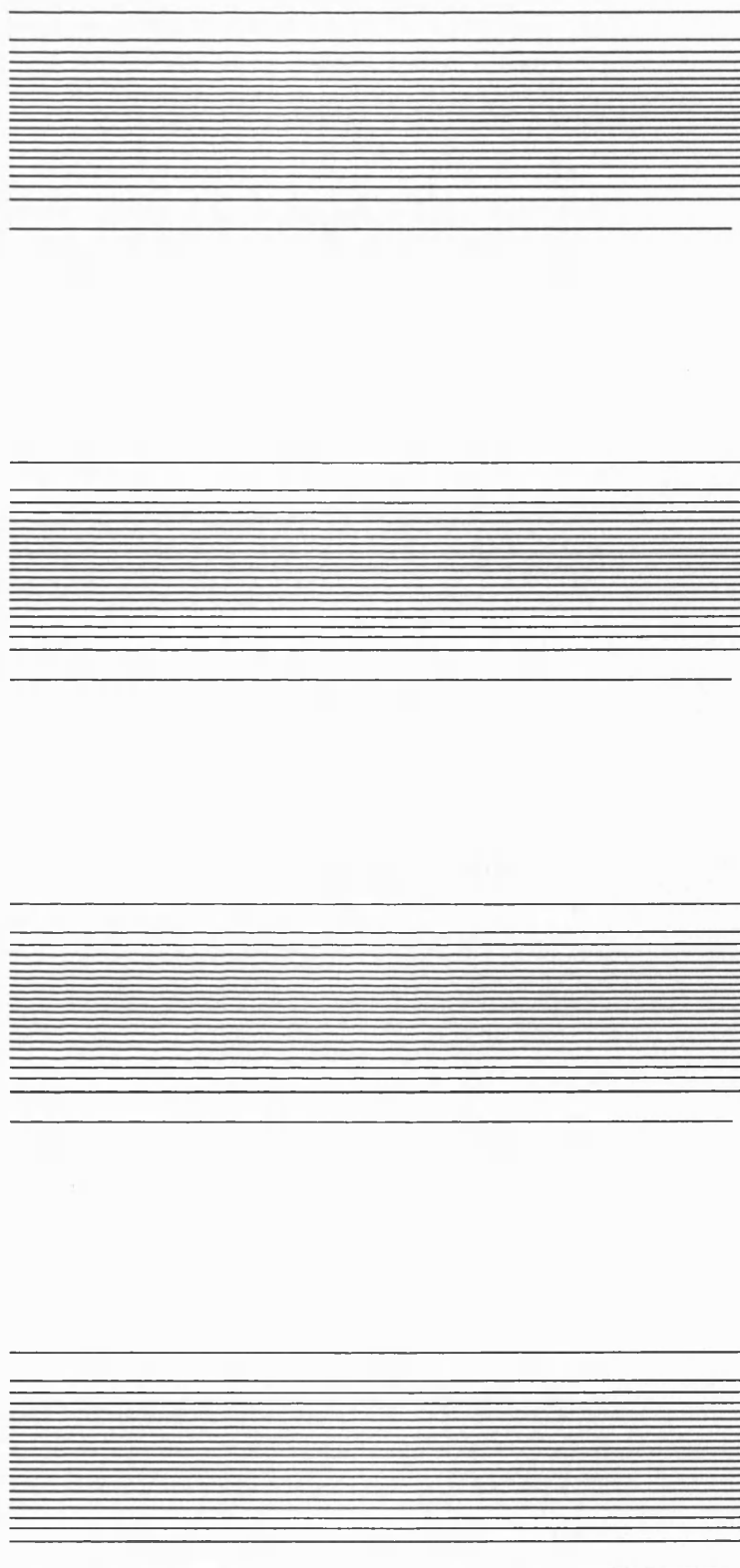
Figure 13 The time evolution t = .25, .5, .75 and 1. for $Re_n = 70$, $\beta = 0$ and $\lambda = 1.5$ in rectangular channel

3.1.2 Steady flow pattern with wall suction

In this section wall suction is considered for steady flow in both tubular and rectangular module. Wall suction here is characterised by the dimensionless wall flux v_w, which is equal to the ratio of dimensional wall flux to the dimensional maximum pulsed velocity, more precisely,

$$v_w = \begin{cases} \dfrac{\bar{v}_w}{v_p} & \text{\textit{tubular channel}} \\[3mm] 2*\dfrac{\bar{v}_w}{v_p} & \text{\textit{rectangular channel}} \end{cases} \qquad (43)$$

$$v_p = U_R \quad \text{\textit{in steady case}}$$

Two geometrical cells were used for the computational region that is $0 < r$ (or y) < 1 and $0 < x < 2L$ so that a linearly decreasing stream function (equivalent to a fixed wall flux) can be simulated at the porous wall region which is simply then a open window with the length one quarter of the one cell length. The initial stream functions were distributed by linear interpolation (see Figure 7 in Chapter 2 and Appendix A2.5.1). The periodic nature of the walls was modified to be consistent with wall suction (see Appendix A2.5.1).

Figure 14 - Figure 16 shows the numerically predicted steady flow patterns for a tubular module with both wall and central baffles using the same geometric and hydraulic conditions as Figure 9 except with wall fluxes now $v_w = 10^{-2}$, 10^{-3} and 10^{-4} respectively. In the case of the wall baffle, as the net flow Reynolds number Re_n increases a downstream vortex develops behind the baffle. The

central baffle case is partially different where the vortex formed behind the baffle intensifies with increasing Reynolds Number but does not fill the entire space between the obstructions as in the case of non-porous wall shown as Figure 9. Because of the porous wall, near the wall region for the wall baffle case some flow moves into the porous wall area from upstream via the outside of the vortex. For the central baffles case some flow moves into the porous wall area without encountering the body vortex. In the non-porous case a second vortex forms near the tube wall when the Reynolds number reaches about 200 shown in Figure 9. There is no such kind of vortex when $v_w = 10^{-2}$ which may has been destroyed by the boundary flows which arrive from the upstream region.

Figure 17 - Figure 18 shows the numerically predicted steady flow patterns for rectangular module with the same geometric and hydraulic conditions as Figure 12 except with wall flux now $v_w = 10^{-3}$ and 10^{-4} respectively.

In our membrane filtration device (Finnigan 1990 and Howell et al. 1992b) the ratio of dimensional wall flux to the dimensional maximum pulsed velocity is about 10^{-5} to 10^{-4}. At this range, as shown in Figure 16 and Figure 18, there is not much difference in these flow patterns compared with the base case of no suction.
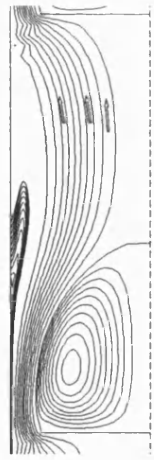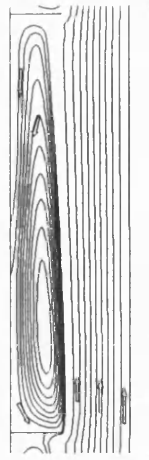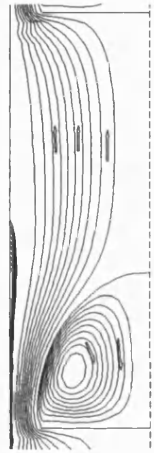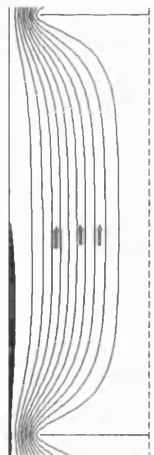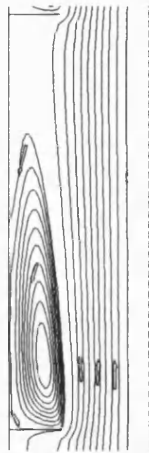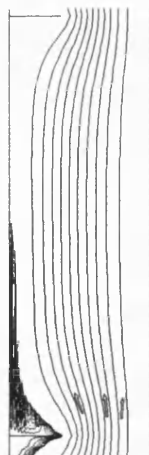
Figure 14 Simulation of steady flow within wall and central baffled tube $v_w = 10^{-2}$
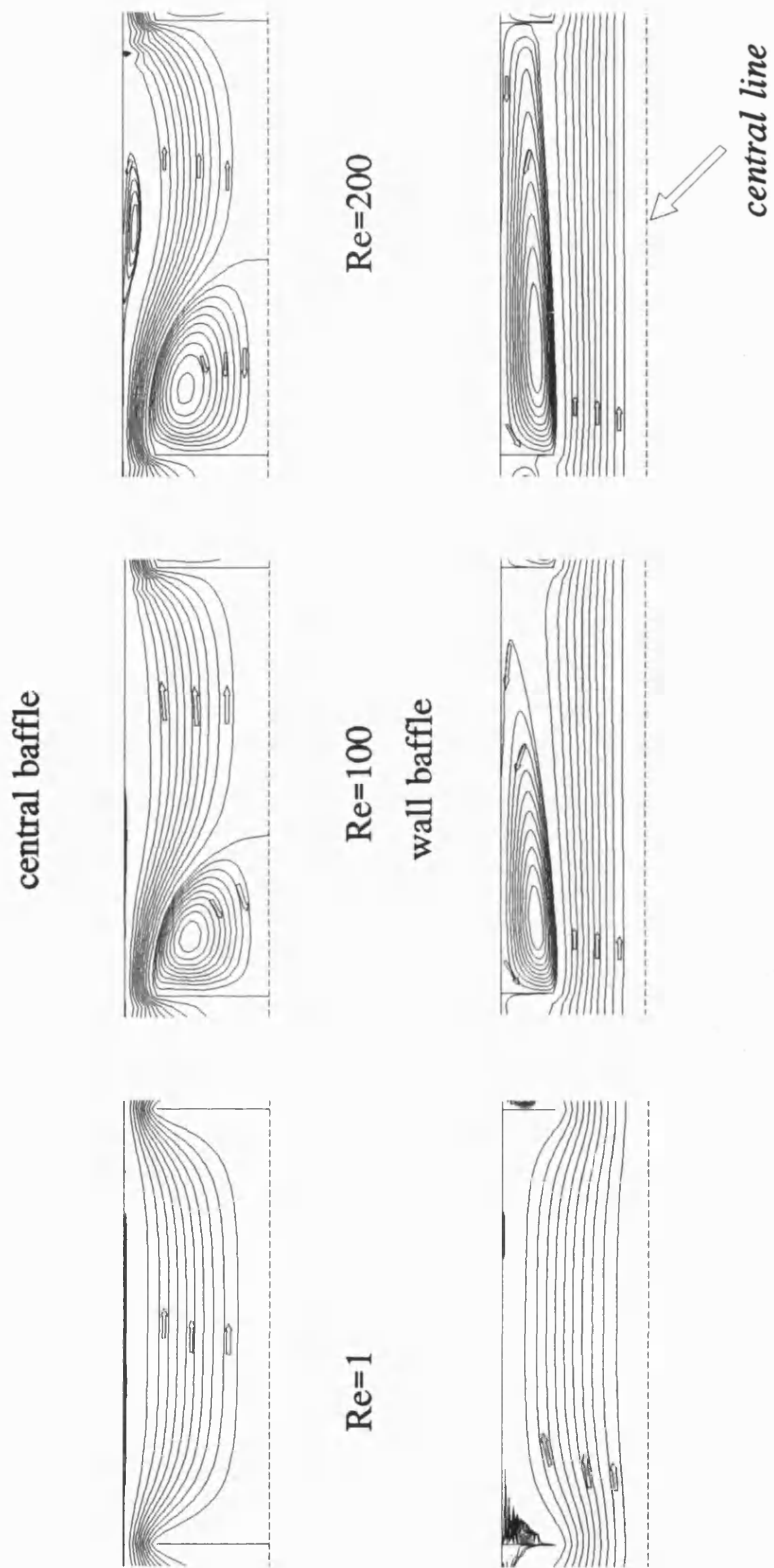
Figure 15 Simulation of steady flow within wall and central baffled tube $v_w = 10^{-3}$
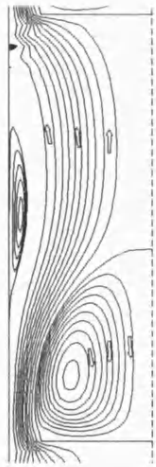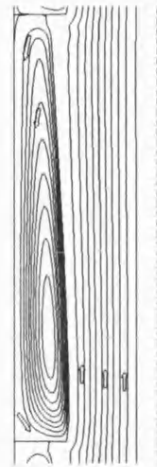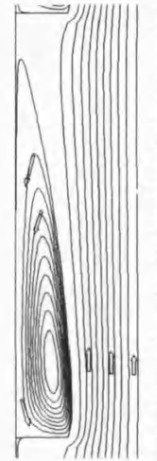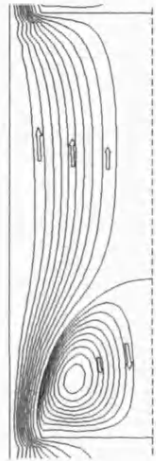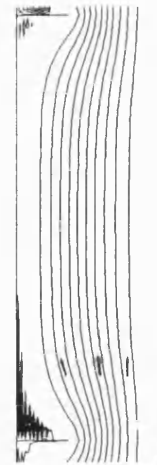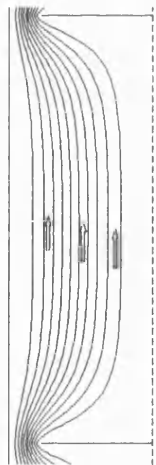
Figure 16 Simulation of steady flow within wall and central baffled tube $v_w = 10^{-4}$

Re=1
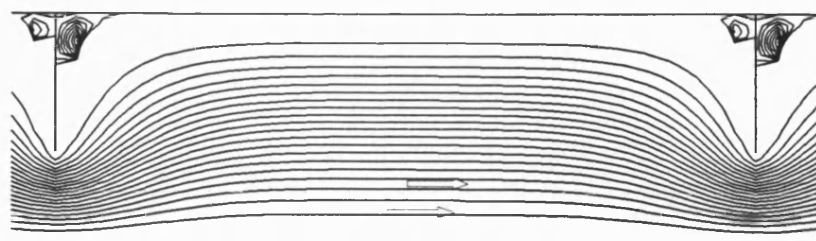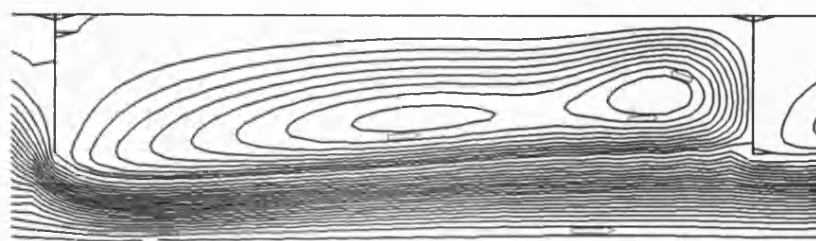
Re=100
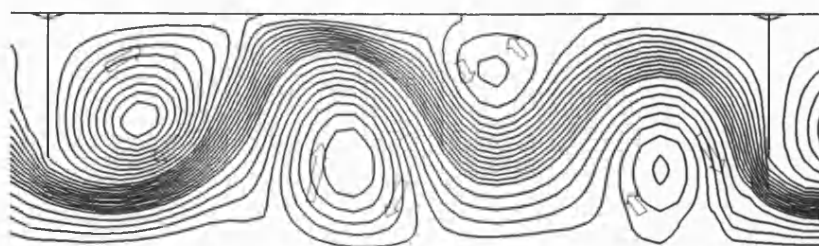
Re=200

Figure 17 Simulation of steady flow in rectangular channel $v_w = 10^{-3}$

Re=1
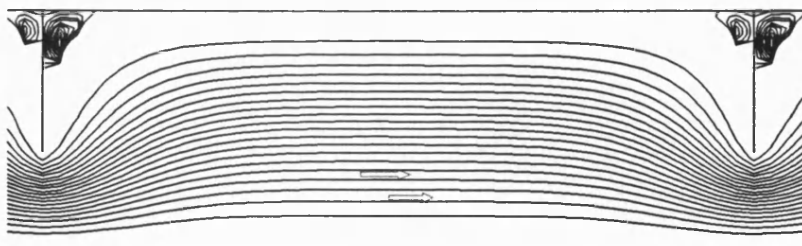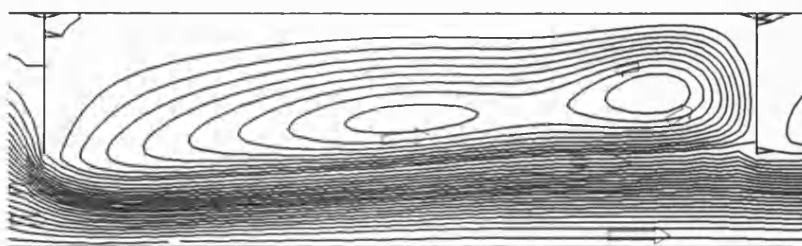
Re=100
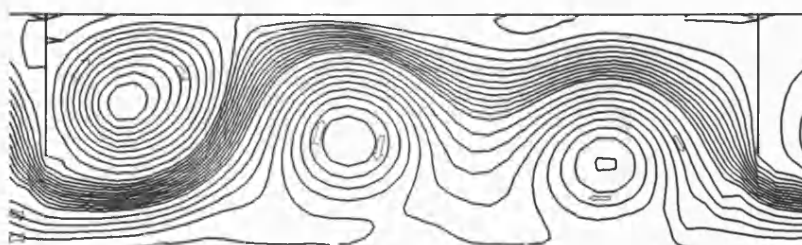
Re=200

Figure 18 Simulation of steady flow in rectangular channel $v_w = 10^{-4}$

3.2 Oscillatory flow patterns

3.2.1 Oscillatory flow pattern without wall suction

3.2.1.1 Comparison with experiment

In Figure 19 we compare the experimentally observed flow pattern with the numerical simulation (Mackay et al. 1991). Figure 19 a, b, c relate to central baffles and d, e, f to wall baffles. The patterns are split along the symmetry axis showing the experimental situation on the top and the corresponding numerical simulation below. For any given flow condition i.e. Re_o, St only one situation is shown for a given t^*. Each of the flows however have an important time dependence.

In Figure 20 we compare for a centrally baffled system the instantaneous experimental visualisation obtained by Finnigan (1990) with the numerical simulation over the evolution of a complete time cycle with Density $\rho = 998.5$ kg/m^3, Viscosity $\mu = 0.001056$ Pa s and characterised by $Re_o = 906$ and St$= 0.0326$. It seems that this experimental visualisation lies between time$= 0.50$ and 0.55. This simulation shows that the assertion which was made by Sobey (1980) and Mackley (1987) in relation to a wall baffled channel namely that pulsatile, reversing flow provides a mechanism for forming eddies and convecting the eddy from the wall to the main body of the fluid still holds at high Reynolds number with large amplitude of oscillation in the central baffles case.
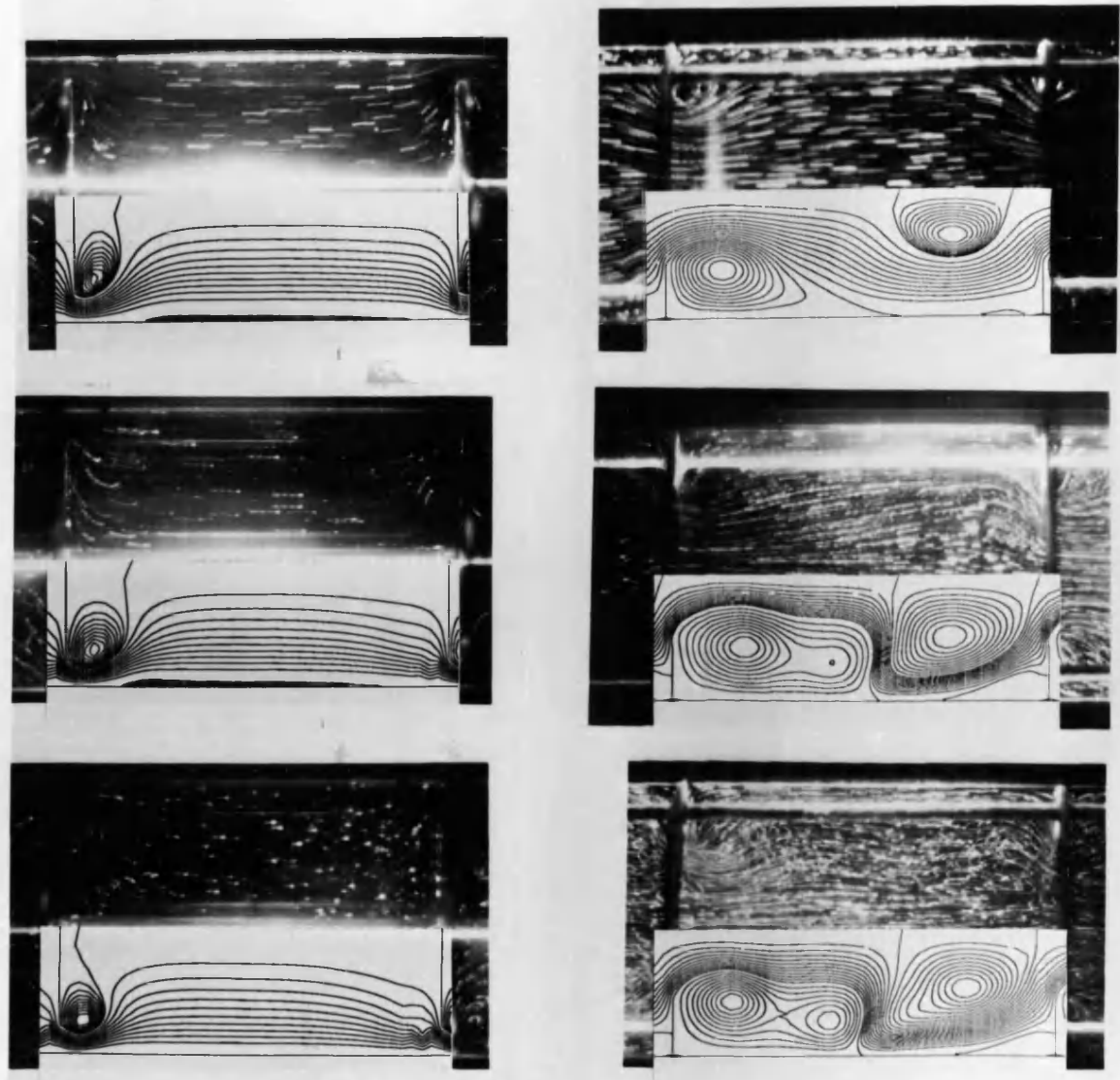
$$\beta = 0.39 \qquad \beta = 0.35$$
$$St = 1.0$$

(A) central $Re_o = 41$
    time $= 0.4$

(B) central $Re_o = 101$
    time $= 0.4$

(C) central $Re_o = 171$
    time $= 0.3$

(D) wall $Re_o = 45$
    time $= 0.4$

(E) wall $Re_o = 105$
    time $= 0.5$

(F) wall $Re_o = 160$
    time $= 0.4$

Figure 19 Comparison between numerical and experiment flow patterns
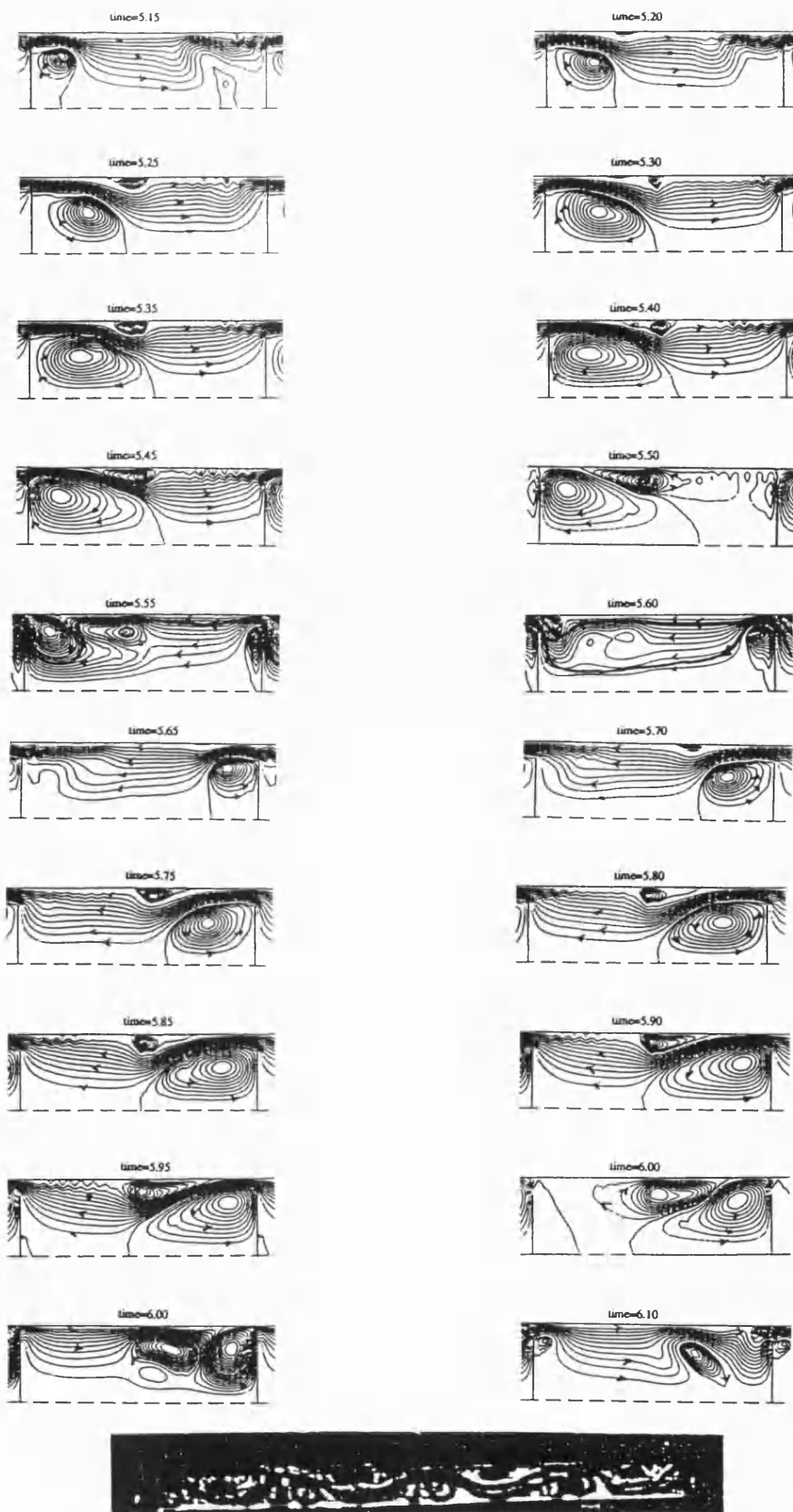
Figure 20 Comparison between numerical and experiment flow patterns

3.2.1.2 The occupied proportion

There is only some proportion of each cell in which secondary motion occurs. The occupied proportion(x) is defined by the distance(xL) between adjacent baffles over which the snake motion occurs. To measure the occupied proportion the length is determined over which a secondary motion occurs somewhere across the channel perpendicular to the average flow direction. If only one vortex occurs the reattachment length was taken as the length of occupied proportion. The qualitative analysis was carried out for the centrally baffled system and the quantitative results for the rectangular system.

The influence of x_0 and λ on the occupied proportion by the see-saw motion for central baffle with $v = 1 \times 10^{-5}$ (m^2/s), $D = 12.5 \times 10^{-3}$ (m) and $f = 5$ (Hz) is presented in Table VI below.

Table VI Influence of x_0 and λ on the
Proportion of a cell contouring a vortex

λ x_0(m)	10^{-3}	2×10^{-3}	4×10^{-3}
0.8	22%	52%	93%
1.6	10%	22%	35%
3.2	5%	9%	17%
Re_o, St	39.27, .995	78.54, .498	157.8, .2488

It can be seen from this table that x_0 is approximately proportional to the occupied proportion and λ is roughly inversely proportional to it.

Figure 21 shows flow patterns of the influence of λ on the occupied proportion by the see-saw motion for central baffle with $\beta = 0.4$, $v = 1x10^{-5}$ (m^2/s), $D = 12.5x10^{-3}$ (m), $St = .498$ and $Re_0 = 157.8$, Figure 21 a, b and c are for $\lambda = 0.8$, $\lambda = 1.6$ and $\lambda = 3.2$ respectively. There is a great proportion of each cell in which no secondary motion occurs in Figure 21 c.

The influence of λ, St and Re_0 on the occupied proportion are shown in Figure 22, Figure 23 and Figure 24 respectively for $\lambda 1 = 0.8$, $\lambda 2 = 11.6$ and $\lambda 3 = 3.2$, $St1 = .995$, $St2 = .498$ and $St3 = .2488$, and $Re_0 1 = 39.27$, $Re_0 2 = 78.54$ and $Re_0 3 = 157.8$. These figures show that the occupied proportion is a monotonic decreasing function of λ, St and almost $1/Re_0$.

For rectangular module the influence of λ can be seen from Figure 25, Figure 26 and Figure 31. It seems that $\lambda = 3$ give best performance.
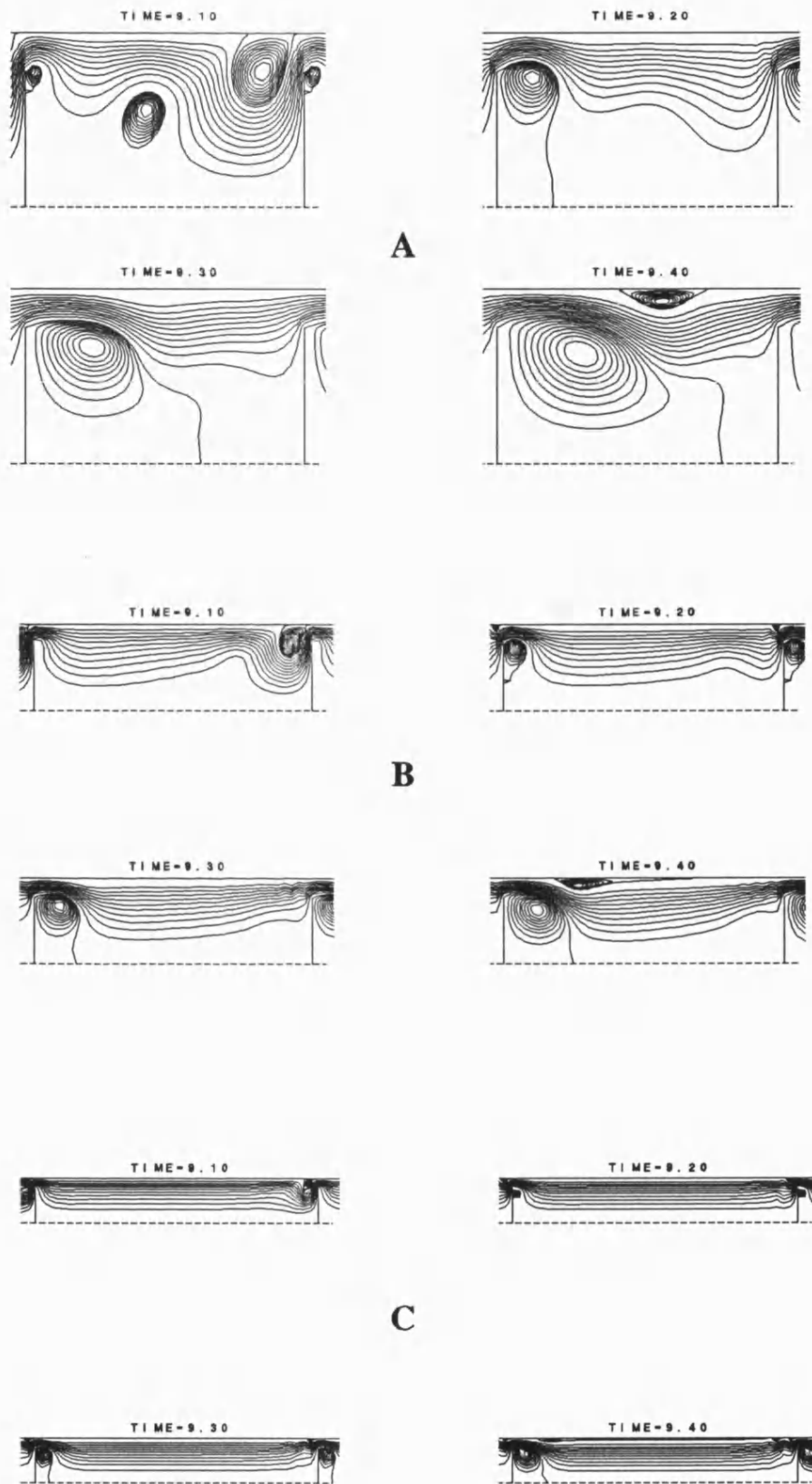
Figure 21 Flow patterns of the influence of λ on the occupied proportion

Influence of λ on the Occupied Proportion
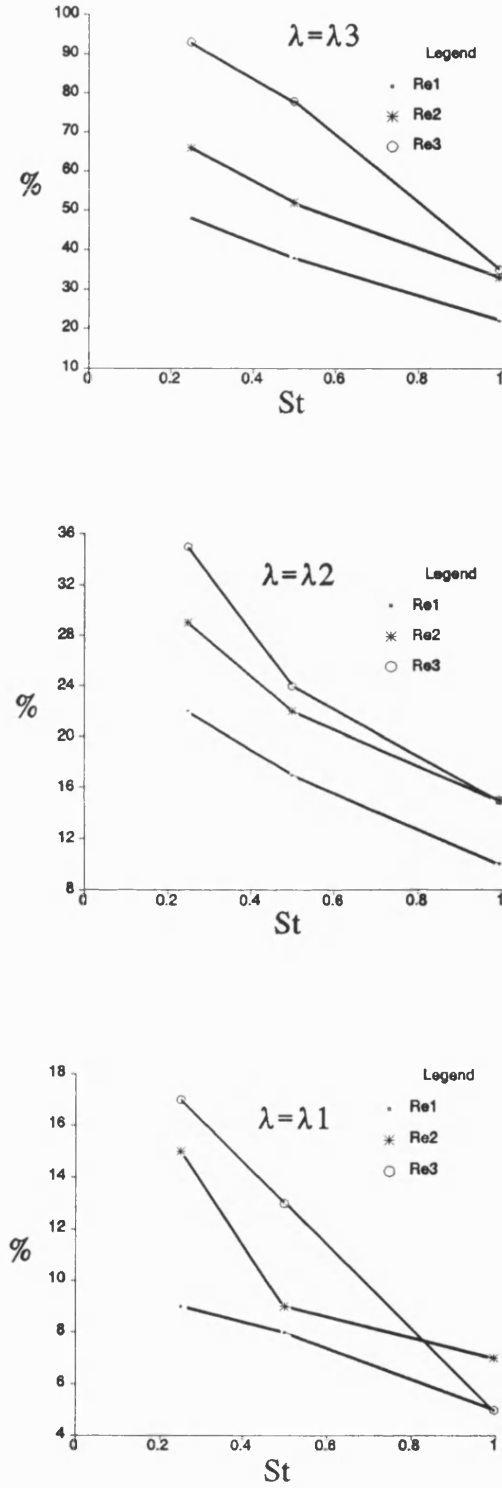
Figure 22 for the occupied proportion

Influence of St on the Occupied Proportion
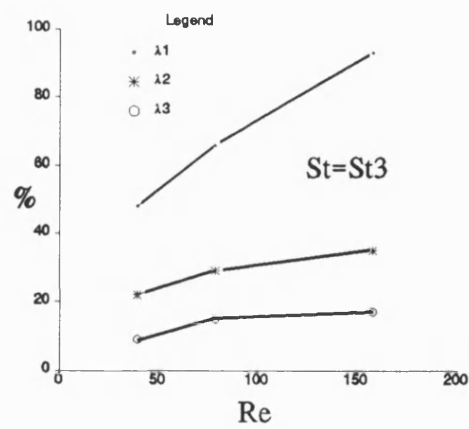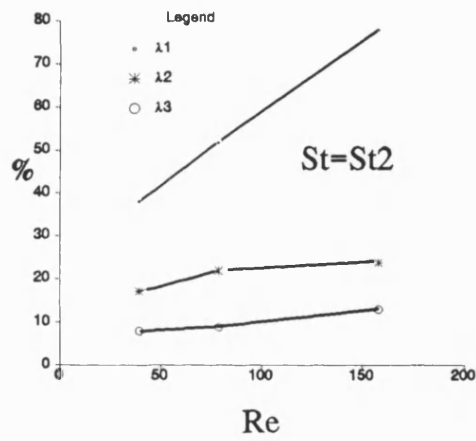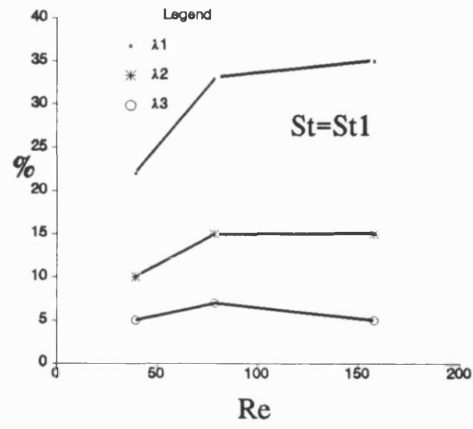
Figure 23 for the occupied proportion

Influence of Re on the Occupied Proportion
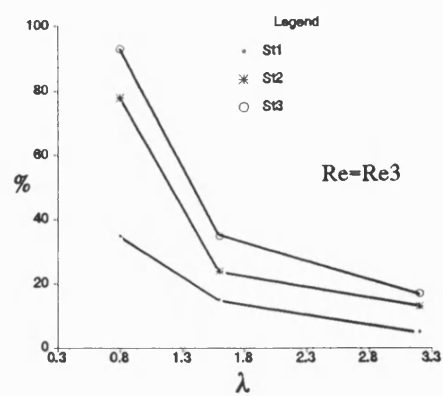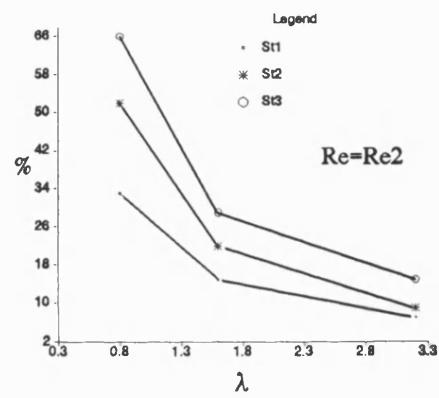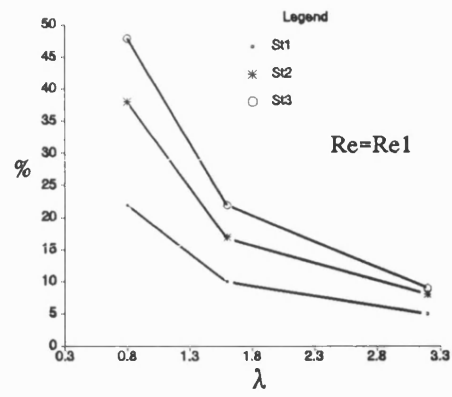
Figure 24 for the occupied proportion

Re$_o$ =200, Re$_n$ =0, St=1, ß=.4 and λ=4 for rectangular module
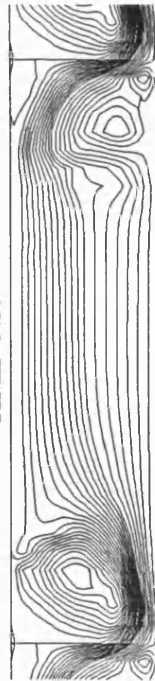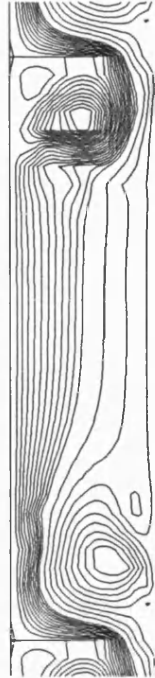
TIME=5.35
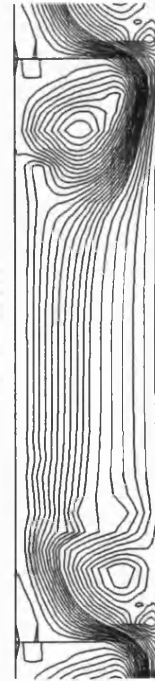
TIME=5.60
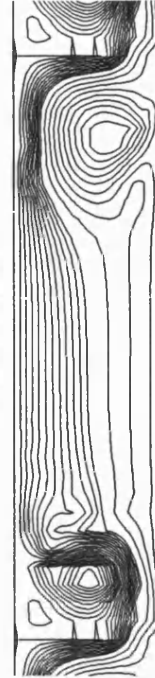
TIME=5.85

TIME=6.10

Figure 25 for the occupied proportion

Re, =200, Re n =0, St=1, ß=.4 and λ=8 for rectangular module

TIME=5.35

TIME=5.60

TIME=5.85

TIME=6.10

Figure 26 The occupied proportion

3.2.1.3 Flow patterns and velocity vector fields

Figure 27 and Figure 28 show the time evolution of the flow pattern for wall and central baffles for the condition $Re_o = 200$, $St = 1.0$. The pattern is shown at dimensionless times 0.25, 0.50, 0.75 and 1.00. For the wall baffles there is a complex time dependent eddy pattern where on each oscillation a vortex is formed downstream from each baffle which is then subsequently ejected into the body of the cavity on flow reversal. The central baffle has a different characteristic in that a second vortex forms near the tube wall. The bulk flow moves around and between the downstream vortex formed behind the baffles and this second vortex in a convoluted fashion referred to as the snake effect by Finnigan (1990). This snake effect is the dominant feature of this type of flow regime.

Figure 29 and Figure 30 (the dimensionless time = 0.7) show the velocity vector fields for wall baffle without pulsation and a wall baffle with pulsation for the condition $\lambda = 1.5$, $\beta = 0.4$, $Re = 200$ and $St = 1..$ To see the details, these two plots are mapped onto a unit square, allowing us to see not only the direction but also the magnitude of the velocity. Although a baffle induces vortices, a baffle with pulsating flow creates eddies and also moves the main flow to the membrane surface.

Figure 31 and Figure 32 show the time evolution of the flow pattern for the rectangular module for the condition $Re_o = 250$, $St = 1.0$ and $Re_o = 650$, $St = 1.0$.

A rectangular module has a different characteristic from a tubular module in that the vortex formed downstream from each baffle is not subsequently ejected into the body of the cavity but stays where it is created and reversing flow causes it to erode partially or completely, depending on the St number. When Re_0 is above about 250 a vortex on the membrane surface starts to form. It is believed that these are the vortices which enhance most the mixing on the membrane surface with the body flow and increase the membrane flux. Increasing the Strouhal number or Reynolds number increases the strength and the area of these surface vortices.
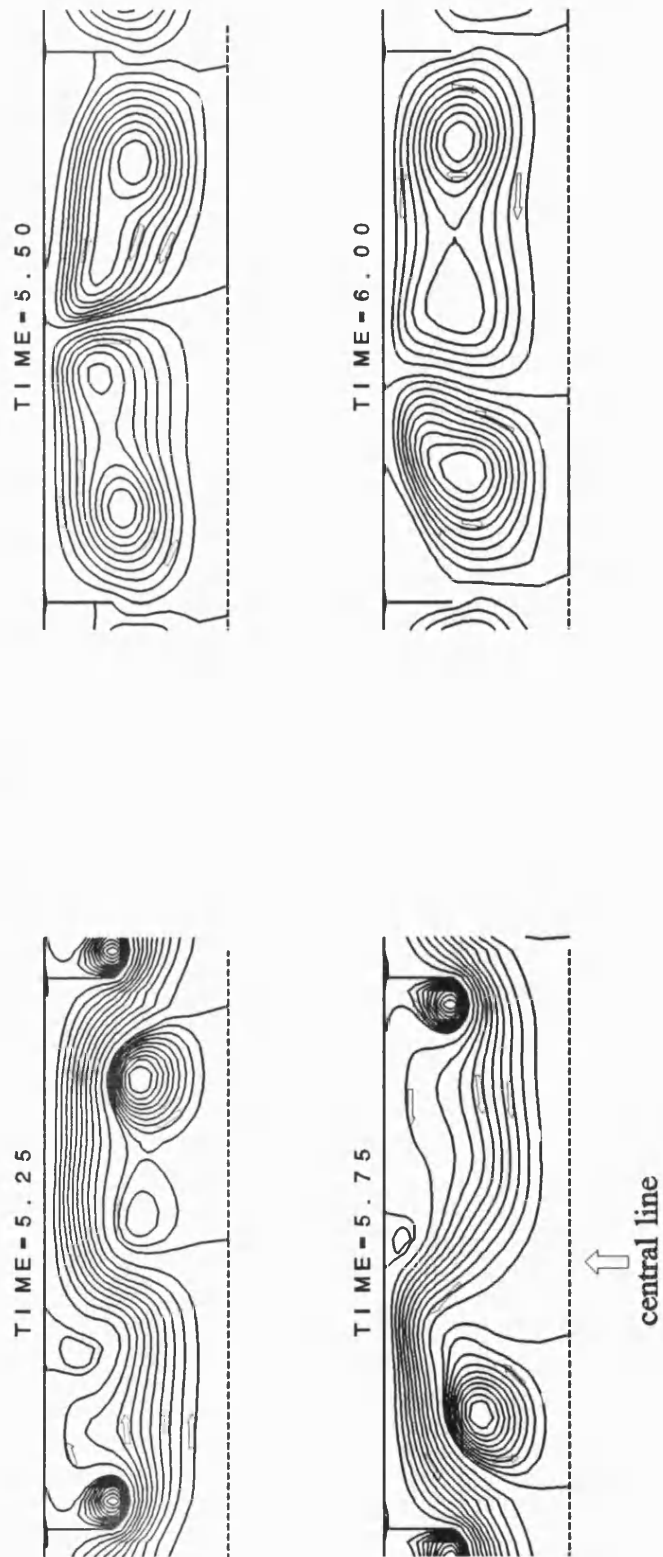
Figure 27 The time evolution of the flow pattern for wall baffles
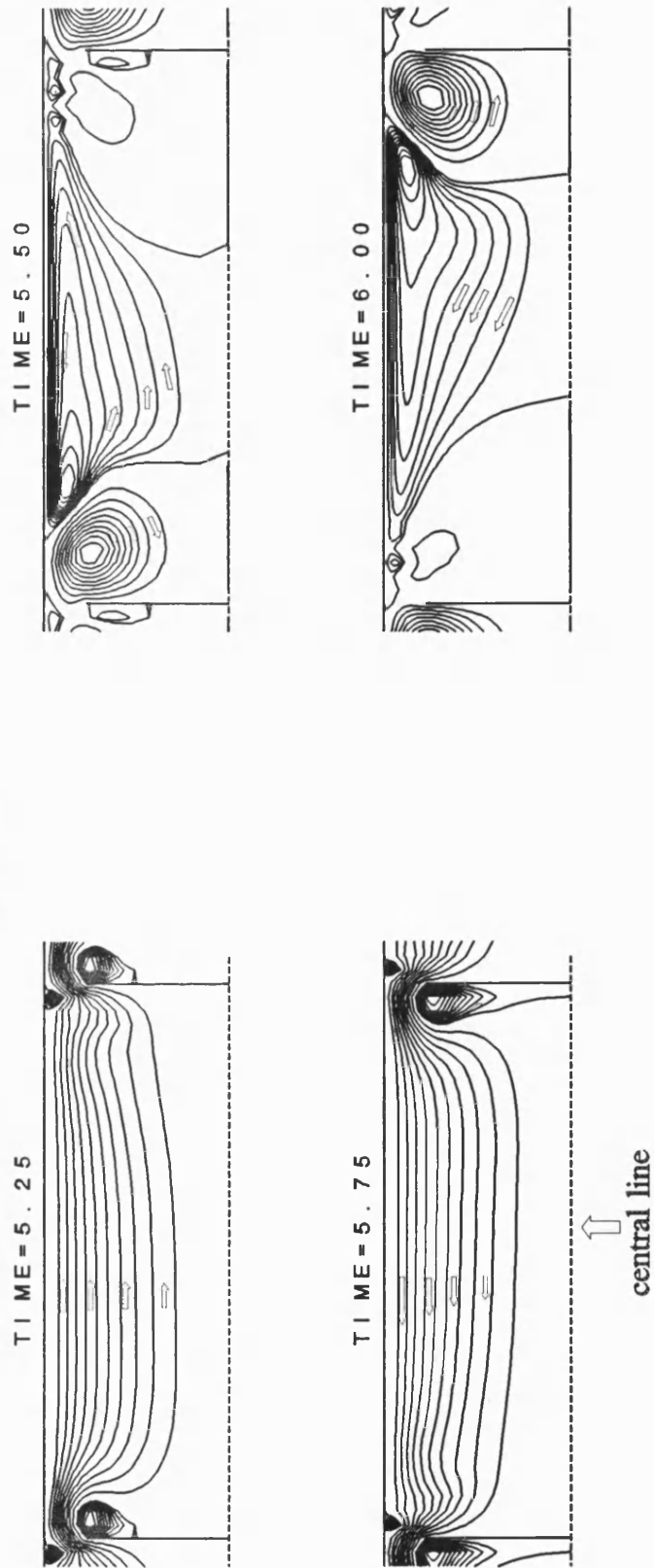
Figure 28 The time evolution of the flow pattern for central baffles

$Re_o=0$, $Re_n=200$, $\lambda=1.5$, $\beta=0.4$, tubular wall module

membrane surface
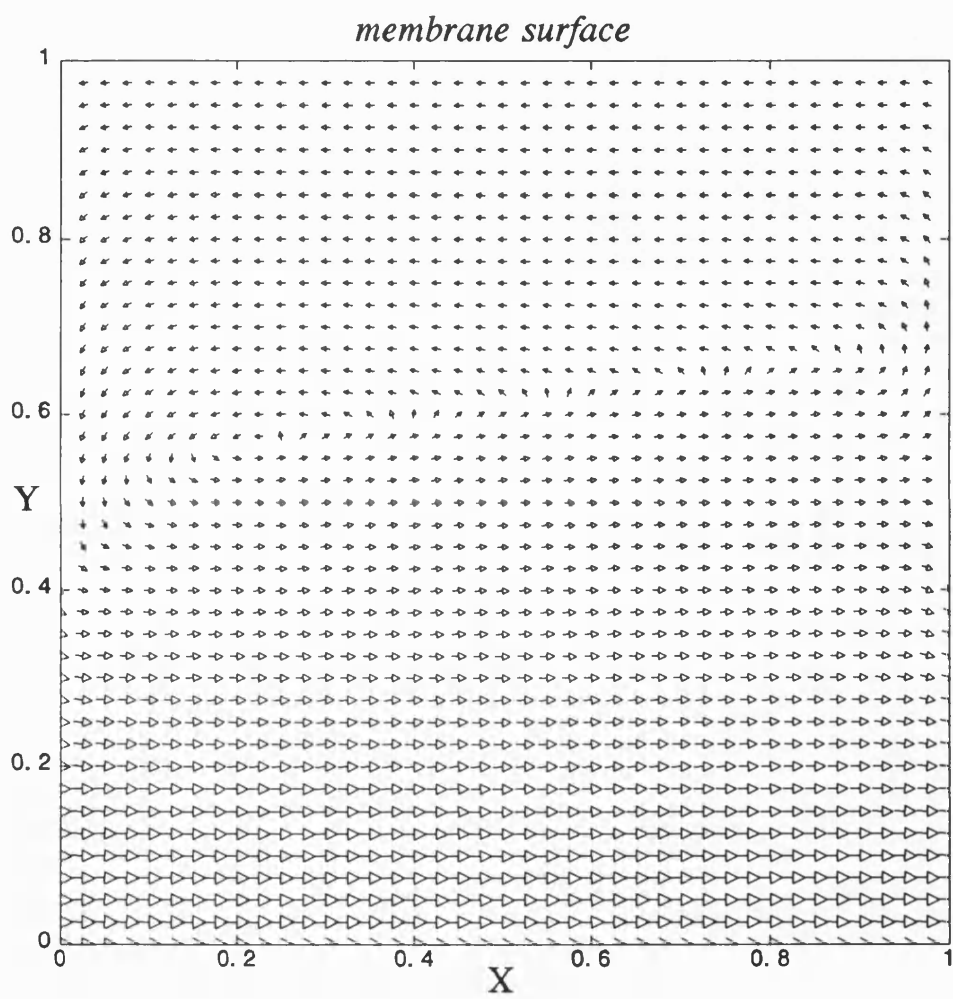
Figure 29 Velocity vector fields for steady flow

Re₀=200, Reₐ=0, St=1, λ=1.5, β=0.4, tubular wall

t=0.7
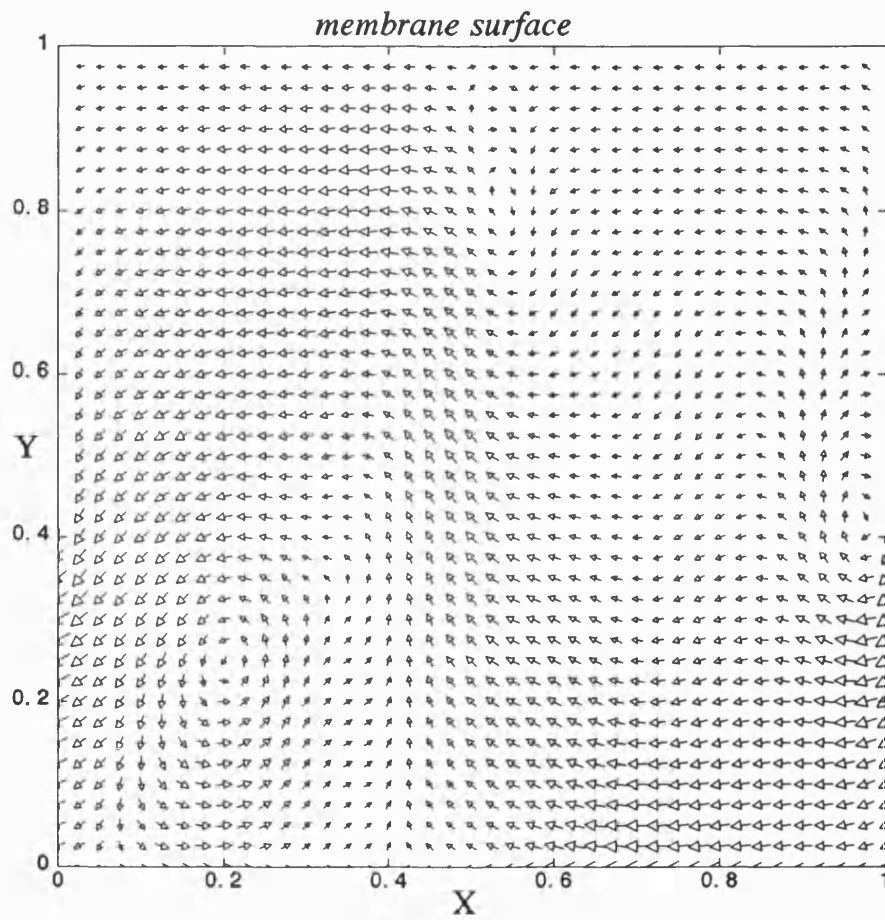
Figure 30 Velocity vector fields for oscillatory flow

$Re_o = 250$, $Re_n = 0$, $St=1$, $ß=.4$, and $\lambda=3$ for rectangular module
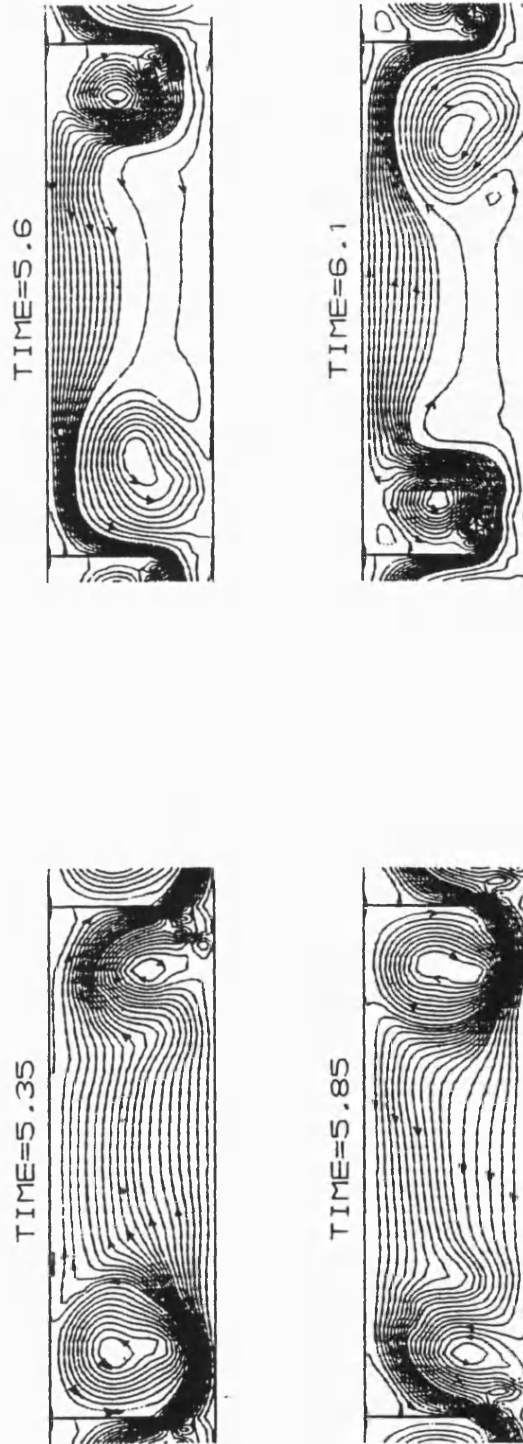
Figure 31 Flow pattern for rectangular module
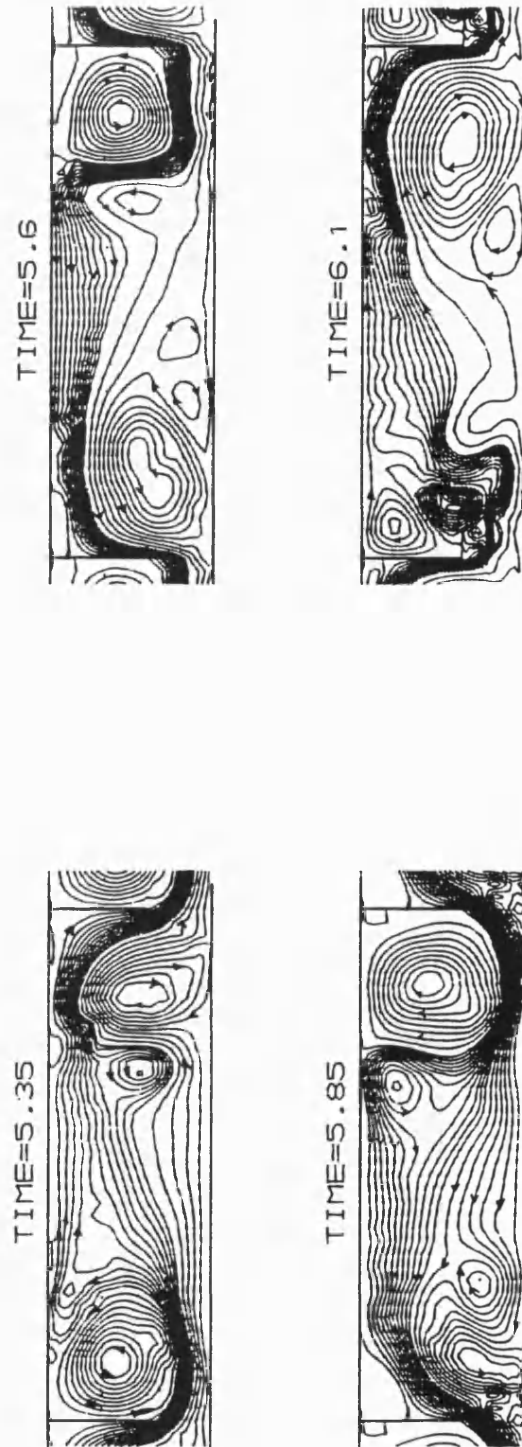
Figure 32 Flow pattern for rectangular module

Re$_o$ =650, Re$_n$ =0, St=1, ß=.4, and λ=3 for rectangular module

3.2.1.4 Influence of flow area ratio β

Figure 33 shows the influence of flow area restriction ratio on the flow pattern with a central baffle under the condition $\beta = 0.2 \sim 0.8$, $\lambda = 1.5$, $Re_o = 200$, $Re_n = 0$, $St = 1.0$. It seems that for $\beta = 0.4 \sim 0.7$ a bigger recirculating vortex is formed at the occurence of zero net flow time ($t = 0.5$).

3.2.1.5 Influence of St

The dependency on St is less straight forward but in very simplistic terms the vortex mixing process is inertia dominated at low St and viscous dominated at high St (Sobey 1980). Howes stated that increasing St while keeping Re_o constant increases the complexity of the flow with a wall baffle (Howes 1988).

With a central baffle a second vortex forms near the tube wall when the Reynolds number exceeds about 200. When St decreases this second one becomes stronger and bigger, and finally dominates. Figure 34 shows that, with $Re_o = 200$, $Re_n = 0$, at the small Strouhal number $St = 0.05$, which is about the order in the membrane filtration device of Finnigan (1990) and Howell (1992b), a third vortex is formed close to the wall in central baffles case. In this time evolution of the flow patterns one can see that at the middle of first half time cycle the third vortex starts to form and grows and finally occupies the whole cavity at no flow time along with the first vortex which formed just behind the baffle. When flow reverses this third vortex merges with the second one behind the baffle from right to left direction and squeezes the first vortex to the left-hand side consecutive cell. Later this second vortex was pressed out by the unification of

third and first one in the left towards the right-hand side consecutive cell in the similar way.

For rectangular module when Re_o is about to 250 a vortex on the membrane surface starts to form near the membrane surface. When St decreases this third one becomes stronger and bigger, and dominates finally. Figure 35 shows, with $Re_o = 400$, $Re_n = 0$, at medium Strouhal number $St = 0.4$, one time cycle evolution of the flow pattern. In this time evolution of the flow patterns one can see that at dimensionless time $= 0.25$ the surface vortex begin to form and grows and finally reaches to the peak at no flow time $t = 0.5$. When flow reverses this vortex moves through the body flow to the other side of the wall and floats with the main stream flow to the left and finally dissipates near the place where it starts.

INFLUENCE OF BAFFLE FLOW AREA RATIO ON CENTRAL BAFFLE FLOW PATTERN
$Re_o=200, Re_n=0, St=1$ and $\lambda=1.5$

$\beta = 0.8$

$\beta = 0.7$

$\beta = 0.6$

$\beta = 0.5$

$\beta = 0.4$

$\beta = 0.2$
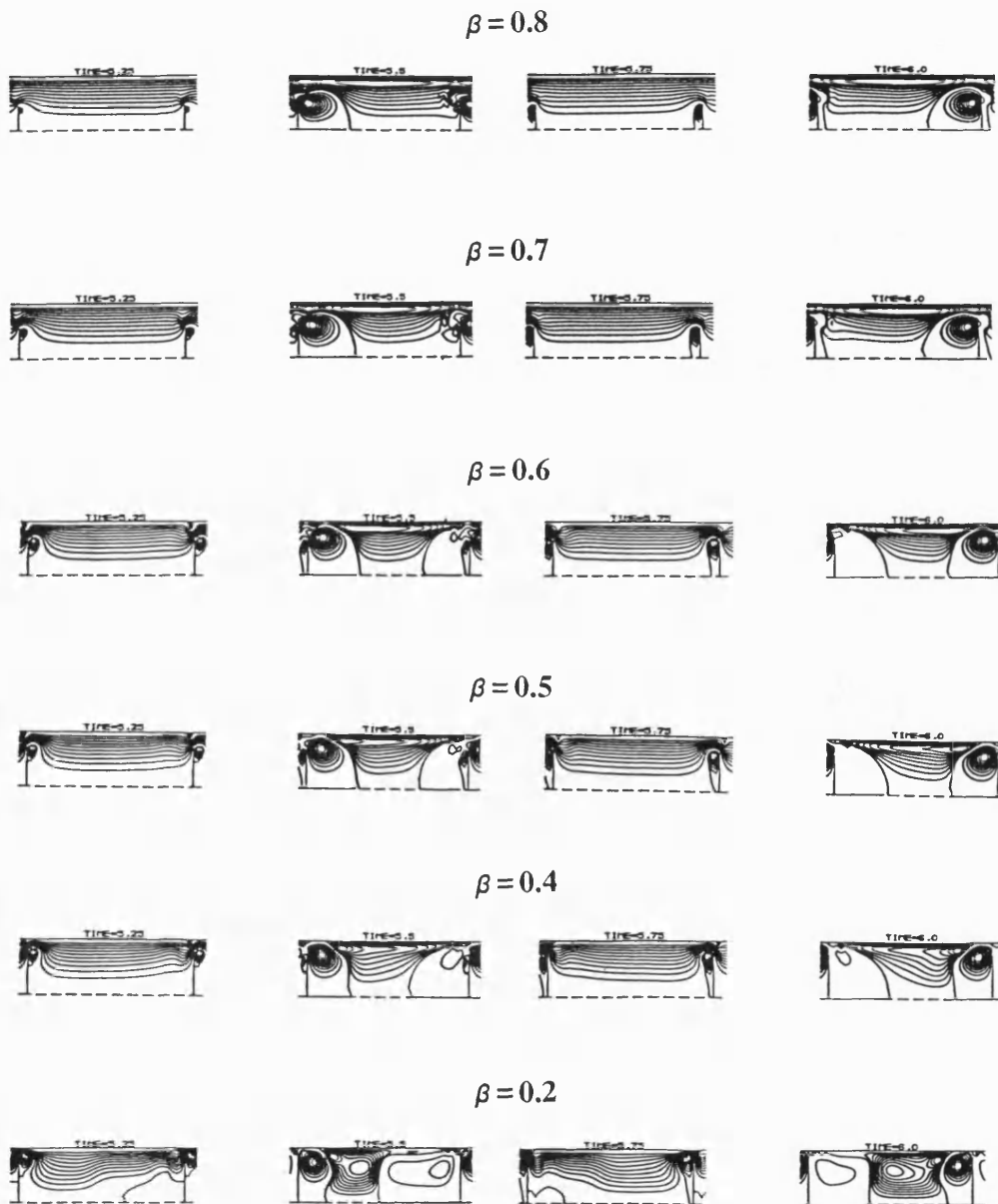
Figure 33 The influence of β on central baffles flow pattern.

Re$_o$ =200, Re$_n$ =0, St=.05, ß=.4, and λ=1.5 for central baffle

TIME=5.15   TIME=5.20

TIME=5.25   TIME=5.30

TIME=5.35   TIME=5.40

TIME=5.45   TIME=5.50

TIME=5.55   TIME=5.60

TIME=5.65   TIME=5.70

TIME=5.75   TIME=5.80

TIME=5.85   TIME=5.90

TIME=5.95   TIME=6.00

TIME=6.05   TIME=6.10
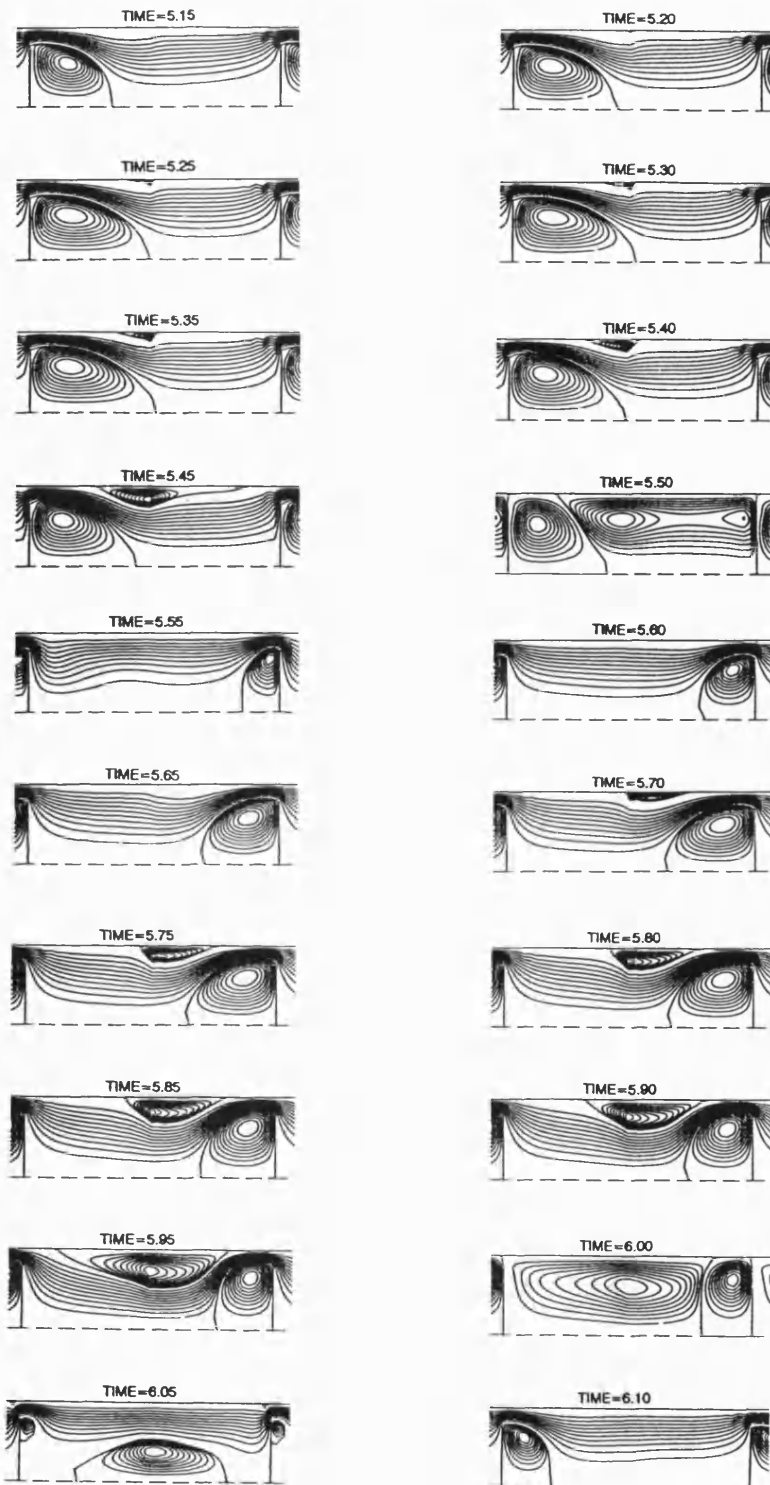
Figure 34 Third vortex for small St

Re$_o$ =400, Re$_n$=0, St=.4, ß=.4, and λ=3 for rectangular module

TIME=5.15   TIME=5.20
TIME=5.25   TIME=5.30
TIME=5.35   TIME=5.40
TIME=5.45   TIME=5.50
TIME=5.55   TIME=5.60
TIME=5.65   TIME=5.70
TIME=5.75   TIME=5.80
TIME=5.85   TIME=5.90
TIME=5.95   TIME=6.00
TIME=6.05   TIME=6.10
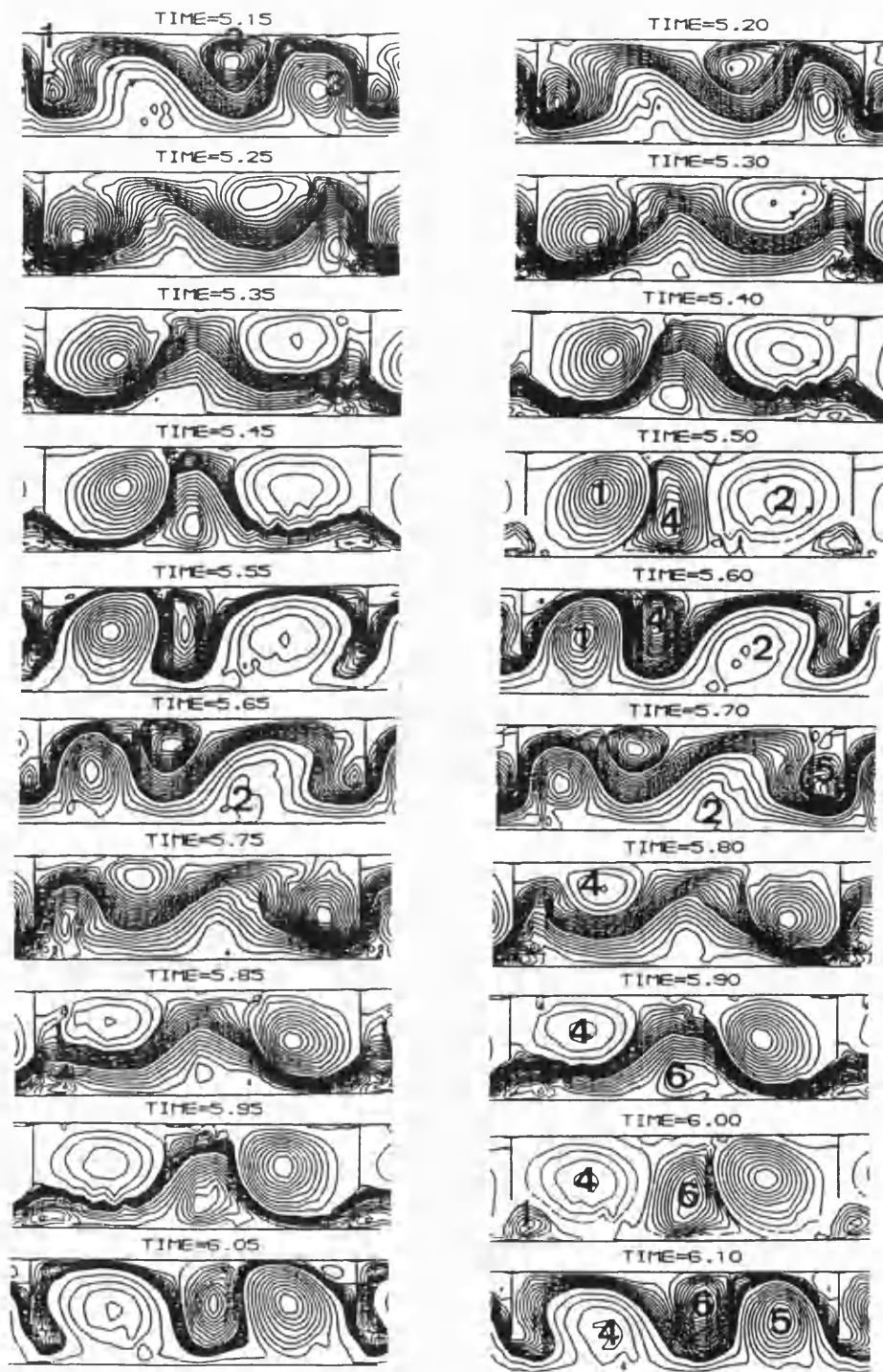
The numbers here indicate the generated vortices during one time cycle

Figure 35 Flow pattern for rectangular module with small St

3.2.1.6 Influence of different pulsating source

In this section the effects of different pulsating source on the flow patterns are examined. Fluid oscillations are generated by oscillating the instantaneous velocity through the channel, such that $\bar{U}_i = U_R \cdot FNT$ where FNT is the oscillatory source function. In most cases, sinusoidal source function are employed:

$$FNT = \begin{cases} 1 & \textit{steady} \\ NFR + \sin(2\pi t) & \textit{oscillatory} \end{cases} \qquad (44)$$

Finnigan reported that as the amplitude is decreased the pulsed velocity waveforms consist of progressively smaller fraction of the full wave observed at 100% until at 10% only the very top fraction of the 100% wave was seen. Hence, the waveform is periodic but truncated (Finnigan 1990). The break-sin wave as the oscillatory source function simulates this truncated triangular nature of the waveforms. The square-wave form simulates the valve-switching pulsating system of Howell et al. (1992b) (see Table V in Section 2.2.1).

Figure 36 and Figure 37 show the comparison of the sinusoidal and the square-wave source for wall baffles. Figure 38 and Figure 39 illustrate the comparison of the sinusoidal and the square-wave source for central baffles. Figure 40, Figure 41 and Figure 42 display the comparison of the sinusoidal, the square-wave and the break-sin wave source for wall baffles. Figure 43 and Figure 44 demonstrate the comparison of the sinusoidal and the square-wave

source for rectangular module. There is not much difference on the over all flow

patterns among the standard sinusoidal, the square-wave and the break-sin wave

source except for the fact that the break-sin wave source causes more growth of

all the eddies near the no flow time and more erosion and shrinking of the

vortices near the peak time as shown in Figure 42.

Re $_o$ =200, Re $_n$ =0, St=1, ß=.4 and λ=1.5 for wall baffle
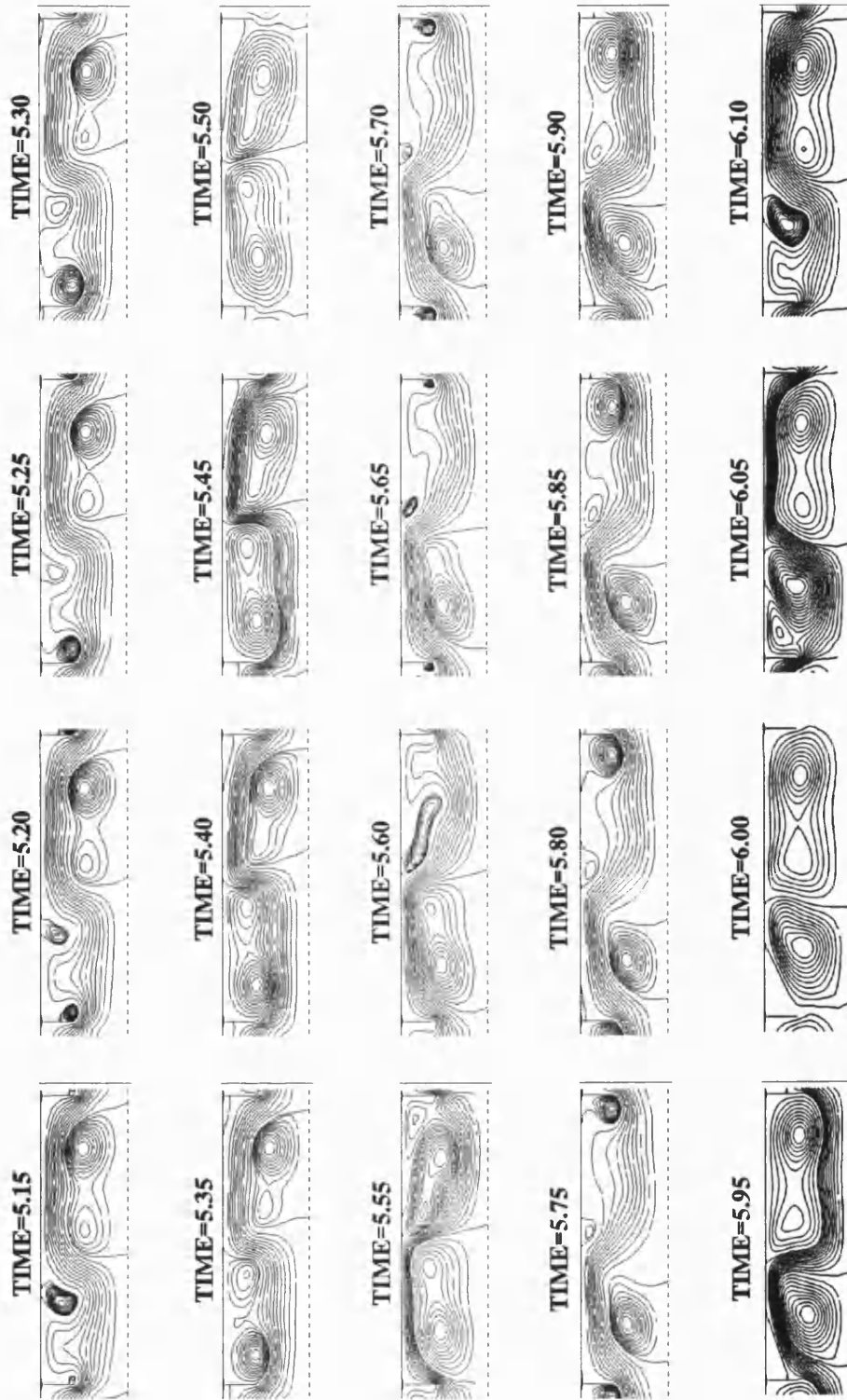
Figure 36 The influence of different pulsating source

Re$_o$ =200, Re$_n$ =0, St=1, ß=.4, and λ=1.5 for wall baffle with Square-wave pulsatile source

Figure 37 The influence of different pulsating source

Re$_o$ =200, Re$_n$ =0, St=1, ß=.4, and λ=1.5 for central baffle
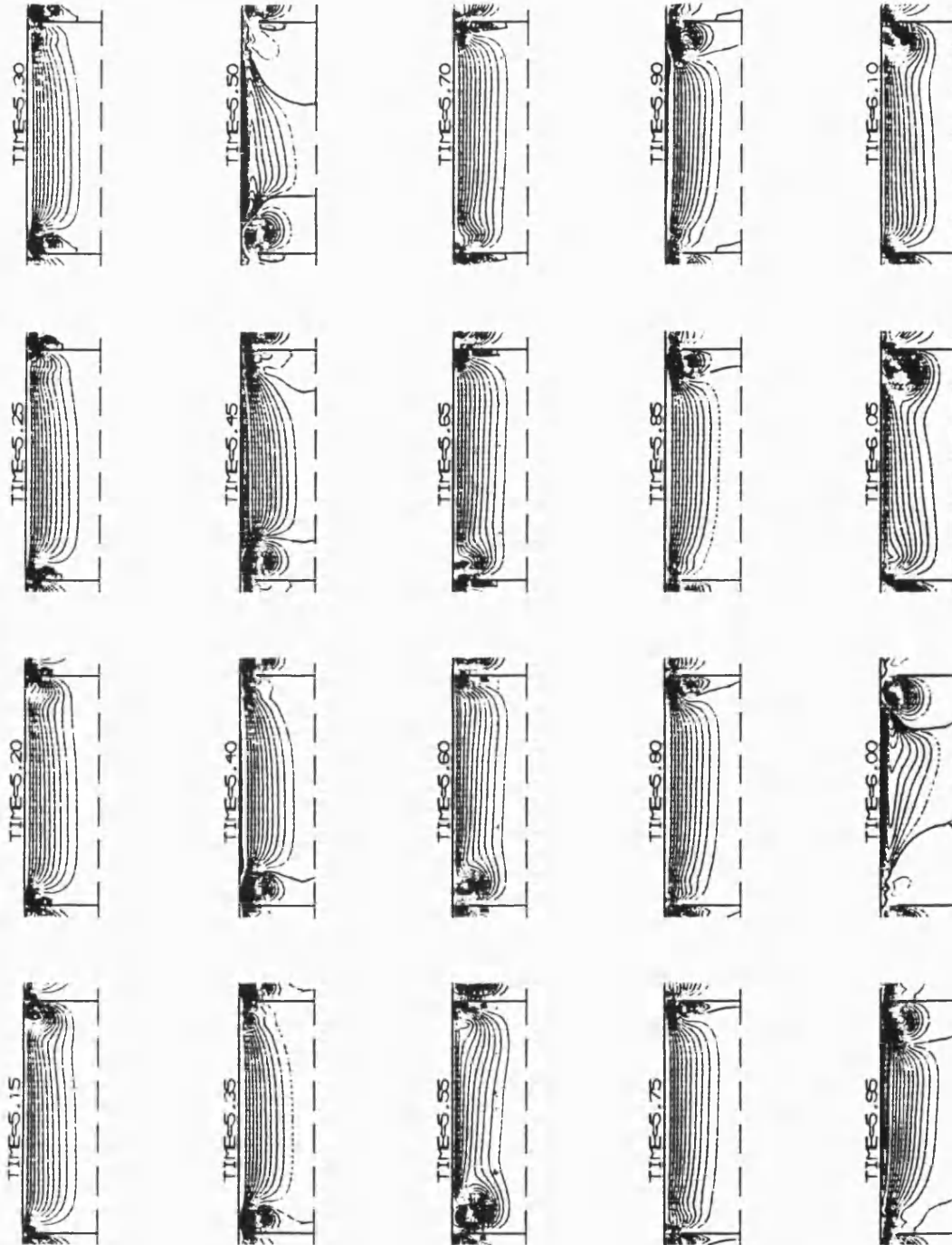
Figure 38 The influence of different pulsating source

Re$_o$ =200, Re$_n$ =0, St=1, ß=.4, and λ=1.5 for central baffle with Square-wave pulsatile source
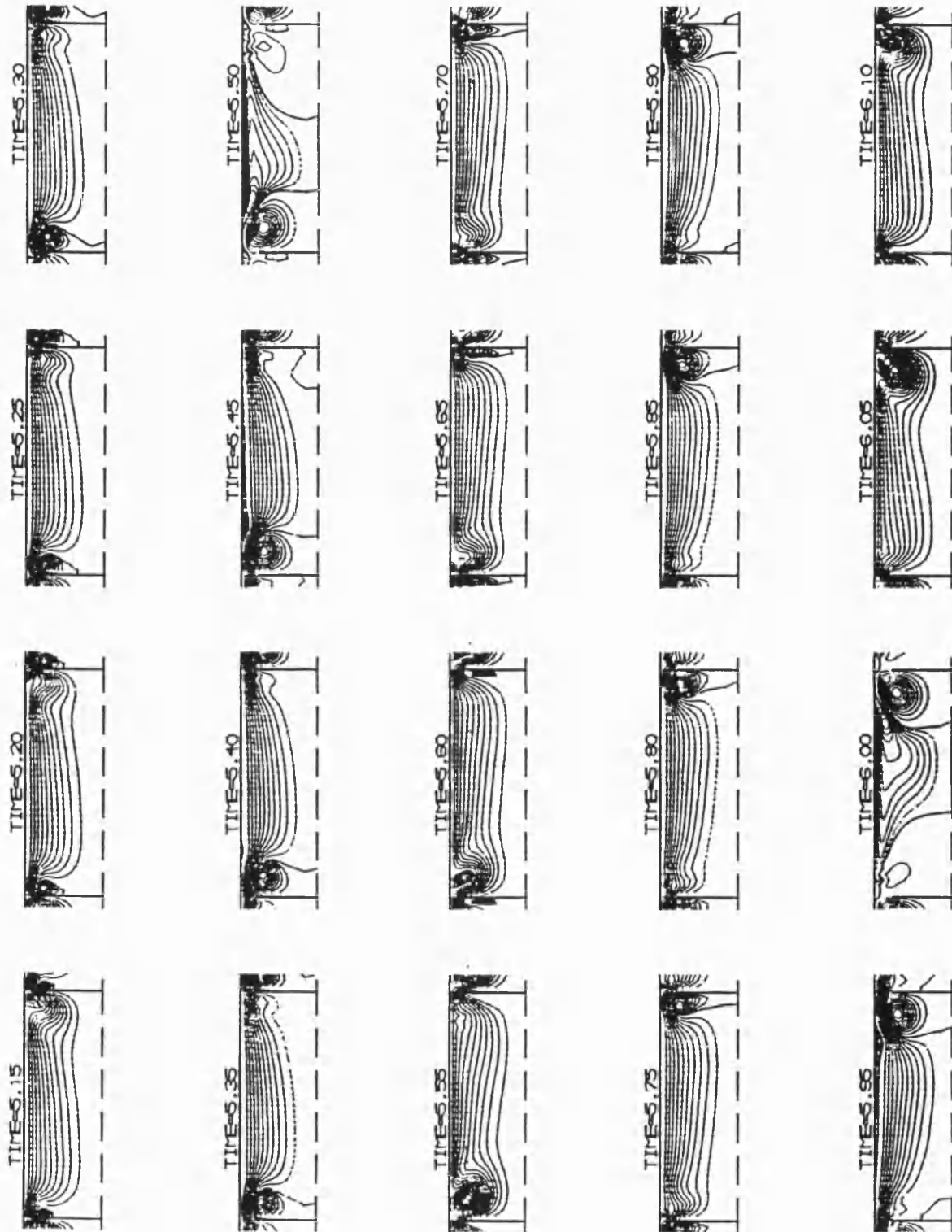
Figure 39 The influence of different pulsating source

Figure 40 The influence of different pulsating source

$Re_0 = 100$, $Re_n = 0$, $St = 1$, $\beta = .4$ and $\lambda = 1.5$ for wall baffle

TIME=5.15 TIME=5.20 TIME=5.25 TIME=5.30

TIME=5.35 TIME=5.40 TIME=5.45 TIME=5.50

TIME=5.55 TIME=5.60 TIME=5.65 TIME=5.70

TIME=5.75 TIME=5.80 TIME=5.85 TIME=5.90

TIME=5.95 TIME=6.00 TIME=6.05 TIME=6.10

$Re_o = 100$, $Re_n = 0$, St=1, ß=.4 and λ=1.5 for wall baffle

with Square-wave pulsatile source
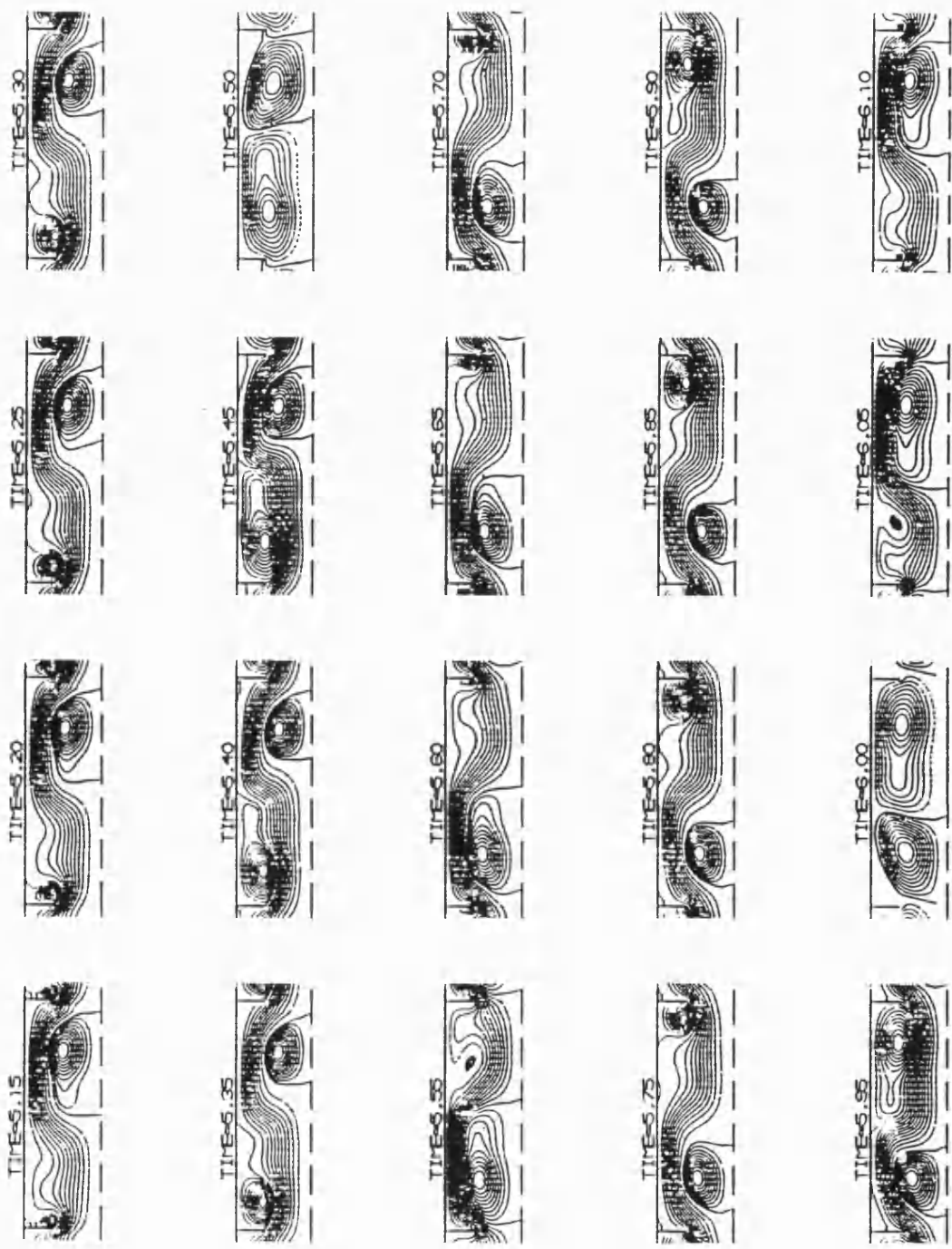
Figure 41 The influence of different pulsating source

Re_o =100, Re_n =0, St=1, ß=.4, and λ=1.5 for wall baffle with Break-sin wave pulsatile source
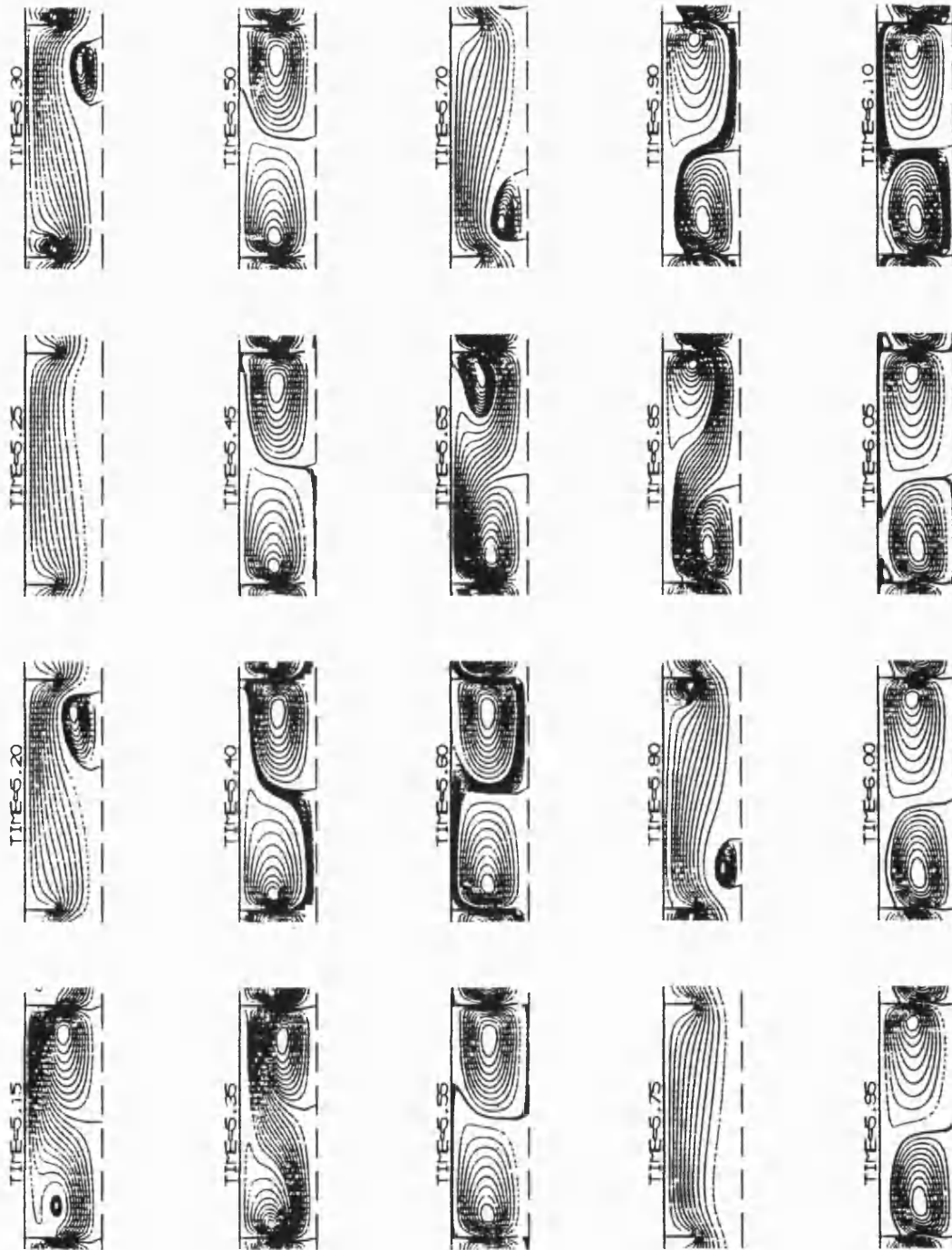
Figure 42 The influence of different pulsating source

Re$_0$ =200, Re $_n$=0, St=1, ß=.4, and λ=3 for rectangular module
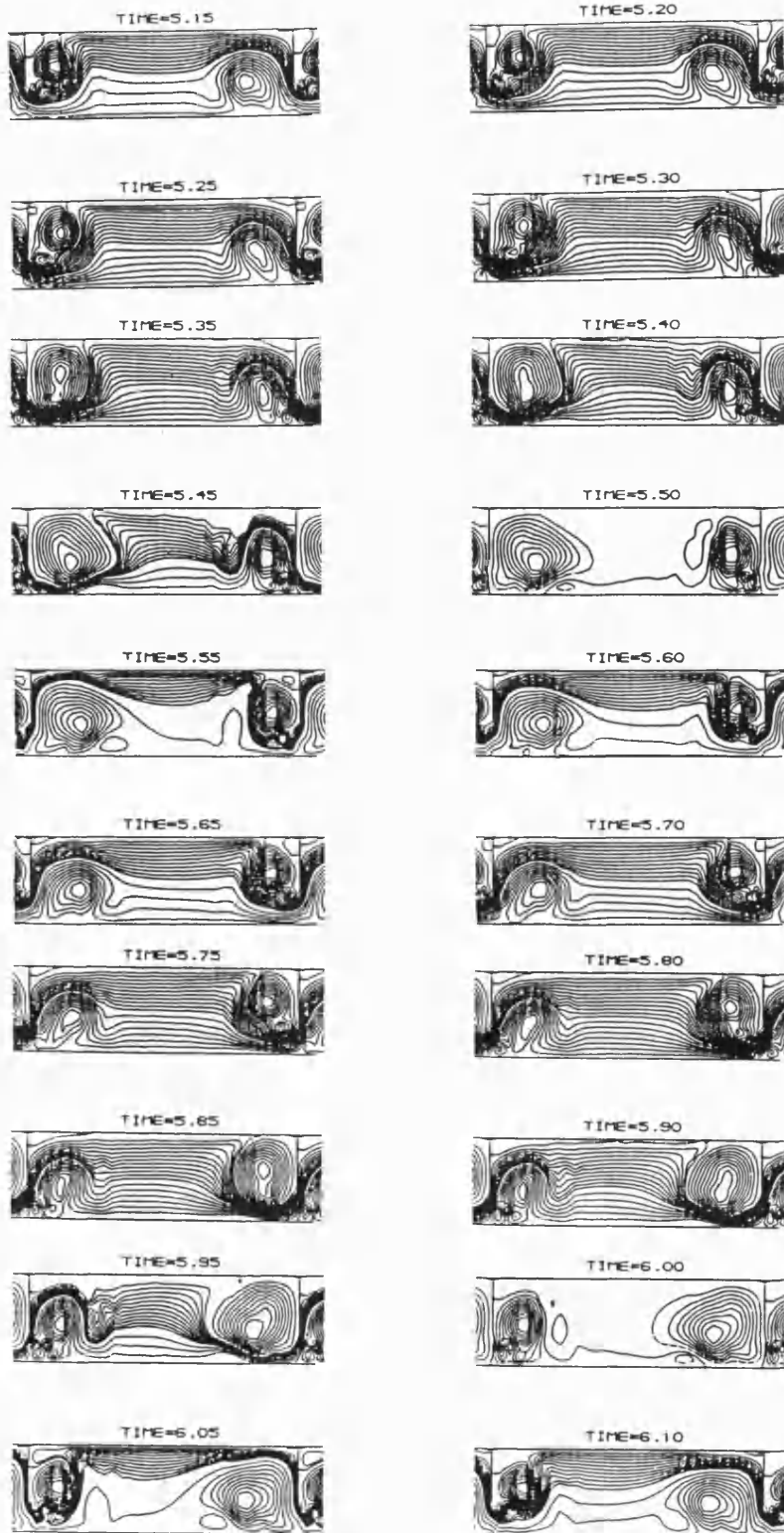
Figure 43 The influence of different pulsating source

Re₀ =200, Re ₙ=0, St=1, ß=.4, and λ=3 for rectangular module with Square-wave pulsatile source

Re$_0$ =200, Re $_n$=0, St=1, ß=.4, and λ=3 for rectangular module with Square-wave pulsatile source
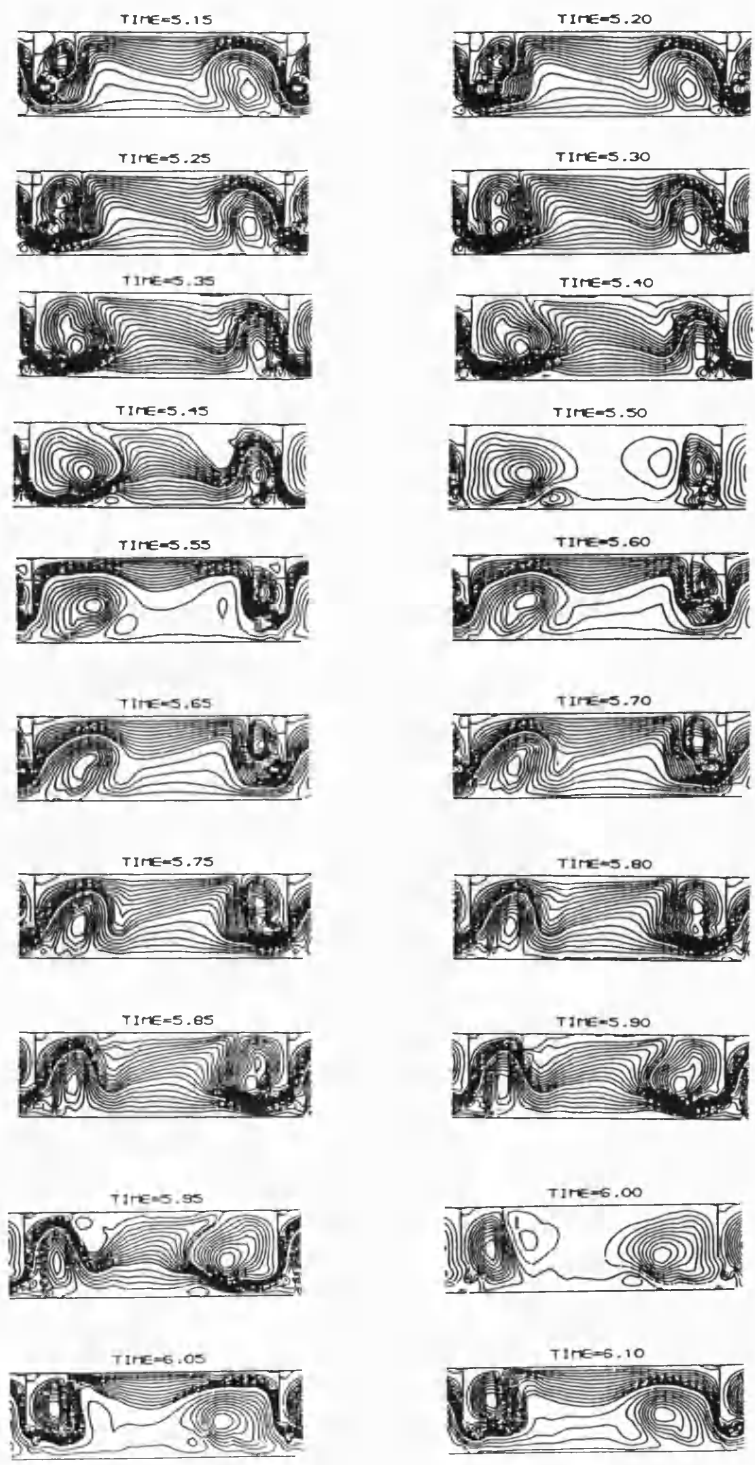
Figure 44 The influence of different pulsating source

3.2.1.7 Flow regime summary

Figure 45, Figure 46 and Figure 47 summarise the flow regimes observed for wall baffles, central baffles in tubular module and rectangular module respectively on a Re_o/St diagram. The Re_o/St diagram for wall baffles in tubular module has been previously calculated by Howes (1988). His result does not appear to differ from the result of this numerical simulation. The definition of the complexity of the flow as used by Howes is when more vortices exist in each cell at flow reversal. In wall baffles case as Re_o is increased, the flow becomes more complicated. The vortex strength and disordered nature of the flow increases until a point is passed where the motion becomes chaotic or numerically unstable. Increasing the St while keeping the Re_o constant increases the complexity of the flow.

The central baffle has a different characteristic in that increasing the St while keeping the Re_o constant does not necessarily increases the complexity of the flow, and decreasing the St while keeping the Re_o constant decreases forming-erosion time in small Re_o and allows third vortex occur earlier.

In the rectangular case Figure 47 shows that flow becomes less complicated in medium St for St in [0.1 , 4]. Time asymmetric flows are observed for Re_o reaching 320 when St≤0.5 or St≥2.

FLOW REGIMES
wall baffle tubular module
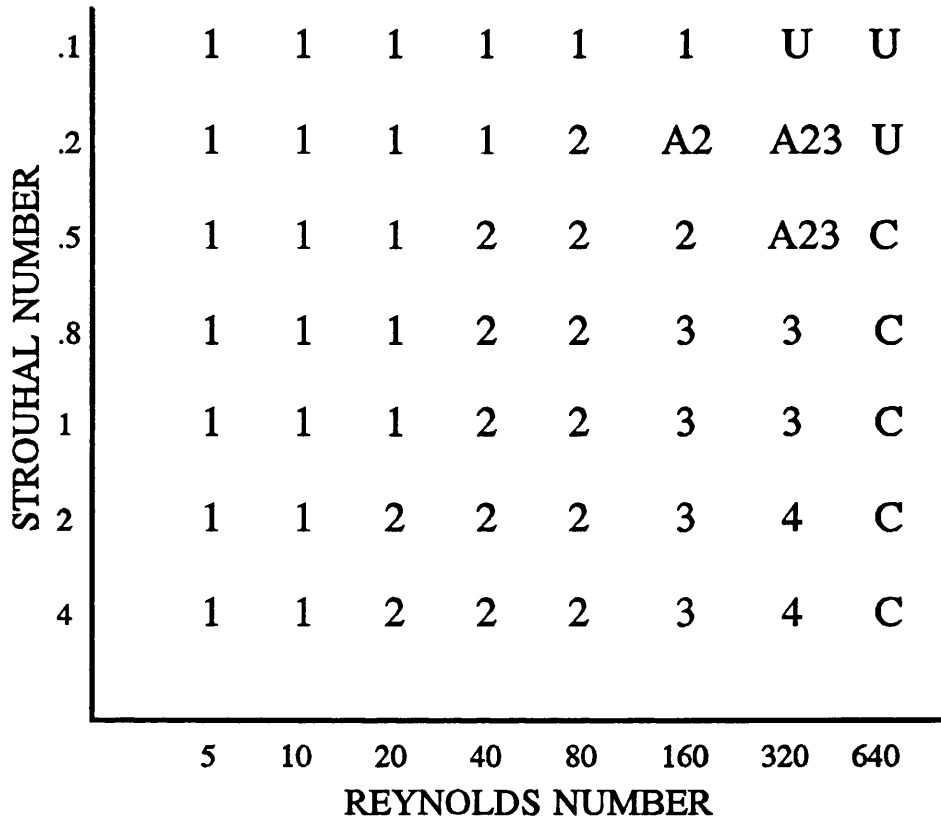
STROUHAL NUMBER	5	10	20	40	80	160	320	640
.1	1	1	1	1	1	1	U	U
.2	1	1	1	1	2	A2	A23	U
.5	1	1	1	2	2	2	A23	C
.8	1	1	1	2	2	3	3	C
1	1	1	1	2	2	3	3	C
2	1	1	2	2	2	3	4	C
4	1	1	2	2	2	3	4	C

REYNOLDS NUMBER

1 to 4 number of eddies in each cell at flow reversal, A2 asymmetric flow with 2 eddies at flow reversal, A23 asymmetric flow with 2 eddies at one flow reversal and 3 at the other, C chaotic flow, U numerically unstable.

Figure 45 Observed flow regimes for $Re_{net} = 0$, $\beta = 40\%$, $\lambda = 1.5$
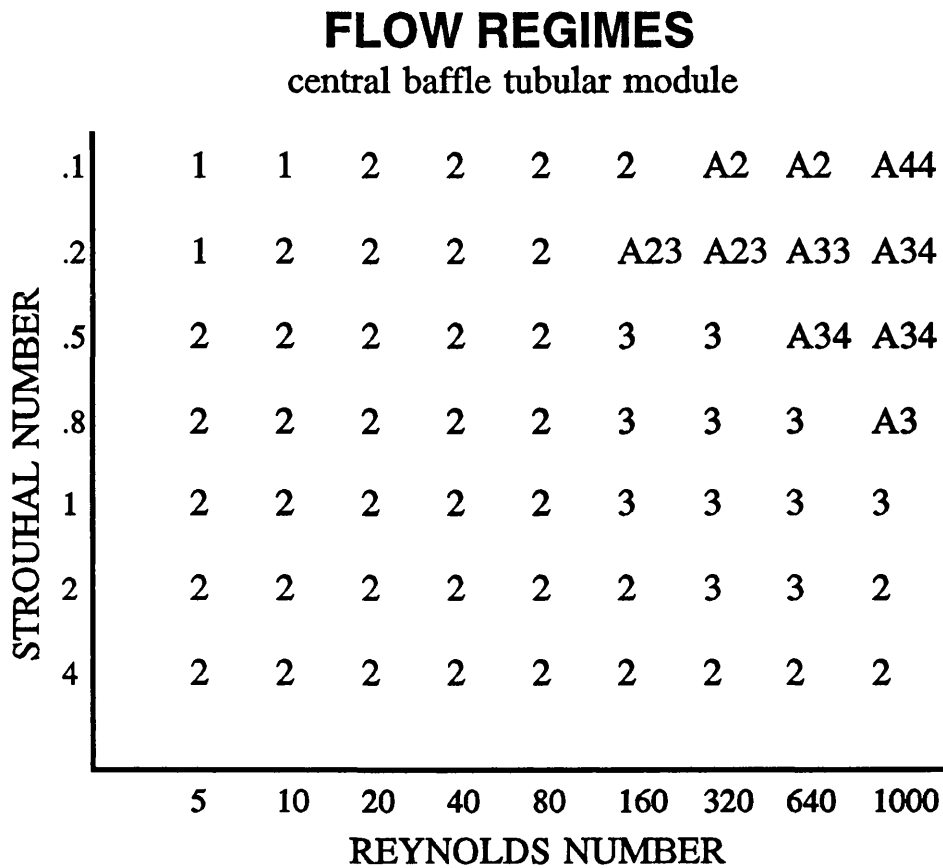
FLOW REGIMES
central baffle tubular module

STROUHAL NUMBER	5	10	20	40	80	160	320	640	1000
.1	1	1	2	2	2	2	A2	A2	A44
.2	1	2	2	2	2	A23	A23	A33	A34
.5	2	2	2	2	2	3	3	A34	A34
.8	2	2	2	2	2	3	3	3	A3
1	2	2	2	2	2	3	3	3	3
2	2	2	2	2	2	2	3	3	2
4	2	2	2	2	2	2	2	2	2

REYNOLDS NUMBER

1 to 4 number of eddies in each cell at flow reversal, A2 asymmetric flow with 2 eddies at flow reversal, A23 asymmetric flow with 2 eddies at one flow reversal and 3 at the other and so on

Figure 46 Observed flow regimes for $Re_{net}=0$, ß=40%, $\lambda = 1.5$

FLOW REGIMES
rectangular module

STROUHAL NUMBER

	5	10	20	40	80	160	320	640	1000
.1	2	2	2	2	2	3	A3	A4	U
.2	2	2	2	2	2	3	A3	A4	U
.5	2	2	2	2	2	3	A3	A3	U
.8	2	2	2	2	2	3	3	A3	A34
1	2	2	2	2	2	3	3	4	A34
2	2	2	2	2	2	3	A23	A24	C
4	2	2	2	2	2	3	A23	A3	C

REYNOLDS NUMBER
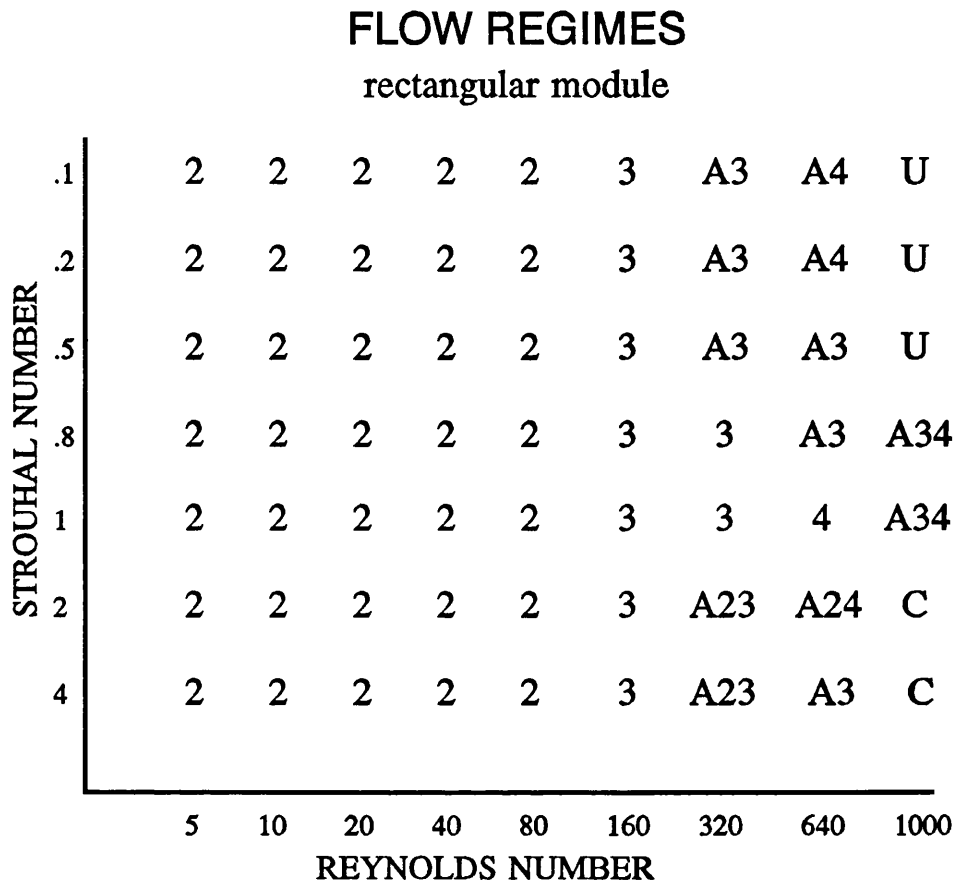
2 to 4 number of eddies in each cell at flow reversal, A2, A3 and A4 asymmetric flow with 2, 3 and 4 eddies respectively at flow reversal, A23 asymmetric flow with 2 eddies at one flow reversal and 3 at the other and so on A24 and A34, C chaotic flow, U numerically unstable.

Figure 47 Observed flow regimes for $Re_{net} = 0$, $\beta = 40\%$, $\lambda = 1.5$

3.2.2 Oscillatory flow pattern with wall suction

Figure 48, Figure 49 and Figure 50 show the numerically simulated flow patterns for wall, central and rectangular module with the same geometric and hydraulic conditions as Figure 27, Figure 28 and Figure 31 except with wall flux now $v_w = 10^{-3}$ respectively. In our membrane filtration device (Finnigan 1990 and Howell et al. 1992b) the ratio of dimensional wall flux to the dimensional maximum pulsed velocity is about 10^{-5} to 10^{-4}. These results show that the wall suction at levels realistic for membrane permeation does not distort the macroscopic flow field.

Wall Baffles
Re=200, St=1, Baffle spacing=1.5 and flow area=40%

Unsteady Flow

TIME=5.25

TIME=5.50

TIME=5.75

TIME=6.00

⇧
central line
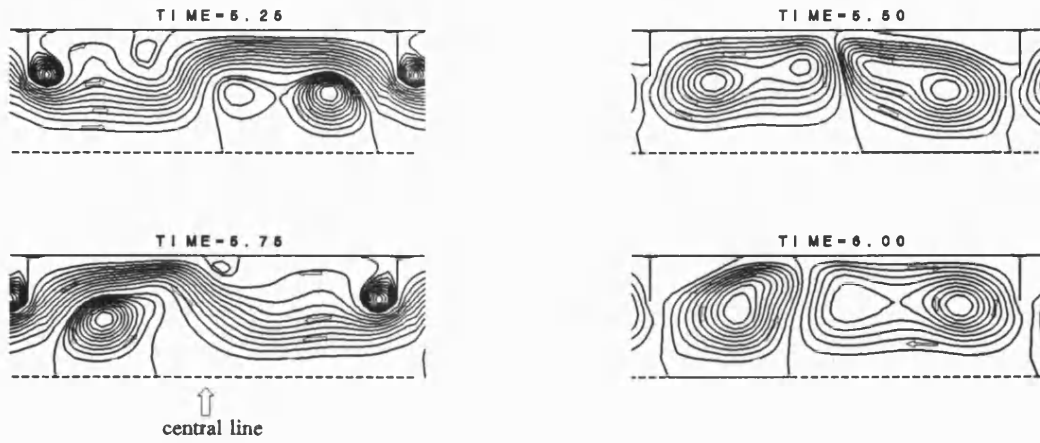
Figure 27 for comparison

Re. =200, Re. =0, St=1, ß=.4, λ=1.5 and γ=0.001 for wall baffle

TIME=5.25

TIME=5.50

TIME=5.75

TIME=6.00
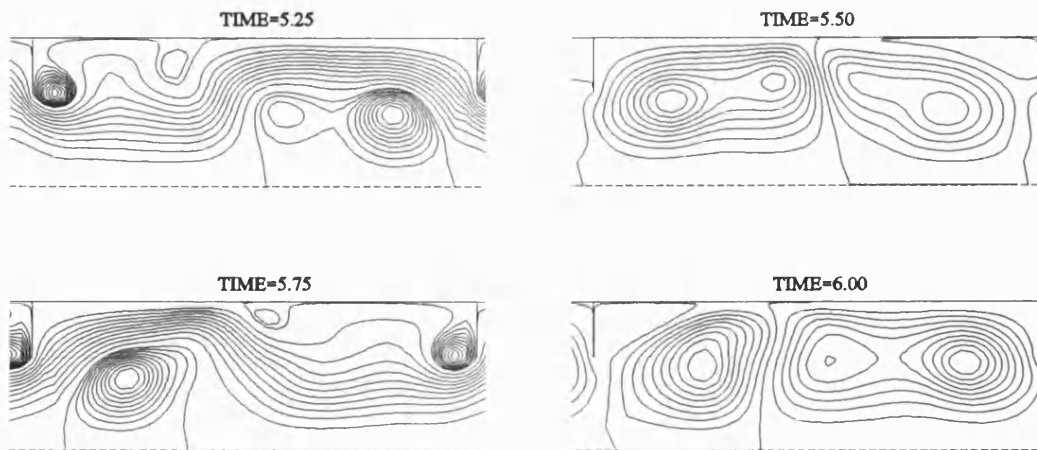
Figure 48 Simulation of oscillatory flow with wall suction for wall baffle

Central Baffles
Re=200, St=1, Baffle spacing=1.5 and flow area=40%

Unsteady Flow

TIME=5.25

TIME=5.50

TIME=5.75

TIME=6.00

⇧
central line
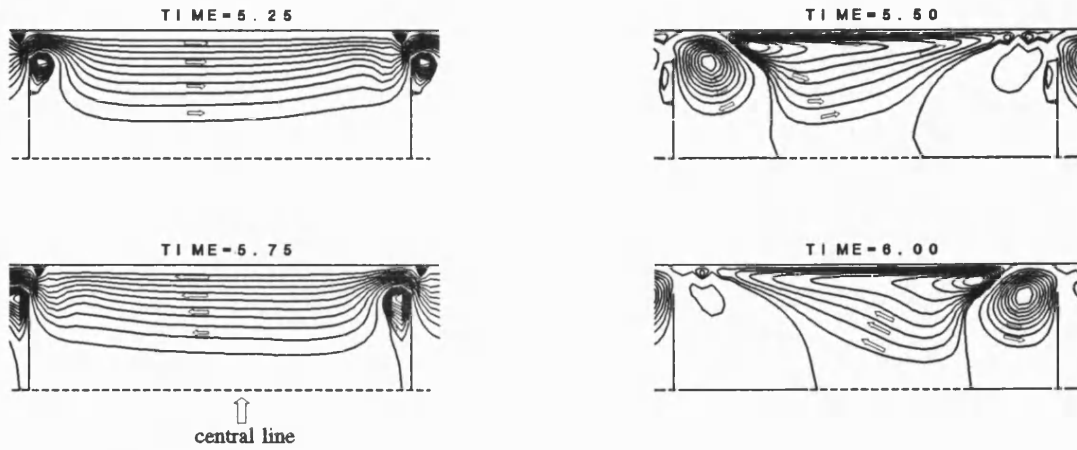
Figure 28 for comparison

Re$_o$ =200, Re$_a$ =0, St=1, ß=.4, λ=1.5 and γ=0.001 for central baffle

TIME=5.25

TIME=5.50

TIME=5.75

TIME=6.00
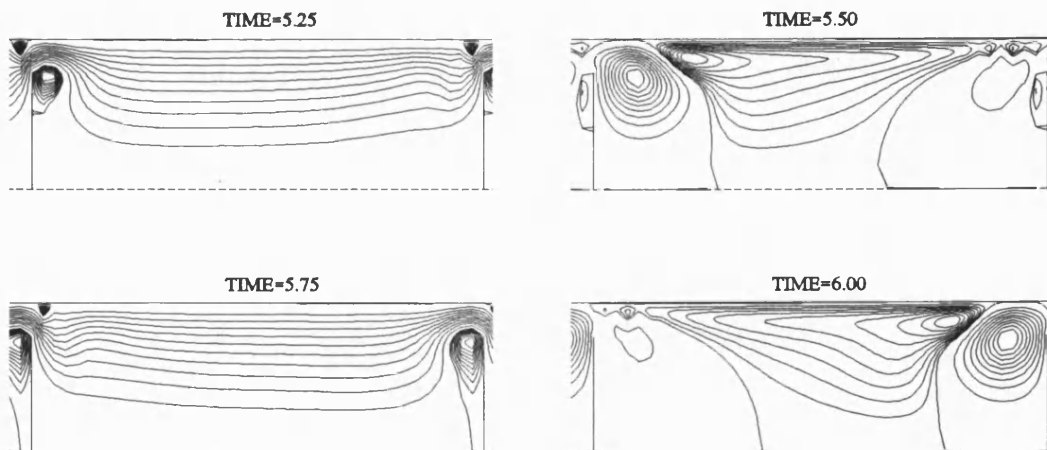
Figure 49 Simulation of oscillatory flow with wall suction for central baffle

Re. =250, Re .=0, St=1, ß=.4, and λ=3 for rectangular module

TIME=5.35   TIME=5.6

TIME=5.85   TIME=6.1
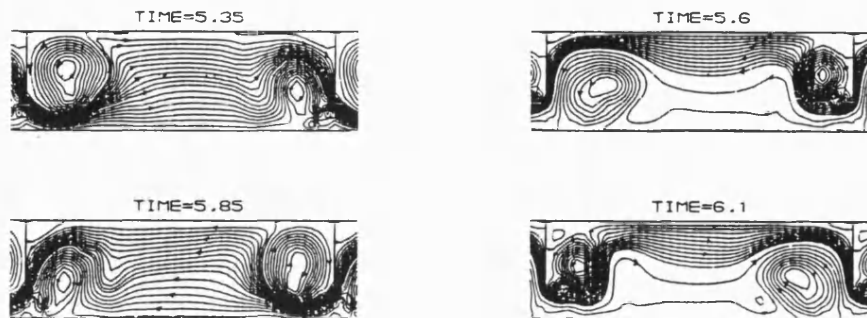
Figure 31 for comparison

Re. =250, Re. =0, St=1, ß=.4, λ=3 and γ=0.001 for rectangular module

TIME=5.35   TIME=5.60

TIME=5.85   TIME=6.10
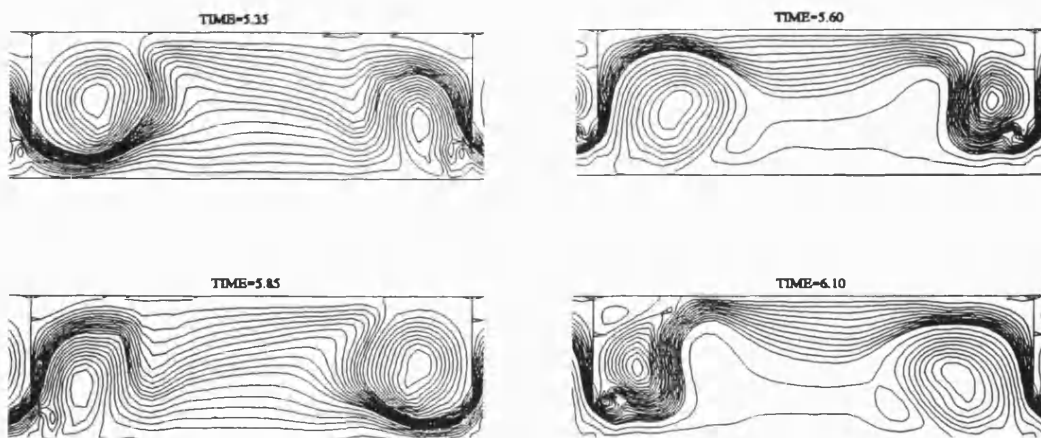
Figure 50 Simulation of oscillatory flow with wall suction for rectangular module

CHAPTER 4

QUANTITATIVE ANALYSIS

— maximum vortex strength and wall shear rate

In chapter 3, vortex formation/ejection has been shown over wide ranges of Reynolds and Strouhal numbers which characterise oscillatory flows. It is not obvious under what conditions optimum mass transfer enhancement, which is certainly related to overall fluid mixing, will take place. It is necessary to find a global flow parameter to serve as a useful design criterion. For example, the strength of the vortex formed within the channel is considered to be a global flow parameter for steady flow if we suppose that strong vortices give good fluid mixing. However, since vortex strength varies with time for oscillatory flow, estimation of the design criterion would be difficult. Nishimura et al (1989) used steady streaming as a global flow parameter to study the effect of the Strouhal number on flow characteristics in a wavy-walled channel with oscillatory flows. They studied the flow both numerically and experimentally and found that the persistence of the ejected vortex at the centerline of the channel is closely related to the vortex strength at the instant of zero flow, and also that the peak of vortex strength appears at same range of Strouhal number for both instantaneous flow and steady streaming. For simplicity, the dimensionless vortex strength at the instant of zero flow is chosen here as a global flow parameter to study the effect of the Reynolds and Strouhal numbers on flow characteristics. The dimensionless vortex strength at the instant of zero flow is given by the maximum value of the

stream function ψ_{max} at dimensionless times $t=n$, where n is an integer (or

equivalently the minimum value of the stream function at times $t=n+0.5$) Where

several vortices are present ψ_{max} represents the strength of the largest one in the

half-cycle immediately preceding the zero-flow instant.

It is known that in cross flow microfiltration the depth of cake which builds

up is limited and that the excess is somehow removed by the liquid flow. Several

mechanisms have been proposed for this. The first is shearing of the top face of

the cake. This would require a diminishing adhesion force of successive layers

leading to an unstable top layer, or an extreme sensitivity to a particular shear so

that as the flow channel diminished in width with increasing cake depth (very

small) eventually a shear rate would be reached which would exceed the strength

of the interparticle bonds. The back transport of the cells away from the surface

of the membrane is also aided by shear induced diffusion. The dependence of the

mass transfer rates on velocity does not accord with the mass transfer correlations

for laminar or turbulent flow even in simple channels (Porter 1972). An

alternative method for our complex geometry is to directly use wall shear rate to

evaluate the local mass transfer coefficient after the Lèvêque equation is first

converted to a form where the velocity is expressed by the wall shear rate

equation. The influence of flow and geometry conditions on wall shear rate is

therefore investigated in this chapter as another global flow parameter along with

the dimensionless vortex strength at the instant of zero flow. Recalling Equation (41) in Chapter 2, wall shear rates are given by

$$\dot{\gamma} = \frac{\partial \bar{u}}{\partial \bar{r}}\Big|_{\bar{r}=1} = \frac{U_R}{R}\frac{\partial u}{\partial r}\Big|_{r=1} = \frac{U_R}{R}\dot{\gamma} = \frac{\mu\,Re}{2R^2\rho}\dot{\gamma} \quad \textit{for tubular channel}$$

$$\dot{\gamma} = \frac{\partial \bar{u}}{\partial \bar{y}}\Big|_{\bar{y}=0} = \frac{U_R}{H}\frac{\partial u}{\partial y}\Big|_{y=0} = \frac{U_R}{H}\dot{\gamma} = \frac{\mu\,Re}{H^2\rho}\dot{\gamma} \quad \textit{for rectangular channel}$$

$$(45)$$

4.1 Vortex strength

The values of the vortex strength Ψ_{max} are shown in Figure 51, Figure 52 and Figure 54 as a function of Reynolds number for fixed Strouhal number for a tubular module with and without wall suction and rectangular module respectively. Ψ_{max} is also shown in Figure 53 and Figure 55 as a function of Strouhal number for fixed Reynolds number for tubular and rectangular modules respectively. No data is available in Figure 55 for Strouhal number St smaller than 0.5 when oscillatory Reynolds number $Re_o \geq 300$ because flow becomes asymmetric under these hydraulic conditions as shown in the flow regimes results in Figure 47 in Chapter 4. However it is yet obvious enough for one to see the tendency in Figure 55

Ralph (1986) reported vortex strenght on a Re_o/St diagram for the wavy-walled tube geometry of a membrane oxygenator device. His results suggest that best conditions in term of vortex strength in the wavy-walled tubes correspond to

best conditions in term of vortex strength in the wavy-walled tubes correspond to oscillation stroke lengths greater than the wave period of the channel (low St in the range 0.02 to 0.05) as the separation vortex is very weak in viscous dominated flows when the stroke is short. Howes (1988) explained that when a sharp edge exists this is not necessarily the case and in general vortex mixing is present in the baffled tube for stroke lengths considerably less than the baffle spacing (higher St). Our results in Figure 53 and Figure 55 corroborate Howes' explanation qualitatively in term of vortex strength for the wall baffled tube and suggest that this also is the case for the central baffled tube and the rectangular module.
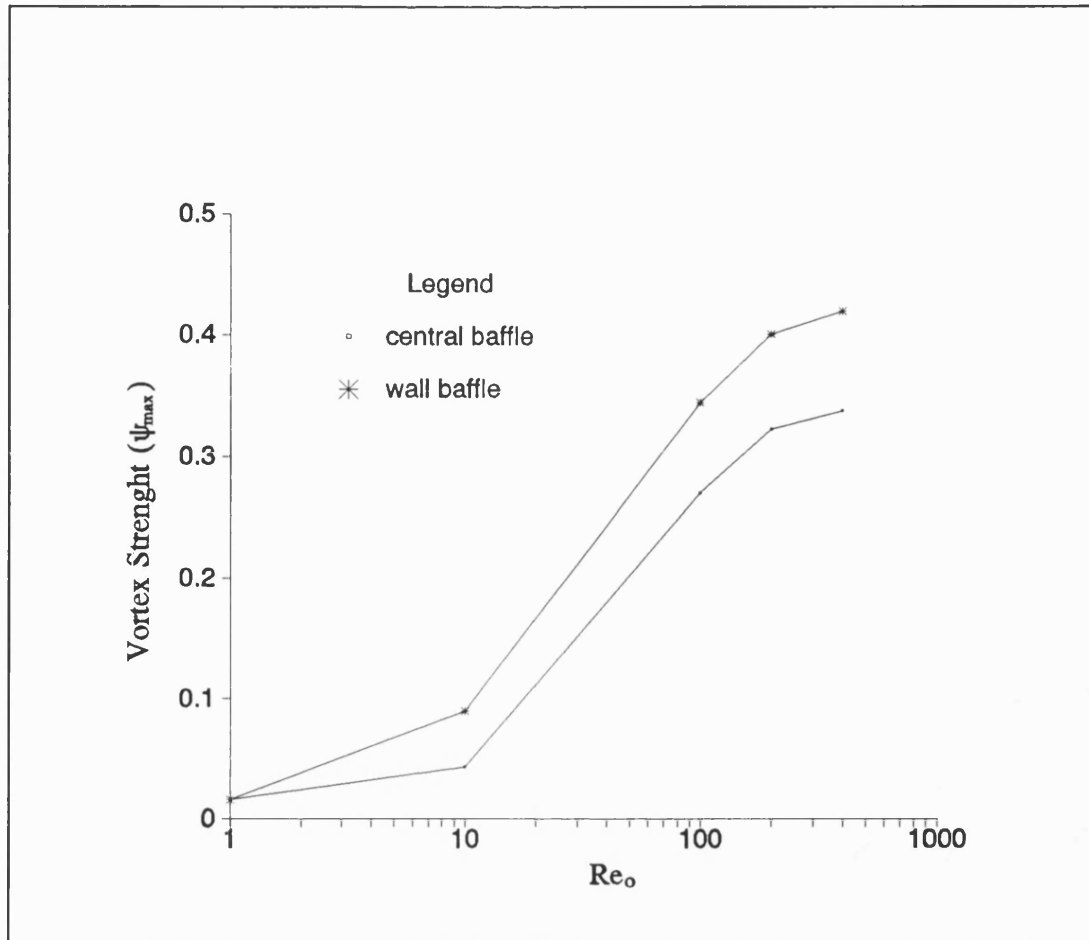
Figure 51 Vortex strength with $Re_n=0$, $St=1$, $\beta=0.4$ and $\lambda=1.5$ for tubular module

The essential features of these figures are the monotonic increase in Ψ_{max} with Reynolds number at fixed Strouhal number, and the existence of an maximum with respect to Strouhal number as the fixed Reynolds number. The vortex strength at the instants of zero flow is larger for wall baffles than with central baffles for all the indicated Reynolds number range at $St=1$, and greater with central baffles than with wall ones at small St. The existence of an maximum with respect to Strouhal number could act as one of the guideline for membrane filtration application.
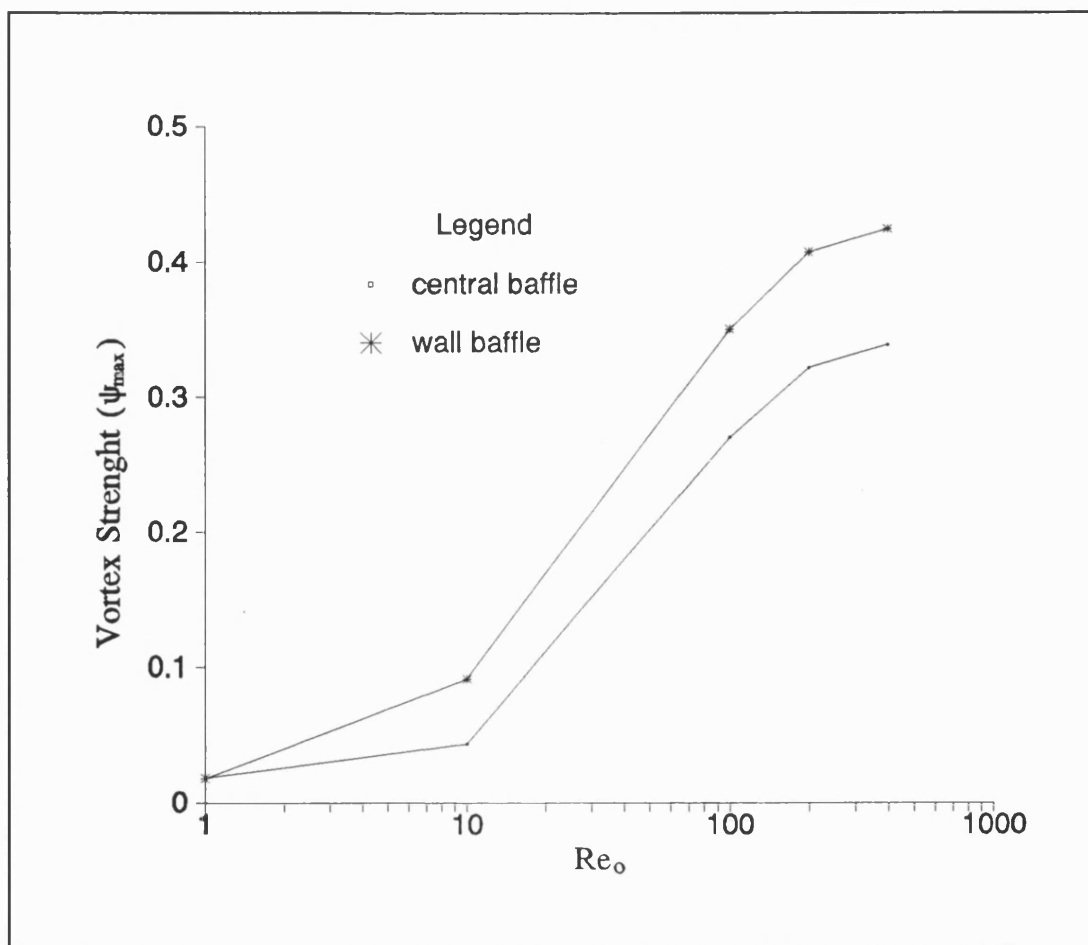
Figure 52 Vortex strength with $Re_n=0$, $St=1$, $\beta=0.4$, $\lambda=1.5$ and flux ratio $\gamma=0.01$ for tubular module

The influence of the baffle flow area ratio β on the vortex strength are shown in Figure 56 and Figure 57 for one time cycle. It appears that the time dependent profile of the vortex strength fluctuates in a sinusoidal way with a slight phase shift from the oscillatory source. When the free area ratio β decreases, the sinusoidal form is gradually distorted meanwhile the zero flow vortex strength slowly increases.
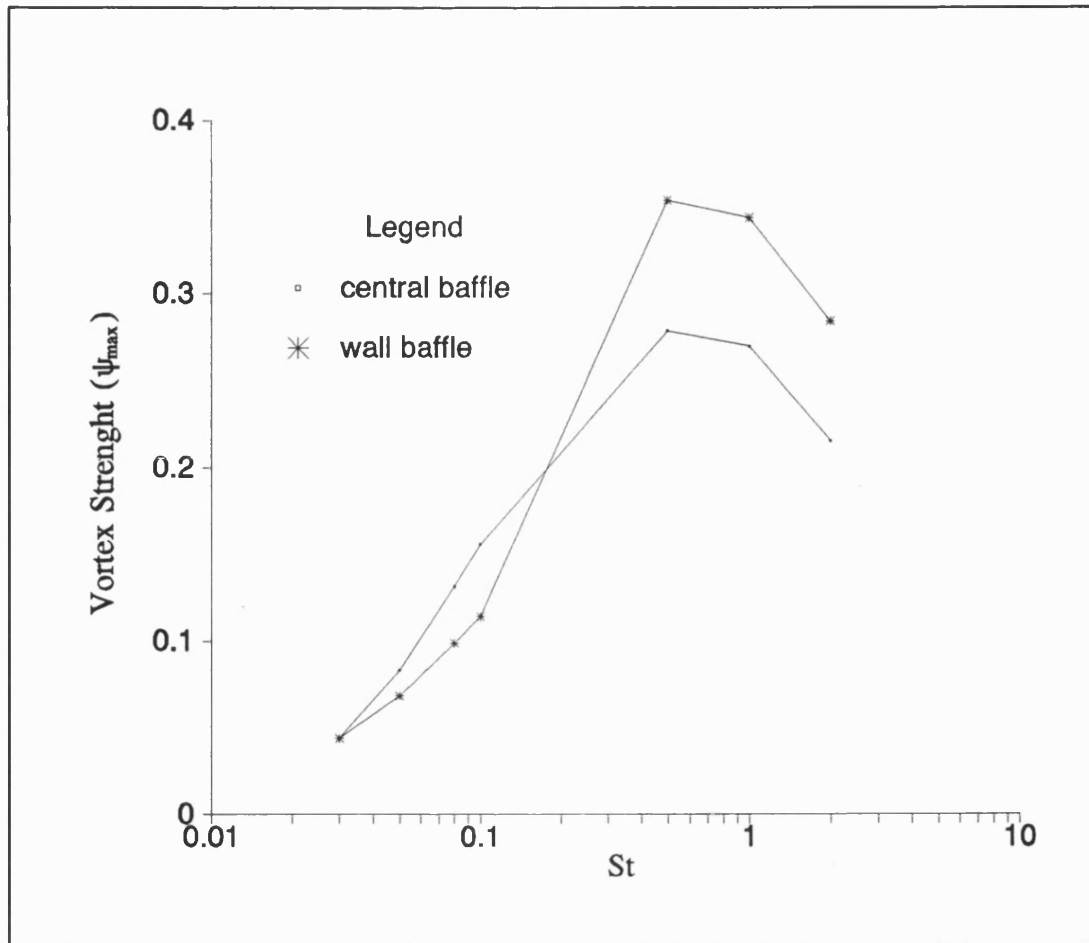
Figure 53 Vortex strength with $Re_o=100$, $Re_n=0$, $\beta=0.4$ and $\lambda=1.5$ for tubular module
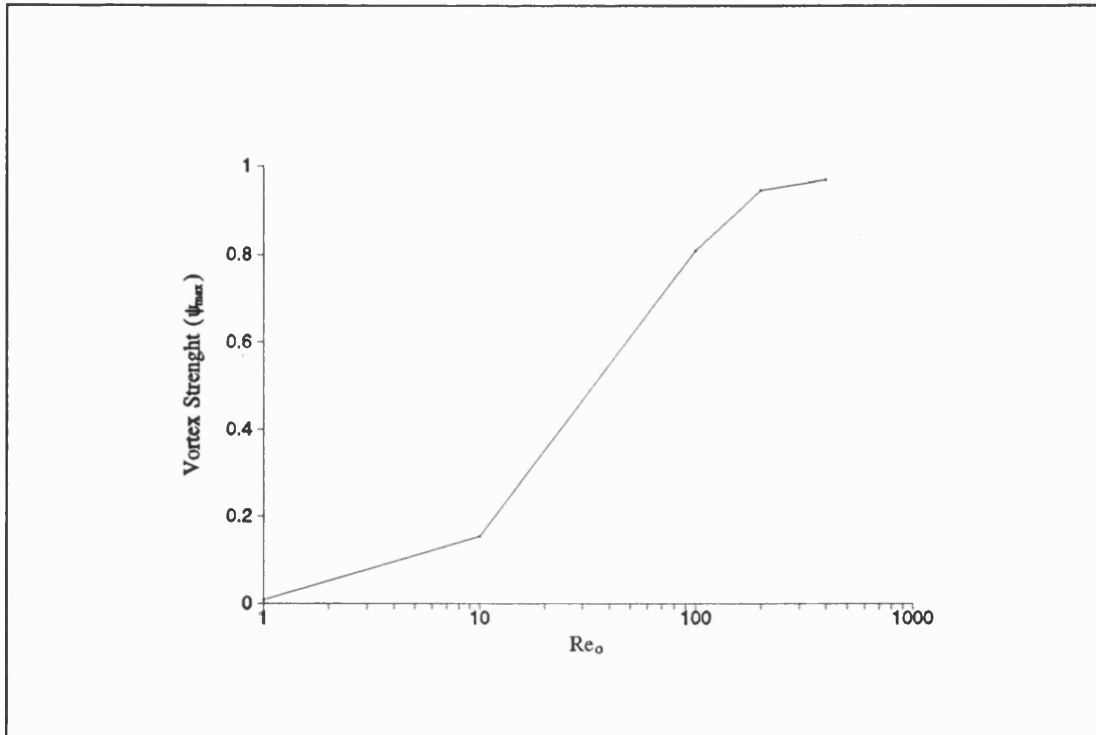
Figure 54 Vortex strength with $Re_n = 0$, $St = 1$, $\beta = 0.4$ and $\lambda = 1.5$ for rectangular module
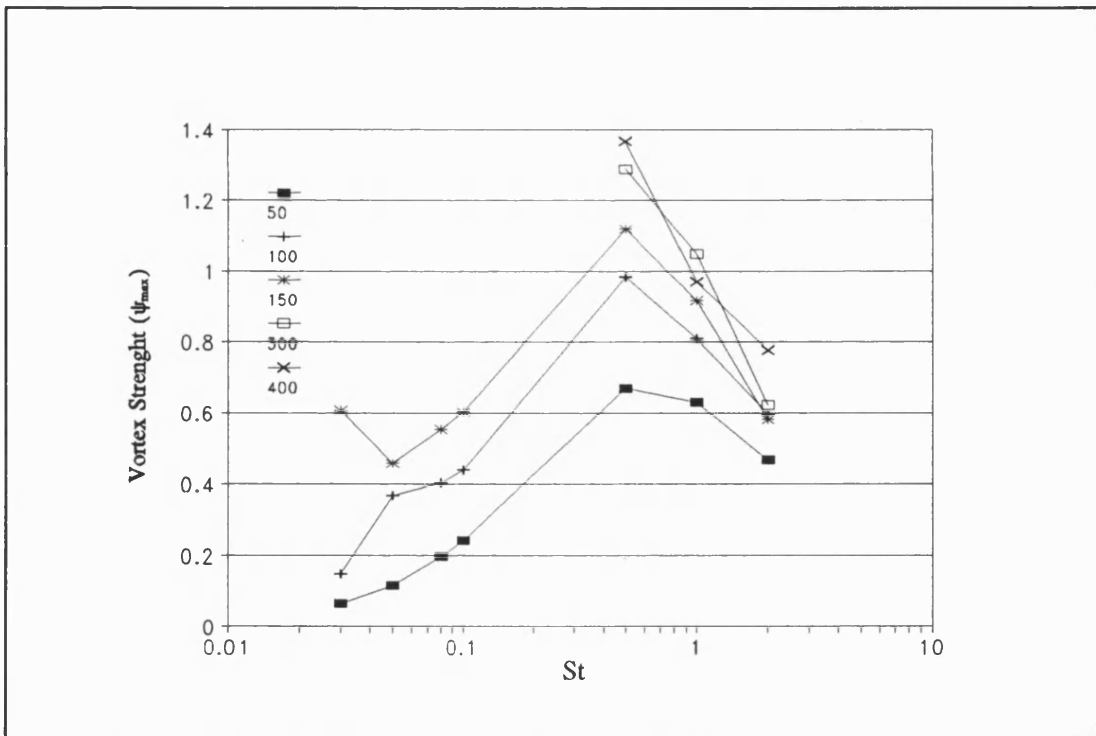
Figure 55 Vortex strength for Re_o/St map with $\beta = 0.4$ and $\lambda = 3.0$ for rectangular module
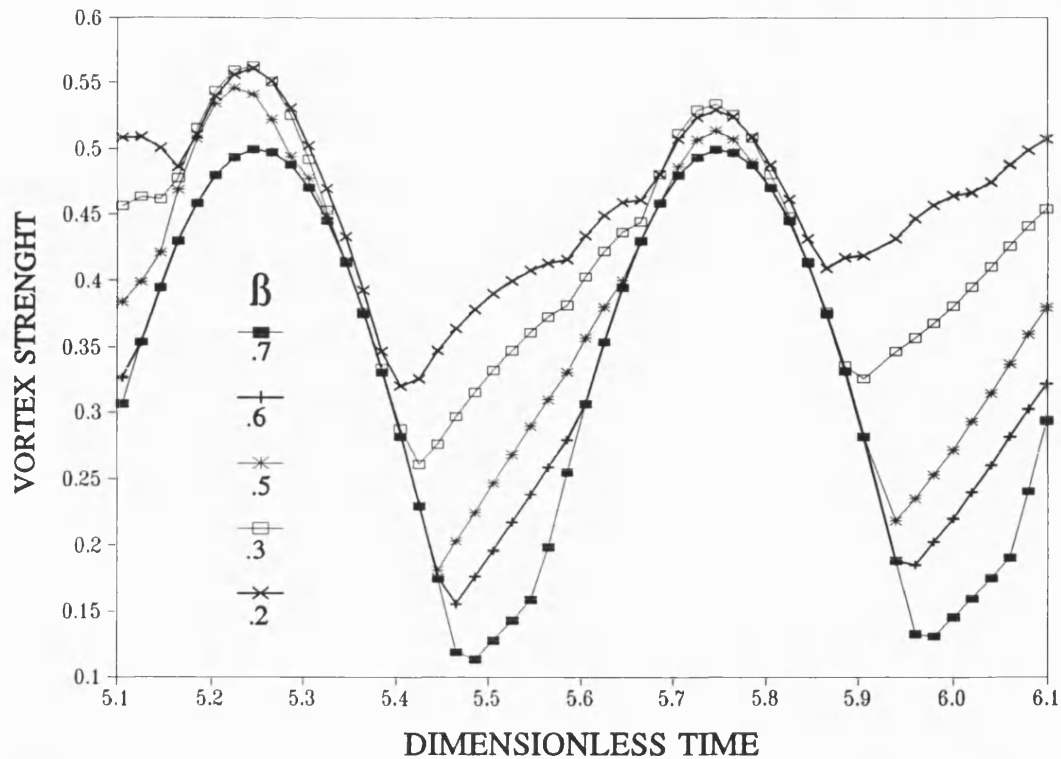
Figure 56 Vortex strength in full time cycle with $Re_o = 200, Re_n = 0$, $St = 1$, $\beta = 0.2$ - 0.7 and $\lambda = 1.5$ for central baffle module
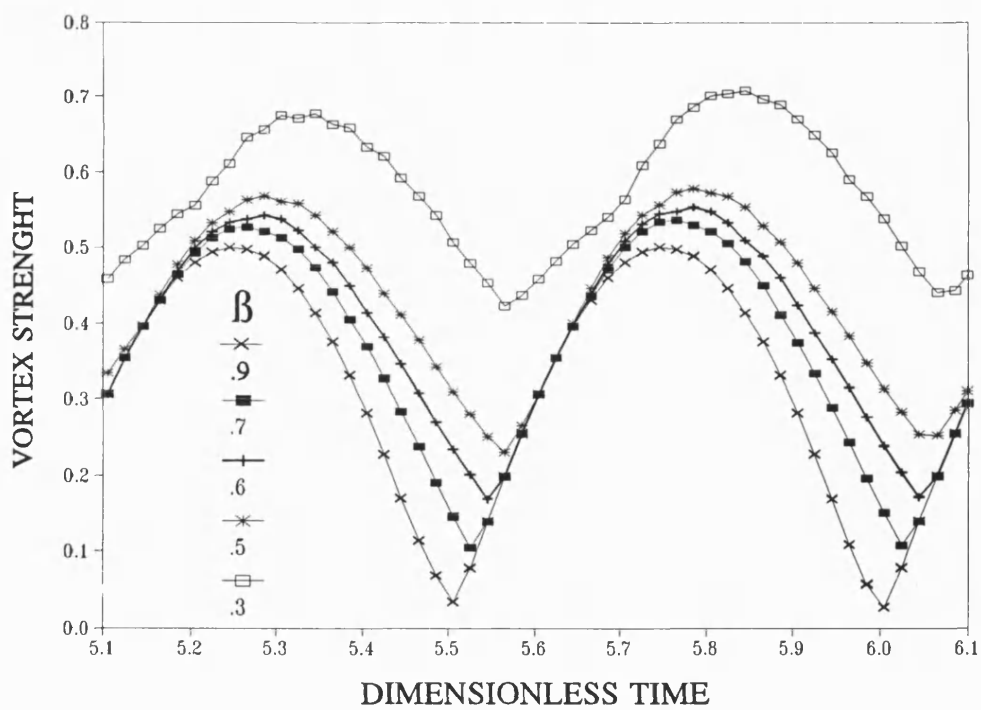
Figure 57 Vortex strength in full time cycle with $Re_o = 200, Re_n = 0$, $St = 1$, $\beta = 0.3$ - 0.9 and $\lambda = 1.5$ for wall baffle module

4.2 Wall shear rate

According to the definition of shear rate, the wall shear rate can be calculated by the following equation (46) or using vorticity variable ω by equation (47)

$$\dot{\gamma}_w = \begin{cases} \dfrac{u(wall)-u(wall-\Delta r)}{\Delta r} = -\dfrac{u(wall-\Delta r)}{\Delta r} & \text{for tubular channel} \\[4mm] \dfrac{u(wall)-u(wall-\Delta y)}{\Delta y} = -\dfrac{u(wall-\Delta y)}{\Delta y} & \text{for rectangular channel} \end{cases} \tag{46}$$

$$\because \ u(wall)=0 \ \textit{for wall suction or none suction.}$$

$$\dot{\gamma}_w = \begin{cases} \dfrac{\partial u}{\partial r}\Big|_{r=1} = 2r\dfrac{\partial u}{\partial s}\Big|_{s=1} = 4\dfrac{\partial^2 \psi}{\partial s^2}\Big|_{s=1} = -\omega\,|_{s=1} & \text{for tubular channel} \\[4mm] \dfrac{\partial u}{\partial y}\Big|_{y=1} = \dfrac{\partial^2 \psi}{\partial y^2}\Big|_{y=1} = -\omega\,|_{y=1} & \text{for rectangular channel} \end{cases} \tag{47}$$

The results of a few comparisons between the above equations suggested that the difference would be expected to lie within the error tolerance. Therefore either one of the above equations can be used to evaluate the wall shear rate. It is obvious to see that $\dot{\gamma}_w$ is dependent on channel side distance x and time t. In order to analyse quantitatively in addition to the qualitative display of wall shear rate in x-t plane, the average wall shear rate $\dot{\gamma}_{at}$ and time average local wall

$\dot{\gamma}_t$ are introduced which are defined by averaging $\dot{\gamma}_w$ over one cell in one time cycle and by averaging $\dot{\gamma}_w$ on one time cycle respectively. More precisely

$$\dot{\gamma}_{at} = \begin{cases} \dfrac{1}{2\lambda} \int\limits_0^1 \int\limits_0^{2\lambda} \dot{\gamma}_w \; dx \, dt & \textit{for tubular channel} \\[20pt] \dfrac{1}{\lambda} \int\limits_0^1 \int\limits_0^{\lambda} \dot{\gamma}_w \; dx \, dt & \textit{for rectangular channel} \end{cases}$$

$$\dot{\gamma}_t = \int\limits_0^1 \dot{\gamma}_w \; dt$$

Simpsons rule was used for the above integrations.

The wall shear rate are investigated in various way of which the purposes and parameters are summarized in the two tables below.

Table for the average wall shear rate Figures

Figure Number	$\dot{\gamma}_{at}$	$\dot{\gamma}_t$	Tube Centre & wall	Flat Sheet	Re's effect	St's effect
Figure 58	✓		✓		✓	
Figure 59	✓		✓ wall suction		✓	
Figure 60	✓		✓			✓
Figure 61	✓			✓	✓	
Figure 62	✓			✓	✓	✓
Figure 63	✓			✓	✓	✓
Figure 64	✓		✓ influence of β			
Figure 65	✓		centre		✓	✓
Figure 66		✓		✓ influence of β for steady		
Figure 67		✓		✓ influence of β for osc.		
Figure 68		✓		✓ influence of β for steady		
Figure 69		✓		✓ influence of β for osc.		

Table for the local wall shear rate Figures

Figure Number	Purpose for the Figure			
	Tube	Flat	Re's	St's
	Centre & wall	Sheet	effect	effect
Figure 70		✓	✓	
Figure 71		✓		✓ small St
Figure 72		✓		✓ bigger St
Figure 73	✓ influence of β for centre baffle			
Figure 74	✓ influence of β for wall baffle			
Figure 75	✓ steady & oscillatory for centre, no and wall baffle			
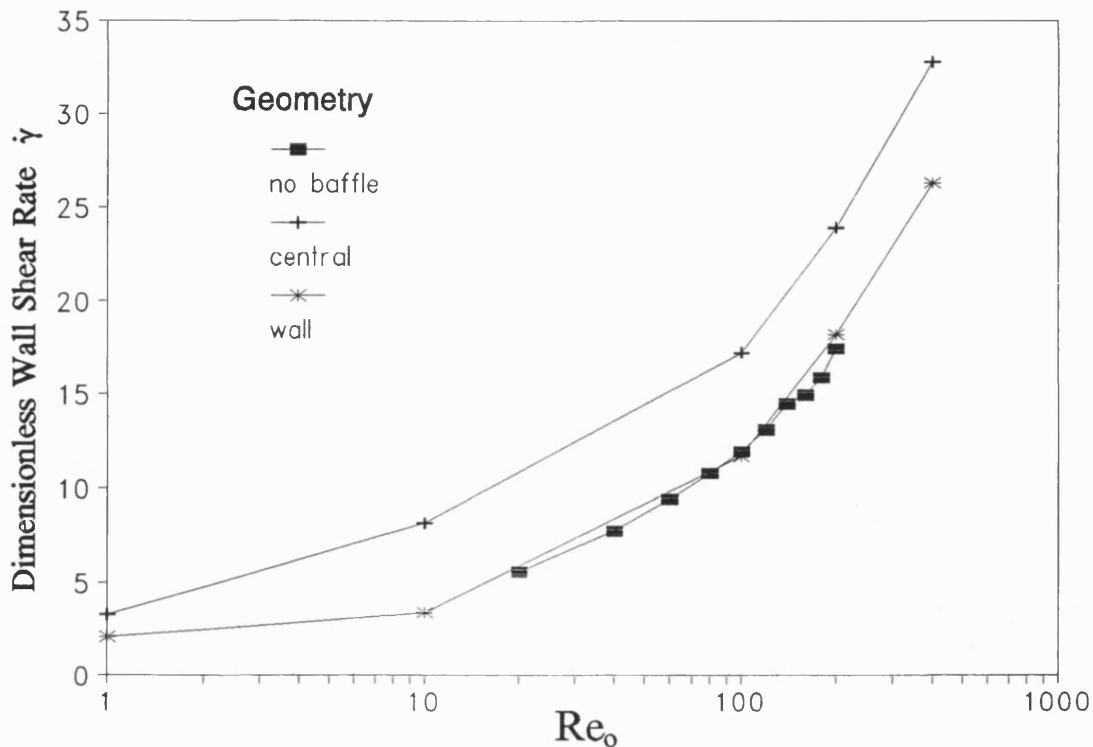
Figure 58 Wall shear rate for St=1, β=1.5, γ=0 in tubular module

Figure 58 shows that the average wall shear rate $\dot{\gamma}_{at}$ in central baffles is much higher than with either wall baffles or without baffle. In steady flow with central baffles, wall shear rate linearly increases as Reynolds number increases whereas with wall baffles and without baffles it stays constant (not shown here). For oscillatory flow, wall shear rate in all three geometry and rectangular module is a monotonically increasing function of Reynolds number which can be seen from Figure 58, Figure 59 and Figure 61.
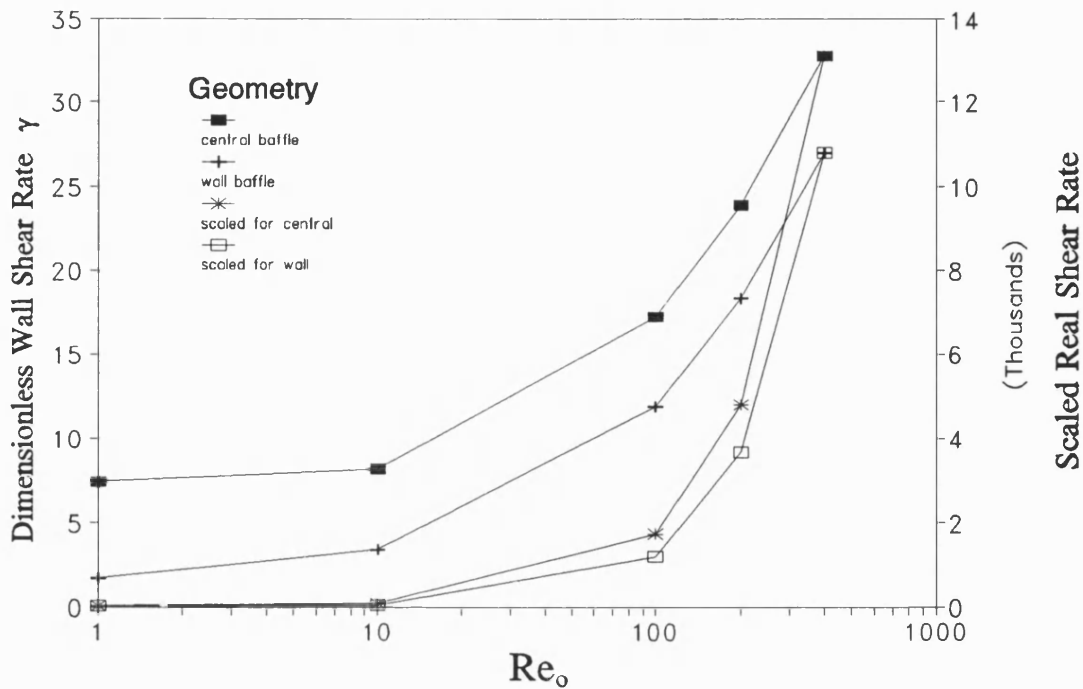
Figure 59 Wall shear rate for St=1, β=1.5, γ=1% in tubular module

In Figure 59 the influence of wall suction is considered and the comparison between Figure 58 and Figure 59 shows that even at much higher than realistic wall suction 1% no difference was observed for Re_o > 10. Scaled real shear rate $Re \cdot \dot{\gamma}$, which is equal to $\left(\dfrac{2\rho R^2}{\mu}\right) \cdot \dot{\bar{\gamma}}$, and $\dot{\bar{\gamma}}$ is the dimensional wall shear rate, are shown in Figure 59 to take Reynolds number into account in the dimensional shear rate profile. Figure 59 displays the tendency between scaled real shear rate which is related to Re_o about $Re_o^{1.545}$ and dimensionless shear rate which is related to Re_o about $Re_o^{0.545}$ is the same and dimensionless shear rate does reflect the real shear rate profile, which supports the use of dimensionless shear rate to investigate the dimensional shear rate.
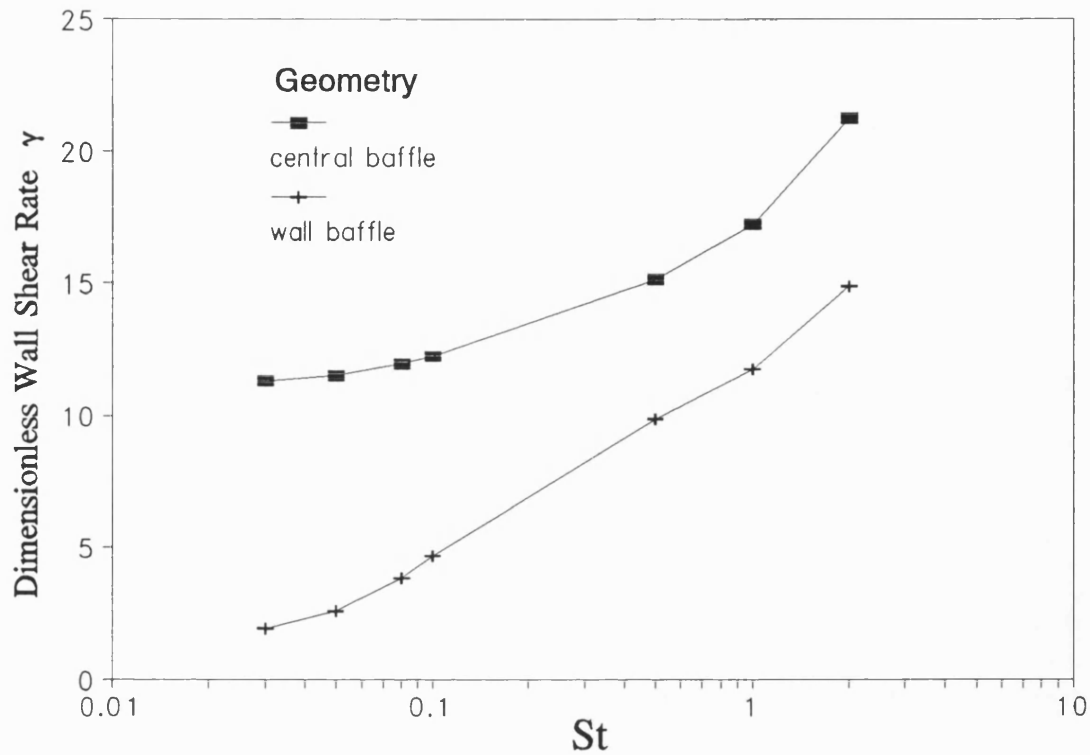
Figure 60 Wall shear rate for $Re_o=100$, $Re_n=0$, $\beta=1.5$ and $\gamma=0$ in tubular module

Figure 60 shows the influence of the Strouhal number on the wall shear rate which is larger for central baffles than wall baffles for a wide range of the Strouhal number. $\dot{\gamma}_{at}$ in the wall baffles case linearly increases as Strouhal number increases for $St > 0.1$ and in the central baffles case it is a monotonically logarithmically increasing function of Strouhal number for $St < 0.5$ and linearly for $St > 0.5$.
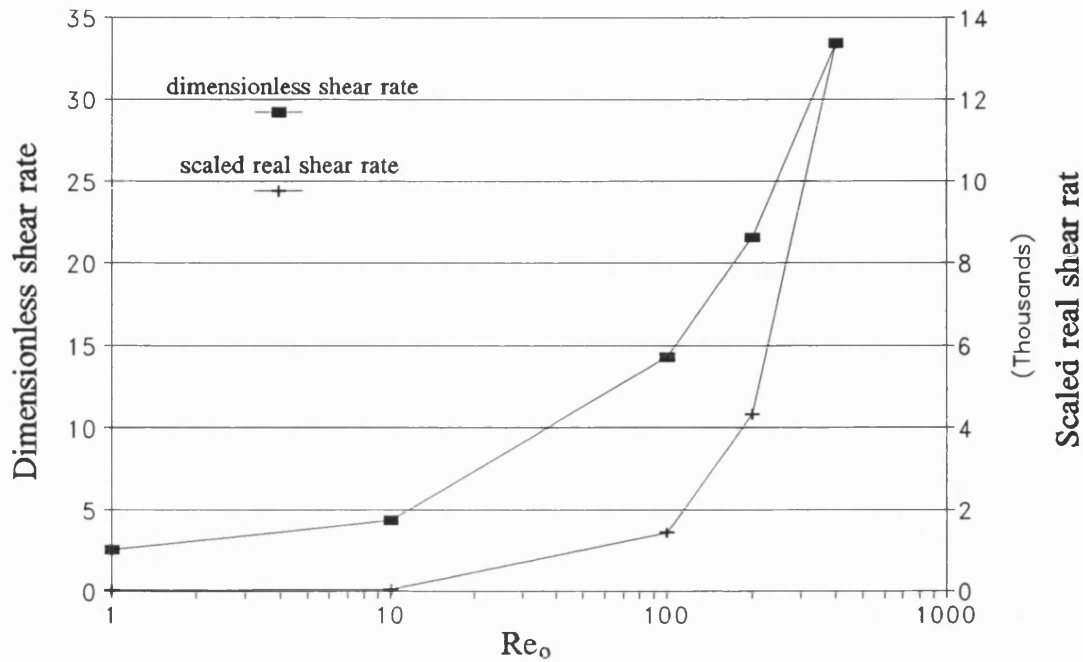
Figure 61 Wall shear rate for $Re_o=1 - 400$, $Re_n=0$, $St=1$, $\beta=0.4$, $\lambda=3$ and $\gamma=0$ in rectangular module

Dimensionless average wall shear rate $\dot{\gamma}_{at}$ and scaled real shear rate are shown in Figure 61 for rectangular module. There is a close resemblance to Figure 59 for tubular module. The 2 degree polynomial curve fit for average wall shear rate is $-0.0001Re_o^2 + 0.116Re_o + 2.922$ with the coefficient of determination 0.9982 and for the scaled real shear rate is $0.06Re_o^2 + 9.448Re_o - 46.04$ with the coefficient of determination 0.9999.
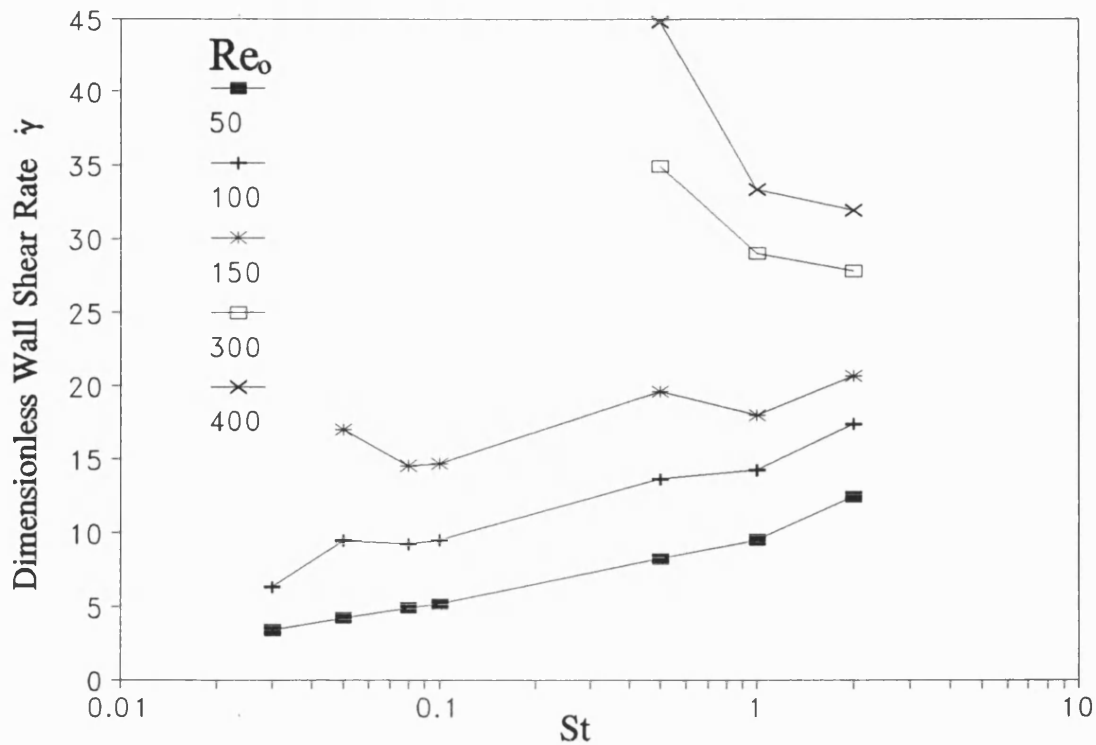
Figure 62 Influence of St on wall shear rate for $Re_o=50 - 400$, $Re_n=0$, $\beta=0.4$, $\lambda=3$ and $\gamma=0$ in rectangular module

The Re_o/St diagram in term of average wall shear rate is shown in Figure 62 for rectangular module with range $50 \leq Re_o \leq 400$ and $0.03 \leq St \leq 2$. No data is available in this diagram for smaller Strouhal number St than 0.5 when oscillatory Reynolds number $Re_o \geq 300$ because flow becomes asymmetric under these hydraulic conditions as shown in flow regimes results in Figure 47 in Chapter 4. One can see the trend that when $Re_o \leq 150$ the average wall shear rate is a monotonically increasing function of Strouhal number and when Re_o is beyond this level the average wall shear rate may have a maximum in the middle of Strouhal number at about St=0.5. The same diagram for the scaled real wall

shear rate is shown in Figure 63.
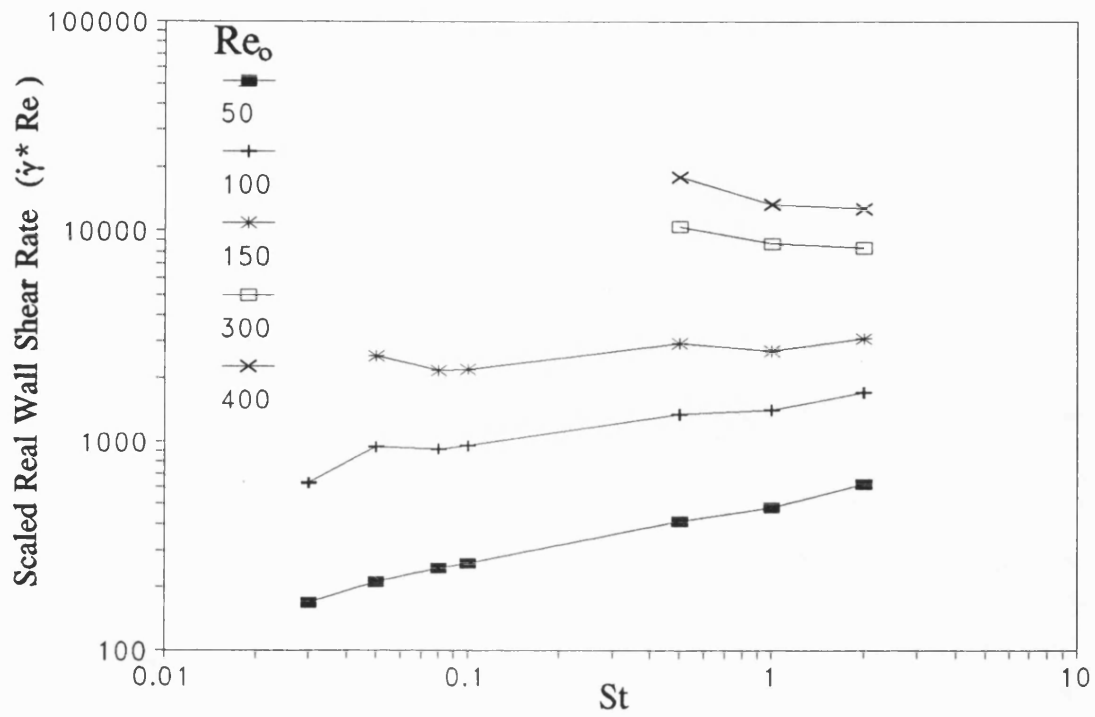
Figure 63 Influence of St on scaled real wall shear rate for Re_o=50 - 400, Re_n=0, β=0.4, λ=3 and γ=0 in rectangular module

Figure 64 Influence of baffle flow area β on wall shear rate for Re_o=200, Re_n=0, St=1, λ=3 and γ=0 in tubular module

The influence of the baffle flow area ratio β on the average wall shear rate is shown in Figure 64. The 2 degree exponential of polynomial curve fit for central baffle is $\exp(3.3289\beta^2 - 4.5916\beta + 4.4632)$ with the coefficient of determination 0.9998 and for the wall baffle is $\exp(3.8007\beta^2 - 4.6995\beta + 4.1987)$ with the coefficient of determination 0.9956.

The comparison between steady and oscillatory flow on $\dot{\gamma}_{at}$ is given in Figure 65 for the central baffle tubular module. The steady flow shear rate stays at nearly the level of that of the oscillatory flow at about St = 1 for the calculated
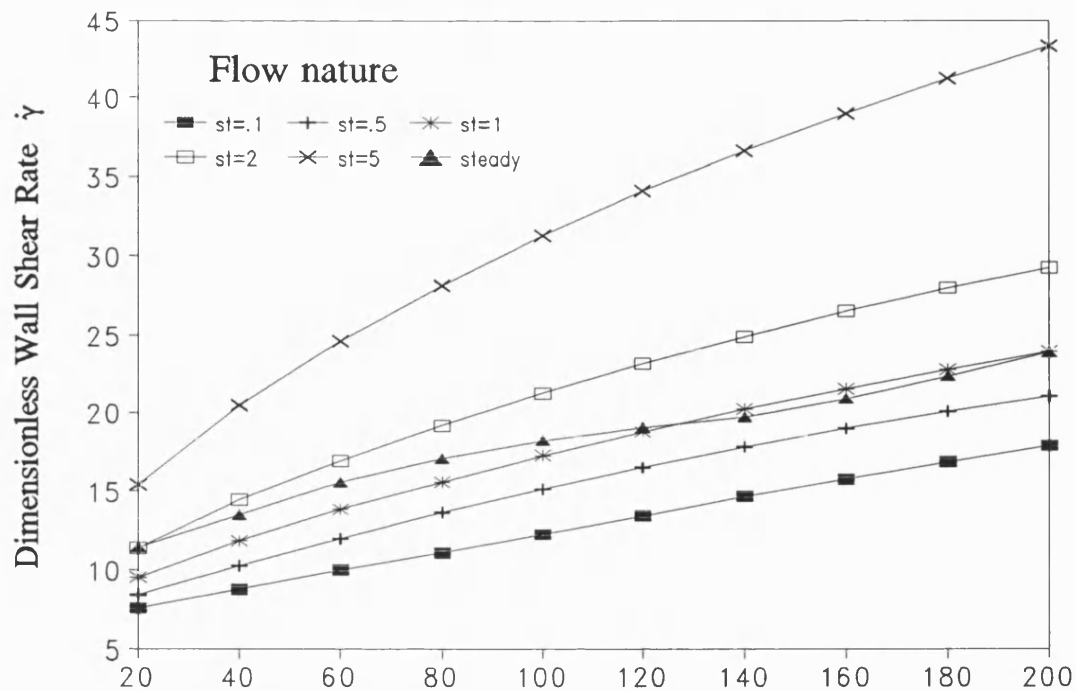
Figure 65 Comparison with steady flow on average wall shear rate for $Re_o=20 - 200$, $Re_n=0$, St$=0.1 - 5$, $\lambda=3$ and $\gamma=0$ in a centrally baffled tubular module

Re_o range. If $\dot{\gamma}_{at}$ could completely discribe the membrane boundary concentration(C_w) and flux(J) this result would suggest that if one try to raise wall shear rate to enhance membrane flux pulsatile flow should be operated at a strouhal number bigger than intermediate oscillation stroke otherwise it is not necessary to use pulsatile flow instead of much easier steady flow. However C_w and J is more directely dependent on local shear rate than the average shear rate.

The influence of baffle flow area β on the time-average wall shear rate $\dot{\gamma}_t$ are shown in Figure 66 to Figure 69 for steady and oscillatory flow in rectangular module with Re$=200$ and 800. As already reported in chapter 3, the introduction of periodic baffles produces a periodic eddy shedding for steady flow when Re_n is above 70. This periodic eddy shedding motion provides a time dependent
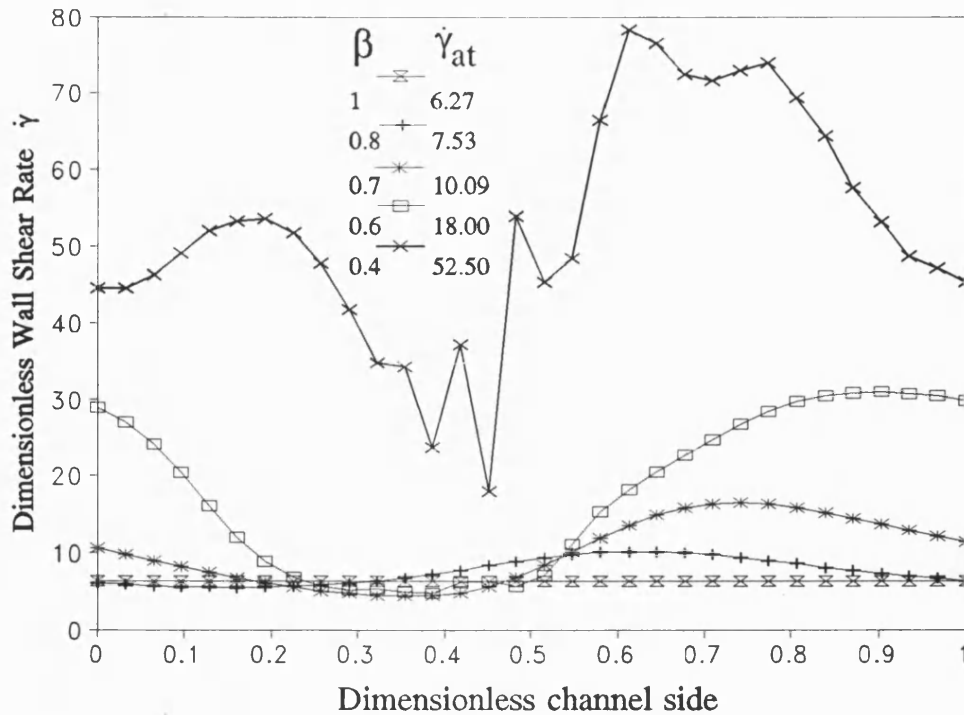
Figure 66 Influence of baffle flow area β on local wall shear rate for $Re_o = 0$, $Re_n = 200$, $St = 1$, $\lambda = 1.5$ and $\gamma = 0$ in rectangular module
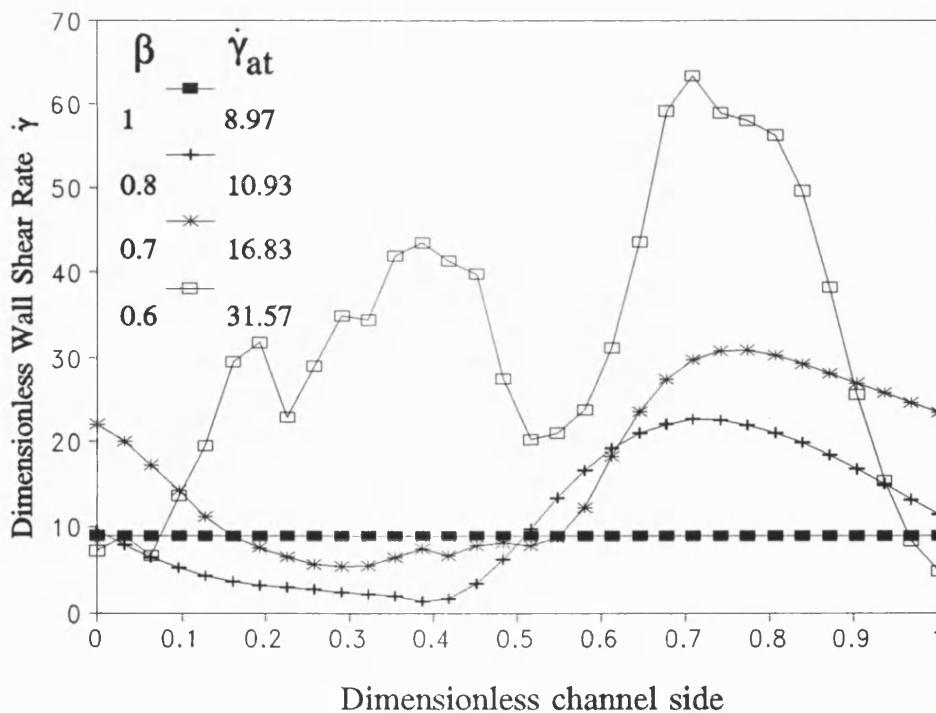
Figure 67 Influence of baffle flow area β on local wall shear rate for $Re_o = 0$, $Re_n = 800$, $St = 1$, $\lambda = 1.5$ and $\gamma = 0$ in rectangular module
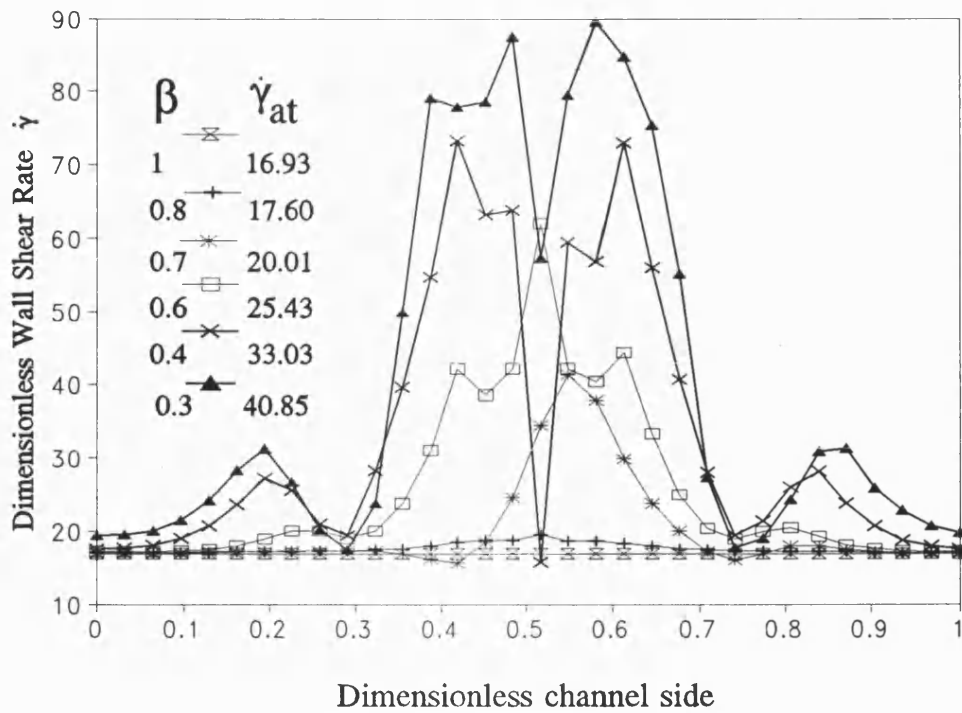
Figure 68 Influence of baffle flow area β on local wall shear rate for $Re_o = 200$, $Re_n = 0$, $St = 1$, $\lambda = 1.5$ and $\gamma = 0$ in rectangular module
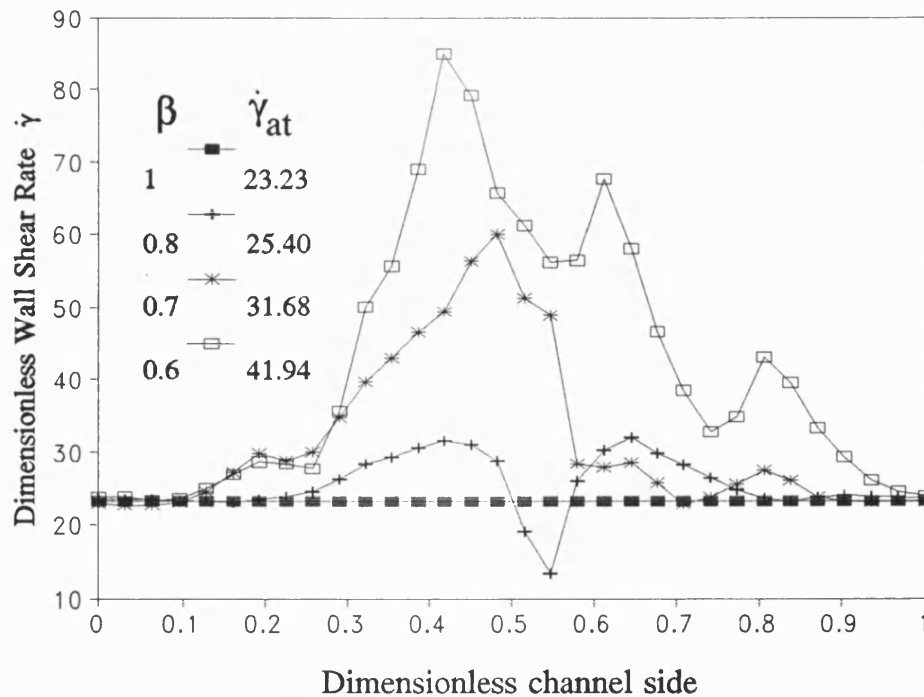
Figure 69 Influence of baffle flow area β on local wall shear rate for $Re_o = 800$, $Re_n = 0$, $St = 1$, $\lambda = 1.5$ and $\gamma = 0$ in rectangular module

wall shear rate and therefore generates the complex time-average local wall shear

rate $\dot{\gamma}_t$ even in steady flow case. In oscillatory flow case the greater $\dot{\gamma}_t$ exists near

the baffle area. In all cases when β increases $\dot{\gamma}_t$ decreases. The comparison

between Figure 66 and Figure 68 shows that the overall wall shear rate $\dot{\gamma}_{at}$ is

enhanced by using pulsatile flow in small to intermediate baffle area. The

comparison between Figure 67 and Figure 69 shows that the enhancement of the

average wall shear $\dot{\gamma}_{at}$ is even greater with bigger Re_o. The explanation for this

might be that pulsatile flow in a baffled channel produces a complex time

dependent eddy pattern, which increases fluid mixing and finally raises the

average wall shear rate.

To inspect the details three dimensional local wall shear rate profiles are

shown in Figure 70 to Figure 75 for central and wall baffle in tubular module and

rectangular module.

The influence of Re_o with $St=1$ is shown in Figure 70 and the influence

of St with $Re_o=100$ is shown in Figure 71 and Figure 72 for rectangular module

respectively. When Re_o increases the local wall shear rate becomes more and

more complex near baffle area while in the area distant to baffle it still fluctuates

sinusoidally with some phase shift. When St is small the local wall shear rate

looks unstable but does not achieve the greater value which is obtained at higher

St when it fluctuates relatively smoothly.

The influence of the baffle flow area ratio β on the local wall shear rate is shown for central and wall baffle in Figure 73 and Figure 74 respectively. When β decreases the regions with bigger shear rate expand as well as its absolute value increasing for both central and wall baffle cases.

The comparison between steady and oscillatory flow on the local wall shear rate is given in Figure 75 for tubular module. In the steady flow, central baffle case shear rate reaches a maximum near the baffle. In the steady flow, wall baffle case shear rate reaches a minimum near the baffle. In oscillatory flow shear rate becomes more complex and fluctuates as the flow pulses and it appears that there is a phase-shift in shear rate fluctuation.

Dimensionless Wall Shear Rate $\dot{\gamma}$
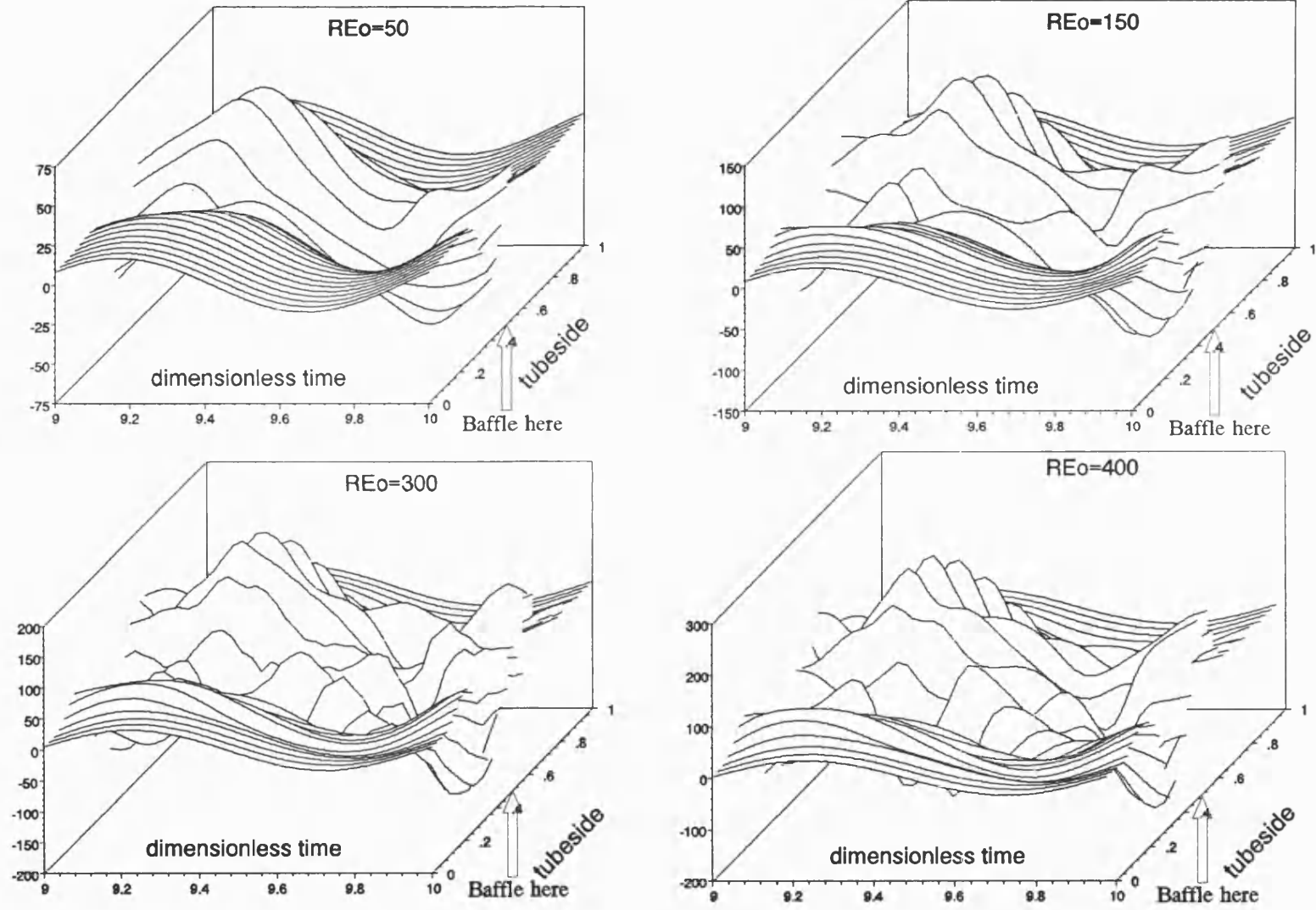
Figure 70 Influence of $Re_o = 50 - 400$ on local wall shear rate for $Re_n = 0$, $St = 1$, $\lambda = 3$ and $\gamma = 0$ in rectangular module

Dimensionless Wall Shear Rate $\dot{\gamma}$

St=0.03

St=0.05

St=0.08

St=0.1
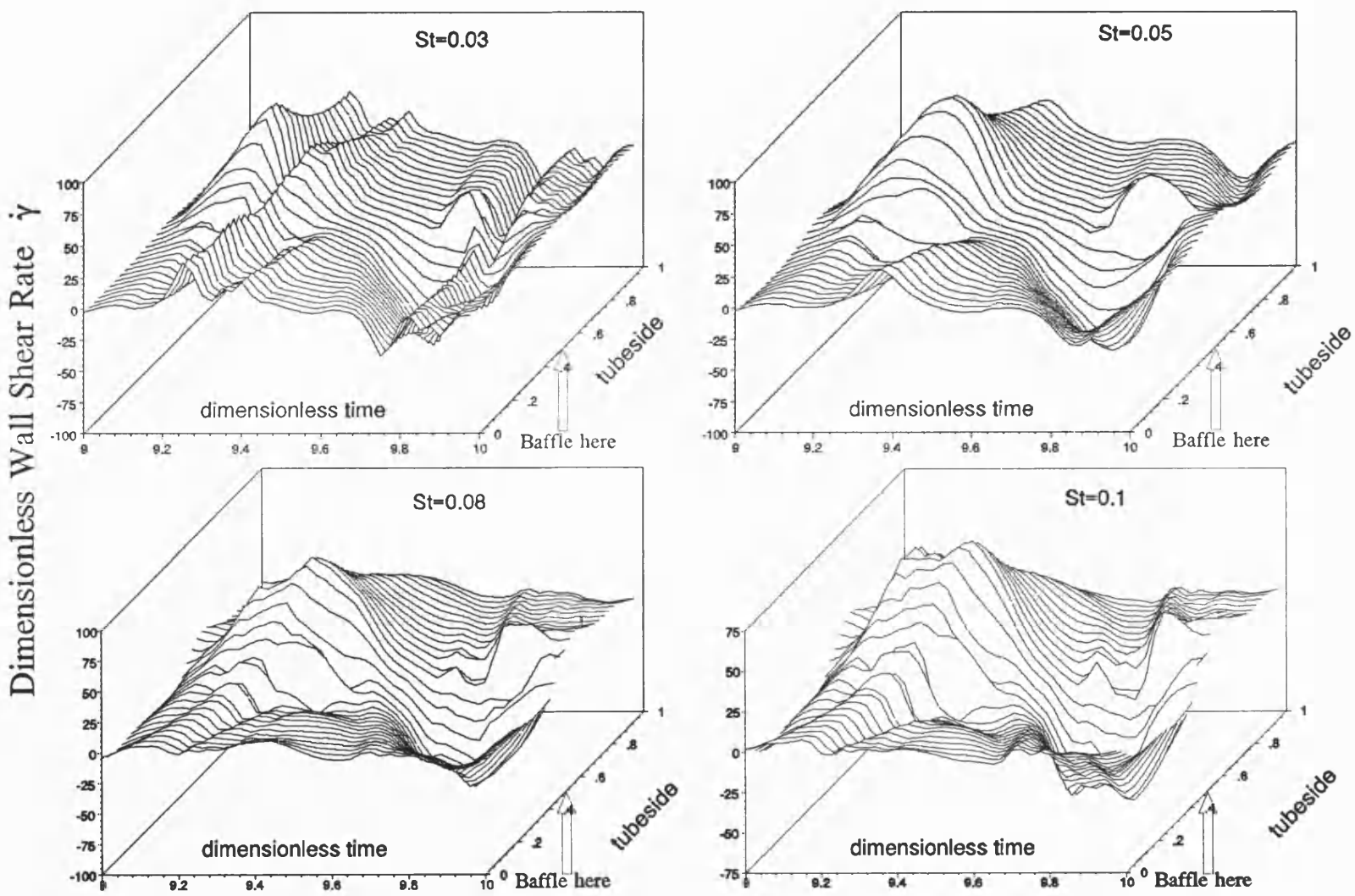
Figure 71 Influence of small St on local wall shear rate for $Re_o = 100$, $Re_n = 0$, $\lambda = 3$ and $\gamma = 0$ in rectangular module

-128-

Dimensionless Wall Shear Rate $\dot\gamma$
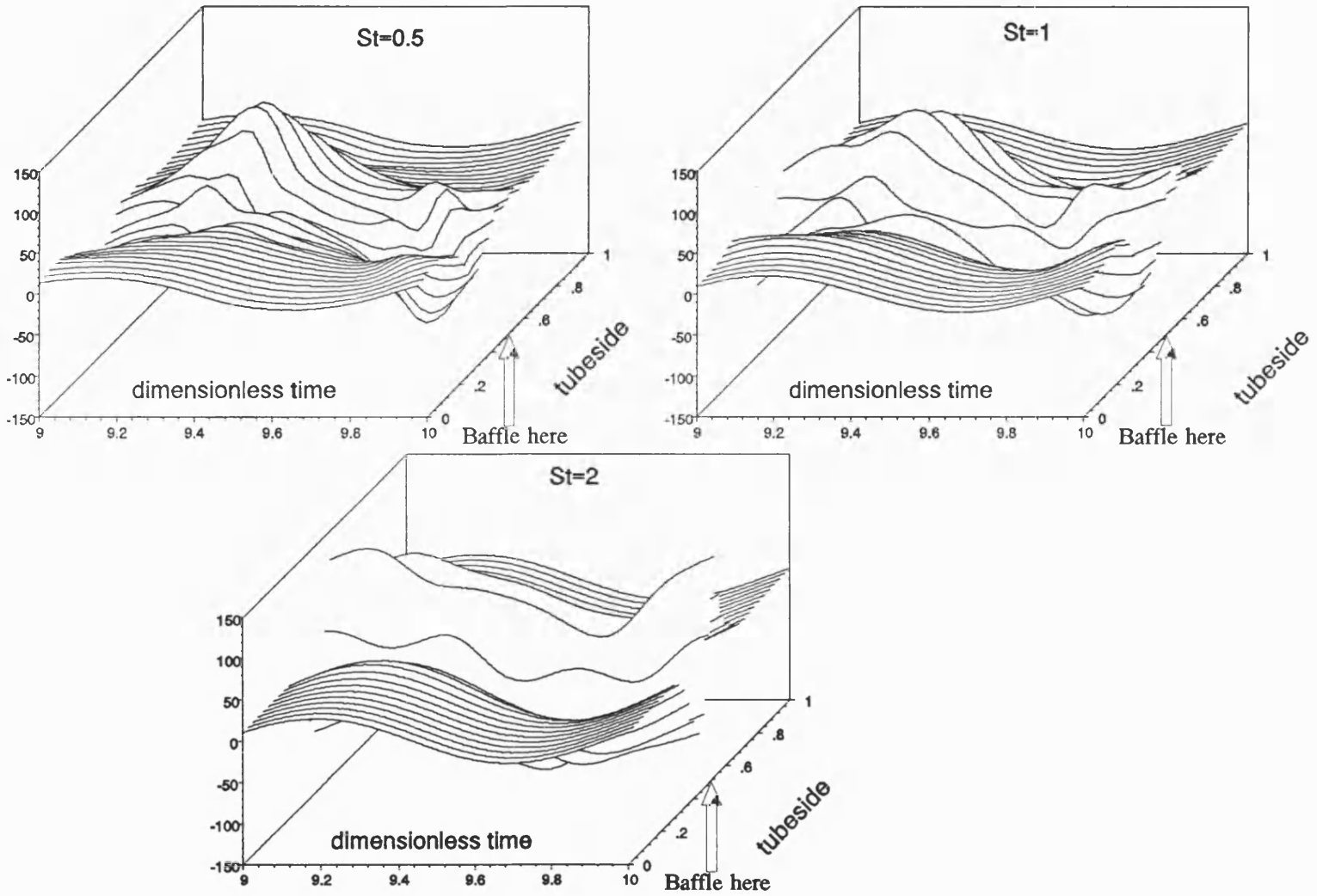
Figure 72 Influence of bigger St on local wall shear rate for $Re_o = 100$, $Re_n = 0$, $\lambda = 3$ and $\gamma = 0$ in rectangular module

-129-
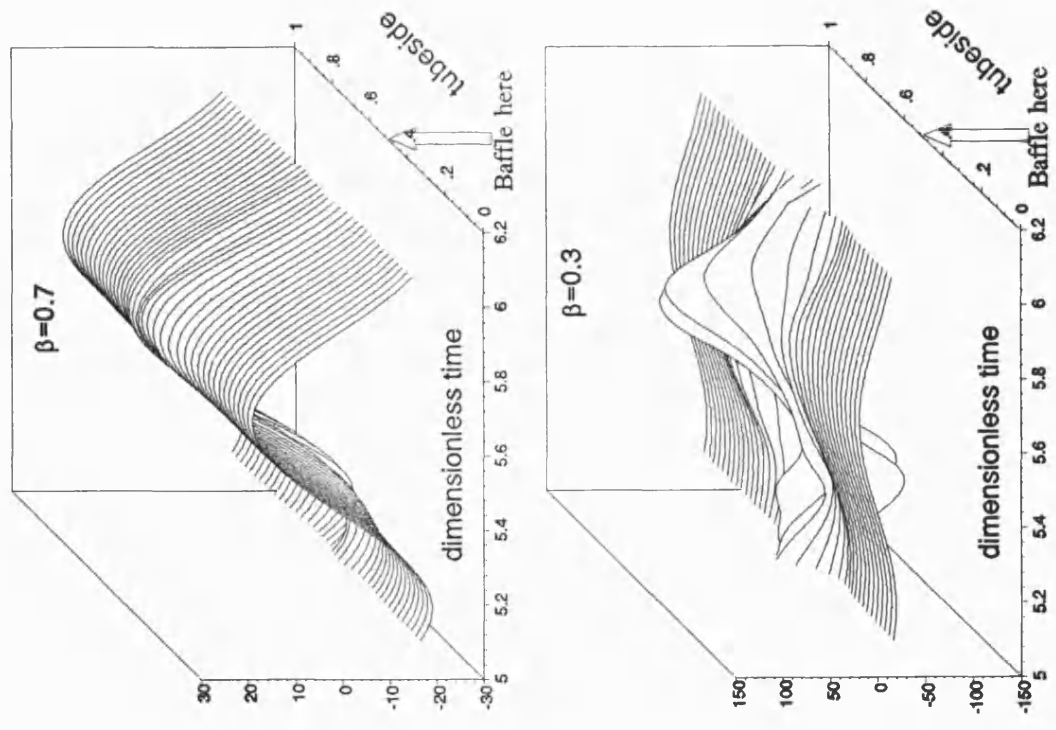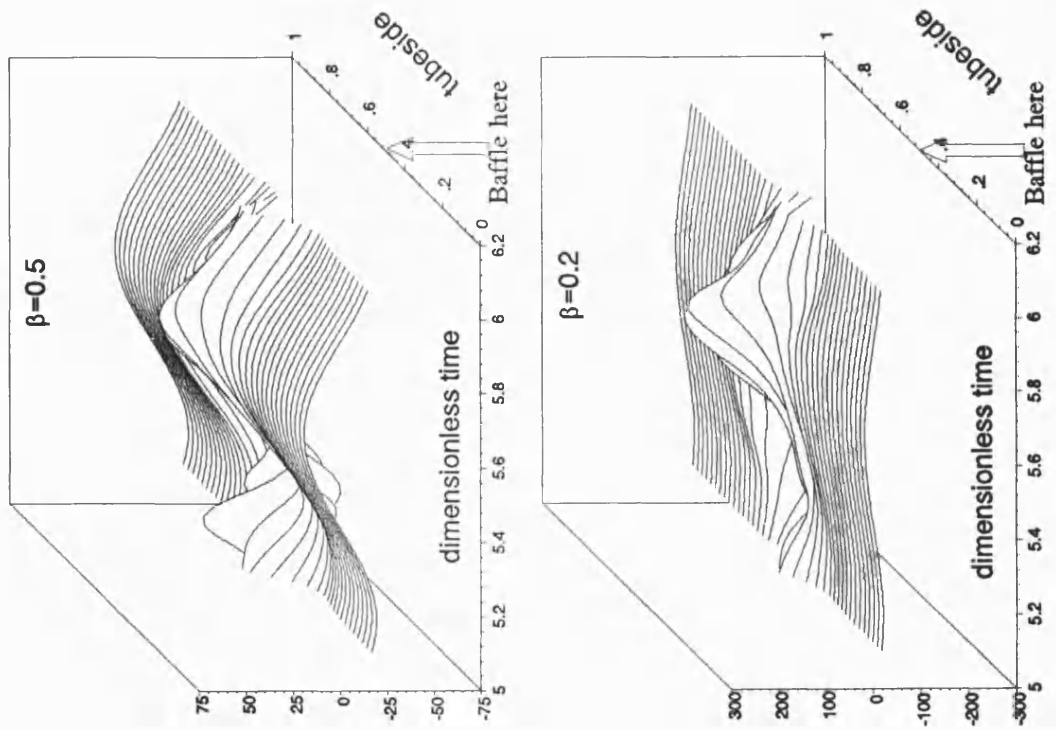
Figure 73 Influence of baffle flow area β on local wall shear rate for $Re_o = 200$, $Re_n = 0$, $St = 1$, $\lambda = 3$ and $\gamma = 0$ in central baffle tube module
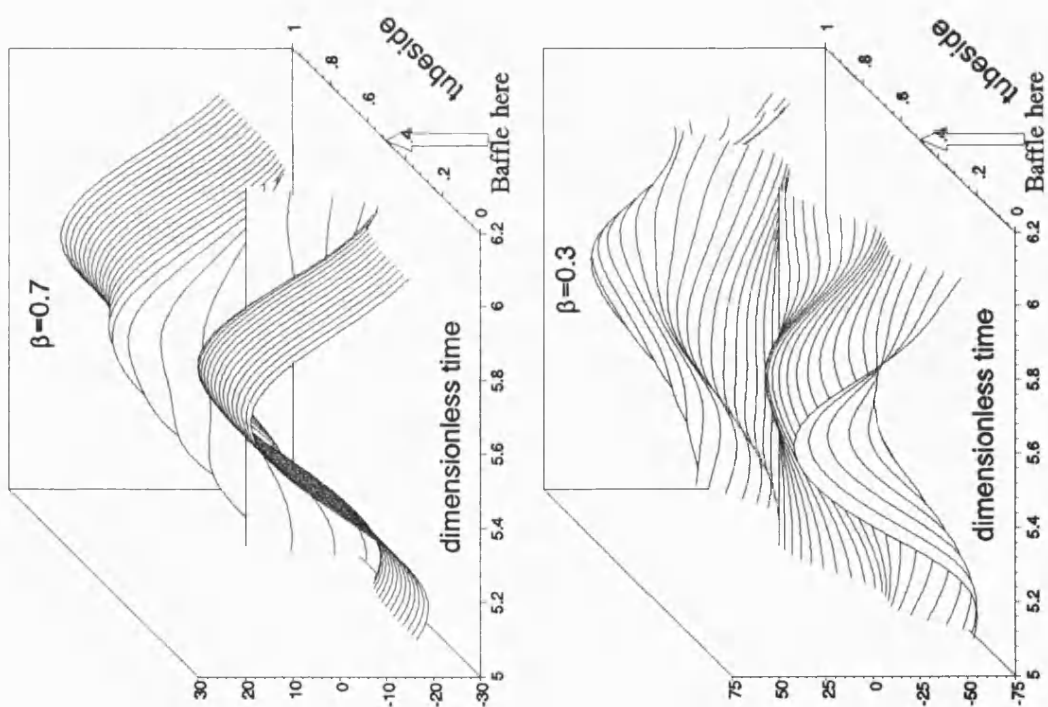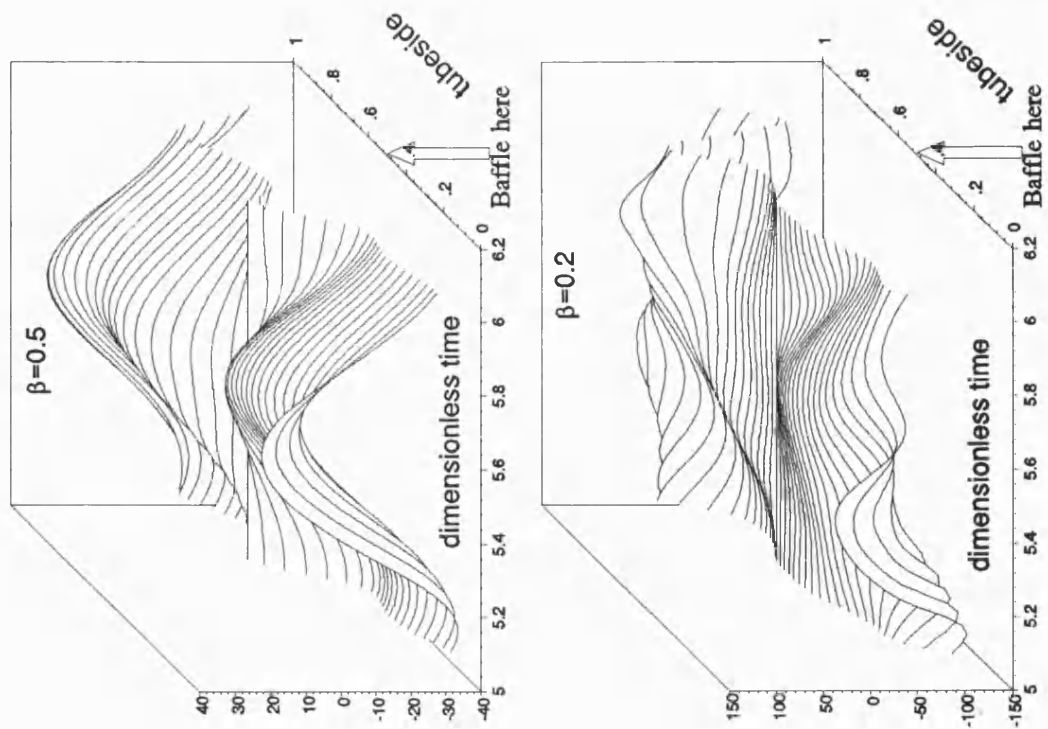
Figure 74 Influence of baffle flow area β on local wall shear rate for $Re_o = 200$, $Re_n = 0$, $St = 1$, $\lambda = 3$ and $\gamma = 0$ in wall baffle tube module

Steady flow

Central baffle

No baffle

Wall baffle

Oscillatory flow

Central baffle

No baffle

Wall baffle

Figure 75 Influence of flow nature and geometry on local wall shear rate for
Re=200, St=1, λ=3 and γ=0 in tube module

-132-
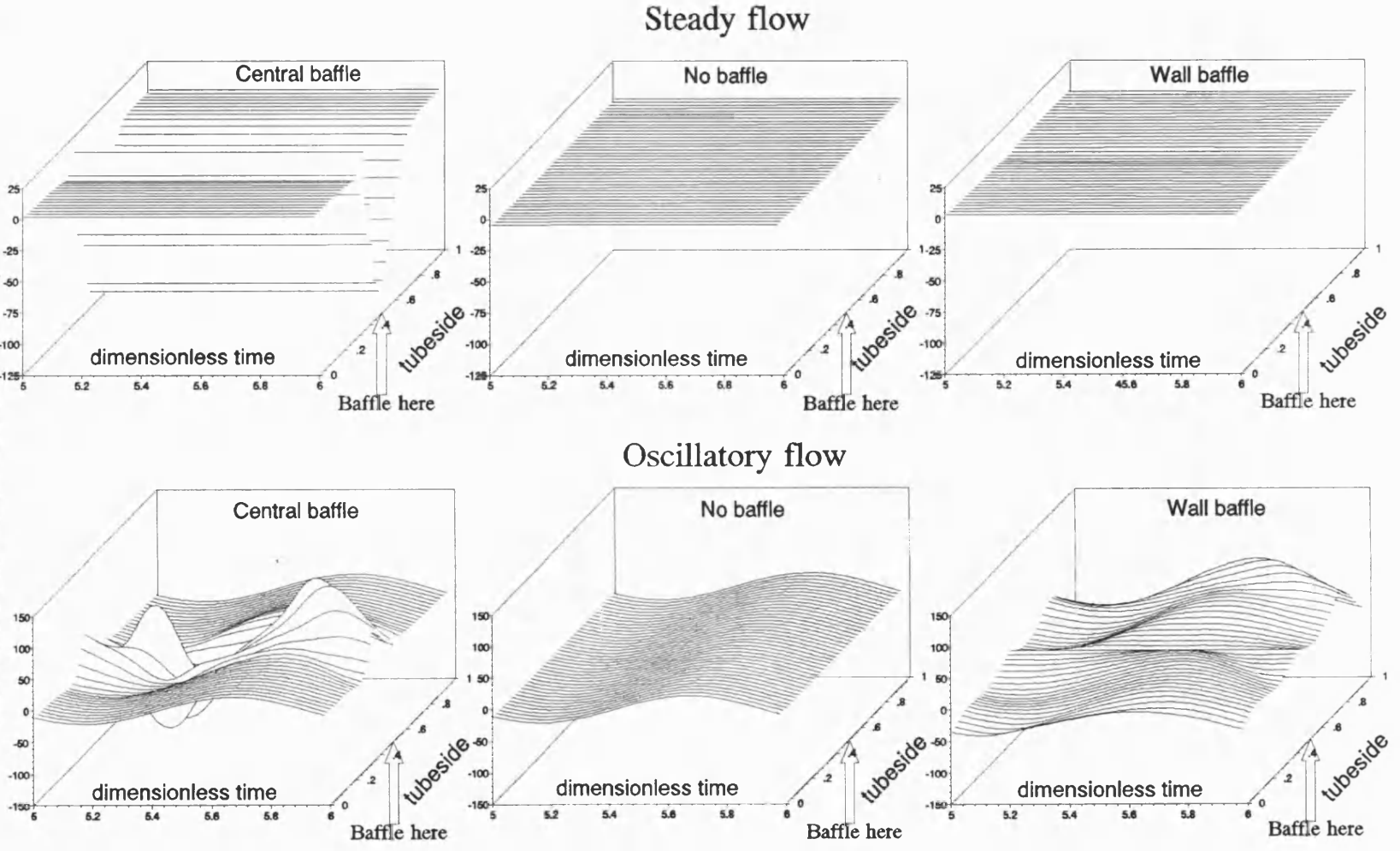
CHAPTER 5

POWER CONSUMPTION

The use of baffles within the channel membrane system increases the pressure drop and hence at a given Reynolds number the power consumption will be greater than a conventional system. The incorporation of pulsed flow further increases power consumption. The pressure drop in a conventional system is primarily due to friction at the wall. These losses are known as viscous losses. With baffles in the channel for steady flow the fluid accelerates and decelerates as it moves around or through each baffle and eddies are generated in the wake of each baffle. The pressure drop is made up of both viscous and eddy losses in this case. The viscous losses are due to both friction at the wall and at the baffle as the fluid moves past it. With pulsatile flow in a conventional system, the acceleration, deceleration and change of the direction of the fluid produces inertia losses. With baffled systems and pulsatile flow viscous, eddy and inertia losses add to produce the total pressure drop in the system. In this chapter, the power consumption of the conventional and baffled systems under steady and pulsatile flow conditions is compared to explore whether the filtration performance of the baffled systems is superior to that of a conventional system at the same power input.

This chapter consists of two sections. Section 5.1 describes the simulation of the pressure drop profile which is required to evaluate power consumption of each system for the hydrodynamic evaluation. The power consumption has been defined in terms of the power dissipated (PD) within the membrane module and on a unit volume basis. This makes scale-up to large units easier; one can convert to different basis such as membrane surface area or permeate volume.

5.1 Calculation of pressure drop

Recalling section 2.2.3 the pressure drop ΔP across one cell was obtained by integrating the axial component of the Navier Stokes equations across one cell,

Tubular channel

$$\Delta P(t,s) = -St \int_0^L \frac{\partial u}{\partial t} dx + \int_0^L v\omega dx - \frac{2}{Re} \int_0^L \left(\frac{\omega}{\sqrt{s}} + 2\sqrt{s} \frac{\partial \omega}{\partial s} \right) dx \qquad (50)$$

Rectangular channel

$$\Delta P(t,y) = -St \int_0^L \frac{\partial u}{\partial t} dx + \int_0^L v\omega dx - \frac{2}{Re} \int_0^L \frac{\partial \omega}{\partial y} dx \qquad (51)$$

It is obvious that ΔP is not only dependent on time t but also on transverse coordinate r or y in equation (50) and equation (51). Fortunately our simulation found that the difference of ΔP between any different transverse coordinates in the open area of baffled flow region was negligible, therefore y^* (the definition

of y^* is given by Figure 76) the mid point of the open area was chosen as the representative point of $\Delta P(t,y^*)$ for $\Delta P(t,r)$ or $\Delta P(t,y)$ as implemented throughout this chapter, and thus $\Delta P(t,y^*)$ represents the unique pressure drop per baffle spacing for all radial positions. Another variable scaled pressure drop which is dimensionless pressure drop divided by the maximum differential pressure drop was used to superimpose more consistently the phase shift which is the phase angle between the pressure signal and the velocity. The dimensionless pressure is used in this chapter for the numerical analysis convenience. Recalling the dimensionless procedure used in the flow model section 2.1.3, the relationship between dimensional $\bar{p}$ and dimensionless pressure p is

$$\bar{p} = p \rho U_R^2 \qquad (52)$$

U_R is the reference velocity:

$$U_R = \begin{cases} 2\pi f x_0, & \textit{for unsteady} \\ \textit{mean velocity}, & \textit{for steady} \end{cases} \qquad (53)$$

5.1.1 Results

The pressure drops are investigated in various way of which the purposes and parameters are summarized in the table below.

Table IX for the dimensionless pressure drop Figures

Figure Number	Purpose for the Figure				
	Re's effect	St's effect	Tube(central, wall) or Flat sheet	β's effect	with wall flux
Figure 77	✓		central		
Figure 78	✓		wall		
Figure 79	✓		central		✓
Figure 80	✓		wall		✓
Figure 81		bigger St	central		
Figure 82		bigger St	wall		
Figure 83		small St	central		
Figure 84		small St	wall		
Figure 85			central & wall		
Figure 86			central & wall		
Figure 87			central	✓	
Figure 88			wall	✓	
Figure 89	✓		flat sheet ✓		
Figure 90		✓	flat sheet ✓		
Figure 91		✓	flat sheet ✓		
Figure 92	middle Re_o		flat sheet ✓	✓	
Figure 93	small Re_o		flat sheet ✓	✓	

y* middle point of transverse coordinate in baffled flow region

Wall baffle

Central baffle

Rectangular module
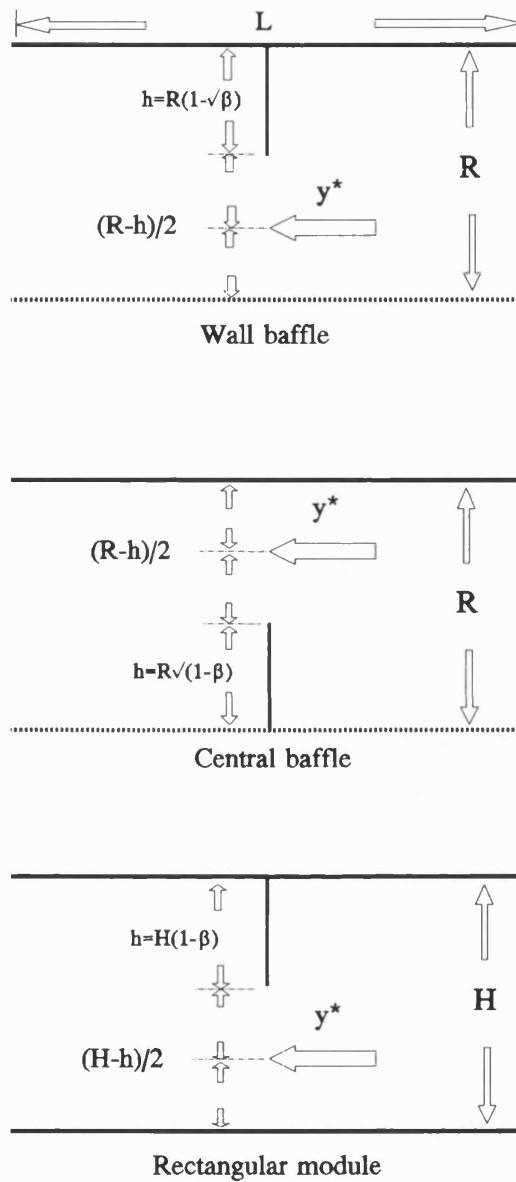
Figure 76 The definition of y^*
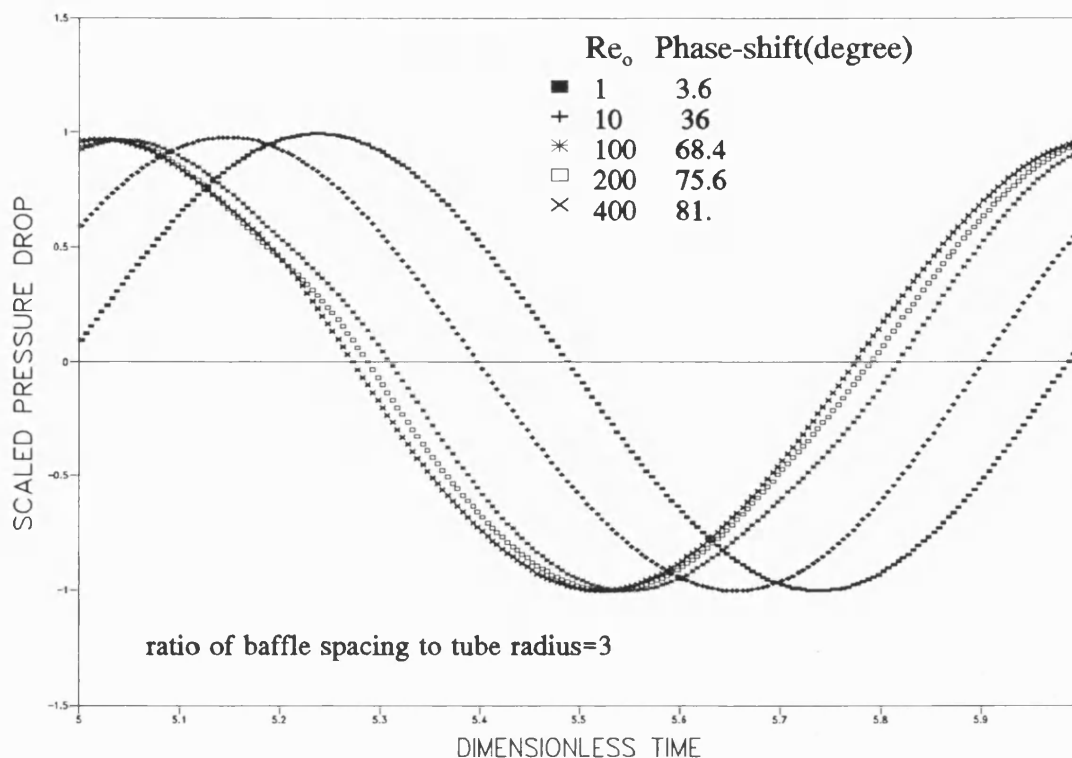
Figure 77 $Re_n=0$, $St=1$, central baffle tubular module

In Figure 77 to Figure 80 pressure profiles are given for wall baffles and central baffles together with values of the phase shift as a function of oscillatory Reynolds number at a fixed Strouhal number, $St = 1$. A comparison of Figure 77 and Figure 78 to Figure 79 and Figure 80 show little difference on pressure drop profiles between non-porous and porous tubes with 1% wall flux. For the case of creeping flow the pressure is in phase with the velocity. As Re_o increases there is a progressive increase in the phase shift for both central baffle and wall baffle
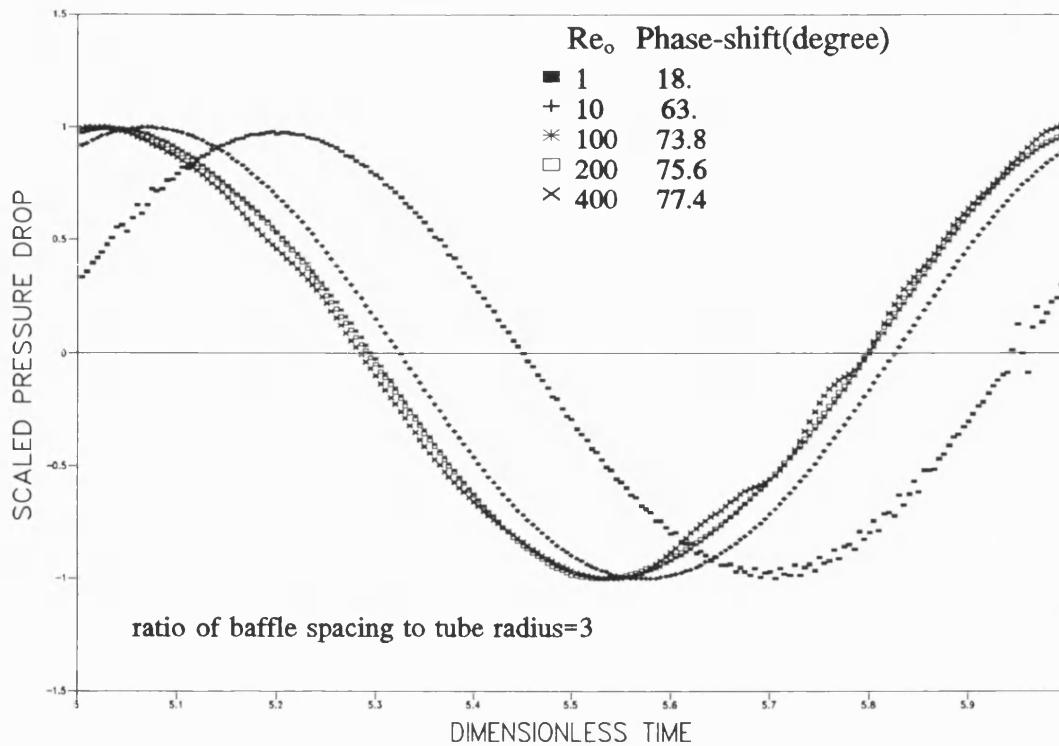
Figure 78 $Re_n=0$, $St=1$, wall baffle tubular module

which reaches, for the non-porous walls, a value of 77.4° (wall baffle in Figure 78) and 81° (central baffle in Figure 77). The maximum values in Figure 79 and Figure 80 are similar. These large phase shifts may lead to a notable power reduction when total power density is considered. At a phase shift of $\pi/2$ the total power density would be zero.
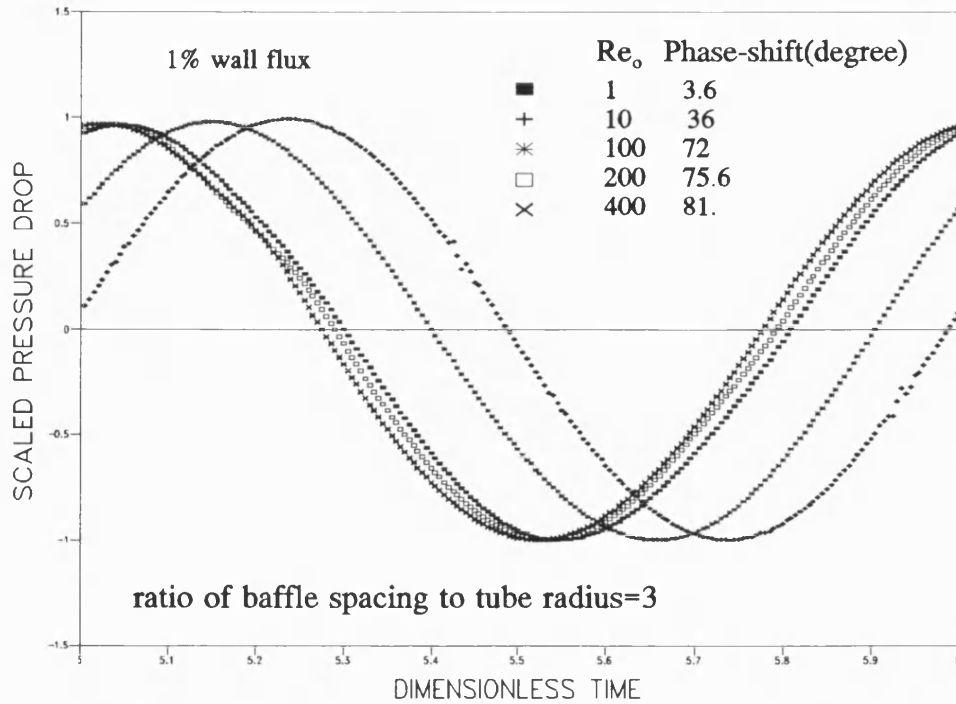
Figure 79 $Re_n=0$, St=1, central baffle tubular module with 1% wall flux
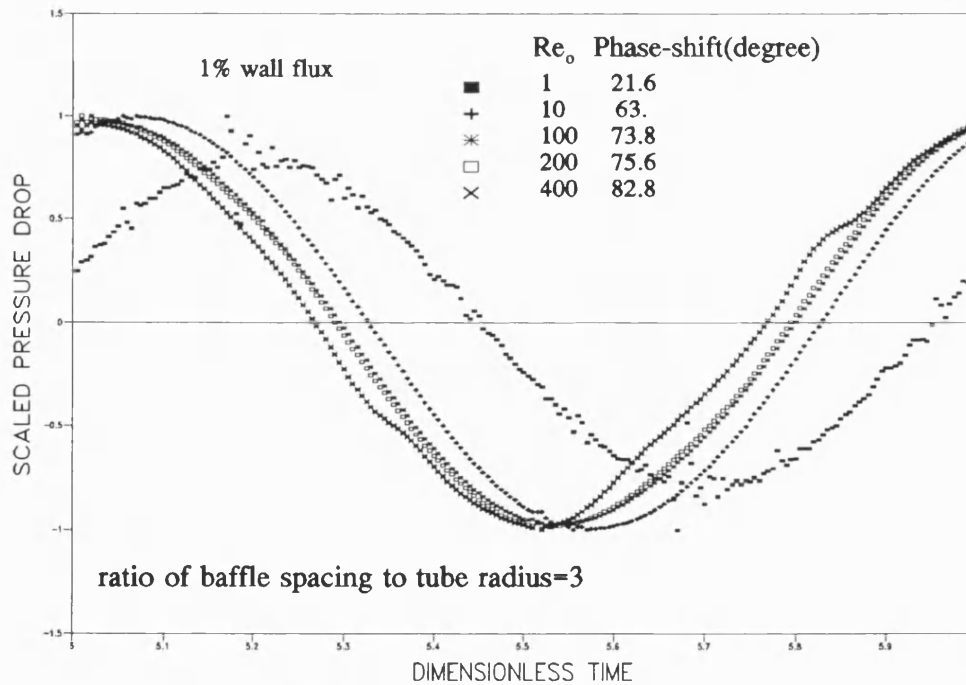
Figure 80 $Re_n=0$, St=1, wall baffle tubular module with 1% wall flux
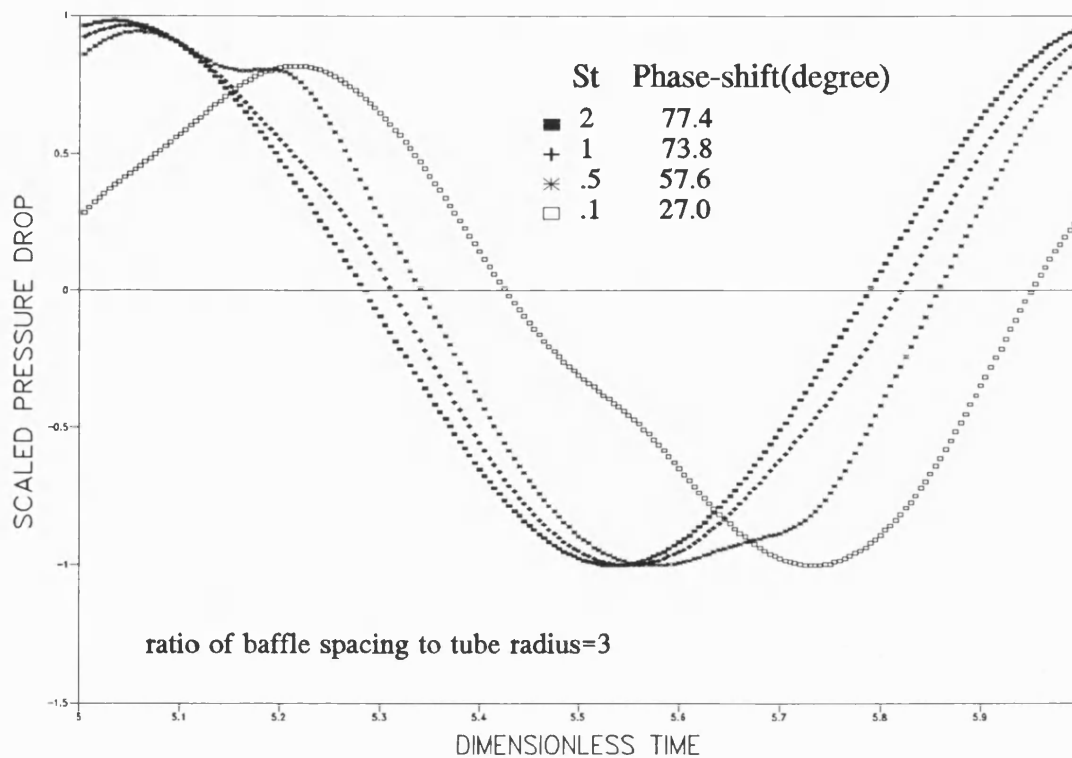
Figure 81 $Re_o=100$, $Re_n=0$, central baffle tubular module

Figure 81 to Figure 84 give data as a function of Strouhal number at a fixed oscillatory Reynolds number with Figure 81 and Figure 82 for bigger Strouhal number and Figure 83 Figure 84 for small Strouhal number and Figure 81 Figure 83 for central baffles and Figure 82 Figure 84 for wall baffles. They show that a non-sinusoidal variation arises more significantly with the wall baffles than with the central baffles when St decreases. This indicates that the former is more distinctly non-quasi-steady(Ralph 1988). As St increases there
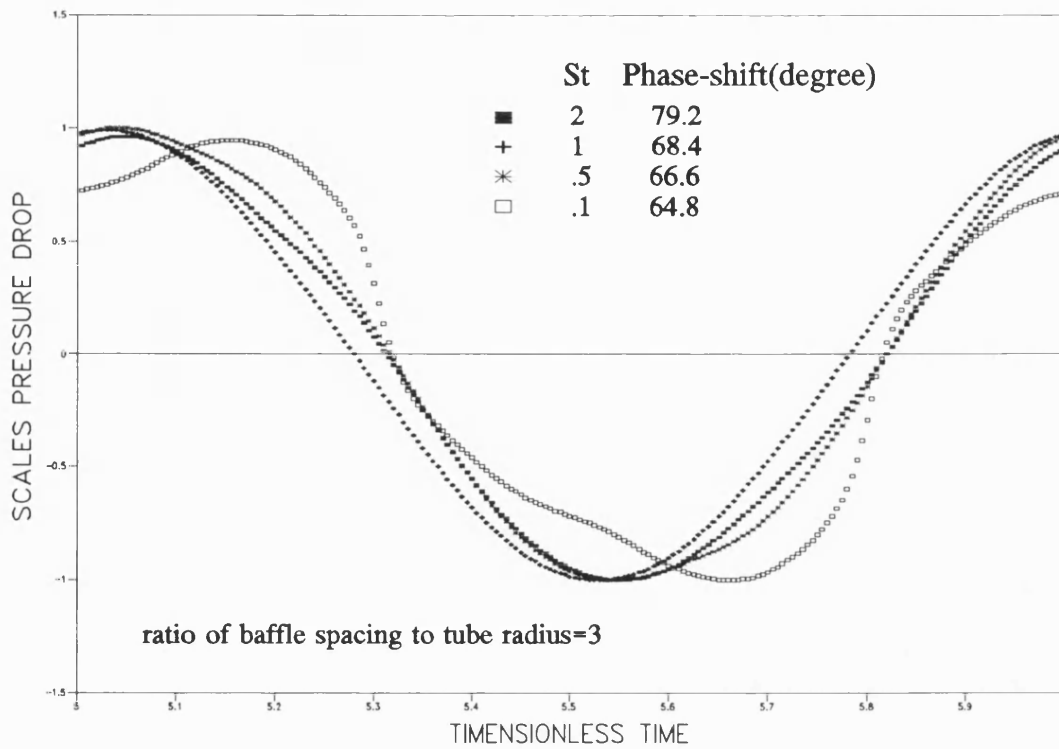
Figure 82 $Re_o=100$, $Re_n=0$, wall baffle tubular module

is a progressive increase inthe phase shift for both central baffle and wall baffle

which reaches a value of 77.4° (central baffle in Figure 81) and 79.2° (wall baffle

in Figure 82). The maximum values in Figure 81 and Figure 82 are similar.
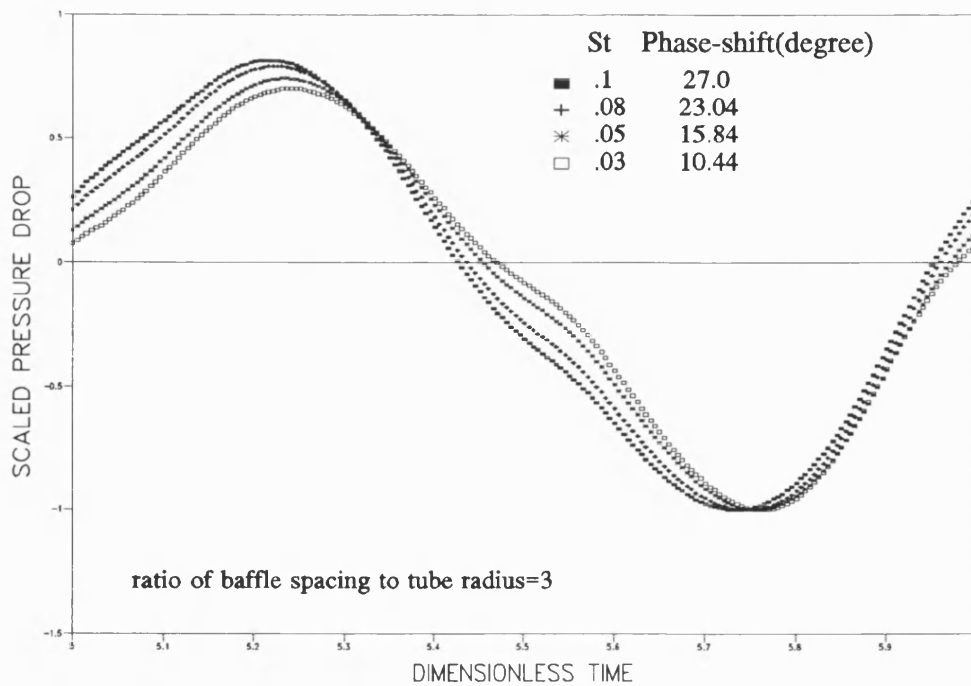
Figure 83 $Re_o=100$, $Re_n=0$, central baffle tubular module
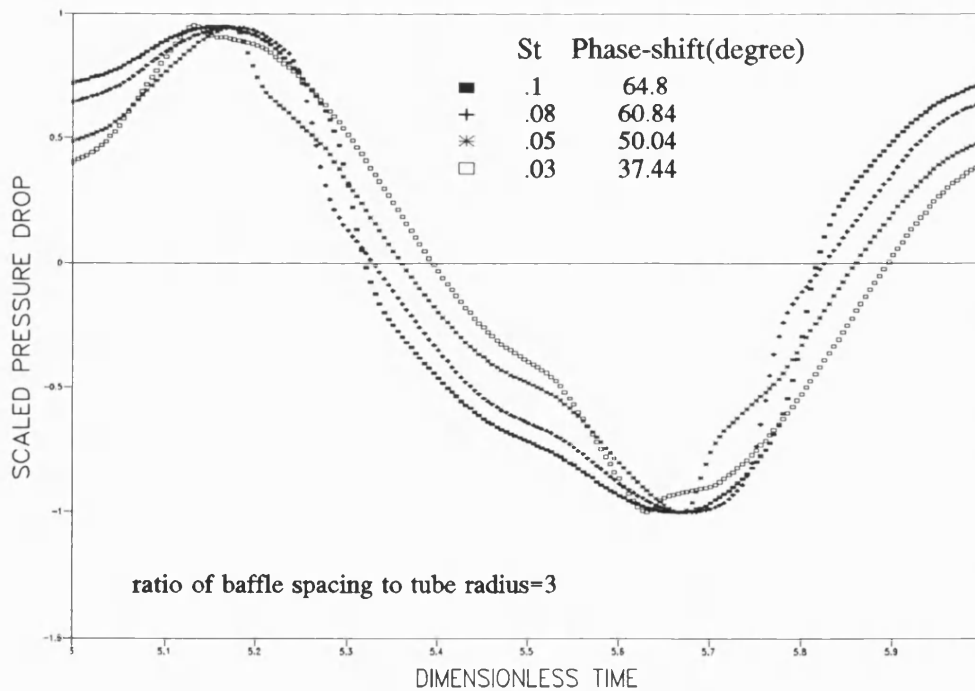
Figure 84 $Re_o=100$, $Re_n=0$, wall baffle tubular module

-143-
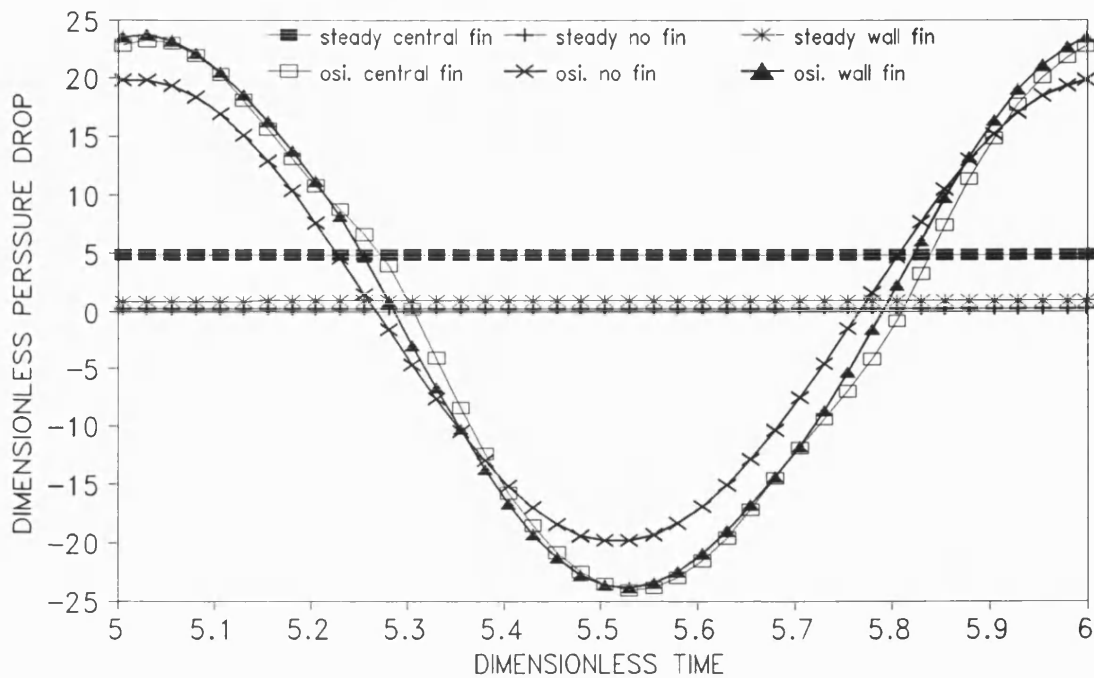
Figure 85 Re=200, St=1 β=0.4 and λ=1.5 for tubular module

Figure 85 and Figure 86 compare dimensionless pressure drop among central baffles($\beta = 0.4$), wall baffles($\beta = 0.4$) and no baffle for a tubular channel with $Re_o = 200$, St = 0.1 and 1 and $\lambda = 1.5$. Both figures show that pressure drop is greater for central baffles than either with wall baffles or without any baffles in steady flow when same baffle flow area ratio is used for both central and wall baffles module. At St = 0.1 the maximum differential pressure drop is greater for central baffles than either with wall baffles or without any baffles in steady flow while at St = 1 it is quite similar for central baffles and wall baffles.
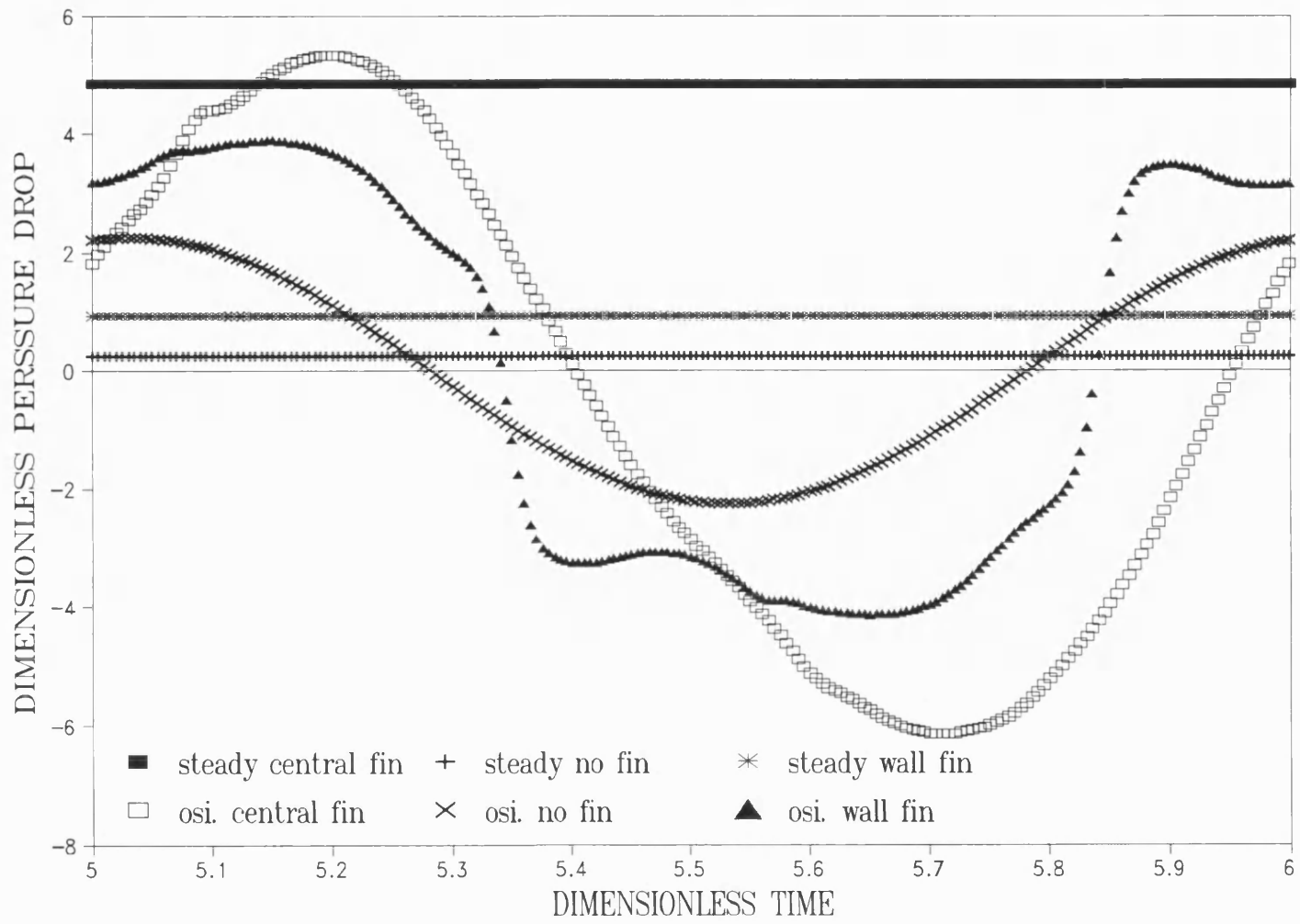
Figure 86 Re=200, St=0.1, β=0.4 and λ=1.5 for tubular module

-145-

Figure 87 and Figure 88 show the influence of baffle flow area ratio on the dimensionless pressure drop. They show that a non-sinusoidal variation arises when the influence of baffle flow area ratio β decreases for both central baffles and wall baffles. When β is 0.5~0.7 the pressure drops are similar for both central baffles and wall baffles. When $\beta = 0.2$ in central baffles pressure drop profile breaks the sinusoidal variation and when $\beta = 0.1$ in wall baffles pressure drop profile severely violates the sinusoidal variation with a sharp increase of the maximum differential pressure drop.
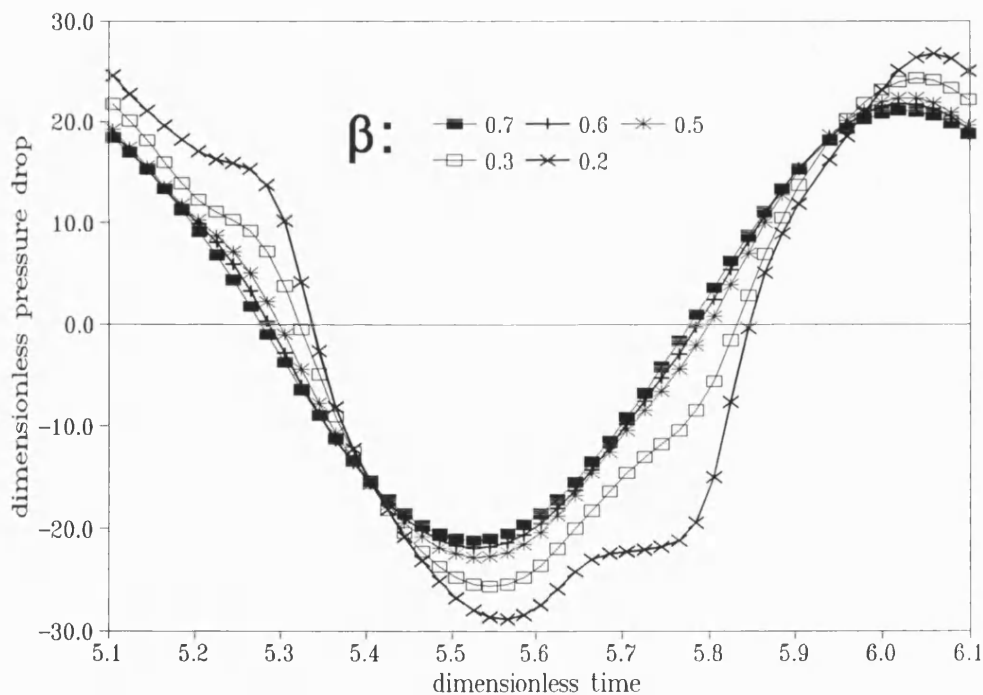
Figure 87 Influence of β with $Re_o=200$, $Re_n=0$, St=1 and $\lambda=1.5$ for central baffle tubular module
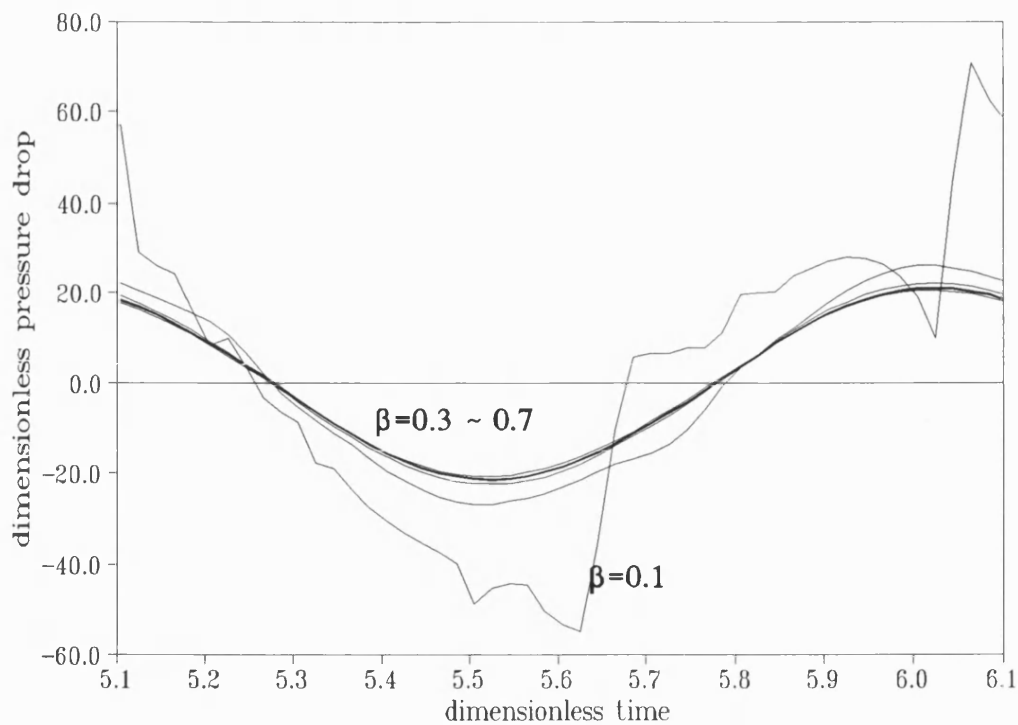
Figure 88 Influence of β with $Re_o=200$, $Re_n=0$, $St=1$ and $\lambda=1.5$ for wall baffle tubular module

The pressure drop profiles for rectangular channel are presented in Figure 89 to Figure 93. In Figure 89 pressure profiles are given together with values of the phase shift as a function of oscillatory Reynolds number at a fixed Strouhal number, $St=1$. It displays a similar phenomenon to flow in a tubular channel Figure 77 and Figure 78, that is for the case of creeping flow the pressure is in the phase with the velocity and as Re_o increases there is a progressive increase in the phase shift reaching as big as $90°$. The confidence in the phase shift result of $90°$ for $Re_o=800$ is significantly affected by the significant distortion of the sinusoidal variation. Certainly one would not expect total power density to be zero.
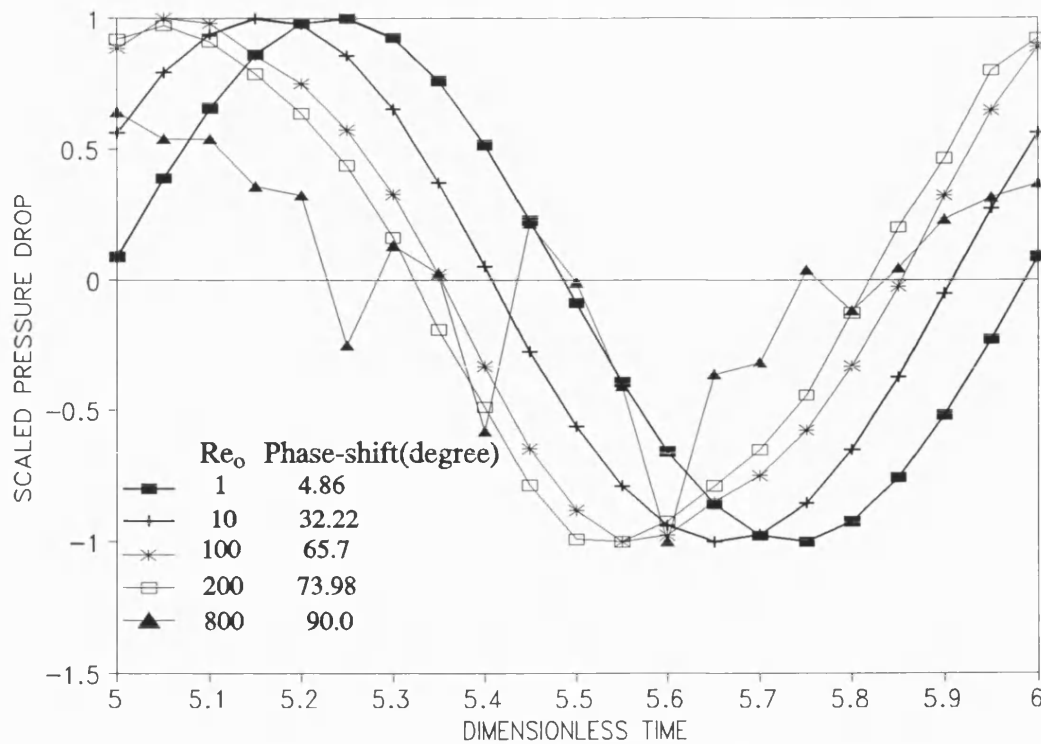
Figure 89 Influence of Re_o with β=0.4, λ=1.5 and St=1 for rectangular channel module
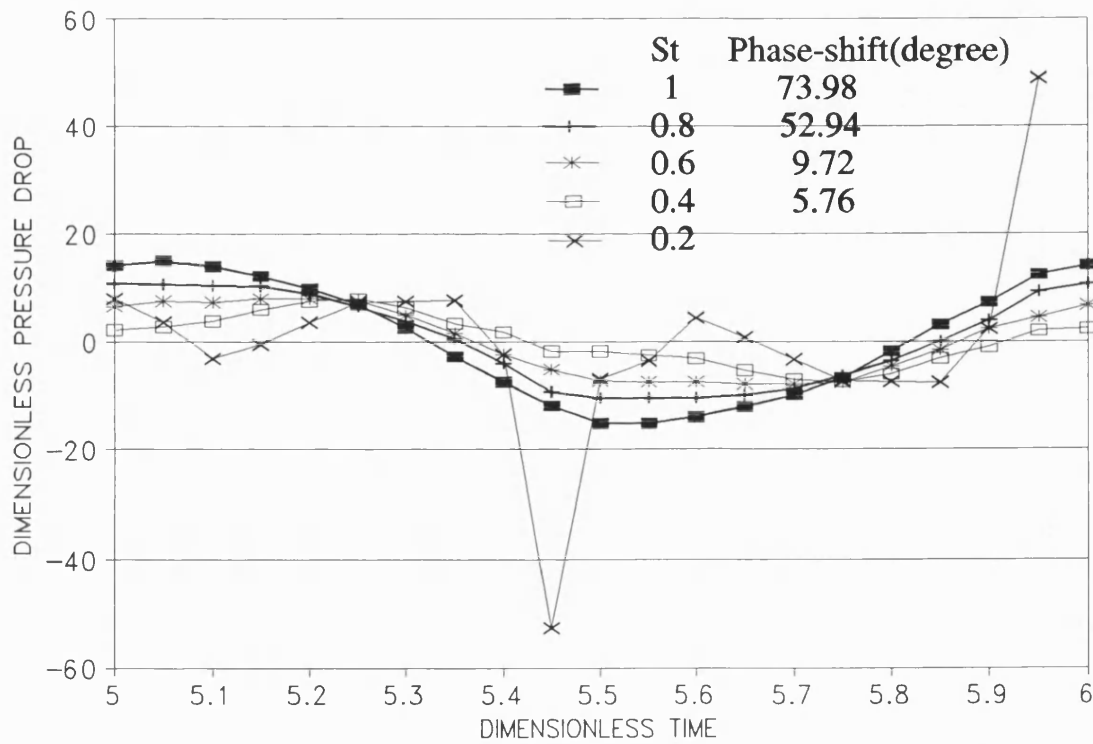
Figure 90 Influence of St with β=0.4, λ=1.5 and Re_o=200 for rectangular channel module

Figure 90 and Figure 91 gives pressure drop as a function of Strouhal number at a fixed oscillatory Reynolds number $Re_o = 200$ and $Re_o = 400$. They show a similar phenomenon to that found in a tubular channel Figure 81 to Figure 84 that is as St increases there is a progressive increase in the phase shift and a non-sinusoidal variation arises more significantly when St decreases. In Figure 90 when St decreases to 0.2 and in Figure 91 the non-sinusoidal variation is so significant that the comparison between the pressure profiles and the sinusoidal velocity profiles becomes worthless and the phase shift in these cases therefore is not calculated.
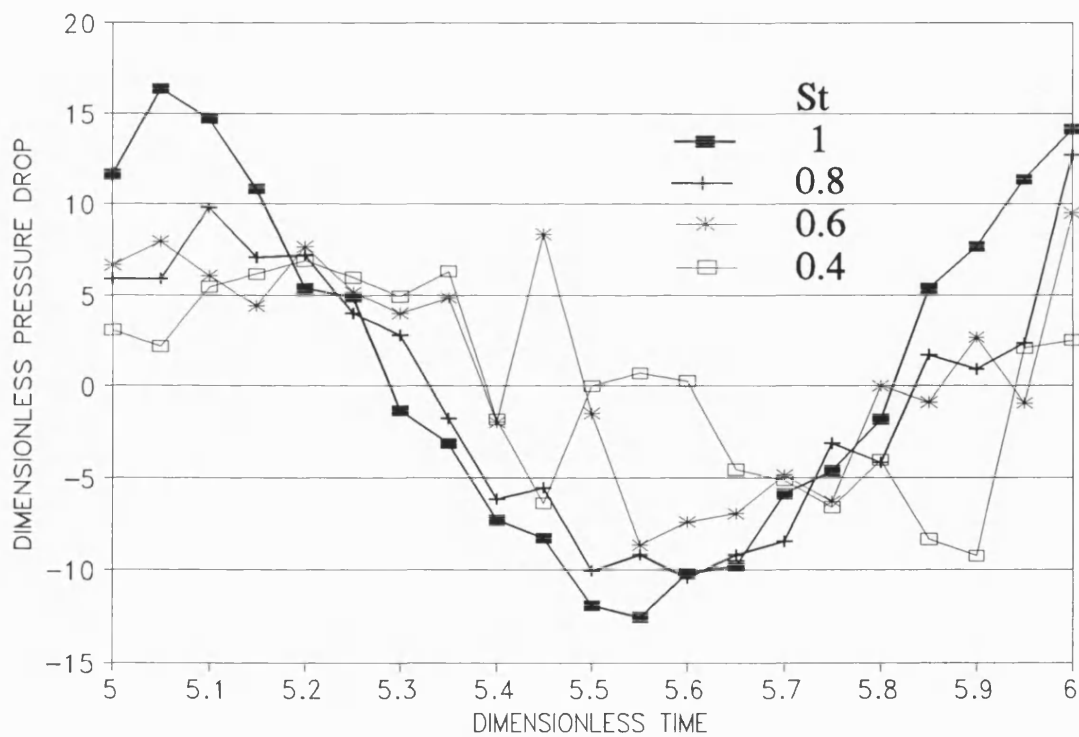
Figure 91 Influence of St with $\beta = 0.4$, $\lambda = 1.5$ and $Re_o = 400$ for rectangular channel module
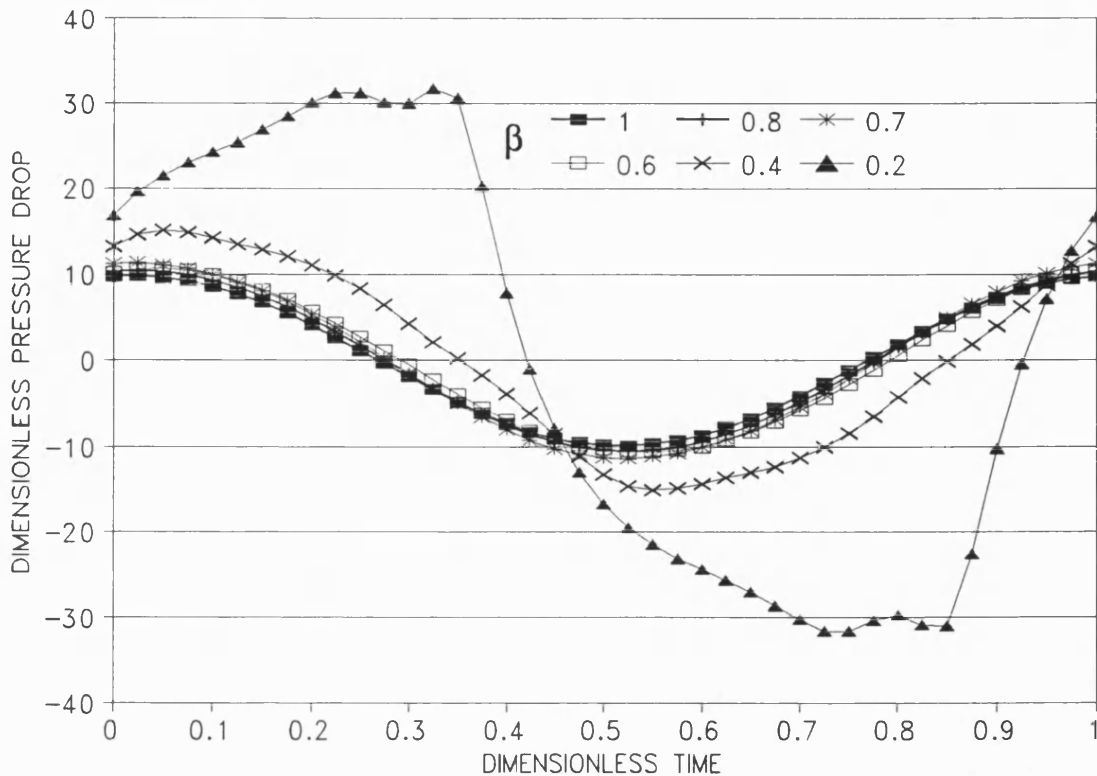
Figure 92 Influence of β with $Re_o=100$, $Re_n=0$, $St=1$ and $\lambda=1.5$ for rectangular channel module

Figure 92 shows the influence of baffle flow area ratio on the dimensionless pressure drop. It show a similar phenomenon to that found in the equivalent tubular channel in Figure 87 and Figure 88. A non-sinusoidal variation arises and phase shift increases when the baffle flow area ratio β decreases. When β is 0.6 ~ 1(that is no baffles) the pressure drops are similar. When $\beta=0.2$ pressure drop profile intensely breaks the sinusoidal variation with sharply increase of the maximum differential pressure drop.
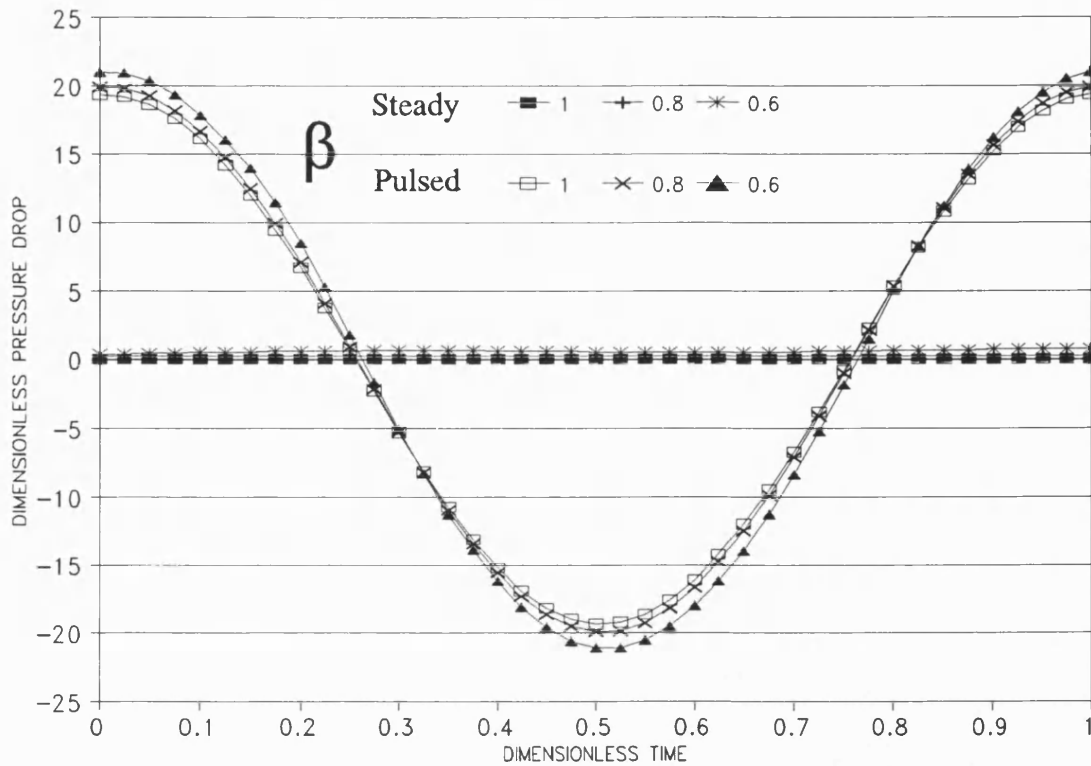
Figure 93 Influence of β with $Re_o=800$, $Re_n=0$, $St=1$ and $\lambda=3$ for rectangular channel module

Figure 93 is the equivalent rectangular channel data to Figure 85 and Figure 86 for the tubular module. It compares dimensionless pressure drop between oscillatory flow and steady flow for different baffle flow area ratio $\beta = 0.6$, 0.8 and 1 with $Re_o = 800$, $St = 1$ and $\lambda = 3$.

5.1.2 Discussion

It is to be expected that the difference of ΔP between any different transverse coordinates in the open area of baffled flow region would be negligible. Because the flow is assumed to be axially periodic with wavelength L, from the Navier-Stokes equations Chapter 2 (10) or (11), the transverse pressure gradient

$$\frac{\partial P}{\partial r} \quad or \quad \frac{\partial P}{\partial y}$$

is also assumed to be axially periodic with wavelength L. Thus $\Delta P(t,y^*)$ represents the unique pressure drop per wavelength L for all transverse positions.

The existence of a phase shift, θ, between the pressure signal and the velocity has been observed by several authors, Edwards et al.(1971), Ohmi et al.(1982), Ralph(1988) and Finnigan(1990) etc. As the definition of θ varies between authors, the results recorded do not at first sight appear to be consistent. For example Finnigan measured θ $90°$ - $162°$ which means the pressure signal lagged behind the flow rate by $28°$ - $90°$. Ralph using time-mean value defined θ as:

$$\cos\theta = \frac{4}{\pi} \frac{\int_0^1 \Delta P(t)\sin 2\pi t\, dt}{\int_0^1 |\Delta P(t)|\, dt}.$$

Note that for any θ

$$\int_0^1 \sin(2\pi t + \theta)\sin 2\pi t\, dt = \frac{1}{2}\cos\theta,$$

Ralph's definition of θ gives the pressure signal ahead of flow rate by θ.

In our definition $\Delta P = P_{inlet} - P_{outlet}$ and θ is calculated in two stages. Firstly scaled pressure drop is obtained by dividing the pressure drop by the maximum differential pressure drop. Secondly by fitting this scaled pressure drop to a sine wave if it appears not far from the sinusoidal wave. If $\sin(2\pi t + \theta)$ is the sinusoidal fit then θ is defined as the phase shift. It is easy to see that this definition of θ is equivalent to that of Ralph's. If pressure drop is found to be highly non-sinusoidal it is not of interest to explore further the phase difference. Ralph's results showed that θ is between $0°$ and $90°$ and when Re_o increases θ increases. Ohmi et. al.(1982) also found that pressure signal is ahead of flow rate.

The explanation as to why Finnigan's θ is a phase lag rather than a phase lead is probably that $\Delta P = P_{outlet} - P_{inlet}$ was used instead of $\Delta P = P_{inlet} - P_{outlet}$ making a half wave shift in the pressure.

5.2 Evaluation of power consumption

The associated power consumption ($\overline{PD}$) for the system was then obtained

by integration over the period of oscillation of equation (57) :

$$\overline{PD} = \frac{1}{TV} \int_0^T \Delta \overline{P}(t) \; \overline{Q}(t) \, dt \qquad (57)$$

Here T is the period of oscillation $T = 1/f$ and V volume of one cell channel.

The dimensionless power density (PD) is defined by

$$PD = \int_0^1 \Delta P(t) \, FNT(t) \, dt \qquad (58)$$

Here $\Delta P(t)$ is the dimensionless pressure and FNT(t) is the oscillatory source

function defined in Table V of Section 2.2.1. In most of the cases, a sinusoidal

source function was employed:

$$FNT = \begin{cases} 1 & steady \\ NFR + \sin(2\pi t) & oscillatory \end{cases} \qquad (59)$$

It is easy to establish the relationship between dimensional power consumption

($\overline{PD}$) and dimensionless power density (PD)

$$\overline{PD} = \frac{\rho U_R^3}{L} PD \qquad (60)$$

where U_R is the reference velocity

Using dimensionless power density for numerical analysis is straightforward and PD will be employed throughout this chapter unless otherwise stated. To evaluate the dimensionless power Simpsons rule is used for integrating equation (58). The detailed FORTRAN program is listed in Appendix 3.

5.2.1 Results

The power consumption is investigated in various way of which the purposes and parameters are summarized in the table below.

Table X for the power density Figures

Figure Number	Purpose for the Figure			
	Re's effect	St's effect	Tube(central,wall) or Flat sheet	β's effect
Figure 94	$\omega x_0 D$		central & wall	
Table XII		✓	central,no,wall	
Figure 95	✓	bigger St	central,no,wall	
Figure 96	✓	smaller St	central,no,wall	
Figure 98	✓		central & wall	
Figure 99			central & wall	✓
Figure 100	✓		flat sheet ✓	
Figure 101		✓	flat sheet ✓	

First of all, the total power density data for a wall baffled tube is presented (Mackay 1991). The results include data for both numerical simulations and experiments. The experimental work was carried out by Mackay in Department of Chemical Engineering, University of Cambridge. Experimental data covers three fluid viscosities which are summarized in the table below.

Table XI Physical properties of water/glycerol solutions

Fluid	Density $\rho(kg/m^3)$	Viscosity $\mu(Pa\ s)$	Kinematic viscosity $v(m^2/s)$
A	1065	0.0022	2.05×10^{-6}
B	1190	0.028	23.5×10^{-6}
C	1060	0.077	72.8×10^{-6}
Water	1000	0.001	1.00×10^{-6}

It was found that the experimental data for different viscosity fluids appears to superimpose more consistently if the data is plotted as a function of $\omega x_0 d$, ω is the angular frequency $2\pi f$, rather than Re_0. The total power density data plotted as a function of $\omega x_0 d$ is shown for wall baffles in Figure 94. The numerical simulation covers the lower values of $\omega x_0 d$ and the experimental data the higher values. The graph shows that at values of $\omega x_0 d$ of less than order 10^{-5} m^2/s the power density variation follows a power law of order 2 and above 10^{-5} the numerical prediction is cubic. The experimentally determined power densities appears to be below that of the extrapolated simulation although of course flow symmetry breaking occurs after the final simulation plot.
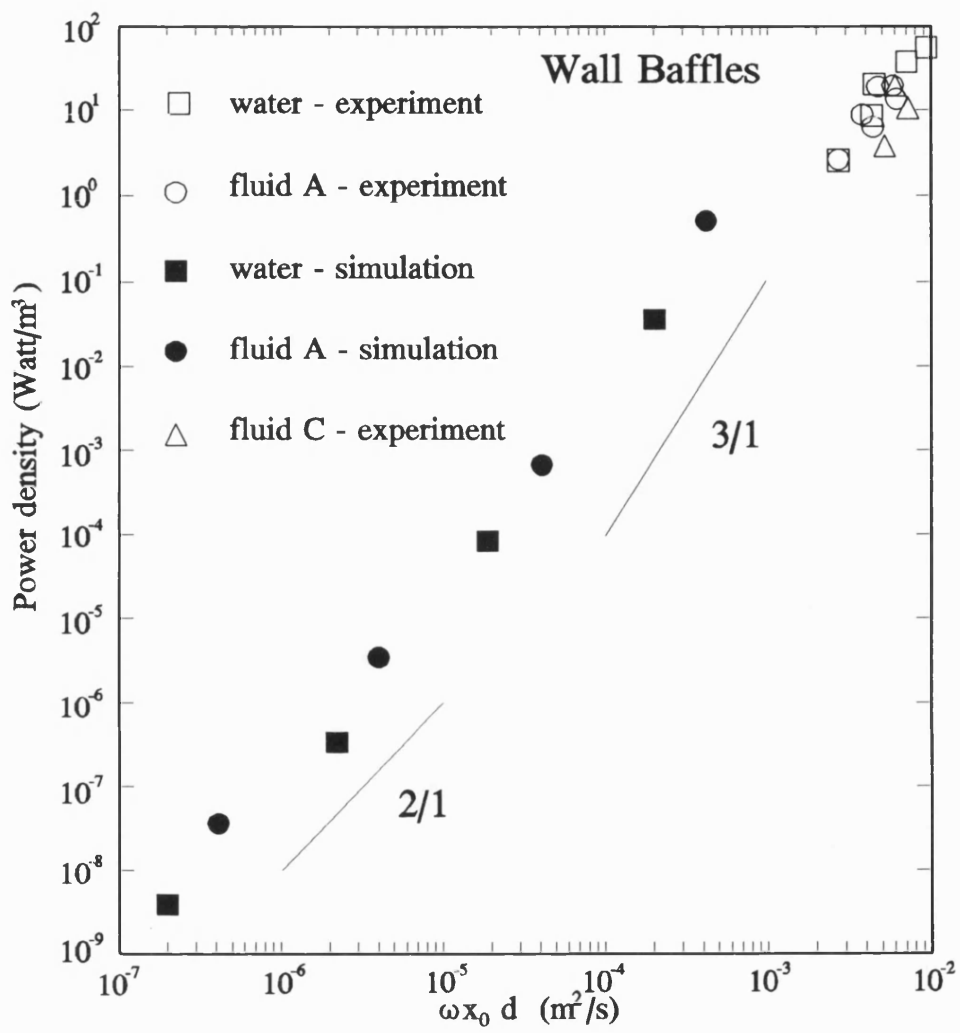
Figure 94 Power density plotted as a function of $\omega x_0 d$ for wall baffles. Both simulation and experimental data.
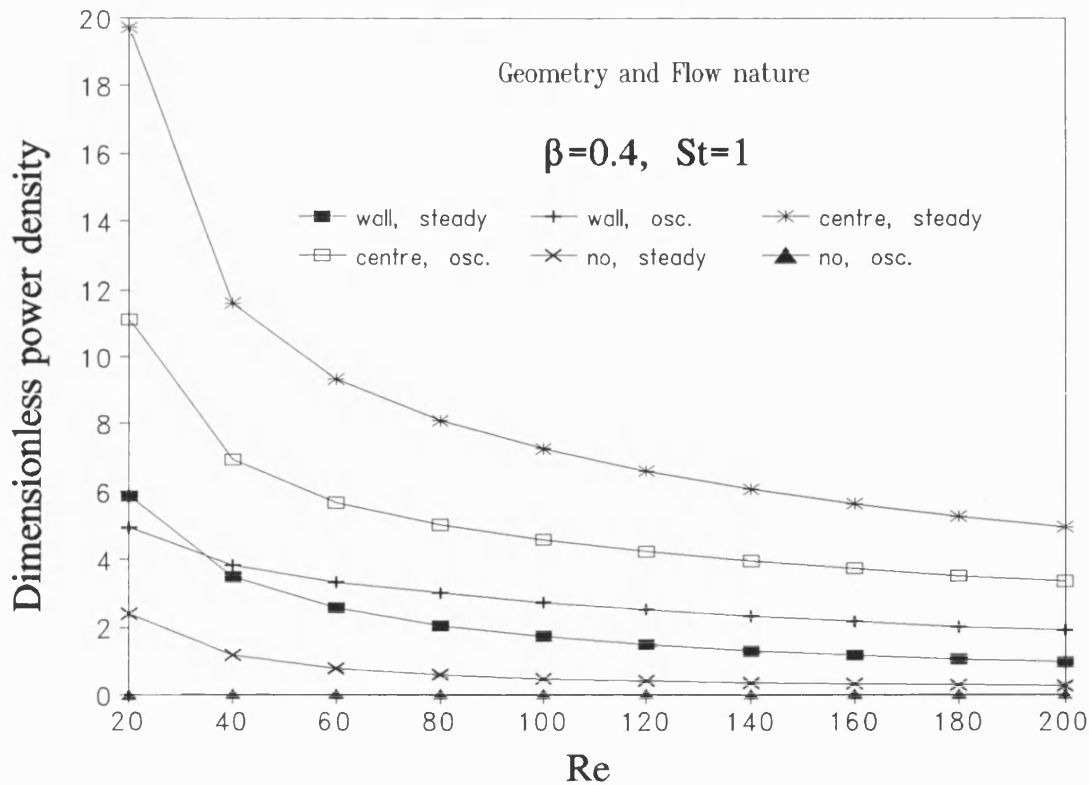
Figure 95 Comparison of power density at Re_o basis for steady and oscillatory flow among different geometry in tubular module with St=1, β=0.4 and λ=1.5.

The comparison of power consumption for steady and oscillatory flow using different baffles (Figure 95 and Figure 96) shows that central baffles uses more energy than wall baffles and illustrates that pulsatile flow uses less energy than steady flow in the central baffles and no baffles case. With wall baffles the curves for steady and oscillatory flow are similar, with the later being lower, for the greater part of the Re range when St=1 (Figure 95). This has also been found experimentally (Finnigan 1990).
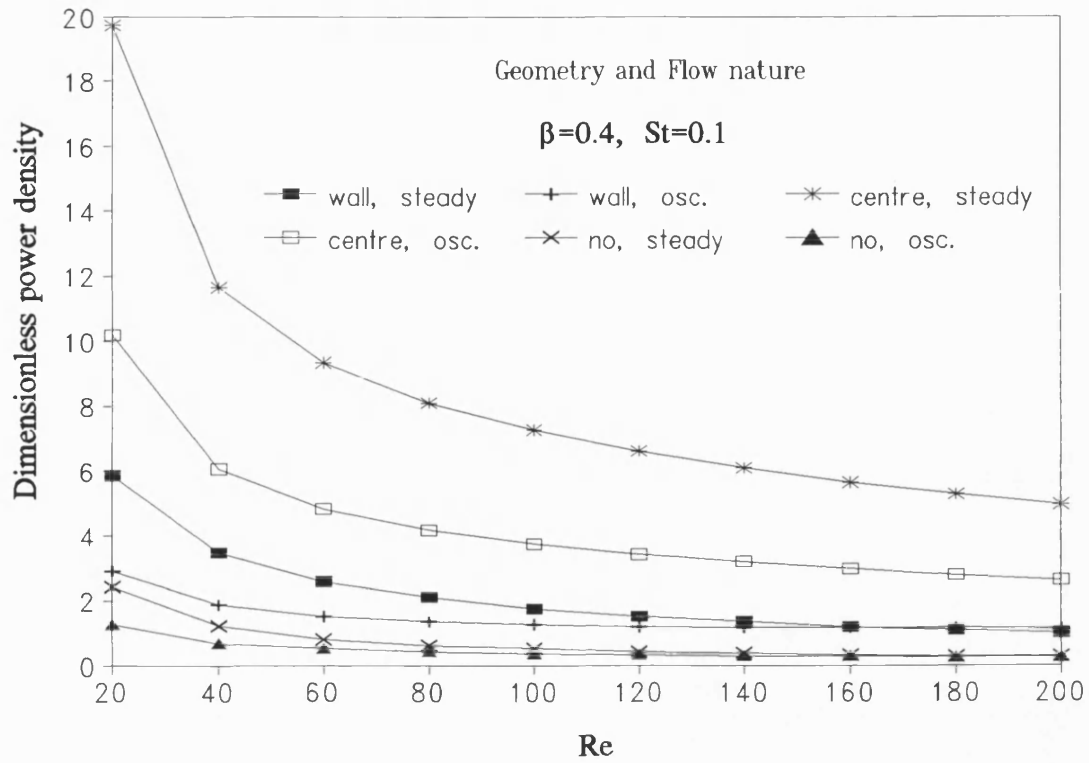
Figure 96 Comparison of power density at Re_o basis for steady and oscillatory flow among different geometry in tubular module with St=0.1, β=0.4 and λ=1.5.

To establish the analytical relationship between PD and Re the 2nd degree polynomial curve fits for PD is shown in Figure 97. Within the coefficient of determination 0.999 the curve fit results are:
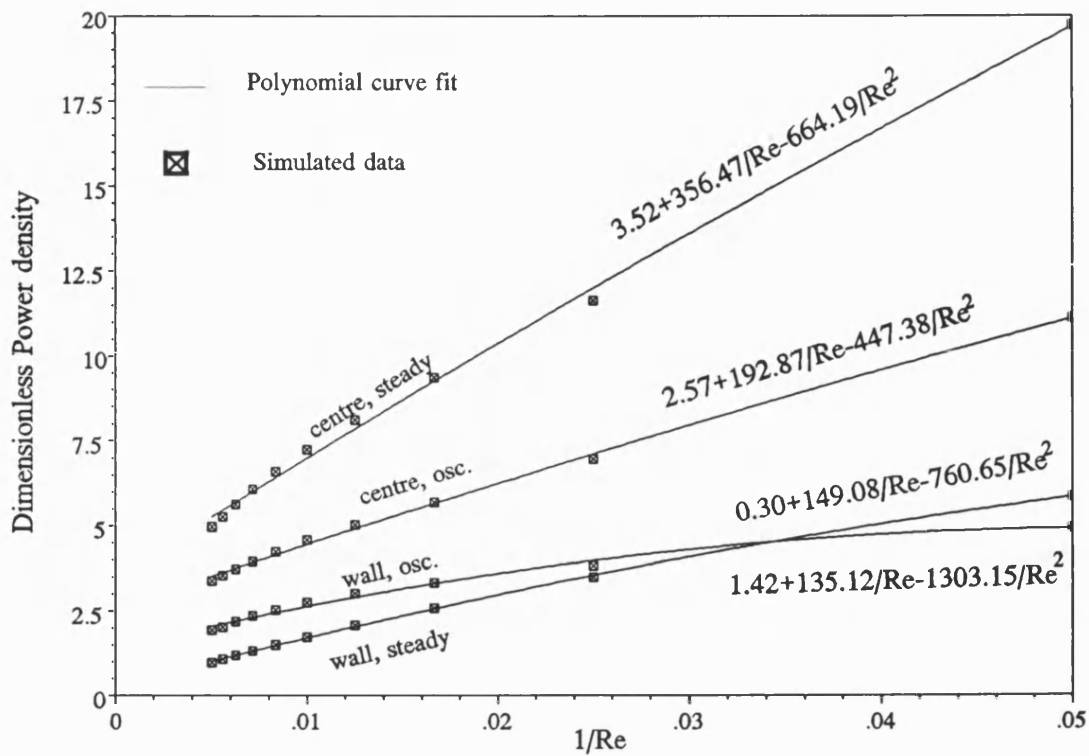
Figure 97 Comparison of power density at 1/Re basis for steady and oscillatory flow among different geometry in tubular module with St=1, β=0.4 and λ=1.5.

$$0.30 + 149.08\frac{1}{Re} - 760.65\frac{1}{Re^2} \quad \textit{for wall, steady}$$

$$1.42 + 135.12\frac{1}{Re} - 1303.15\frac{1}{Re^2} \quad \textit{for wall, osc.}$$

$$3.50 + 356.47\frac{1}{Re} - 664.19\frac{1}{Re^2} \quad \textit{for centre, steady}$$ (61)

$$2.57 + 192.87\frac{1}{Re} - 447.38\frac{1}{Re^2} \quad \textit{for centre, osc.}$$

Incorporating the above with equation (60) it can be easily seen that the dimensional power density variation follows a power law of order between 2 and 3 over shown Re range. The critical point Re* so that when Re < Re* power density variation follows a power law of order 2 and when Re > Re* power density variation follows a power law of order 3 is dependent on the physical properties and the geometrical parameters.

The pressure drop in a conventional system is primarily due to viscous friction at the wall. The pressure drop in a long horizontal pipe with steady flow is:

$$\Delta \overline{P} = \frac{32 \mu U_{av} L}{d^2} \tag{62}$$

Substituting this analytical formula in the dimensionless power density calculation (58) the PD can be readily calculated:

$$PD = \frac{32 \lambda}{Re} \tag{63}$$

Table XII comparison of the analytically calculated and simulated PD for the steady flow in a no baffle tube

Re	Analytical results by (63)	Simulation results	The relative error(%)
20	2.4	2.415157	0.157388
40	1.2	1.207781	0.16158
60	0.8	0.806988	0.217425
80	0.6	0.609303	0.384643
100	0.48	0.492883	0.662104
120	0.4	0.416619	1.017537
140	0.342857	0.362889	1.41919
160	0.3	0.322982	1.8445
180	0.266667	0.292137	2.279023
200	0.24	0.267549	2.713907

Table XII gives the comparison between the analytically calculated PD using equation (63) and numerical simulated PD. The results show the relative error increasing with the Re probably because flow symmetry breaking occurs when Re approaching 200. Nevertheless these errors (< 3%) are acceptable comparing with the PD results obtained here, which therefore suggest not only

qualitatively correct but also quantitative accuracy for the pressure drop, power density and later for the membrane concentration and flux simulation in the ensuing discussion and next chapter.
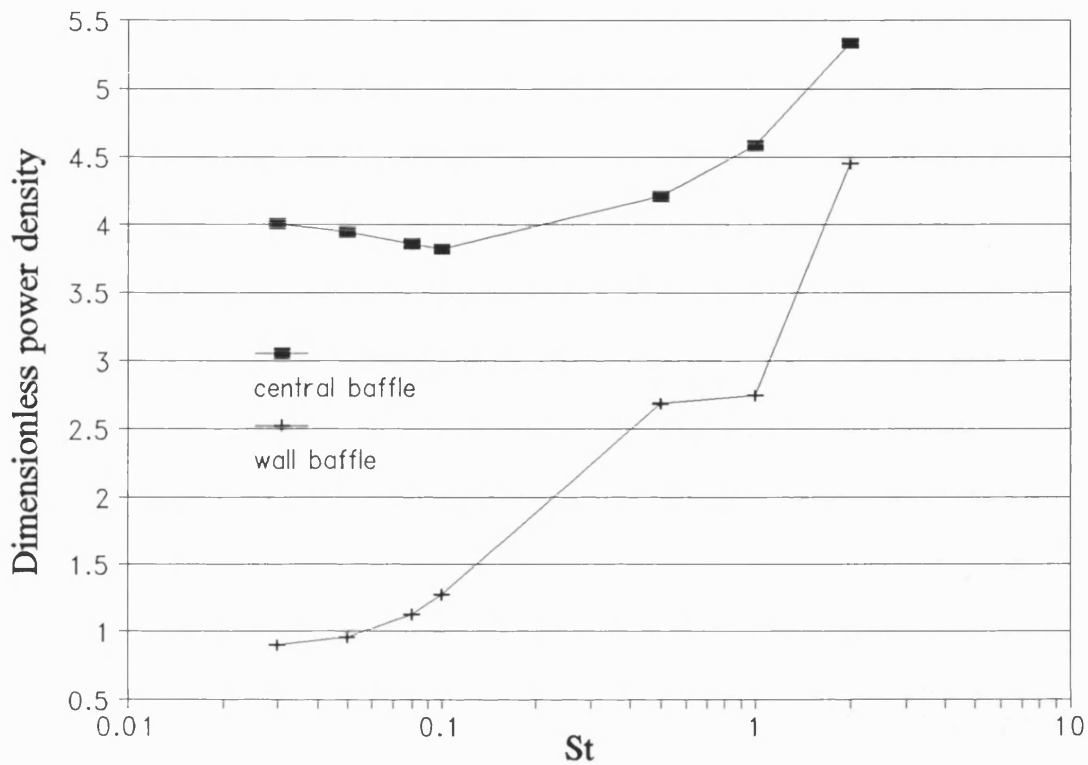
Figure 98 The influence of St on power density for Re_o=100, Re_n=0, β=0.4 and λ=1.5 with tubular module.

Figure 98 gives data as a function of Strouhal number at a fixed oscillatory Reynolds number 100. With central baffles an optimum St=0.1 exists for the minimum power density. In wall baffles a small St which means a large amplitude when the Reynolds number is fixed uses less energy. As St increases the Power density difference between central and wall baffles appears to narrow.
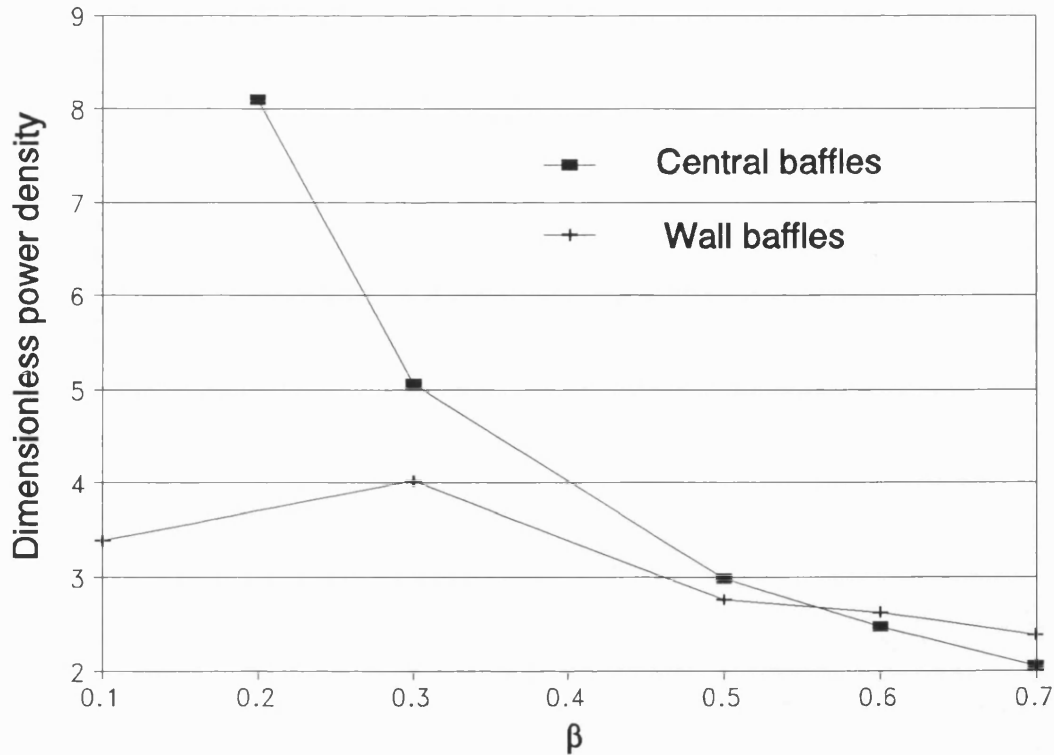
Figure 99 Influence of β on power density with $Re_o=200$, $Re_n=0$, St=1 and $\lambda=1.5$ for tubular module

Figure 99 shows the influence of baffle flow area ratio on the dimensionless power density. There is a cross point at $\beta=0.561$ between the two curves. At this baffle flow area ratio these two baffle systems use the same amount of the energy. With central baffles PD increases sharply when baffle area increases while with wall baffles it appears more constant. As shown in Figure 88 when $\beta=0.1$ with wall baffles the pressure drop profile varies severely from the sinusoidal pattern with a sharp increase of the maximum differential pressure drop and dramatic change of the sign of the gradient, which conceivably causes the PD calculation to be inaccurate but apparently $PD(\beta=0.1)<PD(\beta=0.3)$ for the wall baffle case.
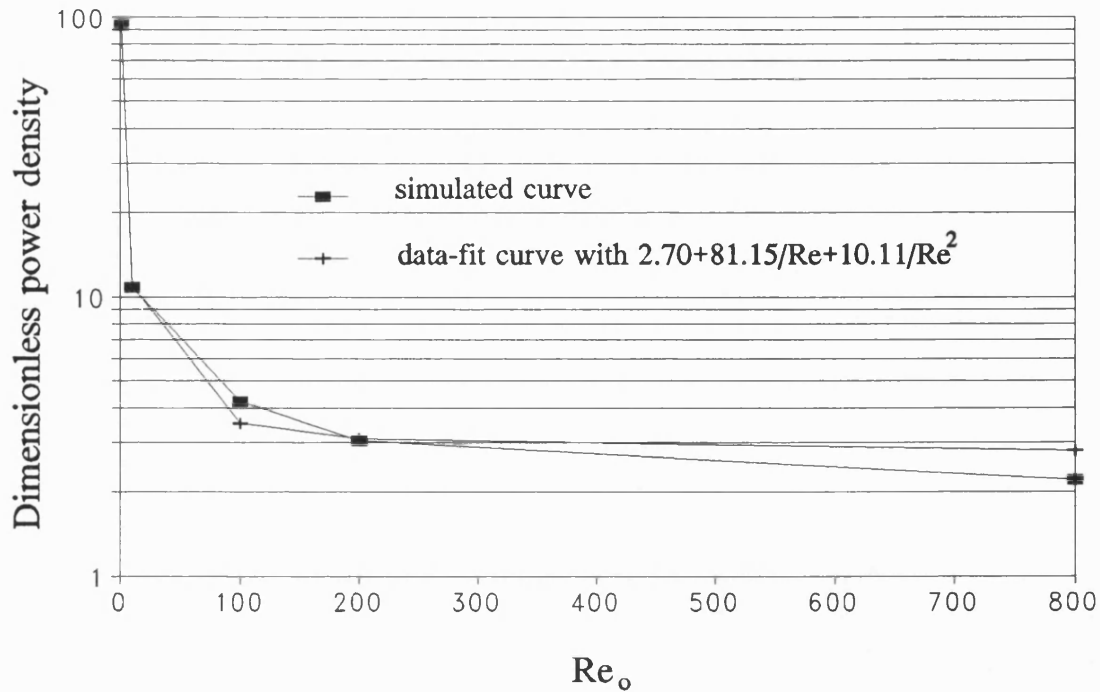
Figure 100 Influence of Re_o with $\beta=0.4$, $\lambda=1.5$ and St=1 for rectangular channel module

The power density results for rectangular channel are presented in Figure 100 and Figure 101. In Figure 100 PD is given together with the data fit curve as a function of oscillatory Reynolds number at a fixed Strouhal number, $St = 1$. It displays a similar phenomenon to that in tubular channel Figure 95. The second degree polynomial data fit is

$$PD = 2.70 + \frac{81.15}{Re_o} + \frac{10.11}{Re_o^2} \tag{64}$$

with coefficient determination 0.9999. Incorporating the above with equation (60) shows that the dimensional power density variation follows a power law of order between 2 and 3 in the shown Re_o range.
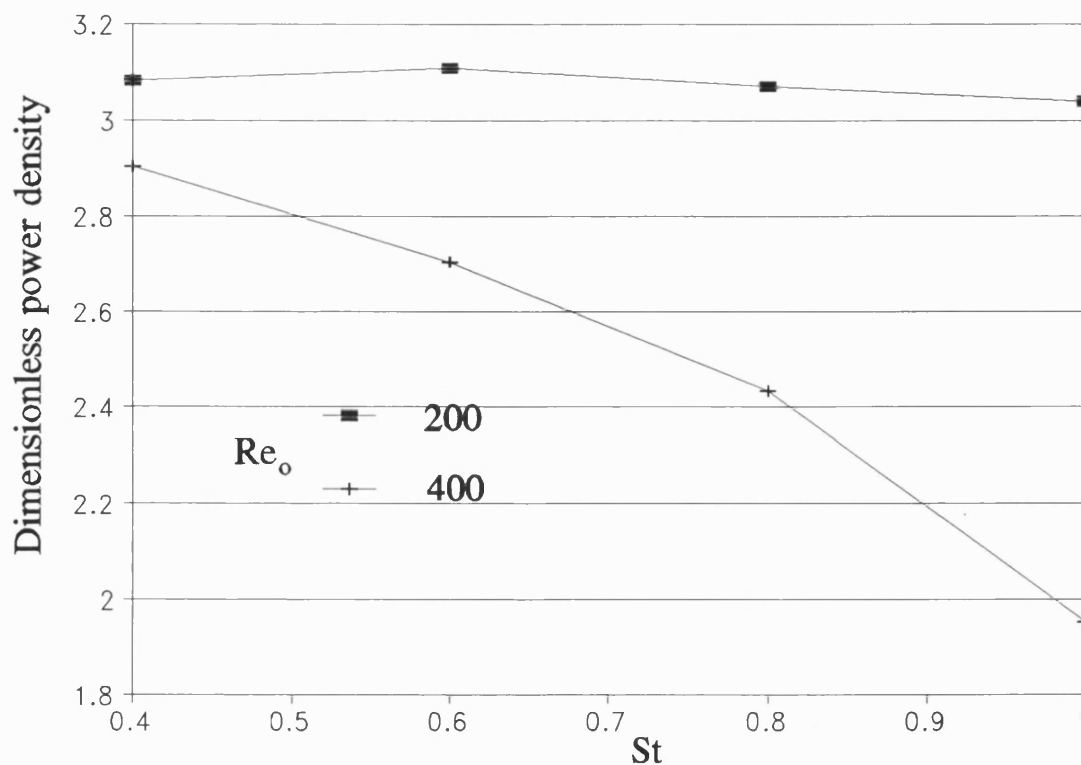
Figure 101 Influence of St with $\beta=0.4$, $\lambda=1.5$ and $Re_o=200$ – 400 for rectangular channel module

Figure 101 gives data as a function of Strouhal number at a fixed oscillatory Reynolds number $Re_o=200$ and $Re_o=400$. The dependency on St is less straight forward. At $Re_o=200$ PD is more or less constant while at $Re_o=400$ it is a monotonically decreasing function of St. Curiously this appears to be different from a wall baffled tubular module where PD is a monotonically increasing function of St.

5.2.2 Discussion

The power consumption can also be calculated by the following method using the maximum differential pressure drop $\Delta \overline{P_0}$ and the phase angle between the velocity and pressure signal θ. For oscillatory motion the forcing displacement and corresponding velocity is given by

$$x = x_0 \cos \omega t, \qquad \dot{x} = x_0 \omega \sin \omega t \qquad (65)$$

The pressure drop response $\Delta \overline{P}$ will also approximate to a sinusoidal signal for St > 1 given by,

$$\Delta \overline{P} = \Delta \overline{P_0} \sin(\omega t + \theta), \qquad (66)$$

By substituting equation (66) into equation (57) this yields

$$\overline{PD} = \frac{1}{2} \frac{\Delta \overline{P_0} \, \omega \, \overline{x_0} \cos \theta}{L}, \qquad (67)$$

where L is the length of tube. Equation (67) is useful for evaluating the power consumption experimentally by only determining ΔP_0 and θ. In this work equation (57) was used, this is always accurate regardless of the non-sinusoidal signal of the pressure drop.

One explanation is put forward to explain the dependency of critical point Re^* on the physical properties and the geometrical parameters. As shown by curve fitting results in Figure 97 the dimensionless power density is related to Re in a form of $a + b/Re$. Incorporating with equation (60) this yields that the dimensional power density $\overline{PD}$ variation follows a power law of order between 2 and 3 as $Re^2(c_1 Re + c_2)$. Here a, b, c_1 and c_2 are the physical properties and geometrical parameters related constants. In some Re range c_2 dominates $c_1 Re + c_2$ and thus $\overline{PD} \sim Re^2$, and in some other Re range c_1 dominates $c_1 Re + c_2$ and thus $\overline{PD} \sim Re^3$. Therefore this critical point of Re is dependent on c_1 and c_2 and thus dependent on ρ, μ, L and D and could be calculated individually by analyzing formula $Re(c_1 Re + c_2)$. As shown in Figure 94 the critical point of $\omega x_0 D$ is 10^{-5} m^2/s, and thus Re^* appears equal to 20.5, 235 and 10 for fluid A, fluid B and water respectively.

The relationship between power consumption and membrane flux will be further explored in the next chapter on membrane flux enhancement.

CHAPTER 6

MEMBRANE FLUX ENHANCEMENT

Concentration polarization and fouling are the major bottleneck limiting more extensive large scale industrial implementation of membrane technology. One of the common approaches taken to combat concentration polarization and fouling is to improve the hydrodynamic conditions at the membrane surface thereby reducing the concentration build-up at the wall. This is achieved most simply by operating with turbulent cross-flow or by modification of the channel geometry. The performance can, for ultrafiltration (Finnigan et al. 1989) and microfiltration (Howell et al. 1992b), also be improved by using pulsatile flow in baffled systems.

The novelty of the work in this chapter is the inclusion of the effects of concentration polarization in a rigorous mathematical simulation of pulsatile membrane filtration. The analysis will be limited to a tubular system and a rectangular system with the baffle arrangements shown in the Figure 3 and Figure 4 in Chapter 2. The fluid mechanics model is in the form of a vorticity-stream function as developed in Section 2.1.3 and an assumption of axial symmetry for tubular system is implicit. The Reynolds number for a tubular system is limited to 200 because the flow is no longer axial symmetric above this

value and for a rectangular system is limited to 800. The numerical simulation converges with difficulty for Reynolds numbers above these levels (requiring very small time steps). Asymmetry above these limits was discovered experimentally for wall baffles (Howes 1988) and for central baffles (Mackay 1991) in tubular system.

The model presented consists of two parts. The first part is a Navier-Stokes solver which generates the flow field, shear rate and pressure gradients. The second part is a polarisation and osmotic model for calculating boundary concentration and flux which uses the output data from the first part of the model as input data to evaluate the mass-transfer coefficient using a standard correlation (Porter 1972). Modelling in two steps does not need an excessive amount of computing time. Moreover it overcomes the difficulty of using a moving boundary condition when solving the Navier-Stokes equations with periodic conditions in the axial direction. It is shown that the existence of realistic wall fluxes does not alter the bulk flow fields in Section 3.1.2 and 3.2.2. This justifies the use of two consecutive steps.

6.1 Introduction

As the flow proceeds downstream, permeate flux occurs through the boundary wall owing to the transmembrane pressure drop which is the pressure difference between retentate and the filtrate side of the membrane. This permeate flux transports solutes or particles normal to the axial flow and causes a concentration increase along the wall. For particle suspensions it leads to the build-up of a deposit layer at the wall where a dense packing of the particles is

achieved. The high concentration layer on the membrane surface acts as a secondary membrane offering added resistance to flow across the wall. For soluble components a locally high wall concentration occurs which may have an osmotic pressure of the same order of magnitude as the applied pressure reducing flux. This results in flux decline which is a time-dependent phenomenon characteristic of all porous cross flow membrane filtration. The intense mixing generated by pulsatile flow in baffled systems limits the osmotic pressure and the thickness of any secondary membrane layers. Hence the degree of flux decline is ameliorated.

6.2 Problem formulation

The difficulty with this particular problem is that even with the transformation $s = r^2$ the region very close to the wall is not easy to include in the solution if it is to be completed on a reasonable time scale. Even the simplified Navier Stokes equations in a periodically baffled channel under periodic flow take considerable computation. The concentration boundary layer for liquid permeation lies very close to the membrane surface as the Schmidt number is large ($\sim 10^5$). Fortunately we have shown in the foregoing Chapter 3 that the wall suction at levels realistic for membrane permeation does not distort the macroscopic flow field. No distortion was observed with 1% of the flow going through the wall in a length of one tube diameter (Howell et al.1992a). Membrane flux is typically 15% in a length > 250 tube diameters (i.e. < 0.1% for a length of one tube diameter).

The above observation allow us to store the results of the flow field calculation and then solve the membrane permeation problem locally. We define a local mass transfer coefficient k'. Assuming complete rejection by the membrane, transport equation for convection of solute to the membrane surface, where C_w and C_b are the wall surface and bulk solute concentrations respectively, can be written as:

$$C_w = C_b \exp(J/k')$$ (68)

where J is the local flux. If we assume that the solute is a macromolecule it is now considered that the build up of osmotic pressure(Π) close to the surface limits flux and a form of Darcy's Law can be written.

$$J = \frac{\Delta P'_{TM} - \Pi}{R_m + R_f}$$ (69)

where R_m is the membrane resistance

R_f the resistance of any fouling layer (assumed zero here)

$\Delta P'_{TM}$ the local transmembrane pressure

The osmotic pressure may be expressed in terms of C_w as

$$\Pi(C_w) = a_1 C_w + a_2 C_w^2 + a_3 C_w^3$$

The assumptions retained here are those of Clifton et al. (1984).

Having associated equations (68) and (69) together, we are able to predict membrane J and boundary concentration C_w at any point along the membrane

surface provided transmembrane pressure $\Delta P'_{TM}$ and mass transfer coefficient k'

are given. This is done by solving the following nonlinear equation using a

Newton-Raphson algorithm.

$$R_m k' \ln(C_w) + a_1 C_w + a_2 C_w^2 + a_3 C_w^3 - \Delta P'_{TM} - R_m k' \ln(C_b) = 0 \qquad (70)$$

Values of $\Delta P'_{TM}$ can be obtained through the use of equation (37) or (38) in

Chapter 2 because:

$$\Delta P'_{TM} = P_{inlet} + \frac{\Delta P}{2} \qquad (71)$$

The local mass transfer coefficient is assumed to be given by a combination

of local fluid dynamic and physical properties. Traditional correlations give the

Sherwood Number as a function of the Reynolds Number but this has little

meaning in a local sense where flow is changing rapidly in space and time. The

tubular Lèvêque equation was converted to a form where the velocity was

expressed by the wall shear rate. This is then used to give the value of k' using

the previously computed flow field to give wall shear rates. For pipe flow with

closed walls this leads to (Porter 1972)

$$k' = 0.816 \left(\frac{\dot{\gamma}}{L} D^2 \right)^{0.33} \qquad (72)$$

6.3 Results

6.3.1 Summary

Membrane filtration, for a baffled tubular system and a baffled rectangular system, has been rigorously simulated for Reynolds numbers up to 200 for tube and 800 for rectangular channel respectively by using baffles alone and in combination with pulsed flow. Concentration polarization effects have been included. Wall and central baffles with and without the addition of pulsations are the four cases considered for tubular channel, and with and without the addition of pulsations are the two cases for rectangular channel. The numerical simulation generates the flow field by solving the time-dependent Navier-Stokes equations. Then the local flux, pressure and the wall concentration along the membrane are calculated by mass balances and an osmotic pressure model using the pre-generated flow field and a relationship between the mass transfer coefficient and the shear stress. The absolute values of flux are higher for the central baffles. Comparisons between the different geometrical arrangements and hydrodynamic conditions are drawn on a flux and power density basis. The addition of pulsations improved the fluxes, the relative improvement being greater for the wall baffles.

6.3.2 Boundary concentration and membrane flux

We start with the comparison on dimensionless shear rate, and thus mass transfer coefficient k' between the analytical solutions and the numerical simulated results to check the accuracy of the numerical simulation. For a

Newtonian fluid in a long horizontal pipe with steady flow the wall shear stress is:

$$\tau_0 = \frac{8\mu U_{av}}{d} \qquad (73)$$

Therefore the dimensionless shear rate for steady flow in an unbaffled tube:

$$\dot{\gamma} = \bar{\dot{\gamma}}\frac{R}{Uav} = 4 , \qquad (74)$$

The simulated dimensionless shear rate results for steady flow in an unbaffled tube are given in the following table:

Table XIII Simulated dimensionless shear rate
results for steady flow in no baffle tube

Simulation parameters	Re		Calculating method	The relative error(%)	
	100	200		Re = 100	Re = 200
Tstop[1] = 10	3.971	4.1	direct[3]	0.7	2.5
$\Delta t^2 = 0.001$	4.018	4.168	using ω[4]	0.5	4.2
Tstop = 5	4.1	4.55	direct	2.5	13.7
$\Delta t = 0.005$	4.16	4.67	using ω	4.0	16.7
Tstop = 15	3.962	3.997	direct	0.9	0.07
$\Delta t = 0.005$	4.013	4.0537	using ω	0.3	1.3

[1] The dimensionless time used for the establishment of complete development of the flow.

[2] The size of time step.

[3] Using direct difference referring to Section 4.2 Equation 2.

[4] Using vorticity variable ω referring to Section 4.2 Equation 3.

The results show the relative errors increasing with the Re probably because flow symmetry breaking occurs when Re approaches 200. Nevertheless these errors (< 5%) are acceptable when $\Delta t = 0.005$ and Tstop = 10 which were used throughout this chapter except when St is small.

In this chapter, all the calculation were made at the conditions shown in Table XIV (unless otherwise stated).

Table XIV Values of physical property used in simulation

concentrations of whey protein	C_b (kg/kg)	0.001
osmotic virial coefficient[+]	a_1	$4.4*10^5$
	a_2	$-1.7*10^5$
	a_3	$7.9*10^5$
diffusivity[#]	D (m$_2$/s)	$7*10^{-11}$
membrane resistance	R_m (Pa.s/m)	$5.8*10^9$
viscosity of bulk solution	μ (Pa.s)	0.001
density of bulk solution	ρ (kg/m^3)	1000
inlet pressure	P_{inlet} (bar)	1.0
baffle flow area ratio	β (-)	0.4
baffle spacing	L (m)	0.03
tube radius	r (m)	0.01
Strouhal number	St	0.1, 1

[+] Turker et al. (1987)

[#] Aimar et al. (1989)
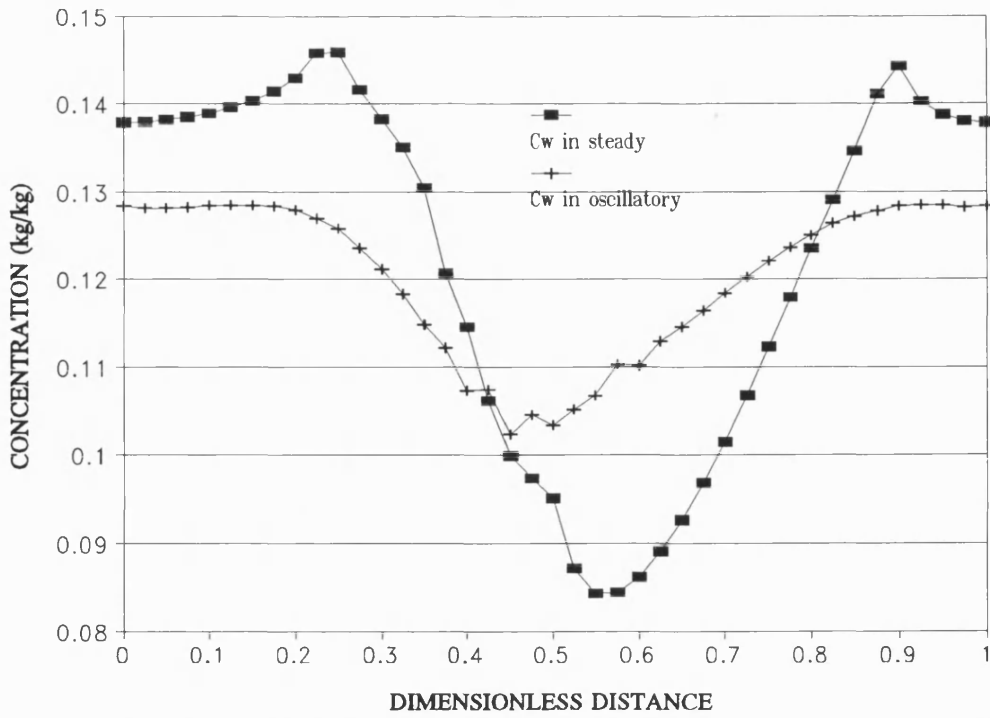
Figure 102 Comparison between steady and oscillatory on C_w for Re=200, St=0.1 in central baffle tubular module.
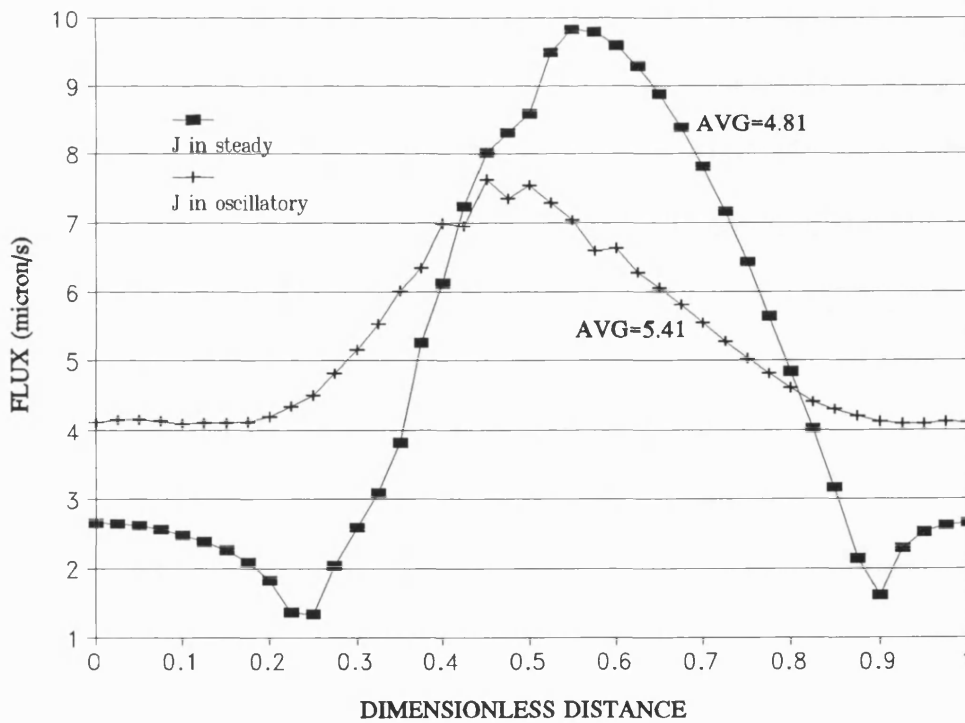
Figure 103 Comparison between steady and oscillatory on J for Re=200, St=0.1 in central baffle tubular module.

-177-
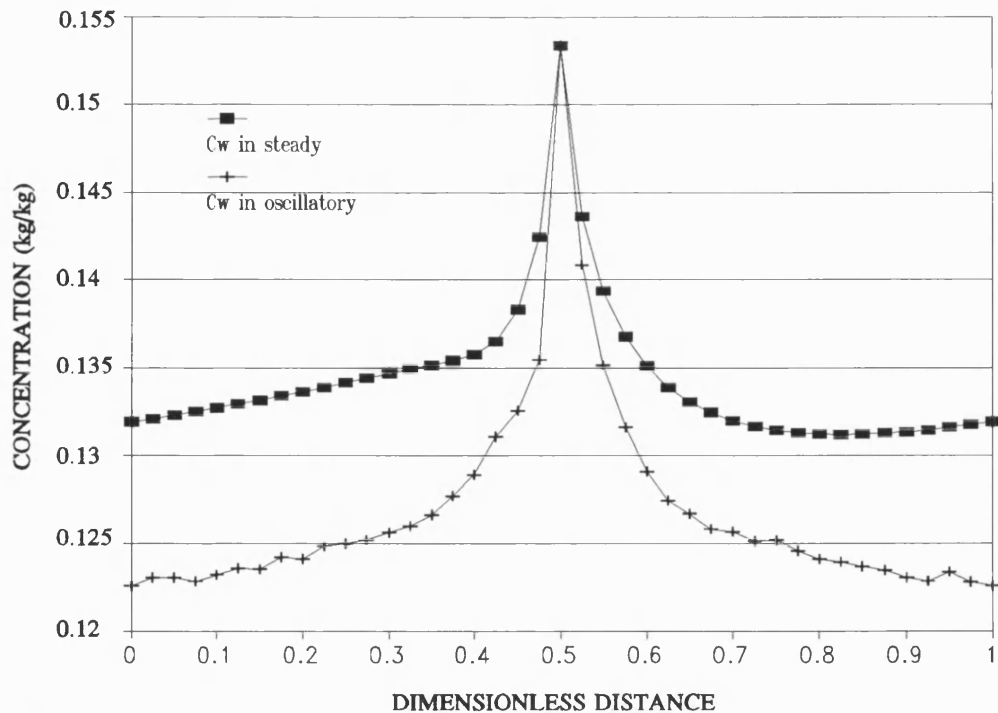
Figure 104 Comparison between steady and oscillatory on C_w for Re=200, St=0.1 in wall baffle tubular module.
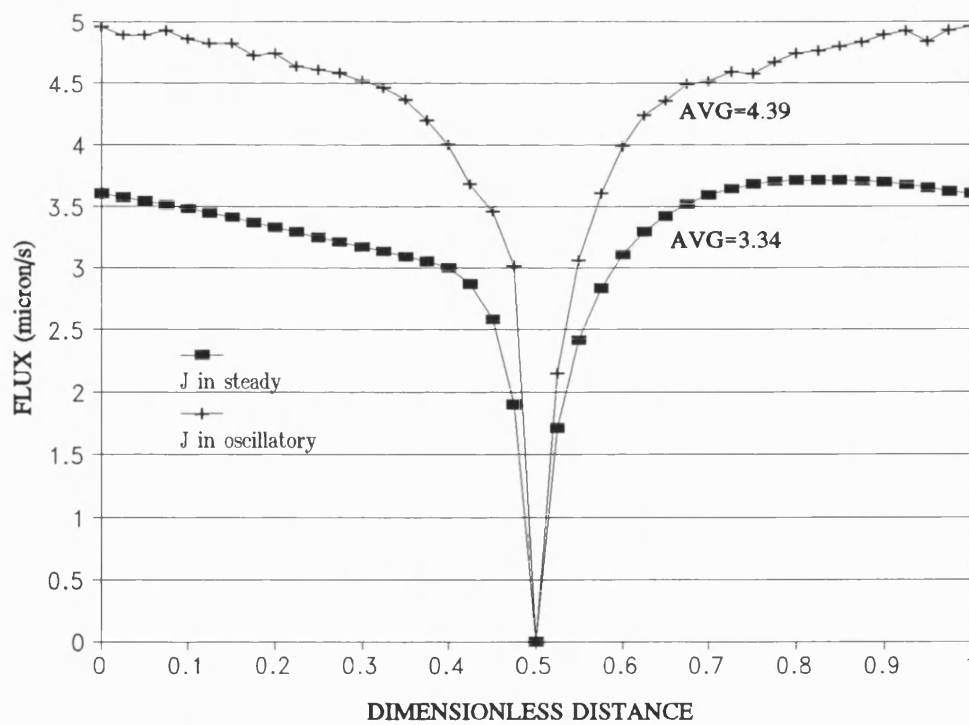
Figure 105 Comparison between steady and oscillatory on J for Re=200, St=0.1 in wall baffle tubular module.
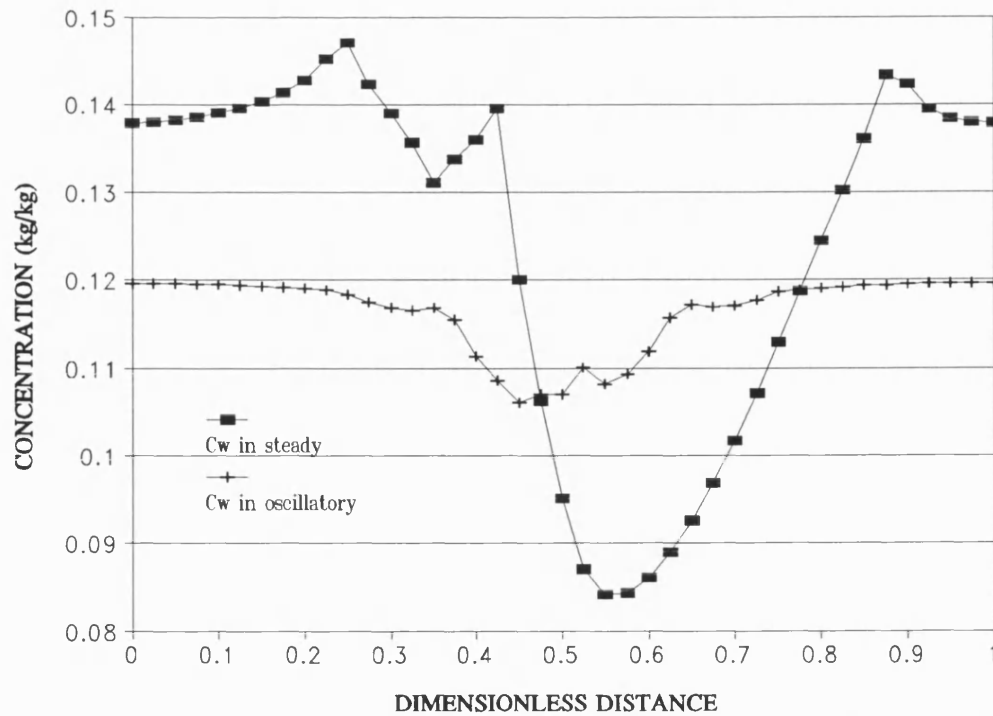
Figure 106 Comparison between steady and oscillatory on C_w for Re=200, St=1 in central baffle tubular module.
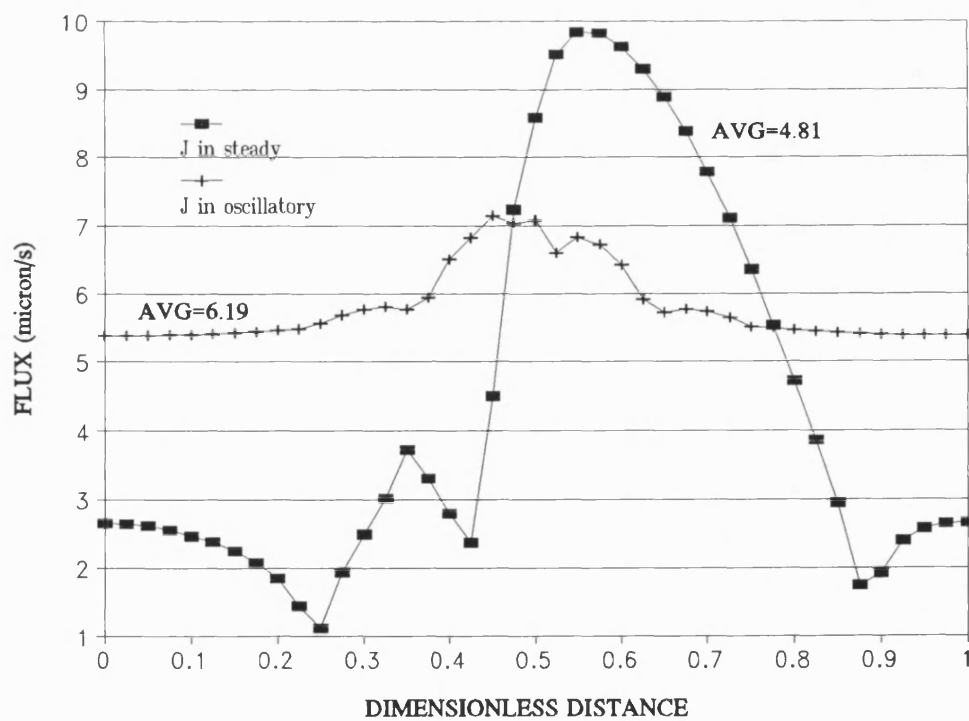
Figure 107 Comparison between steady and oscillatory on J for Re=200, St=1 in central baffle tubular module.
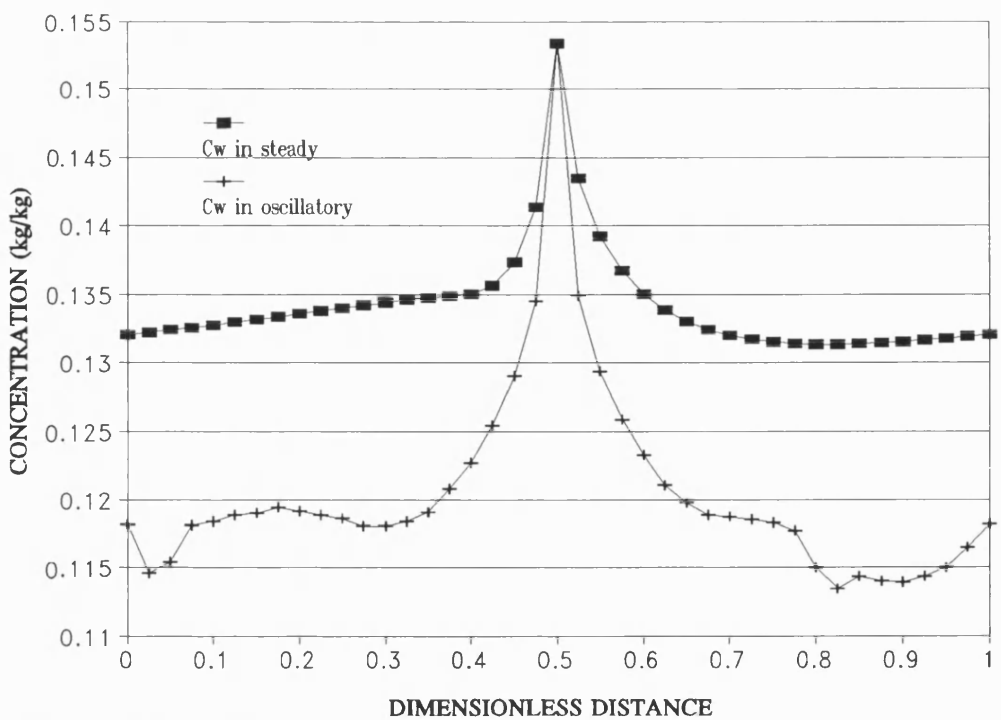
Figure 108 Comparison between steady and oscillatory on C_w for Re=200, St=1 in wall baffle tubular module.
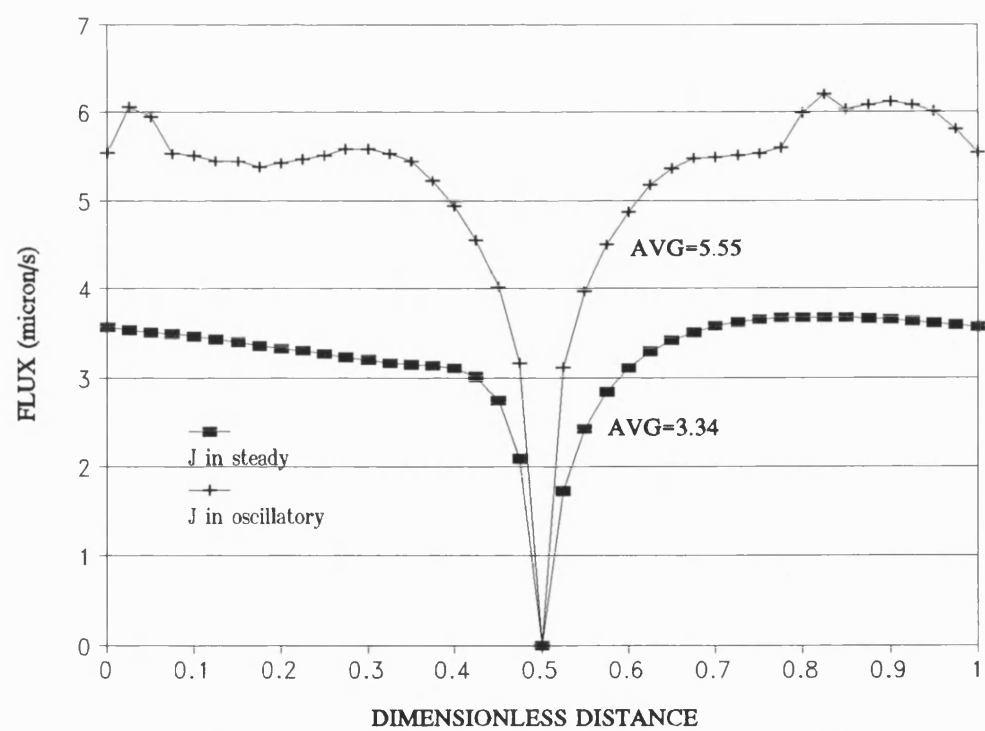
Figure 109 Comparison between steady and oscillatory on J for Re=200, St=1 in wall baffle tubular module.
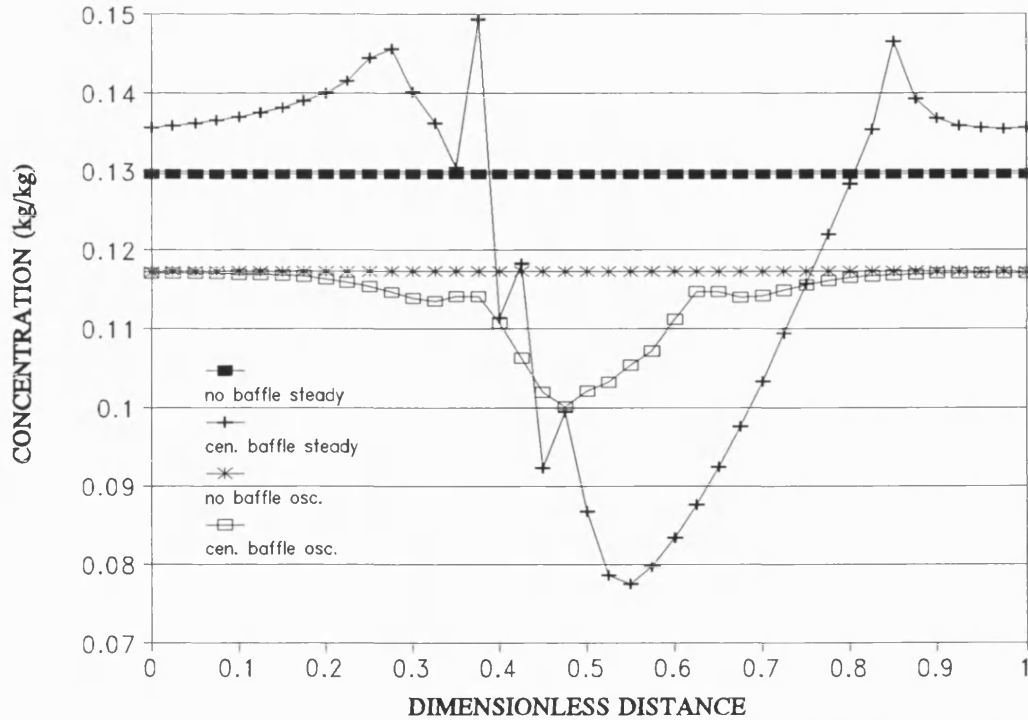
Figure 110 Comparison between conventional tubular system and centrally baffled tubular system on C_w for Re=200, St=1.
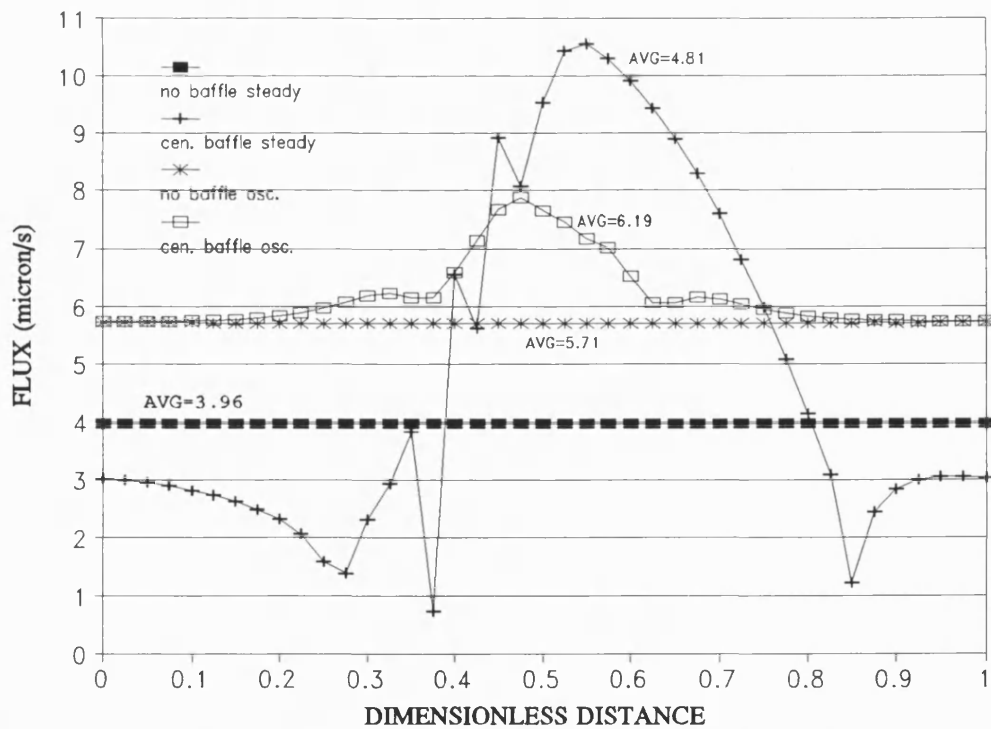
Figure 111 Comparison between conventional tubular system and centrally baffled tubular system on J for Re=200, St=1.
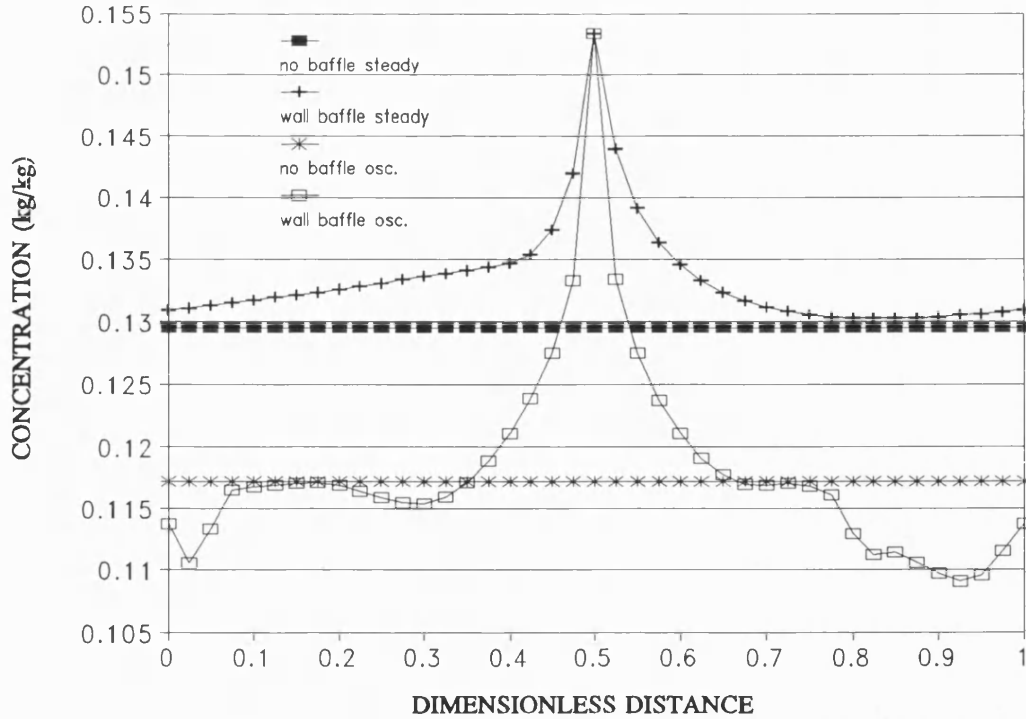
Figure 112 Comparison between conventional tubular system and wall baffled tubular system on C_w for Re=200, St=1.
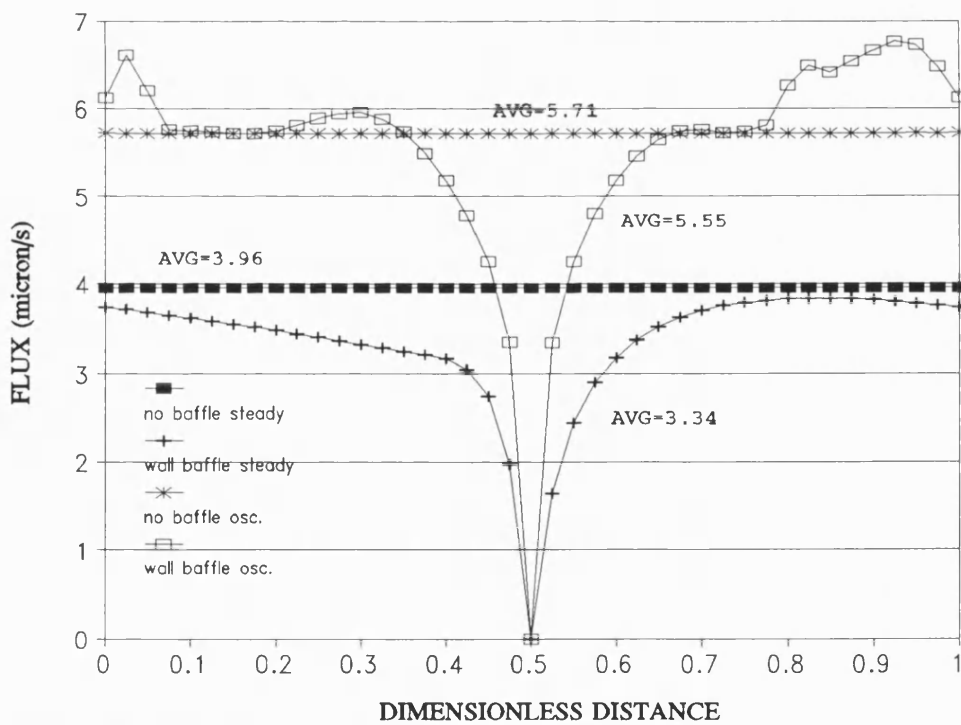
Figure 113 Comparison between conventional tubular system and wall baffled tubular system on J for Re=200, St=1.

Figure 102 - Figure 109 give comparisons between steady and oscillatory flow for the boundary concentration C_w and membrane flux J averaged over one cycle time in a tubular module. Figure 110 - Figure 113 give comparisons between conventional tubular system and baffled tubular system for the boundary concentration C_w and membrane flux J averaged over one cycle time. The twelve figures cover three different geometries and two values of St. The flux enhancement by using oscillatory flow and baffles is summarised in the table below.

Table XV Flux Enhancement (Re = 200 for tube)

Arrangement	Average flux(μm/s)	Flux increase compared with steady flow(%)	Flux increase compared with no baffle(%)
Central baffles			
Steady	4.81	-	21.5
St=0.1	5.41	12.5	28.5
St=1	6.19	29	8.4
Wall baffles			
Steady	3.34	-	-15.7
St=0.1	4.39	31.4	4.3
St=1	5.55	66.2	-2.8
No baffle			
Steady	3.96	-	-
St=0.1	4.21	6.3	-
St=1	5.71	44.2	-
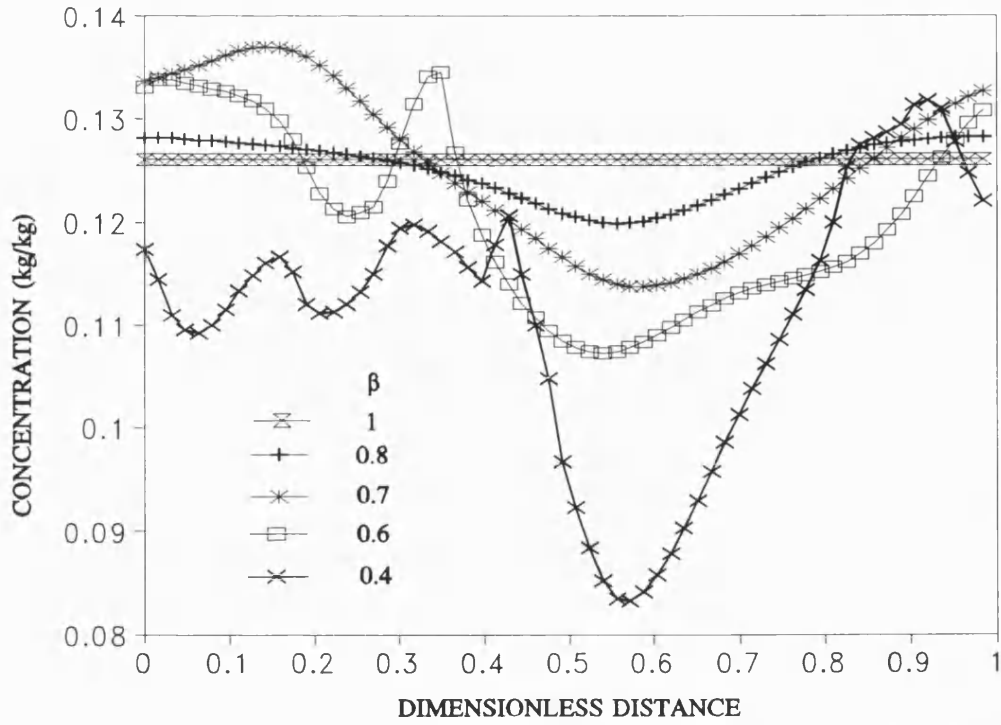
Figure 114 Influence of baffle flow area ratio on C_w for steady flow Re=200 in rectangular module.
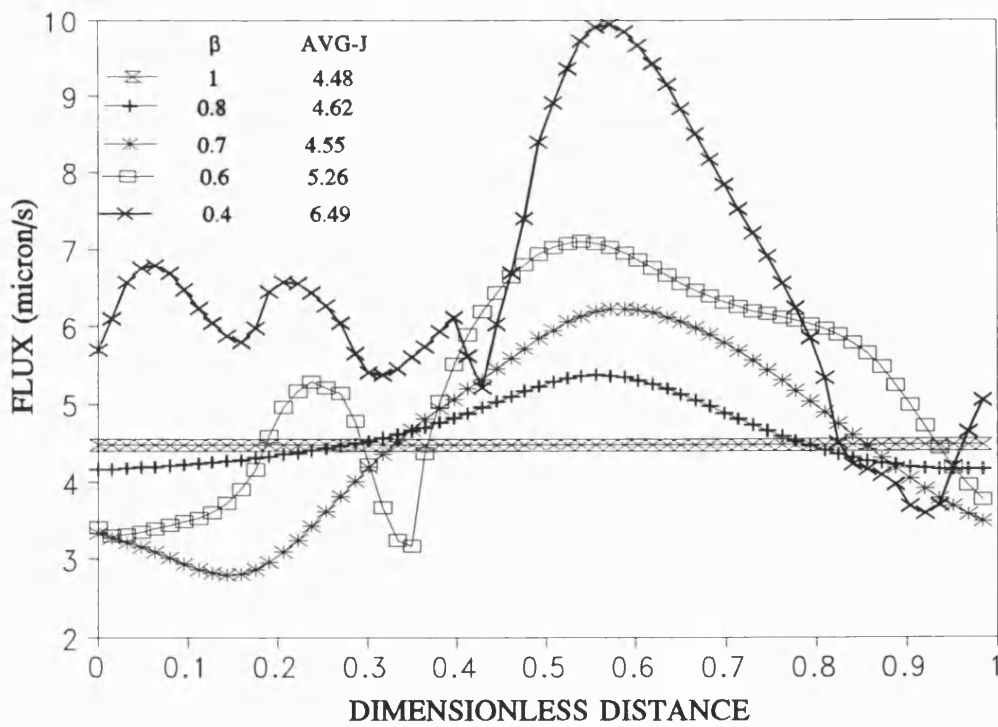
Figure 115 Influence of baffle flow area ratio on J for steady flow Re=200 in rectangular module.
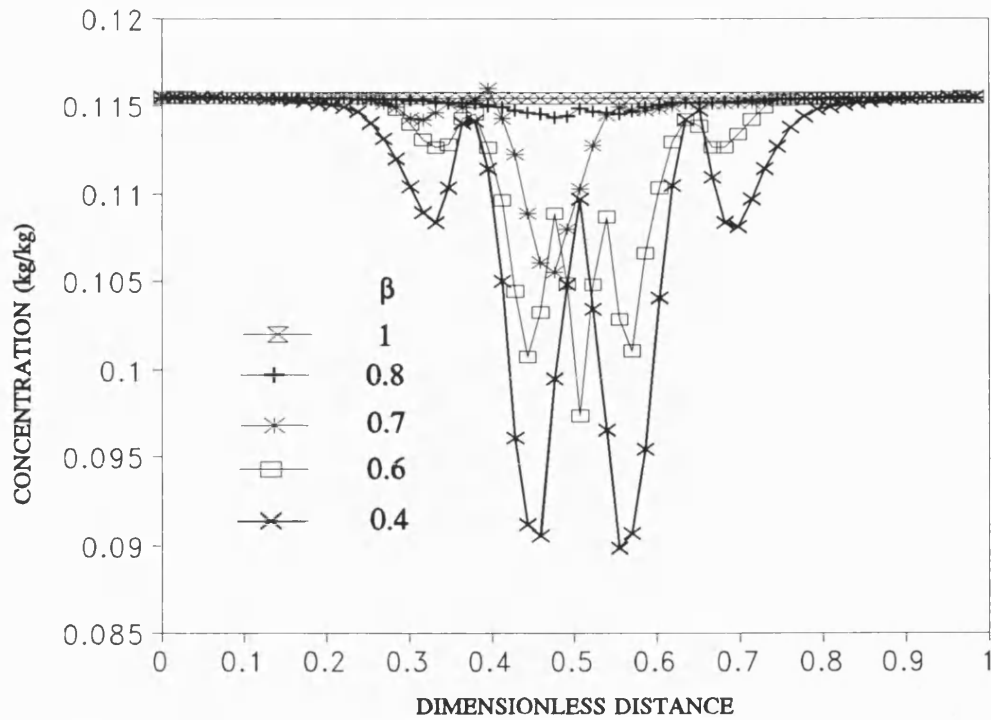
Figure 116 Influence of baffle flow area ratio on C_w for oscillatory flow $Re_o=200$ and $St=1$ in rectangular module.
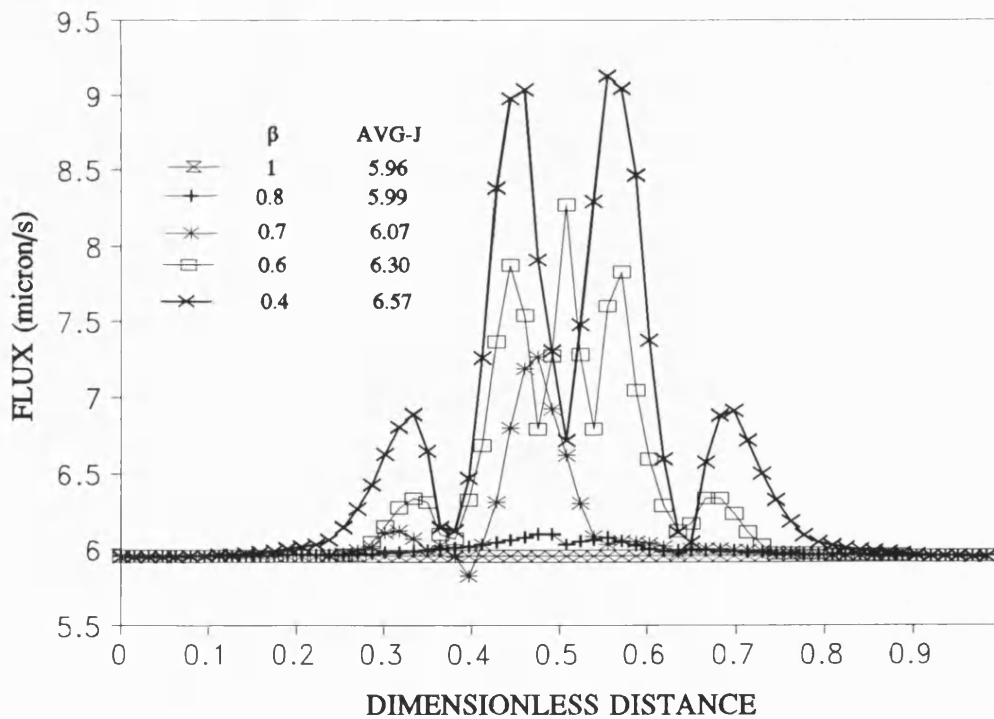
Figure 117 Influence of baffle flow area ratio on J for oscillatory flow $Re_o=200$ and $St=1$ in rectangular module.
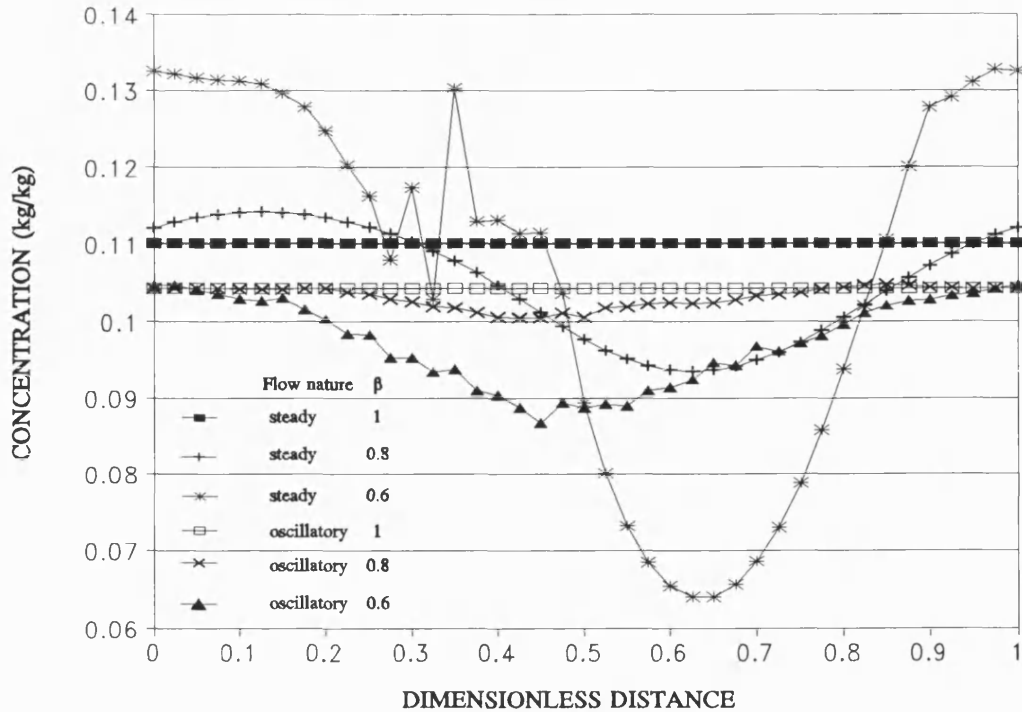
Figure 118 Influence of baffle flow area ratio on C_w for steady flow Re=800 in rectangular module.
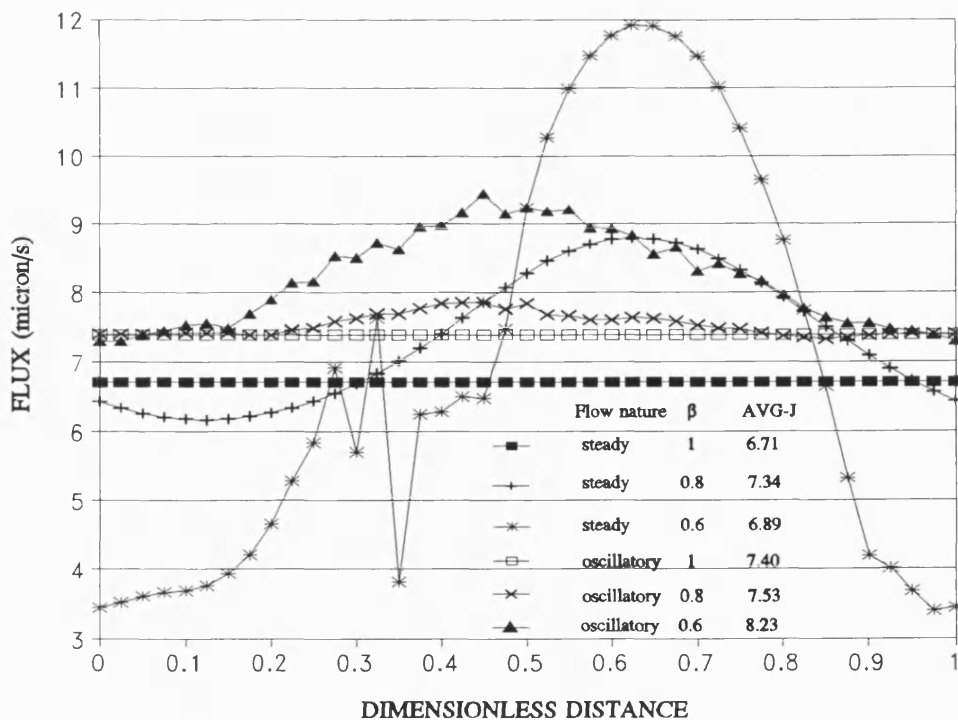
Figure 119 Influence of baffle flow area ratio on J for steady flow Re=800 in rectangular module.
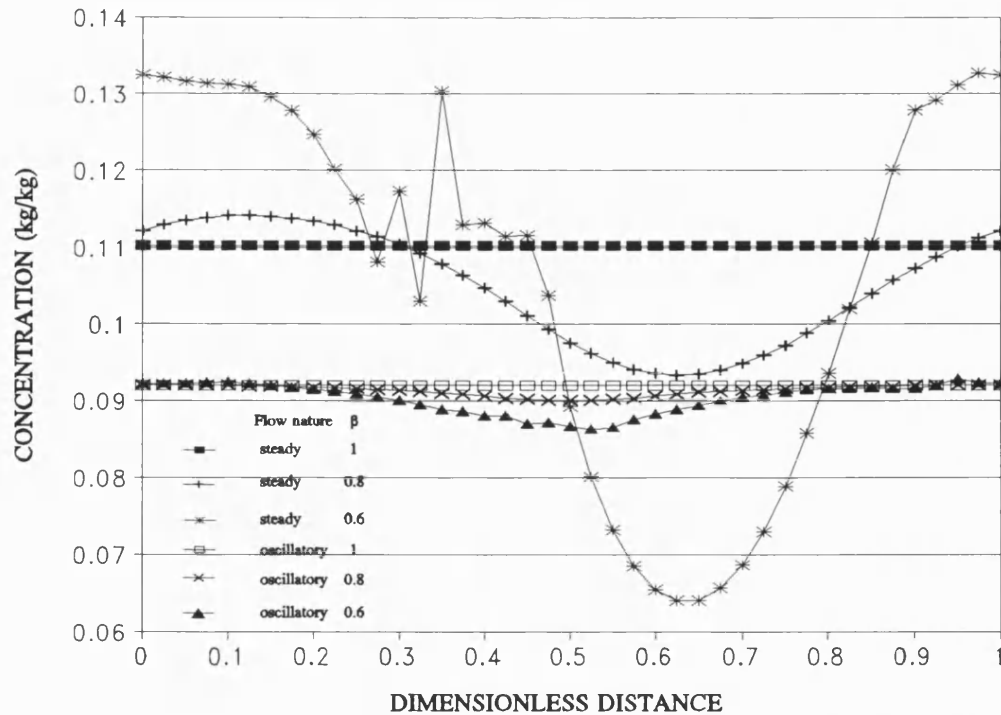
Figure 120 Influence of baffle flow area ratio on C_w for oscillatory flow Re_o=800 and St=1 in rectangular module.
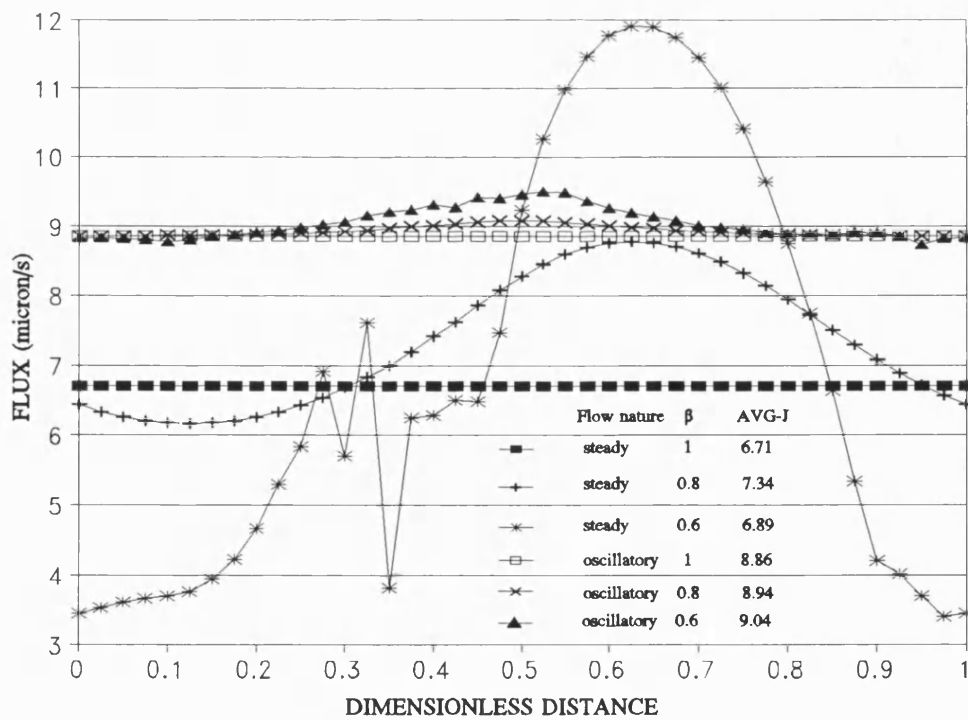
Figure 121 Influence of baffle flow area ratio on J for oscillatory flow Re_o=800 and St=1 in rectangular module.

-187-

Pulsatile flow in a baffled tube produces a complex time dependent eddy pattern (Mackay 1991), which increases fluid mixing near the membrane surface and raises the shear rate and ultimately flux enhancement is achieved. Table XV gives the average fluxes as a function of St. It appears that short strokes (big St) rather than long strokes (small St) is more effective at the same oscillatory Reynolds number. Because Re_o is proportional to the oscillation frequency (f) and displacement (x_0), increasing f means reducing x_0 when Re_o is fixed, quick pulsation is more effective at the same oscillatory Reynolds number. Although the percentage increase due to oscillation was less for the central baffles the absolute fluxes for this system are higher. Thus the central baffle achieves better flux enhancement than the wall baffle and conventional tubular system. This may be due to the existence of a third vortex in central baffle case (Howell et al. 1992a). Furthermore the lower wall concentrations will reduce fouling and hence the overall benefit will in practise be greater than that indicated in Table XV.

The similar comparisons for rectangular module by using baffles alone and in combination with pulsed flow are given in Figure 114 to Figure 121 which cover two values of Re = 200 and 800 with Figure 114, Figure 116, Figure 118 and Figure 120 for boundary concentration and Figure 115, Figure 117, Figure 119 and Figure 121 for membrane flux. The flux enhancement by using oscillatory flow and baffles is shown in Figure 122. In Re=200 even in conventional channel pulsating flow produces flux enhancement which means it is not necessary to incorporate baffles with flow pulsation when Re is at this level. When Re = 800 and St = 0.1 pulsating flow coupled with baffles (β = 0.6) gives the

higher flux enhancement. It has already been found experimentally by Finnigan (1990) that curtain values of frequency and displacement must be exceeded to avoid the formation of semi-stagnant regions and to ensure that vortex mixing occurs.
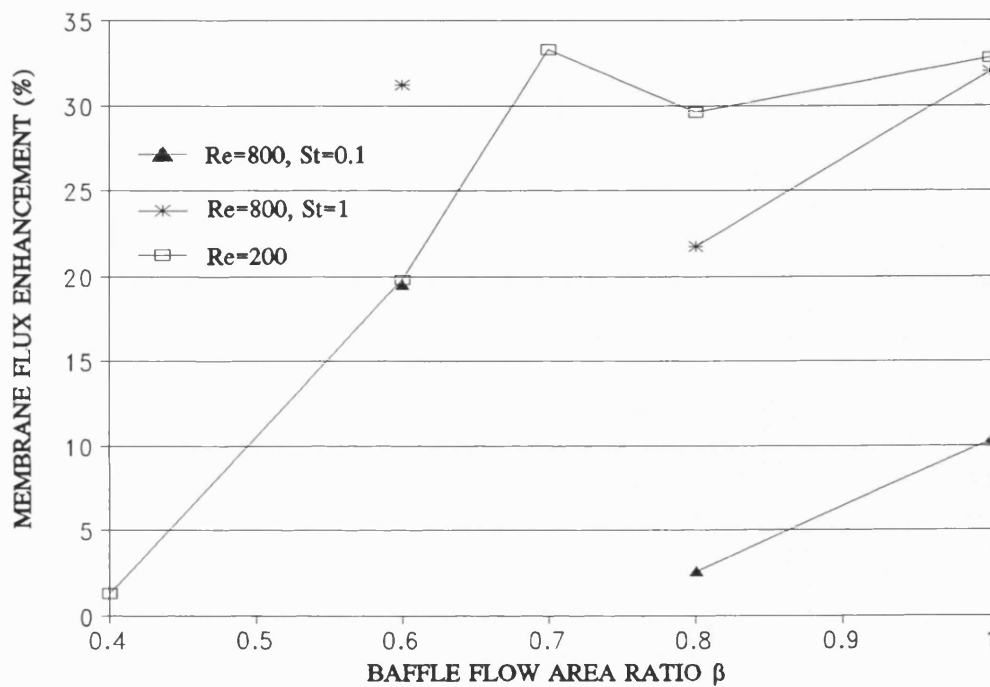
Figure 122 The flux enhancement by using oscillatory flow in various baffle flow area ratio for rectangular module.

As shown in the foregoing Chapter 5 the pressure fluctuation can be significantly out of phase with the flowrate. This phase angle has consequences in terms of power dissipation. The power consumption has been defined in terms of the power dissipated within the membrane module and on a unit volume basis. On a flux per unit energy basis, Figure 123 shows that using the same energy a pulsatile process achieves higher membrane flux. For pulsatile flow with central baffles, the constriction ratio also influences results, in the range studied. Figure 124 compare the membrane flux on per unit energy basis for baffles alone and in combination with pulsed flow which demonstrates that pulsatile flow without any baffle achieves highest membrane flux using the same energy at lower energy consumption level. It appears that at higher flowrate the combination of central baffles with pulsatile flow is superior.
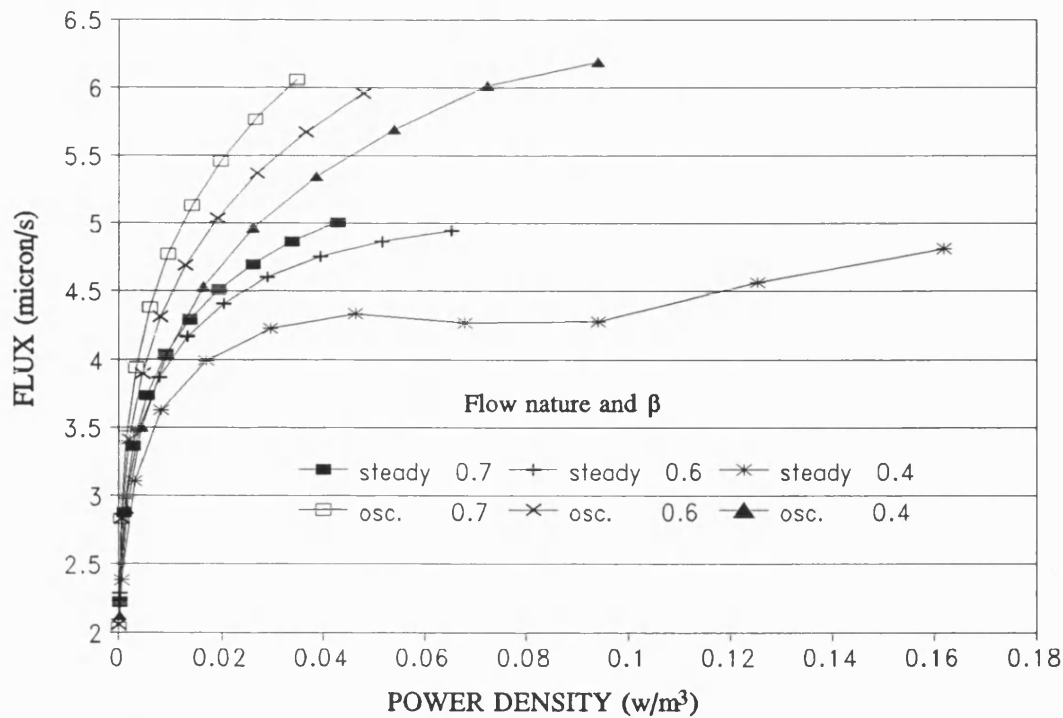
Figure 123 Power vs. flux for central baffle module.
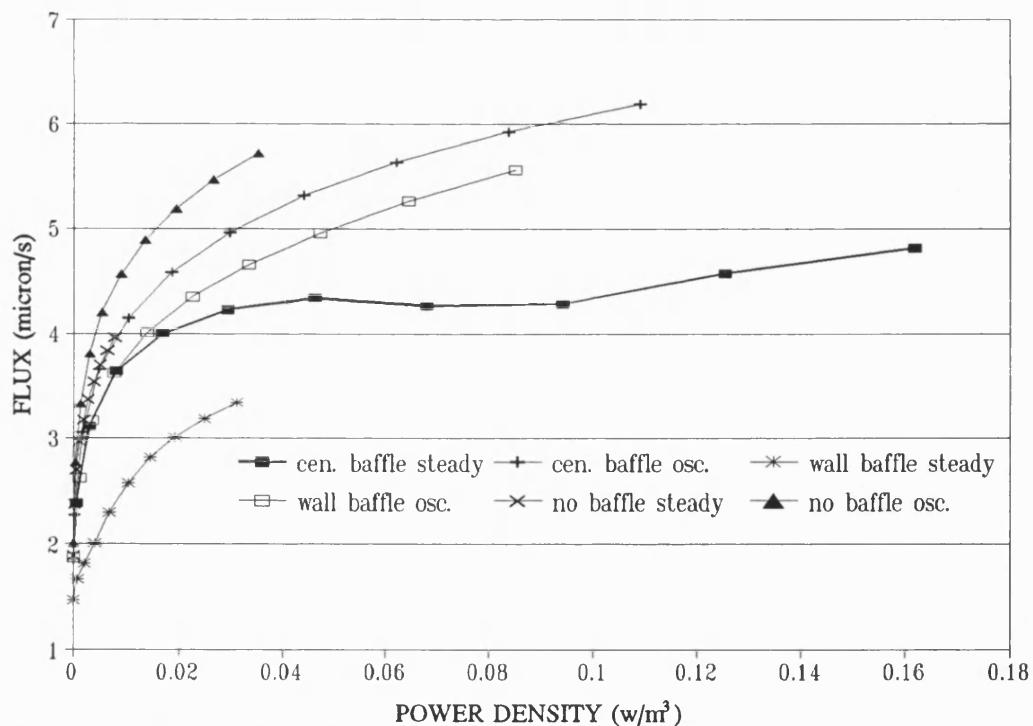
Figure 124 Power vs. flux for all six combination of geometry arrangement and flow nature in tubular module.

As the converted Lèvêque equation shows in equation (72) the local mass transfer coefficient k′ can be assumed to be dependent upon length. Two further different lengths 0.05 and 0.07 (m) were chosen to examine the flux enhancement and the results are shown in Figure 125 and Figure 126; in both cases there was about 40% flux enhancement.
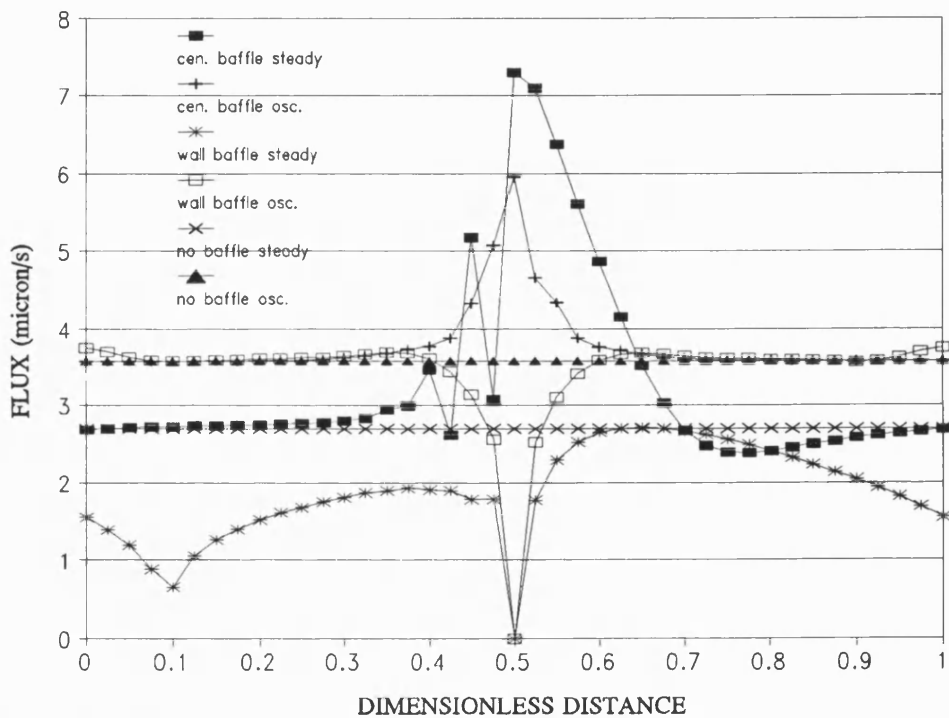
Figure 125 Membrane flux for all six combination of geometry arrangement and flow nature in tubular module λ=2.5.
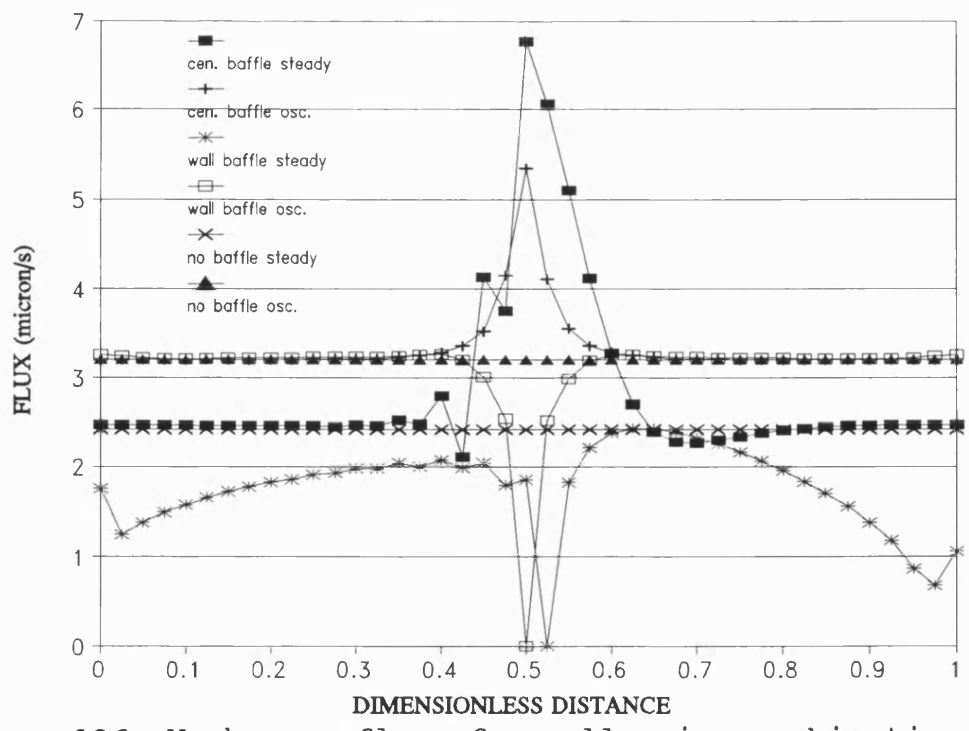
Figure 126 Membrane flux for all six combination of geometry arrangement and flow nature in tubular module $\lambda=3.5$.

6.4 Discussion

A numerical simulation program for the calculation of membrane flux and wall concentrations in pulsatile baffled tubular and rectangular channel systems has been outlined. It is applicable to incompressible Newtonian fluids at flow conditions maintaining axial symmetry for tubular channel and at geometrical conditions maintaining that the channel width is sufficiently great to allow variations in the width coordinate to be neglected for rectangular channel. For these conditions it was found that (a) central baffles are superior to wall baffles

in tubular module and baffles are superior to no baffle for rectangular module at large Re and (b) the addition of pulsations significantly enhanced the fluxes and reduced the wall concentrations for Re greater than 100. (c) Short strokes rather than long strokes and quick pulsation are more effective at the same oscillatory Reynolds number.

Three reasons below could possibly expect the greater flux enhancement than predicted here. (a) the lower wall concentrations will reduce fouling and hence the overall benefit will in practise be greater than that indicated in Table XV because the impact of the fouling has not yet been included in our models. (b) If the condition $Re_o = (\pi/2)Re$ were used for comparison between steady and oscillatory flow performance viz. the same kinetic energy between steady and oscillatory flow rather than $Re_o = Re$ used here, the greater flux enhancement could also be anticipated. (c) The effect of flow motion on mass transfer except through the shear rate is not encompassed yet in this consideration. By incorporating the effect of the particle advection and diffusion (Howell 1992a), the higher flux enhancement could be assumed.

It is not totally accurate to use the converted Lèvêque equation (71) if local viscosity changes as a result of concentration polarisation leading to non-Newtonian rheology close to the wall. This needs to be further investigated.

Lastly it is not difficult to compare the results upon a different power consumption basis such as power per unit membrane surface area $(\overline{PD_s})$ and per

unit permeate volume ($\overline{PD_p}$). For instance in a tubular module

$$\overline{PD}_s = \frac{R}{2} \cdot \overline{PD} \tag{75}$$

$$\overline{PD}_p = \frac{\int_0^T \Delta \overline{P}(t) \, \overline{Q}(t) \, dt}{\text{Filtrate within time period } T \text{ per cell}}$$

$$= \frac{1}{J} \cdot \overline{PD}_s$$

$$= \frac{R}{2J} \cdot \overline{PD} \tag{76}$$

CHAPTER 7

CONCLUDING REMARKS

7.1 Summary and conclusions

An approach is developed using Computational Fluid Dynamics(CFD) for the calculation of flow pattern, shear rate, vortex strength, pressure drop and phase shift, power consumption, particles advection and diffusion and boundary concentration and flux in a permeable channel by using baffles alone and in the combination of pulsatile flow with a group of numerical simulation programs. It is applicable to incompressible Newtonian fluids at flow conditions maintaining axial symmetry for tubular channel and at geometrical conditions maintaining that the channel width is sufficiently great to allow variations in the width coordinate to be neglected for rectangular channel.

Experimental flow visualisation and simulated flow patterns are compared with a reasonable consistency. The comparisons between the analytically calculated and numerically simulated shear rate, pressure drop and power density in the conventional tube with steady flow suggest that the models are not only qualitatively correct but also provide quantitative accuracy.

Flow patterns in a central baffle situation are somewhat different from

those with wall baffles. In the former case the vortex formed behind the baffle intensifies with increasing Reynolds Number but does not fill the entire space between the obstructions, whilst, in the latter case the recirculating region grows to fill the entire baffle space. For central baffles, there is an additional vortex formed near the tube wall when the Reynolds Number reaches about 200. The wall suction at levels realistic for membrane permeation does not distort the macroscopic flow field. No distortion was observed with 1% of the flow going through the wall in a length of the tube diameters. Flow patterns are identified on a Re_o/St diagram for Re_o in the range [5 , 1000] and St in the range [0.1 , 4].

The wall shear rate with central baffles is much higher than that with either wall baffles or without baffle. In steady flow with central baffles, the dimensionless wall shear rate linearly increases as Reynolds number increases whereas with wall baffles and without baffles it stays constant. For unsteady state, the dimensionless wall shear rate in all three cases is a monotonically increasing function of Reynolds number. In a rectangular module the Re_o/St diagram in term of average wall shear rate has shown when $Re_o > 150$ it may have a maximum in the middle of the Strouhal number range at about $St = 0.5$.

The vortex strength at the instant of zero flow is larger for wall baffles than with central baffles at $St = 1$, and greater with central baffles than with wall ones at small St and vice versa at intermediate St. The maximum with respect to Strouhal number exists at about $St = 0.5$ for both tubular and rectangular modules.

There is a phase shift between the pressure and velocity fluctuation which can lead to a significant power consumption reduction for the system. For the case of creeping flow the pressure is in phase with the velocity. As Re_o or St

increases there is a progressive increase in the phase shift for both tubular and rectangular module.

The comparison of power consumption among baffles alone and in the combination of pulsatile flow shows that central baffles uses more energy than wall baffles and illustrates that pulsatile flow uses less energy than steady flow in the central baffles and no baffles case. With wall baffles the curves for steady and oscillatory flow are similar, with the latter being lower, for the greater part of the Re range when St=1. With central baffles an optimum St=0.1 exists for the minimum power density. For the dependency on baffle flow area ratio with central baffles PD increases sharply when baffle area increases while with wall baffles it appears more constant.

By solving the coupled mass balance and osmotic model the local flux and wall concentration are obtained. The illustrative results of flux enhancement up to 66% and less energy consumption support the earlier experimental discovery that ultrafiltration and microfiltration performance can be improved by using pulsatile flow in a baffled membrane system. Central baffles are superior to wall baffles in tubular module and baffles are superior to no baffle in rectangular module at large Re. The addition of pulsations significantly enhanced the fluxes and reduced the wall concentrations for Re greater than 100. When expressed on a power consumption basis, using the same energy a pulsatile process achieves higher membrane flux. At low flowrate pulsatile flow without any baffle provides a better performance because baffled systems were shown to dissipate energy more effectively and at higher flowrate the combination of central baffles with pulsatile flow is the best.

7.2 Other Observations

7.2.1 Particle motion

The use of colour graphics to display the results of a 'moving particle' simulation enables a direct visual image of aspects relating to particle motion, which show that greater mixing can be achieved using wall baffles than central baffles at low Reynolds number while central baffles can also gain good mixing at higher Re_0 with large amplitude of oscillation. In a rectangular module it demonstrates good global mixing with dead spots only at the corner even at medium Re_0.

7.2.2 The nonlinear equation (40) for boundary concentration

The detailed program for solving the nonlinear equation (40) for boundary concentration is listed in appendix 4. Newton-Raphson iterative method was used and proved to converge very quickly. In experimental procedure the same transmembrane pressure $\Delta P'_{TM}$ has to be measured by adjusting the inlet pressure to compare between steady and oscillatory system alone or in combination with baffles. Because the sensitivity to transmembrane pressure $\Delta P'_{TM}$ variation is not high in equation (40) it does not really matter whether we use the individual pressure drop to calculate $\Delta P'_{TM}$ or keep $\Delta P'_{TM}$ same in the numerical simulation.

The equation (40) is highly sensitive to the local mass transfer coefficient k′. The relation between k′ and membrane flux J is linear until J reaches to a certain value and then gradually approaches to a limit as k′ increases further.

7.3 Recommendations

This is not totally accurate if local viscosity changes as a result of concentration polarisation leading to non-Newtonian rheology close to the wall. For a concentration-dependent Newtonian viscosity the Lèvêque equation could be modified with a Sieder-Tade type correction factor for a tubular model:

$$k' = 1.82 \left(\frac{D^2 U_{av}}{Ld} \right)^{1/3} \left(\frac{\mu_B}{\mu_W} \right)^{0.27} \tag{77}$$

For a non-Newtonian flow Pritchard's formula (Pritchard 1992) could be used:

For tubular module

$$k' = \left\{ \frac{3D^2}{4L} \left[\left(\frac{3n_B+1}{4n_B} \right) \left(\frac{8U_{av}}{d} \right) \right]^{\frac{n_B}{n_{bi}}} \right\}^{1/3} \cdot \left\{ \frac{K_B}{K_W} \right\}^{\frac{0.27}{n_{bi}}} \tag{78}$$

For rectangular module

$$k' = \left\{ \frac{3D^2}{4L} \left[\left(\frac{3n_B+1}{4n_B} \right) \left(\frac{2U_{av}}{H} \right) \right]^{\frac{n_B}{n_{bi}}} \right\}^{1/3} \cdot \left\{ \frac{K_B}{K_W} \right\}^{\frac{0.27}{n_{bi}}} \tag{79}$$

Here n and K are the power-law index and power-law consistency index respectively.

The effect of the particle motion may be incorporated within the membrane pulsatile flow filtration simulation by advecting the marked particle

using flow field with equation (19) in Chapter 2 and diffusing it by the random walk procedure using a Monte-Carlo simulation. The inclusion of particle motion could possibly predict the higher flux enhancement by using baffles alone or in combination with the pulsed flow.

The lower wall concentrations will reduce fouling and hence the overall benefit will in practise be greater than that indicated in Chapter 6. Therefore the inclusion of the fouling model would be desirable.

This 2D work is blemished by the restriction to flows with axial symmetric. To understand better high Reynolds number operation or turbulent phenomena and compare it with the experimental membrane system, it is necessary to extend this 2D work to 3D. This series of programmes for simulation of pulsatile flow in baffled permeable channel takes a long execution time because of large flow simulation although a sophisticated multigrid convergence enhancement routine has been carefully used. Some runs need even more than 500 minutes CPU time in our university mainframe GDR (Encore UTX/32) which is equivalent to about one weeks processing time. This problem will be even more serious when modifying 2D code to 3D.

Parallel computing architectures offer greater potential than vectorisation for rapid execution of large flow simulation tasks. Some (reasonably) flexible routines for running a grid-based multigrid code in parallel after the mesh is split up for a number of processors is now available in PPSUN (16 node i860 based Meiko Computing Surface, provided to Bath CFD community by SERC). Equipped with these routines, our pulsatile flow code could be effectively modified to a parallel code.

APPENDIX

Appendix 1. Programs developed in this study

The main programs developed in this research are listed here with some brief description for them in alphabetic order. All the programs are double precision with consistent input and output and are highly portable except for the NAG library called in the streamline, velocity vector field and particle motion plot programs (contour4.f, flat4x5.f, flatpic.f, picture.f and velvect.f). In order to improve flexibility which could make it easier to port the software to a commercial package an attempt was made to use one dimension array declare instead of two or three dimensions, but it took more running time. Every program now has its one dimensional clone leaving open the possibility for incorporation in commercial packages such as PHOENICS, FLUENT, FLOW3D and STAR etc..

CONTOUR4.F

Contour4.f produces a streamline contour map of the flow patterns for two cell format(N4), one cell format(N3) or symmetric format(SN). It reads data from unit 1 which is generated by **wstartn.f, uni.f or wfinish.f** and writes runtime message to unit 3. It will produce the output file in unit 7 in GINO-F SAVDRA file format and may be previewed on a graphics terminal, or plotted on a desk-top plotter using draw, or sent for plotting on the CalComp plotter using plot, or

converted to HPGL (via GINO-F) for subsequent exporting to a general word processor. Here unit.n is equivalent to the file fort.n in the university mainframe GDR. SAVDRA file format is acting as the standard graphics metafile. There different computational regions -- two cell format, one cell format and symmetric format -- are used. The two cell format is for the wall suction case. In the one cell format or the symmetric format the baffle is placed at axial grid node 3 or in the middle.

FLAT.F

This is a Stream Function/Vorticity Rectangular Coordinate Navier-Stokes solver for a periodic geometry with a periodic sharp edge at one edge or in the middle (wall or central baffles) in SN format. The input data is in unit 1 and the program opens this unit to the file ~/input/$* by calling **getarg** routine. The streamline output ~/output/$* is in unit 2 using **flat4x5.f** to plot it. The output pressure drop and full vorticity strength ~/output/pressure/$* is in unit 3 using **pdsolver.f** to obtain power density. The output shear rate and vortex strength ~/output/shear/$* is in unit 4 and pointwise shear rate output near the one to five grid distance from the wall ~/output/sh1 - sh5/$* are in unit 11-15 respectively which can be plotted in three dimensional surface for the details. In this way the huge amount of the input and output data can be well managed

FLAT4X5.F

Flat4x5.f makes a streamline contour map of the flow patterns for flat sheet rig for two cell format (N4) or symmetric format (SN).

Input file: unit 2 which is generated by flat.f or flatuni.f.

Output file: unit 7 in SAVDRA file format.

FLATPIC.F

This is a particle distribution generator using pre-calculated data from flatfini.f (one cell) or fwfinish.f (two cell).

Input file: ~/output/$* (unit 1) for the particle position points

               ~/input/title/$* (unit 4) for the plot title

Output file: unit 7 in SAVDRA file format.

FLATUNI.F

This is a Stream Function/Vorticity Rectangular Coordinate Navier-Stokes solver for a periodic geometry with a periodic sharp edge in one side or in the middle (wall or central baffles) with *open window* at the wall in N4 format.

Input file: ~/input/$* (unit 1)

Output file: ~/output/$* (unit 2) for streamline which can be further plotted by flat4x5.f.

               ~/output/pressure/$* (unit 3) for pressure drop and full vorticity strength

               ~/output/shear/$* (unit 4) for shear rate.

FWFINISH.F

This is a Stream Function/Vorticity Rectangular Coordinate Navier-Stokes solver for a periodic geometry with a periodic sharp edge in one side or in the

middle (wall or central baffles) with *open window* at the wall and *particle movement* in N4 format.

Input file: ~/input/$* (unit 1).

Output file: ~/output/$* (unit 2) for particle image which can be later plotted by flatpic.f.

GEL_OSM.F

This one calculates the C_w and J using the combination of mass balance and osmotic pressure model.

Input file: ~/input/$1 (unit 1) for shear rate,

~/input/$2 (unit 2) for pressure drop, which are generated by wstartn.f or flat.f

Output file: ~/output/$1 for pointwise C_w,

~/output/$2 for pointwise J,

unit 21 for average C_w,

unit 22 for average J.

PDSOLVER.F

This program calculates power density and phase shift by call NAG library.

Input file: unit 1 for pressure drop generated by flat.f or wstartn.f.

Output file: unit 6.

PICTURE.F

This is a particle distribution generator for tubular channels using pre-

calculated data wfinish.f.

Input file: ~/output/$* (unit 1) for the particle position points

              ~/input/title/$* (unit 4) for the plot title

Output file: unit 7 in SAVDRA file format.

UNI.F

This is a Stream Function/Vorticity Cylindrical Coordinate Navier-Stokes

solver for a periodic geometry with a periodic sharp edge in one side or in the

middle (wall or central baffles) with *open window* at the wall in N4 format.

Input file: ~/input/$* (unit 1).

Output file: ~/output/$* (unit 2) for streamline which can be further plotted

by contour4.f,

              ~/output/pressure/$* (unit 3) for pressure drop and full vorticity

strength,

              ~/output/shear/$* (unit 4) for shear rate.

VELVECT.F

This is a velocity field plot program for both cylindrical and rectangular

coordinate module with NAG library calling.

Input file: ~/output/vel,

Output file: unit 7 in SAVDRA file format.

WFINISH.F

This is a Stream Function/Vorticity Cylindrical Coordinate Navier-Stokes

solver for a periodic geometry with a periodic sharp edge in one side or in the middle (wall or central baffles) with *open window* at the wall and *particle movement* in N4 format.

Input file: ~/input/$* (unit 1)

Output file: ~/output/$* (unit 2) for colour particle image plotted by picture.f later on.

WSTARTN.F

This is a Stream Function/Vorticity Cylindrical Coordinate Navier-Stokes solver for a periodic geometry with a periodic sharp edge in one side or in the middle (wall or central baffles) in SN format.

Input file: ~/input/$* (unit 1).

Output file: ~/output/$* (unit 2) for streamline plotted by using flat4x5.f,

              ~/output/pressure/$* (unit 3) for pressure drop,

              ~/output/shear/$* (unit 4) for shear rate and vortex strength.

Appendix 2. Finite-difference Analogue Equations

This appendix details the finite-difference equations used for the program

flat.f as an example to determine

(1)velocities at internal grid points

(2)wall and baffle vorticities

(3)updated vorticity for internal grid points

(4)stream function for internal grid points

(5)stream function boundary and initial condition for wall suction case

The nomenclature used in Appendix is as follows; ψ is the stream-function,

ω is the vorticity and u and v are the axial and transverse velocity respectively.

$\omega_k(i,j)$ refers to the value of vorticity at grid point (i,j) after k time steps. If

subscripts are omitted, then all of the values in that equation are for the same

time steps. Δx and Δy are the grid spacings axially and transversely respectively.

Δt is the time step length. $i=b$ is the axial coordinate of the baffle. $j=w$ is the

channel wall grid point, and $j=e$ is the value of the radial grid point at the sharp

edge. Some of the information given in this appendix is the rectangular channel

variation from the tube version of Howes' (1988).

A2.1 Velocities

Finite difference analogues to equations (12) and (13) are made using

centred differences,

At the channel wall without wall suction and along the baffle, $u=v=0$. However,

$$u(i,j) = \frac{[\psi(i,j+1)-\psi(i,j-1)]}{2\Delta y} \qquad (A2.1)$$

$$v(i,j) = -\frac{[\psi(i+1,j)-\psi(i-1,j)]}{2\Delta x} \qquad (A2.2)$$

At the channel wall without wall suction and along the baffle, u = v = 0. However, at the sharp edge of the baffle, (A2.1) and (A2.2) are used to determine the velocity at that point.

A2.2 Wall vorticity

The wall vorticity is calculated by taking a Taylor expansion of stream function from the wall.

A2.2.1 Channel wall

The channel wall vorticity,

$$\omega = -\frac{\partial^2 \psi}{\partial y^2} - \frac{\partial^2 \psi}{\partial x^2} \Big|_{y=w} \qquad (A2.3)$$

is solved using the Taylor expansion, as $u|_{y=w} = 0$,

$$\omega(i,w) = \frac{\psi(i,w)-\psi(i,w\pm1)}{(\Delta y)^2/2} \qquad i=1 \; or \; N4$$

$$\omega(i,w) = \frac{\psi(i,w)-\psi(i,w\pm1)}{(\Delta y)^2/2} - \frac{\psi(i+1,w)+\psi(i-1,w)-2\psi(i,w)}{(\Delta x)^2} \quad else$$

$$(A2.4)$$

Equation (A2.4) is simplified to (A2.5) when there is no wall suction.

$$\omega(i,w) = \frac{\psi(i,w)-\psi(i,w\pm1)}{(\Delta y)^2/2} \qquad (A2.5)$$

It was found that there is not difference between using a higher order Taylor expansion and the second order as used here.

A2.2.2 Baffle

The vorticity along the baffle, $\omega(b,j)$, is

$$\omega(b,j) = -\partial^2 \psi/\partial x^2 \big|_{y=b}$$

Along the baffle the vorticity has two values depending on which side of the baffle the wall vorticity is required to update the vorticity of internal grid points. Again, by a Taylor expansion,

$$\omega(i,b) = \frac{\psi(b,j) - \psi(b \pm 1,j)}{(\Delta x)^2/2} \qquad (A2.6)$$

At the sharp edge, the vorticity is three-valued. When the vorticity of the two grid points either side of the baffle are updated, the sharp edge vorticity is calculated using (A2.5). For the point directly below or above the baffle, the baffle edge vorticity is calculated by an analogue of equation (17),

$$\omega(b,e) = \frac{\psi(b,e) - \psi(b,e \pm 1)}{(\Delta y)^2/2} - \frac{\psi(b+1,e) + \psi(b-1,e) - 2\psi(b,e)}{(\Delta x)^2} \qquad (A2.7)$$

A2.3 Internal point vorticity

The method of Dufort and Frankel is used to determine the finite-difference analogue of the vorticity transport equation. For the viscous terms, the vorticity of the point being updated, $\omega_k(i,j)$, is replaced by the average of the vorticity at $t-\Delta t$ and $t+\Delta t$, $[\omega_{k-1}(i,j) + \omega_{k+1}(i,j)]/2$. The vorticity transport equation becomes

$$\frac{\omega_{k+1}(i,j)-\omega_{k+1}(i,j)}{2\Delta t} = -\frac{1}{St}\left[\frac{u_k(i+1,j)\omega_k(i,j)-u_k(i-1,j)\omega_k(i-1,j)}{2\Delta x}\right.$$

$$\left.+\frac{v_k(i,j+1)\omega_k(i,j+1)-v_k(i,j-1)\omega_k(i,j-1)}{2\Delta y}\right]$$

$$+\frac{1}{Re\cdot St}\left[\frac{\omega_k(i+1,j)+\omega_k(i-1,j)-\omega_{k+1}(i,j)-\omega_{k-1}(i,j)}{\Delta x^2}\right.$$

$$\left.+\frac{\omega_k(i,j+1)+\omega_k(i,j-1)-\omega_{k+1}(i,j)-\omega_{k-1}(i,j)}{\Delta y^2}\right]$$

(A2.8)

Equation (A2.8) is then rearranged so that $\omega_{k+1}(i,j)$ may be determined explicitly.

A2.4 Stream function for internal grid points

The finite-different analogue of (17) using centred differences is

$$-\omega(i,j) = \frac{\psi(i+1,j)-\psi(i-1,j)-2\psi(i,j)}{(\Delta x)^2} + \frac{\psi(i,j+1)-\psi(i,j-1)-2\psi(i,j)}{(\Delta y)^2}$$ (A2.9)

A2.5 Stream function boundary and initial condition for wall suction

A2.5.1 Boundary condition for wall suction

For the wall suction case, a linearly distributed wall stream function is used, the stream function difference at the wall becomes $\Delta\psi=\gamma L_{win}$, here $\gamma=-\partial\psi/\partial x=v_w$ is the dimensionless velocity and L_{win} the dimensionless open window length. The periodic condition is implemented as

$$\psi(N4,j) = \frac{Q - \Delta\psi/2}{Q + \Delta\psi/2}\psi(2 \quad ,j)$$

$$\psi(1 \quad ,j) = \frac{Q + \Delta\psi/2}{Q - \Delta\psi/2}\psi(N4-1,j)$$

(A2.10)

Here Q is the instantaneous flowrate, N4 the grid number for two geometrical cells. Equation A2.10 is consistent with the periodic condition without wall suction.

A2.5.2 Initial condition for wall suction

The steam function initial condition used here is

$$\psi(i,j) = Q(j-1)\Delta y - (Q + \gamma L_{win}/2)(1-(j-1)\Delta y) \text{ for } 1 \leq i \leq i_L - 1$$

$$\psi(i,j) = Q(j-1)\Delta y - (Q + \gamma L_{win}/2 - \gamma(i-i_L)) \quad \text{ for } i_L \leq i \leq i_R$$

$$\psi(i,j) = Q(j-1)\Delta y - (Q - \gamma L_{win}/2)(1-(j-1)\Delta y) \text{ for } i_R \leq i \leq N4$$

Here i_L and i_R are the left and right grid for the open window.

Appendix 3 Source codes list for calculating power density

Two FORTRAN programs are listed for calculating the dimensionless power density and the phase shift from the dimensionless pressure drop. The program appendix 3.1 was developed by using NAG library and was exclusively run in GDR (Bath mainframe). The second programe appendix 3.2 was developed by employing some routines in *numerical recipes* (W.T. Vetterling et al. 1985) and thus can be run in PC.

Appendix 3.1 Code developed by using NAG library

```
      IMPLICIT DOUBLE PRECISION(A-H,O-Z,K)
      PARAMETER(OMEGA=.628318531718D1,A=0.D0,B=1.D0,ERR1=1.D-40,
     1 ERR2=1.D-2,DMU=1.D-3,RO=1.D3,RADIUS=.0125D0,TWOFOUR=24.D0,
     2 NTABLE=201,LW=50000,LIW=LW/8+LW/4+2,N=NTABLE,LCK=N+4,
     3 LWRK=6*N+16,DELTNEW=.0005D0)
      DIMENSION W(LW),IW(LIW),T(NTABLE),X(NTABLE),Z(NTABLE)
      DIMENSION C(LCK),K(LCK),WRK(LWRK),XNEW(2001),ZNEW(2001)
      CHARACTER INPUTDIR*60,OUTPUTDI*60,FNAME*20
      COMMON K,C
      EXTERNAL TLU
      CALL GETARG(1,FNAME)
      INPUTDIR='/USER/GDR/CE/S/CESYW/OUTPUT/PRESSURE/'//FNAME
      OPEN (1,FILE=INPUTDIR)
      PRINT*,'INPUT PLEASE REO AND BTA(=REN/REO)'
      READ(*,*)RE,BTA
      PDCONT=RE*RE*RE*DMU*DMU*DMU/TWOFOUR/RADIUS**4/RO/RO
C========= ZPRESSURE( AT POINT X) ========================
      DO 100
      I=1,NTABLE
      READ(1,*)X(I),Z(I)
100   WRITE(*,*)X(I),Z(I)
C========= FOR STEADY PD , JUST TO FETCH FIRST LINE =====
C    WRITE(*,21)Z(1)
C    STOP
C=========================================================
      DO 101 I=1,NTABLE
101   X(I)=DBLE(I-1)/(NTABLE-1)
C====== E01BAF FOR CALCULATING SPLINE COEFFIENT,STORING IN COMMON====
      CALL E01BAF(N,X,Z,K,C,LCK,WRK,LWRK,IFAIL)
C====== INTERPOLATE ZNEW(2001) FOR PHASELAG ONLY=========
      DO 102 I=1,2001
      XNEW(I)=DELTNEW*DBLE(I-1)
102   ZNEW(I)=TLU(XNEW(I))
C====== FIND MAX ZNEW(XI) AND I ==========================
      ZMAX=ZNEW(1)
      DO 10 I=1,2001
      ZZ=ZNEW(I)
      IF(ZZ.GE.ZMAX)THEN
      ZMAX=ZZ
      IMAX=I
```

```
        ENDIF
10      CONTINUE
        PHASELAG=3.6D2*(.25D0-XNEW(IMAX))
        CALL D01ANF(TLU,A,B,OMEGA,2,ERR1,ERR2,RESULT1
     1  ,ABSERR,W,LW,IW,LIW,IFAIL)
        IFAIL=0
        CALL D01AJF(TLU,A,B,ERR1,ERR2,RESULT2,ABSERR,W
     1  ,LW,IW,LIW,IFAIL)
        RESULT=RESULT1+BTA*RESULT2
C FOR PURE STEADY FLOW
C       RESULT=RESULT2
        PD=RESULT*PDCONT
C       WRITE(*,20)PD,RESULT,PHASELAG,ZMAX
        WRITE(*,21)RESULT,PHASELAG
20      FORMAT(1X,'(REAL,SCALED)POWER DENSITY=',D20.7,2X,D20.7,/,
     1  1X,'PHASELAG=',F10.3,2X,'DEGREE',2X,'MAX=',F10.5
21      FORMAT(1X,F10.4,3X,F8.3)
        END
        FUNCTION TLU(XINTER)
C----------SPLINE INTERPOLATION----------------
C N: THE NUMBER OF THE BASE POINTS
C X(N):INDEPENTENT INPUT
C Y(N):DEPENDENT INPUT
C XINTER:NEM INDEPENDENT POINT TO BE INTERPOLATED
        PARAMETER(N=201,LCK=N+4)
        IMPLICIT DOUBLEPRECISION(A-H,O-Z,K)
        DIMENSION C(LCK),K(LCK)
        COMMON K,C
        CALL E02BBF(LCK,K,C,XINTER,YINTER,IFAIL)
        TLU=YINTER
        RETURN
        END
```

Appendix 3.2 Portable code

```
C INTEGRATION FOR INT (FROM 0 TO 1)PDROP(X)SIN(2PIX)DX
C INPUT DATA: PDROP
C OUTPUT DATA: POWER DENSITY
C ONLY NEED TO CHANGE N IN NEXT LINE WHEN DATA LENGTH CHANGES.
        PARAMETER (N=41)
        IMPLICIT DOUBLE PRECISION(A-H,O-Z)
        DIMENSION XA(N),YA(N)
        CHARACTER INPUTDIR*60,OUTPUTDI*60,FNAME*20
        EXTERNAL FUNC
        DATA ZERO/0.D0/,ONE/1.D0/
        CALL GETARG(1,FNAME)
        INPUTDIR='/USER/GDR/CE/S/CESYW/INPUT/PRESSURE/'//FNAME
        OPEN (1,FILE=INPUTDIR)
        DO 10 I=1,N
        READ(1,*)XA(I),YA(I)
10      XA(I)=DBLE(I-1)/(N-1)
        CALL QROMB(XA,YA,N,FUNC,ZERO,ONE,RESULT)
        WRITE(*,990)RESULT
990     FORMAT(1X,F10.5)
        END
      SUBROUTINE QROMB(XA,YA,N,FUNC,A,B,SS)
      PARAMETER(EPS=1.D-6,JMAX=20,JMAXP=JMAX+1,K=5,KM=4)
      IMPLICIT DOUBLE PRECISION(A-H,O-Z)
      EXTERNAL FUNC
      DIMENSION S(JMAXP),H(JMAXP),XA(1),YA(1)
      H(1)=1.D0
      DO 11 J=1,JMAX
        CALL TRAPZD(XA,YA,N,FUNC,A,B,S(J),J)
        IF (J.GE.K) THEN
          L=J-KM
```

```fortran
          CALL POLINT(H(L),S(L),K,0.D0,SS,DSS)
          IF (ABS(DSS).LT.EPS*ABS(SS)) RETURN
        ENDIF
        S(J+1)=S(J)
        H(J+1)=0.25*H(J)
11    CONTINUE
      PAUSE 'TOO MANY STEPS.'
      END
      SUBROUTINE TRAPZD(XA,YA,N,FUNC,A,B,S,J)
      IMPLICIT DOUBLE PRECISION(A-H,O-Z)
      DIMENSION XA(1),YA(1)
      EXTERNAL FUNC
      IF (J.EQ.1) THEN
          CALL FUNC(XA,YA,N,A,YYA)
          CALL FUNC(XA,YA,N,B,YYB)
          S=0.5*(B-A)*(YYA+YYB)
          IT=1
      ELSE
          TNM=IT
          DEL=(B-A)/TNM
          X=A+0.5*DEL
          SUM=0.D0
          DO 11 JJ=1,IT
          CALL FUNC(XA,YA,N,X,YYX)
            SUM=SUM+YYX
            X=X+DEL
11        CONTINUE
          S=0.5*(S+(B-A)*SUM/TNM)
          IT=2*IT
      ENDIF
      END
      SUBROUTINE POLINT(XA,YA,N,X,Y,DY)
C HERE N=K IN SUBROUTINE QROMB
      IMPLICIT DOUBLE PRECISION(A-H,O-Z)
      PARAMETER (NMAX=10)
      DIMENSION XA(N),YA(N),C(NMAX),D(NMAX)
      NS=1
      DIF=DABS(X-XA(1))
      DO 11 I=1,N
          DIFT=DABS(X-XA(I))
          IF (DIFT.LT.DIF) THEN
            NS=I
            DIF=DIFT
          ENDIF
          C(I)=YA(I)
          D(I)=YA(I)
11    CONTINUE
      Y=YA(NS)
      NS=NS-1
      DO 13 M=1,N-1
          DO 12 I=1,N-M
          HO=XA(I)-X
          HP=XA(I+M)-X
          W=C(I+1)-D(I)
          DEN=HO-HP
          IF(DEN.EQ.0.)PAUSE 'SOMETHING WRONG IN POLINT'
          DEN=W/DEN
          D(I)=HP*DEN
          C(I)=HO*DEN
12        CONTINUE
          IF (2*NS.LT.N-M)THEN
            DY=C(NS+1)
          ELSE
            DY=D(NS)
            NS=NS-1
          ENDIF
```

```
        Y=Y+DY
13    CONTINUE
      END
        SUBROUTINE FUNC(XA,YA,N,X,F)
        IMPLICIT DOUBLE PRECISION(A-H,O-Z)
        DIMENSION XA(1),YA(1)
        DATA OMEGA/.628318531718D1/
C------ IF POLYNOMIAL INTERPOLATION IS EMPLOYED, THE NEXT TWO
C LINES ARE USED TO REPLACE "CALL LOCATE(XA,N,X,J)
C                 F=(YA(J)+YA(J+1))*.5D0*DSIN(OMEGA*X)"
C       CALL POLINT(XA,YA,N,X,F,ERROR)
C       F=F*DSIN(OMEGA*X)
C--------------------------------------------
        CALL LOCATE(XA,N,X,J)
        F=(YA(J)+YA(J+1))*.5D0*DSIN(OMEGA*X)
        END
      SUBROUTINE LOCATE(XX,N,X,J)
      IMPLICIT DOUBLE PRECISION(A-H,O-Z)
      DIMENSION XX(N)
      JL=0
      JU=N+1
10    IF(JU-JL.GT.1)THEN
        JM=(JU+JL)/2
        IF((XX(N).GT.XX(1)).EQV.(X.GT.XX(JM)))THEN
         JL=JM
        ELSE
         JU=JM
        ENDIF
      GO TO 10
      ENDIF
      J=JL
      END
```

Appendix 4

The programe is detailed for calculating membrane concentration and flux

by solving the associated equations of the mass balance and the osmotic pressure

using the dimensionless pressure drop and the dimensionless wall shear rate. This

is developed by employing the Newton-Raphson iterative mothod.

```
C================================================================
C GEL AND OSMOTIC PRESSURE MODEL FOR CALCULATING CW AND J
C INPUT: PRESSURE DROP DP(T) ( THEN TMP=PINLET+DP(T)/2 )
C      WALL SHEAR RATE SH(T,X)
C OUTPUT: CW(T,X),J(T,X)
C INPUT SHEAR UNIT1  GETARG1 ~/INPUT/$1
C      DROPP UNIT2  GETARG2 ~/INPUT/$2
C OUTPUT CW IN UNIT11 ~/OUTPUT/$1 FOR 3D
C      AJ IN UNIT12 ~/OUTPUT/$2 FOR 3D
C      AVG CW IN FORT.21,AVG AJ IN FORT.22,AVG SHEAR IN FORT.23
C================================================================
      IMPLICIT DOUBLE PRECISION(A-H,O-Z)
      PARAMETER (NX=41,NT=40)
      EXTERNAL FUNCD
      DIMENSION DP(NT),SH(NT,NX),CW(NT,NX),AJ(NT,NX),TIME(NT)
      CHARACTER FNAME1*20,FNAME2*20,INPUTDIR*60,OUTPUTDI*60,FNAME3*20,OUTSHEAR*60
      COMMON /USER/RM,AK,A1,A2,A3,CB,TMP
      DATA XACC/1.D-16/,ITERAT/100/,X1/.001/,X2/1./
      DATA PINLET/1.D5/,D/7.D-11/,AL/.03/,R/.01/,AMU/.001/,RO/1.D3/,RE/200./
C================================================================
      A1=4.4D5
      A2=-1.7D5
      A3=7.9D6
      CB=1.D-3
      RM=5.8D9
      CALL GETARG(1,FNAME1)
      INPUTDIR='/USER/GDR/CE/S/CESYW/OUTPUT/SH1/'//FNAME1
      OUTPUTDI='/USER/GDR/CE/S/CESYW/OUTPUT/'//FNAME1
      OPEN (1,FILE=INPUTDIR)
      OPEN (11,FILE=OUTPUTDI)
      CALL GETARG(2,FNAME2)
      INPUTDIR='/USER/GDR/CE/S/CESYW/OUTPUT/PRESSURE/'//FNAME2
      OUTPUTDI='/USER/GDR/CE/S/CESYW/OUTPUT/'//FNAME2
      OPEN (2,FILE=INPUTDIR)
      OPEN (12,FILE=OUTPUTDI)
      CALL GETARG(3,FNAME3)
      INPUTDIR='/USER/GDR/CE/S/CESYW/OUTPUT/CW/'//FNAME1
      OUTPUTDI='/USER/GDR/CE/S/CESYW/OUTPUT/J/'//FNAME2
      OUTSHEAR='/USER/GDR/CE/S/CESYW/OUTPUT/SHEAR/'//FNAME3
      OPEN (21,FILE=INPUTDIR)
      OPEN (22,FILE=OUTPUTDI)
      OPEN (23,FILE=OUTSHEAR)
      READ(1,*)((TIME(I),(SH(I,J),J=1,NX)),I=1,NT)
      DO 100 I=1,NT
100   READ(2,*) TTIME,DP(I)
      DP1=0.D0
      DO 101 I=1,NT
101   DP1=DP1+DP(I)
      DP1=DP1/NT
```

```
        NNX = NX
C  ALWAYS USE STEADY DP TO KEEP TMPSTEADY = TMPOSC, WHICH IS
C  EQUIVALENT TO ADJUST PINLETOSC. TO LET TMPSTEADY = TMPOSC
        TMP = PINLET-.5D0*DP1*.25*RE*RE/RO*AMU*AMU/R/R
        DO 10 I = 1,NT
C       TMP = PINLET-.5D0*DP(I)*.25*RE*RE/RO*AMU*AMU/R/R
        DO 10 J = 1,NNX
        AK = .816*(.5/R/R*AMU/RO*RE*DABS(SH(I,J))/AL*D*D)**(.33)
        CW(I,J) = RTNEWT(FUNCD,X1,X2,XACC,ITERAT)
10      AJ(I,J) = AJFUN(CW(I,J))
        WRITE(11,99)((TIME(I),(CW(I,J),J = 1,NNX)),I = 1,NT)
        WRITE(12,99)((TIME(I),(AJ(I,J)*1.D6,J = 1,NNX)),I = 1,NT)
        AAJ = 0.D0
        DO 3 J = 1,NNX
        DO 3 I = 1,NT
3       AAJ = AAJ + AJ(I,J)
        AAJ = AAJ/NNX/NT
        WRITE(22,990)AAJ*1.D6
        DO 1 J = 1,NNX
        CCW = 0.D0
        AAJ = 0.D0
        AVGSHE = 0.D0
        DO 2 I = 1,NT
        AVGSHE = AVGSHE + SH(I,J)
        AAJ = AAJ + AJ(I,J)
2       CCW = CCW + CW(I,J)
        AAJ = AAJ/NT
        CCW = CCW/NT
        AVGSHE = AVGSHE/NT
        WRITE(21,990)CCW
        WRITE(22,990)AAJ*1.D6
        WRITE(23,990)AVGSHE
1       CONTINUE
99      FORMAT(7(6(E11.4,X),/))
990     FORMAT(1X,F12.5)
        END
        SUBROUTINE FUNCD(X,FN,DF)
        IMPLICIT DOUBLE PRECISION(A-H,O-Z)
        COMMON /USER/RM,AK,A1,A2,A3,CB,TMP
        FN = RM*AK*DLOG(X) + A1*X + A2*X*X + A3*X*X*X-TMP-RM*AK*DLOG(CB)
        DF = RM*AK/X + A1 + A2*X*2. + A3*X*X*3.
        END
        FUNCTION RTNEWT(FUNCD,X1,X2,XACC,ITERAT)
        IMPLICIT DOUBLE PRECISION(A-H,O-Z)
        EXTERNAL FUNCD
        RTNEWT0 = .5*(X1 + X2)
            DO 11 J = 1,ITERAT
            CALL FUNCD(RTNEWT0,F,DF)
            DX = F/DF
            RTNEWT0 = RTNEWT0-DX
            IF((RTNEWT0-X1)*(X2-RTNEWT0).LT.0.)PAUSE'JUMPED OUT OF BRACKETS'
            IF(DABS(DX).LT.XACC)THEN
            RTNEWT = RTNEWT0
            RETURN
            ENDIF
11      CONTINUE
        PAUSE 'RTNEWT EXCEEDING MAXIMUM ITERATIONS,PLEASE INCREASE ITERAT
        1OR REDUCE XACC'
        END
        FUNCTION AJFUN(CW)
        IMPLICIT DOUBLE PRECISION(A-H,O-Z)
        COMMON /USER/RM,AK,A1,A2,A3,CB,TMP
        AJFUN = (TMP-A1*CW-A2*CW*CW-A3*CW*CW*CW)/RM
        END
```

NOMENCLATURE

The section where each term is first used or defined is stated in the last column.

a_i	osmotic virial coefficient	-	2.1.4
A_f	free area of contraction	m^2	2.1.2
A_{et}	flow area of contraction	m^2	2.1.2
C	concentration	kg/l	2.1.2
C_b	bulk concentration	kg/l	2.1.4
C_w	boundary layer concentration	kg/l	2.1.4
d	diameter of tube	m	2.1.2
D	diffusivity	m^2/s	2.1.4
f	frequency of oscillation	1/s	2.1.2
FNT	oscillatory source function	-	2.2.1
H	rectangular channel height	m	2.1.2
k	mass transfer coefficient	m/s	2.1.4
k'	local mass transfer coefficient	m/s	6.2
K	power-law consistency index	-	7.3
J	membrane flux	m/s	2.1.4
L	baffle spacing	m	2.1.2
n	the power-law index	-	7.3
NFR	net to peak flow ratio	-	2.1.2
p	dimensionless pressure	-	2.1.3

Symbol	Description	Unit	Section
$\bar{p}$	dimensional pressure	Pa	2.1.3
ΔP	dimensionless one cell pressure drop	-	2.2.3
$\Delta\bar{p}$	dimensional pressure drop	Pa	5.2.1
ΔP_{TM}	transmembrane pressure	Pa	2.1.4
$\Delta \dot{P}'_{TM}$	the local transmembrane pressure	Pa	6.2
$\overline{PD}$	dimensional power density	Watt/m^3	5.2
P_{inlet}	inlet pressure	Pa	2.2.4
$\overline{PD}_s$	power per unit membrane surface area	Watt/m^2	6.4
PD	dimensionless power density	-	2.2.3,5.2
$\overline{PD}_p$	power per unit permeate volume	Watts/m^3	6.4
r	radial coordinate	-	2.1.3
$\bar{r}$	dimensional radial coordinate	-	2.1.3
R	tube radius	m	2.1.2
R_f	the resistance of fouling layer	Pa.s/m	2.1.4
R_m	membrane resistance	Pa.s/m	2.1.4
Re	Reynolds number	-	2.1.2
Re_n	net flow Reynolds number	-	3.1.1
Re_o	oscillatory Reynolds number	-	1.2
St	Strouhal number	-	1.2
t	dimensionless time	-	2.1.3
$\bar{t}$	dimensional time	s	2.1.3
Δt	dimensionless time step	-	6.3.2

u	dimensionless axial velocity	-	2.1.3
$\bar{u}$	dimensional axial velocity	m/s	2.1.3
U_m	mean velocity	m/s	2.1.2
$\bar{U}_i$	instantaneous velocity	m/s	2.2.1
U_R	reference velocity	m/s	2.2.1
v	dimensionless transverse velocity	-	2.1.3
$\bar{v}$	dimensional transverse velocity	m/s	2.1.3
v_p	maximum pulsed velocity	m/s	2.1.2
$\bar{v}_w$	dimensional wall flux	m/s	3.1.2
v_w	dimensionless wall flux	-	2.2.1
$\dot{v}$	particle random velocity	m/s	2.2.2
x	axial coordinate	-	2.1.3
x_0	amplitude	m	2.1.2
$\bar{x}$	dimensional axial coordinate	-	2.1.3
y	transverse coordinate	-	2.1.3
$\bar{y}$	dimensional transverse coordinate	-	2.1.3
β	baffle flow area ratio	-	2.1.2
λ	interbaffle spacing ratio	-	2.1.2
ρ	density of bulk solution	kg/m^3	2.2.1
μ	viscosity of bulk solution	Pa.s	2.1.2
τ_0	shear stress	Pa	6.3.2
$\dot{\gamma}$	shear rate	1/s	2.2.4

$\dot{\gamma}$	dimensionless shear rate	-	4.2
$\dot{\gamma}_t$	dimensionless time average wall shear rate	-	4.2
$\dot{\gamma}_{at}$	dimensionless average wall shear rate	-	4.2
ω	vorticity	-	2.1.3
Ψ	stream function	-	2.1.3
Ψ_{max}	vortex strength	-	2.1.3
Π	osmotic pressure	Pa	2.1.4

REFERENCE

Aimar, P., Howell, J.A. and Turner, N.M., (1989), "Effects of the Boundary Layer Development on the Flux Limitation in Ultrafiltration", *Chem. Eng. Res. Des.*, **67**, 255

Altena, F.W, Belfort, G., Otis., J., Fiessinger, F., Rovel, J.M. and Nicoletti, J., (1983), "Particels Motion in a Laminar Slit Flow: A Fundamental Fouling Study", *Desalination*, **47**, 221-232

Bashir, I. and Reuss, M., (1992), "Dynamic Model for Cross-Flow Microfiltration of Microbial Suspensions in Porous Tubes", *Chem. Engr. Sci.*, **47**, 189-203

Beeton, S., Millward, H.R., Bellhouse, B.J., Nicholson, A.M., Jenkins, N. and Knowles, C.J., (1991), "Gas Transfer Characteristics of a Novel Membrane Bioreactor", *Biotech. and Bioengr.*, **38**, 1233-1238

Belfort, G. and Nagata, N., (1985), "Fluid Mechanics and Cross-flow Filtration: Some Thoughts", *Desalination*, **53**, 57-59

Belfort, G., (1989), "Fluid Mechanics in Membrane Filtration: Recent Developments", *J. Membrane Sci.*, **40**, 123-147

Bellhouse, B.J., Bellhouse, F.H., Curl, C.M., MacMillan, T.I., Gunning, A.J., Spratt,E.H., MacMurray, S.B. and Nelems, J.M., (1973), "A High Efficiency Membrane Oxygenator and Pulsatile Pumping System, and its application to animal trials", *Trans Amer Soc Artif Int Organs*, **19**, 72-79

Berman, A.S., (1953), "Laminar Flow in Channels with Porous Walls", *J. Applied Phy.*, **24**, 1233

Brunold, C.R., Hunns, J.C.B., Mackley, M.R. and Thompson, J.W., (1989), "Experimental Observations on Flow Patterns and Energy Losses for Oscillatory Flow in Ducts Containing Sharp Edges", *Chem. Eng. Sci.*, **44**, 1227-1244

Chang, L.J. and Tarbell, J.M, (1985), "Numerical Simulation of Fully Developed Sinusoidal and Pulsatile (physiological) Flow in Curved Tubes", *J. Fluid Mech.*, **161**, 175-198

Cheng, R.T., Clark, M.E. and Robertson, J.M., (1972), "Numerical Calculations of Oscillatory Flow in the Vicinity of square Wall Obstacles in Plane Conduits", *J.Biomech.*, **5**, 467

Cheng, R.T., (1972), "Numerical Solution of the Navier-Stokes Equations by the Finite Element Method", *Phys. Fluids*, **15**, 2098

Cheng, R.T., Robertson, J.M. and Clark, M.E., (1973), "Numerical Calculations

of Oscillatory Nonuniform flow. II. Parametric Study of Pressure Gradient and Frequency with Square Wall Obstacles", J.Biomech., **6**, 521

Chow, J.C.F. and Soda, K., (1972), "Laminar Flow in Tubes with Constriction", *Phys. Fluids*, **15**, 1700

Clifton, M.J., Abidine, N., Aptel, P. and Sanchez, V., (1984), "Growth of the Polarisation Layer in Ultrafiltration with Hollow-Fibre membranes", *J. Membrane Sci.*, **21**, 233

Edwards, M.F. and Wilkinson, W.L., (1971), "Review of Potential Applications of Pulsating Flow in Pipes", *Trans. IChemE*, **49**, 85-93

Finnigan, S.M. and Howell, J.A., (1989), "The Effect of Pulsatile Flow on Ultrafiltration Fluxes in a Baffled Tubular Membrane System", *Chem. Eng. Res. Des.*, **67**, 278

Finnigan, S.M., (1990), "Pulsed Flow Ultrafiltration in Baffled Tubular Membranes", *PhD Thesis*, University of Bath

Fulton, S.R., Ciesielski, P. and Schubert, W.H., (1986), "Multigrid Methods for Elliptic Problems: A Review", *Monthly Weather Review*, **114**, 943-959

Gallagher, R.H., Glowinski, R., Gresho, P. M., Oden J.T. and Zienkiewicz, O.C.,

(1987), Finite Elements in Fluids - Volume 7, John Wiley & Sons Ltd., New York

Gekas, V. and Hallström, B., (1987), "Mass Transfer in the Membrane Concentration Polarization Layer under Turbulent Cross Flow: I. Critical Literature Review and Adaptation of Existing Sherwood Correlation to Membrane Operations", *J. Membrane Sci.*, **30**, 153-170

Granger, J., Dodds, J. and Midoux, N., (1989), "Laminar Flow in Channels with Porous Walls", *The Chem. Eng.*,**42**, 193-204

Greenspan, D., (1973), "Numerical Studies of Incompressible Flow through an Orifice for Arbitrary Reynolds Number", *Int. J. Num. Meth. in Eng.*, **6**, 489

Howell, J.A., Field, R.W., Mackley, M.R. and Wang, Y., (1992a), "the Simulation of Particle Advection in a Porous Baffled Channel Subject to Pulsatile Flow", *The 1992 IChemE Research Event*, UMIST, UK, 386-388

Howell, J.A., Field, R.W and Wu, D., (1992b), "Yeast Cell Harvesting:Flux Enhancement in Baffled and Pulsatile Flow Systems", *Conf. of Engineering of Membrane Processes*, Bavaria, Germany

Howes, T., (1988), "On the Dispersion of Unsteady Flow in Baffled Tubes", *PhD Thesis*, University of Cambridge

Howes, T., Mackley, M.R. and Roberts, E.P.L., (1991), "The Simulation of Chaotic Mixing and Dispersion for Periodic Flows in Baffled Channel", *Chem. Engr. Sci.*, **46**, 1669-1677

Hung, T.K. and Macagno, E.O., (1966), "Laminar eddies in a two-dimensional conduit expansion", *La Houille Blanche*, **21**, 391

Ilias, S. and Govind, R., (1988), "Fluid Dynamics of Dilute Suspensions and Fouling of Tubular Membrane Modules", *J. Membrane Sci.*, **39**, 125-141

Johnson, G.A., Borovetz, H.S. and Anderson, J.L., (1992), "A Model of Pulsatile Flow in a Uniform Deformable Vessel", *J. Biomechanics*, **25**, 91-100

Jonsson, G., (1984), "Boundary Layer Phenomena During Ultrafiltration of Dextran and Whey Protein Solutions", *Desalination*, **51**, 61-77

Kleinstreuer, C. and Belfort, G., (1984), "Mathematical Modelling of Fluid Flow and Solute Distribution in Pressure-Driven Membrane Modules", Chapter 5 in *Synthetic Membrane Processes* (Ed. Belfort, G.), Academic Press, Orlando, 131-190

Kozinski, A.A., Schmidt, F.P. and Lightfoot, E.N., (1970), "Velocity Profiles in Porous-Walled Ducts", *Ind. Eng. Chem. Fundam.*, **9**, 502-505

Mackay, M.E., Mackley M.R. and Wang, Y., (1991), "Oscillatory Flow Within Tubes Containing Wall or Central Baffles", *Trans IChemE*, **69 Part A**, 506-513

Mackley, M.R., (1987), "Using Oscillatory Flow to Improve Performance", *The Chem. Engr.*, **43**, 18-20

Mills, R.D., (1968), "Numerical Solutions of Viscous Flow through a Pipe Orifice at Low Reynolds Numbers", *J. Mech. Eng. Sci.*, **10**, 133

Nishimura, T. and Miyashita, H., (1989), "Effect of Strouhal Number on Flow Characteristics in a Symmetric Sinusoidal Wavy-Walled Channel", *J. of Chem. Engr. of Japan*, **22**, 505-511

Ohmi, M. and Iguchi, M., (1982), "Flow patterns and Frictional Losses in an Oscillating Pipe Flow", *Bulletin of the JSME*, **25**, 536-543

Pangrle, B.J, Alexandrou, A.N., Dixon, A.G. and Dibiasio, D., (1991), "An Analysis of Laminar Fluid Flow in Porous Tube and Shell Systems", *Chem. Engr. Sci.*, **46**, 2847-2855

Pantankar, S.V, (1980), *Numerical Heat Transfer and Fluid Flow*, Hemisphere Publishing Corporation, Washington

Peyret, R. and Taylor, T.D., (1986), *Computational Methods for Fluid Flow*, Springer-Verlag, New York

Porter, M.C., (1972), "Concentration Polarization with Membrane Ultrafiltration", *Ind. Eng. Chem. Prod. Res. Develop.*, **11**, 234-248

Pritchard, M., (1990), "The Influence of Rheology upon Mass Transfer in Cross-flow Membrane Filtration", *PhD Thesis*, University of Bath

Ralph, M.E., (1986), "Oscillatory flows in wavy-walled tubes", *J. Fluid Mech.*, **168**, 515

Ralph, M.E., (1987), "Steady Flow Structures and Pressure Drops in Wavy-walled tubes", *J. Fluid Engr.*, **109**, 255-261

Ralph, M.E., (1988), "Pressure Drop and Power Dissipation in Oscillatory in Wavy-walled-tube Flows ", *J. Fluid Mech.*, **187**, 573-588

Rautenbach, R. and Albrecht R., (1989), *Membrane Processes*, Wily-Interscience

Roache, P.J., (1976), *Computational Fluid Dynamics*, Hermosa, Albuquerque

Rowley, G.J.and Patankar, S.V., (1984), "Analysis of Laminar Flow and Heat

Transfer in Tubes with Internal Circumferential Fins", *Int. J. Heat Mass Trans.*, **27**, 553

Schmitz, P., Gouverneur, C., Houi, D. and Madianos, M., (1990), "Theoretical Model at Pore Scale for Particle Deposition on a Crossflow Microfiltration Membrane", *Proceedings--Vth World Filtration Congress*, 571-578

Sharratt, P. N., (1990), "Computational Fluid Dynamics and Its Application in the Process Industries", *Trans. IChemE*, **68 Part A**, 13-18

Sobey, I.J., (1980), "On Flow Through Furrowed Channels. Part 1. Calculated Flow Patterns", *J. Fluid Mech.*, **96**, 1-26

Sobey, I.J., (1983), "The Occurrence of Separation in Oscillatory Flow", *J. Fluid Mech.*, **134**, 247-257

Sobey, I.J., (1985a), "Dispersion Caused by Separation During Oscillatory Flow Through a Furrowed Channel", *Chem. Eng. Sci.*, **40**, 2129-2134

Sobey, I.J., (1985b), "Observation of Waves During Oscillatory Channel Flow", *J. Fluid Mech.*, **151**, 395-426

Stephanoff, K.D., Sobey, I.J. and Bellhouse, B.J., (1980), "On Flow Through Furrowed Channels. Part 2. Observed Flow Patterns", *J. Fluid Mech.*, **96**, 27-32

Trettin, D.R. and Doshi, M.R., (1981), "Pressure-independent Ultrafiltration - Is it Gel Limited or Osmotic-pressure Limited, in: Turbak, A.F.(Ed), *Synthetic Membrane, Vol. II, Hyper and Ultrafiltration Uses*, American Chem. Soc., Washington, 373

Turker, M. and Hubble, J., (1987), "Membrane Fouling in a Constant Flux Ultrafiltration Cell", *J. Membrane Sci.*, 34, 267

Vetterling, W.T., Teukolsky, S.A, Press, W.H and Flannery, B.P, (1985), *Numerical Recipes*, Cambridge University Press, Cambridge

Vilker, V.L., Colton, C.K. and Smith, K.A., (1981), "Concentration Polarization in Protein Ultrafiltration, *AIChE J*, 27, 632

Wales, M., (1981), "Pressure Drop across Polarization Layers in Ultrafiltration, in: Turbak, A.F.(Ed), *Synthetic Membrane, Vol. I, Desalination*, American Chem. Soc., Washington, 159

Wang, Y., Howell, J.A., Field, R.W. and Wu, D., (1993), "Simulation for Cross-flow Filtration in Baffled Channel with Pulsatile Flow", *The 1993 I.Chem.E Research Event*, Birmingham, U.K., 147-149